Technische Universität München
Lehrstuhl für Netzwerktheorie und Signalverarbeitung

Design, analysis and demonstration of a hybrid analog/digital retro-directive antenna system for satellite communications

Andreas R. T. Winterstein

Vollständiger Abdruck der von der Fakultät für Elektrotechnik und Informationstechnik der Technischen Universität München zur Erlangung des akademischen Grades eines

Doktor-Ingenieurs

genehmigten Dissertation.

Vorsitzender: Prof. Dr. sc. nat. Christoph Günther
Prüfer der Dissertation:
1. Prof. Dr. techn. Josef A. Nossek
2. Prof. Dr.-Ing. Marcos V. T. Heckler

Die Dissertation wurde am 30.08.2018 bei der Technischen Universität München eingereicht und durch die Fakultät für Elektrotechnik und Informationstechnik am 27.01.2019 angenommen.

Abstract

The goal of this thesis is to propose and validate a retro-directive antenna (RDA) system which is applicable for satellite communications. RDAs have been suggested at the end of the 1950s and their usage in satellite communications was proposed shortly thereafter. Inherent properties of RDAs are automatic self-tracking of mobile terminals, low complexity and power consumption, good scalability and the lack of complex digital signal processing (DSP). Although these are appealing features, there are no commercial RDAs in use up to the present time. This is due to the additional requirements imposed on antenna systems for satellite communications. We begin this thesis by introducing the retro-directive principle, the so-called phase conjugation, and its advantages. We contrast these properties with the demands in satellite communications. These are the need for different frequency bands for transmit and receive, the use of the antenna gain which plays a crucial role in the link budget, and the ability to operate in full duplex, i.e. to simultaneously receive and transmit. By an extensive literature review, we show that conventional RDAs are not able to fulfill these requirements.

From the demands of satellite communications, we deduce requirements for an ideal retro-directive transceiver for such applications. Using these requirements, we design an analog/digital hybrid system architecture. In contrast to conventional RDAs, the key idea is the separation of analog receiver (Rx) and transmitter (Tx) paths. Information between these paths is exchanged solely via a low-cost DSP unit. This unit processes slowly varying phase information and thus realizes the desired retro-directive behavior of the system. The data carrying signals with high bandwidths are processed exclusively by analog components. Thus we omit the necessity of high speed DSP which is a vital feature of RDAs. Using digital hardware to perform phase conjugation between the Rx and Tx paths, we enable the retro-directive principle for full-duplex, dual frequency operation.

In the following, we focus our analysis on the receiver path which performs the crucial task of extracting the necessary geometric phase information. The proposed receiver system is thereby described by phase transfer functions in the Laplace domain. We propose an optimization technique for the dynamic behavior which aims at improving the location of the slowest system pole. The receiver performance and the effect of the optimization are analyzed by continuous time domain simulations of a C-band example system using Simulink. We find that the receiver is suitable for phase detection down to a signal-to-noise ratio (SNR) of 3 dB. Additionally, we show the capability for phase modulation where we predict a data rate of up to 700 kbit/s.

In order to validate the proposed system architecture, we implement it in digital hardware. For this, we transfer the analytic continuous time system model to the discrete time domain. We show similarity between the continuous and discrete time models both analytically and by simulations. Additionally, we realize the discrete time system on a field-programmable gate array (FPGA) and validate the predicted phase detection performance with errors lower than $\pi/32$ rad. The digital hardware implementation is then used in combination with analog Rx and Tx front-ends as well as an eight element uniform linear array (ULA) to form a complete RDA demonstrator. We characterize this system with antenna measurements in an anechoic chamber where we show direction-of-arrival (DoA) estimation capability with errors smaller than 2.0° over a field-of-view (FoV) of 135°. Finally, we prove the retro-directive capability of our demonstrator system by monostatic and bistatic measurements. We achieve monostatic

behavior using 5.8 GHz Rx and 7.0 GHz Tx frequencies. The variations in the returned Tx power are smaller than 5 dB over a FoV of 113°.

Zusammenfassung

Das Ziel der vorliegenden Arbeit ist, ein retrodirektives Antennensystem (RDA) vorzuschlagen und zu validieren, das in der Satellitenkommunikation verwendet werden kann. Erste RDAs wurden bereits Ende der 1950er Jahre erforscht und auch für Raumfahrtanwendungen vorgeschlagen. Die Grundeigenschaften von RDAs sind automatische Nachverfolgung von sich bewegenden Terminals, niedrige Systemkomplexität und Leistungsaufnahme, gute Skalierbarkeit und das Fehlen von komplexer digitaler Signalverarbeitung. Obwohl diese Eigenschaften sehr attraktiv sind, gibt es bis heute keine kommerziell verwendeten RDAs in der Satellitenkommunikation, da dort zusätzliche Anforderungen an die verwendeten Antennensysteme gestellt werden. In der vorliegenden Arbeit wird zunächst das Funktionsprinzip retrodirektiver Systeme, die sogenannte Phasenkonjugation, und deren Vorteile erklärt. Diese Erkenntnisse werden den Anforderungen an Satellitenkommunikationssysteme gegenübergestellt. Letztere sind zum einen die Notwendigkeit, verschiedene Frequenzbänder beim Senden und Empfangen zu verwenden, zum anderen die Ausnutzung des Antennengewinns, der eine entscheidende Rolle in der Leistungsbilanz der Übertragung spielt. Schließlich muss das System in der Lage sein, im Vollduplexbetrieb zu arbeiten, d.h. gleichzeitig zu senden und zu empfangen. Herkömmliche RDAs können diese Anforderungen nicht umsetzen, was mittels eines Überblicks der relevanten Fachliteratur gezeigt wird.

Aus den Randbedingungen, die Satellitenkommunikationssysteme erfüllen müssen, werden Anforderungen für ein ideales retrodirektives Sende- und Empfangssystem abgeleitet. Unter Berücksichtigung dieser Anforderungen wird daraus eine analog/digitale, hybride Systemarchitektur entwickelt. Im Gegensatz zu herkömmlichen RDAs werden dabei Empfangs- und Sendepfad nicht direkt miteinander verbunden, sondern tauschen über eine kostengünstige digitale Signalverarbeitungseinheit Informationen aus. Diese Digitaleinheit verarbeitet hierbei ausschließlich langsam veränderliche Richtungsinformationen und realisiert dadurch das retrodirektive Verhalten des Systems. Im Gegenzug werden alle datentragenden Signale ausschließlich von breitbandig ausgelegten analogen Systemteilen verarbeitet. Dadurch wird die Notwendigkeit von hochratigen digitalen Systemen vermieden, was eine der wichtigsten Eigenschaften von RDAs ist. Durch die Nutzung digitaler Komponenten für die Phasenkonjugation zwischen Empfangs- und Sendepfad, wird retrodirektives Verhalten im Vollduplexbetrieb auf unterschiedlichen Frequenzen ermöglicht.

Es folgt eine detaillierte Analyse des Empfangszugs, in dem die relevante Phaseninformation gewonnen wird. Das vorgeschlagene Empfangssystem wird dafür mit Hilfe von Phasenübertragungsfunktionen im Laplace Bereich beschrieben. Zur Optimierung des dynamischen Verhaltens wird eine Methode vorgeschlagen, die die Lage der langsamsten Polstelle des Systems verbessert. Die Leistungsfähigkeit des Empfängers und die Auswirkungen der Optimierung werden daraufhin anhand eines C-Band-Beispielsystems in Simulink numerisch untersucht. Dabei zeigt sich, dass der Empfänger bis zu einem Signal-Rausch-Verhältnis von 3 dB Phasenunterschiede erfolgreich detektieren kann. Zudem wird der Nachweis erbracht, dass eine Phasenmodulation der Empfangssignale von bis zu 700 kbit/s direkt verarbeitet werden kann.

Um die vorgeschlagene Systemarchitektur zu validieren, wird eine Implementierung in digitaler Hardware vorgenommen. Dafür wird das zuvor beschriebene zeitkontinuierliche analoge Systemmodel in den diskreten Zeitbereich überführt. Hierbei wird die Ähnlichkeit der kontinuierlichen und diskreten Modelle sowohl analytisch als auch in Simulationen ge-

zeigt. Anschließend wird das zeitdiskrete System auf einem Field Programmable Gate Array (FPGA) implementiert, um die Güte der Phasendetektion zu untersuchen. Dabei werden Abweichungen kleiner als $\pi/32$ rad nachgewiesen. Die digitale Implementierung wird schließlich mit analogen Empfangs- und Sendemodulen sowie einem Linienarray aus acht Antennen zu einem funktionsfähigen retrodirektiven Demonstrationssystem kombiniert. In einer Antennenmesskammer kann mittels der Phasendetektion eine Richtungsschätzung mit Fehlern kleiner 2,0° über einen Winkelbereich von 135° gezeigt werden. Schließlich wird das retrodirektive Verhalten des Gesamtsystems durch monostatische und bistatische Messungen mit einer Empfangsfrequenz von 5,8 GHz und einer Sendefrequenz von 7,0 GHz nachgewiesen. Die dabei zurückgestrahlte Sendeleistung variiert um weniger als 5 dB in einem Sichtbereich von 113°.

Danksagung

Zuallererst möchte ich Professor Josef A. Nossek dafür danken, dass er meine Doktorarbeit betreut hat, obwohl ich nie am Lehrstuhl für Netzwerktheorie und Signalverarbeitung der Technischen Universität München studiert oder gearbeitet habe. Auch wenn mein Thema an seinem Lehrstuhl eine Ausnahme bildete, hat Professor Nossek meine Arbeit von Anfang an unterstützt. Die fachlichen Diskussionen mit ihm haben mir stets weiter geholfen. Besonders möchte ich auch Professor Marcos V. T. Heckler danken, dass er sich als Prüfer meiner Arbeit zur Verfügung gestellt hat und dafür die weite Reise von Alegrete nach München unternommen hat.

Die Rahmenbedingungen für meine Forschungstätigkeit wurden durch die Verantwortlichen am Institut für Kommunikation und Navigation des Deutschen Zentrums für Luft- und Raumfahrt (DLR) geschaffen. Daher möchte ich mich zunächst beim Leiter der Antennengruppe, Dr. Achim Dreher bedanken. Dr. Dreher hat mein Promotionsvorhaben von Anfang an begleitet. Regelmäßige Treffen, das Korrekturlesen meiner Publikationen und angeregte Diskussionen haben mein Vorhaben wesentlich vorangebracht. Mein Dank gilt außerdem dem Leiter der Abteilung Navigation, Professor Michael Meurer, dafür, dass ich das Nischenthema Satellitenkommunikation in seiner Abteilung bearbeiten konnte.

Ohne die Unterstützung meiner Kollegen wäre diese Arbeit nie geschrieben worden. Zuallererst möchte ich Dr. Lukasz Greda danken, mit dem ich von Anfang an eng zusammenarbeiten durfte. Lukasz hat essenziell zu meiner Doktorarbeit beigetragen: Neben ausführlicher fachlicher Beratung hat er die Organisation der Kooperation mit der brasilianischen UNIPAMPA und die Projektleitung bei Vorhaben wie DLR@Uni und RADIANT übernommen. Innerhalb dieser Randbedingungen hatte ich stets die Möglichkeit, mich auf die wissenschaftlich-technischen Arbeiten zu konzentrieren und meine Forschung voranzutreiben.

Besonders viel Freude hat mir dabei das Arbeiten mit Hardware und Messgeräten bereitet. Die hier gezeigten Aufbauten und Messungen wären nicht entstanden ohne die Expertise und den unermüdlichen Einsatz meiner Kollegen Georg Buchner, Wahid Elmarissi und Korbinian Zangl. Ihre Einsätze reichten von Fragen zur Messtechnik, Bestückung meiner Platinen, Gehäusefertigung und mechanische Aufbauten bis hin zu Notfall-Reparaturen meiner Versuchsaufbauten kurz vor wichtigen Terminen. Ebenso möchte ich die Entwicklungsarbeiten meiner beiden brasilianischen Studenten, Marcelo Pereira Magalhães und Daniel Lima Lemes, hervorheben, die wesentlich zum Aufbau der Sendefrontends beigetragen haben. Auch Bernd Gabler vom Institut für Hochfrequenztechnik und Radarsysteme möchte ich für seine Unterstützung und die Durchführung der gezeigten Antennenmessungen danken. Ebenfalls bedanken möchte ich mich bei Lothar Kurz für seine Hilfe bei Fragen zu digitaler Hardware und VHDL-Programmierung sowie für das Bereitstellen des Strahlformungsmoduls für meinen retrodirektiven Demonstrator. Abschließend gilt mein Dank allen übrigen Kollegen der Abteilung Navigation, insbesondere Anja Grosch, Veenu Kamra, Lothar Kurz, Monika Eiber, Stefano Caizzone, Manuel Cuntz, Emilio Perez Marcos, Manuel Appel und Friederike Fohlmeister.

Außerhalb meiner Arbeitsstelle bedanke ich mich bei meinen Freunden für ihre Geduld und ihr Verständnis gerade während der Schreibphasen. Besonders möchte ich dabei die Pfadfinder vom DPSG Parsbergstamm Germering erwähnen, allen voran meine Vorstandskollegin Sylvia Wauthier. Meine Dankbarkeit gilt außerdem meinen Eltern, die früh mein

Interesse für Technik geweckt und gefördert haben. Ihrer Unterstützung konnte ich mir von der Schulzeit über Studium und Beruf bis heute immer sicher sein. Auch bei meinem Bruder möchte ich mich für die aufmunternden Gespräche bedanken.

Abschließend gilt mein größter Dank meiner Frau, Dr. Franziska Winterstein, die mein gesamtes Promotionsvorhaben von Anfang an mit allen Höhen und Tiefen begleitet hat. Im Gegensatz zu mir hat sie immer an den erfolgreichen Abschluss geglaubt und mich zum Weitermachen ermutigt. Dafür werde ich dir immer dankbar sein.

Germering, im März 2019.

Contents

1 Introduction

Retro-directive systems have several features which are desirable in satellite communication. Among these are automatic self-tracking of mobile terminals, simple system architectures compared to smart antenna designs and low power consumption. However, in satellite communication applications we find certain restrictions which hamper the use of classic retro-directive architectures. The necessity of different frequency bands for receive and transmit, modulated signals and high antenna gain are examples [1, c.1].

In this chapter, we shall first discuss the principles behind retro-directivity and illustrate the benefits of this concept. After that, we take a closer look at the specific requirements in the field of satellite communication. In the final section, we will describe the contributions of this thesis to bring these two topics together.

1.1 The retro-directive principle

Retro-directivity is a behavior which is most widely known from optical retroreflectors. Their purpose is to reflect incident light back towards its source. This property makes retroreflective sheeting ubiquitous in everyday items which require high visibility like vehicles, traffic signs, workwear, outdoor clothing, etc.

The corner reflector is a very descriptive example for retro-directive behavior. It consists either of a three sided glass prism or of three perpendicular mirroring sheets. Let us assume the reflector sheets are aligned along the coordinate planes. We can describe the unit vector of the incident direction of a light ray in Cartesian coordinates by

$$\vec{e}_{\mathrm{i}} = \begin{pmatrix} -\sin\theta\cos\phi \\ -\sin\theta\sin\phi \\ -\cos\theta \end{pmatrix}, \tag{1.1}$$

whereby θ and ϕ denote the zenith and azimuth angles as shown in Fig. 1.1a. Ideal reflection

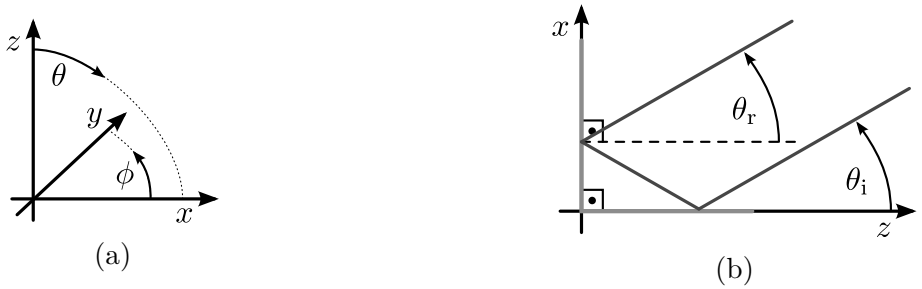

Fig. 1.1: (a) Cartesian coordinate system showing zenith and azimuth angles. (b) Retro-directive operation of a corner reflector in 2D space.

at any plane inverses the sign of the normal component of $\vec{e}_\mathrm{i}$, i.e. reflection at the x,y-plane inverts the z component. Therefore, after encountering all three reflecting sheets, we obtain the direction of the returning light ray to be $\vec{e}_\mathrm{r} = -\vec{e}_\mathrm{i}$. Fig. 1.1b illustrates the corner reflector in 2D space, i.e. for $\phi = 0$ where $\theta_\mathrm{r} = \theta_\mathrm{i}$.

Optical retroreflectors are also used for scientific purposes. During the Apollo missions, some have been left on the Moon [2, 3]. Laser beams are pointed towards their location to measure the distance between Earth and Moon from the round-trip delay. Moreover, retroreflectors are used for satellite laser ranging (SLR) to monitor spacecraft orbits [4].

The corner reflector is an example for a simple retro-directive system. In general, such systems return energy towards the direction it was originally coming from. This is done without any prior knowledge of the incident direction. We shall regard the underlying principles more closely in the following.

1.1.1 Phase conjugation

In optics and radio frequency (RF) applications, retro-directivity implies, that there is an incident and an outgoing electro-magnetic (EM) wave and that their directions of propagation are opposite. A homogeneous, planar, harmonic EM wave of angular frequency ω can be described by its electric field vector [5]

$$\vec{E}(\vec{r},t) = \frac{1}{2}\vec{E}_0(\vec{r})\left(e^{-j\left(\omega t - \vec{k}^T\vec{r}\right)} + e^{\,j\left(\omega t - \vec{k}^T\vec{r}\right)}\right) = \vec{E}_0(\vec{r})\cos\left(\omega t - \vec{k}^T\vec{r}\right), \tag{1.2}$$

where $\vec{r}$ is the position vector, t denotes continuous time and $\vec{E}_0 \in \mathbb{C}^3$ is the complex amplitude vector of the electric field. $\vec{E}_0 = E_0\vec{p}$ incorporates the real amplitude and complex polarization state of the EM wave, whereby $\vec{p}$ is a unitary vector [6, p.392]. $(\cdot)^T$ denotes the transposed of a vector or matrix. $\vec{k}$ is the wave vector, which points towards the direction of propagation and whose length is the wave number. It can be written as

$$\vec{k} = \begin{pmatrix} k_x \\ k_y \\ k_z \end{pmatrix} = \frac{2\pi}{\lambda}\begin{pmatrix} k_x \\ k_y \\ k_z \end{pmatrix}\frac{1}{|\vec{k}|}, \tag{1.3}$$

where $\lambda = \frac{2\pi c_0}{\omega}$ is the wavelength, $|\vec{k}|$ is the wave number and c_0 is the speed of light in vacuum. If an EM wave according to (1.2) is present, the goal of retro-directive operation is to generate an EM wave with wave vector $\vec{k}_r = -\vec{k}$. Inserting this in (1.2), we obtain the retransmitted harmonic wave traveling in opposite direction, i.e.

$$\vec{E}_r(\vec{r},t) = \vec{E}_0(\vec{r})\cos\left(\omega t + \vec{k}^T\vec{r}\right). \tag{1.4}$$

The operation applied to the incident wave is called phase conjugation since the frequency term of the wave remains unaltered but the sign of the phase term has been changed. Any retro-directive system applies this concept but there are different methods to achieve phase conjugation.

1.1.2 Antenna array signal model

In the above example of the corner reflector, geometric optics was used to backscatter energy towards the direction it was received from. However, with an array of antennas capable to

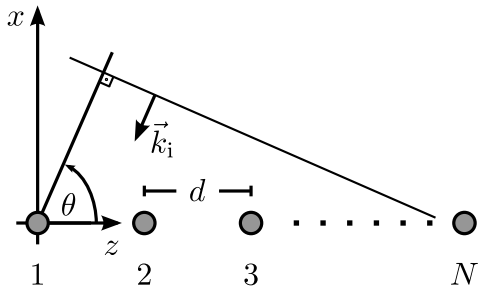

Fig. 1.2: A wave front impinging on a linear array of isotropic radiators.

receive and transmit, it is possible to achieve retro-directive operation as well. Let us regard a uniform linear array (ULA) of N isotropic radiators. The isotropic radiator is a theoretical construct but its behavior in one coordinate plane can be described by a Hertzian dipole [7] and approximated by actual dipoles. Let us assume that a harmonic EM wave is impinging on the ULA as shown in Fig. 1.2. The array elements are positioned along the z-axis at

$$z_n = (n-1) \cdot d, \quad n \in 1, \ldots, N, \tag{1.5}$$

where d denotes the spacing between the array elements. We assume that the ULA is located at a distance far enough from the impinging field source such that far field conditions apply. Thus, we can assume the impinging wave to be planar as depicted in Fig. 1.2. The incident direction of the impinging wave is denoted by θ. Using (1.3), we can determine the wave vector of the incident wave to be

$$\vec{k}_\mathrm{i} = \frac{2\pi}{\lambda} \begin{pmatrix} -\sin\theta \\ 0 \\ -\cos\theta \end{pmatrix}. \tag{1.6}$$

Neglecting any scattering effects of our ULA, we obtain the incident EM field at the position of each ULA element by inserting (1.5) and (1.6) into (1.2) which yields

$$\vec{E}_\mathrm{i}(z_n \vec{e}_z, t) = \vec{E}_0 \cos\left(\omega t + \underbrace{\frac{2\pi d}{\lambda}(n-1)\cos\theta}_{:=\delta_n(\theta)}\right), \tag{1.7}$$

where $\vec{E}_0$ denotes the constant, complex amplitude of the plane wave and $\delta_n(\theta)$ is the phase difference at the n-th array element due to its location and the incident direction. Equivalently, the phase difference results from the wavefront reaching each ULA element after a time difference

$$\Delta\tau_n(\theta) = -\frac{z_n}{c_0}\cos\theta = -\frac{\delta_n(\theta)}{\omega}, \tag{1.8}$$

where we have taken element $n = 1$ as reference, i.e. $\Delta\tau_1(\theta) = 0$. It should be noted that this relation between propagation delay and phase term at the antenna elements is valid as long as the impinging waveform fulfills the narrowband assumption. That means, the propagation time of the impinging wave over the whole array is negligible compared to its inverse bandwidth [8].

In general, an antenna is the interface between guided and radiated EM waves. We shall use the following model for the antennas in our array: The ability of an antenna to transform the EM field (1.2) into a port voltage can generally be described by

$$v_{\mathrm{Ant}}(t) = \underbrace{|\vec{p}_{\mathrm{Ant}}^{H}\vec{p}|^2 l_{\mathrm{eff}} E_0}_{:=\hat{v}_{\mathrm{Ant}}} \cos\left(\omega t - \vec{k}^T\vec{r}_{\mathrm{Ant}}\right), \tag{1.9}$$

where $\vec{r}_{\mathrm{Ant}}$ is the position of the antenna, $\vec{p}_{\mathrm{Ant}}$ denotes the polarization of the antenna [6, 9] and $\vec{p}$ describes the polarization of the EM wave. The effective length of the antenna l_{eff} is an auxiliary quantity dependent on the antenna gain. From (1.9) it is clear that the antenna port voltage amplitude $\hat{v}_{\mathrm{Ant}}$ is proportional to the EM field at the location of the antenna. Using an antenna array, we obtain information about the EM field at different locations. Retro-directivity is then achieved by generating a phase conjugated EM field at these antenna locations. Although the wave which is then transmitted by the array is not planar, its maximum field strength occurs in the direction of the incident plane wave. Thus it acts as a retro-directive system since energy is returned towards the direction of the incident wave. In the following, let us regard two illustrating examples how phase conjugation can be achieved using an array of antennas.

1.1.3 The van Atta array

A simple but efficient way to achieve phase conjugation with an antenna array was patented by Lester Clare van Atta in 1959 [10]. He proposed pairwise connections between the elements of a ULA with transmission lines of equal length ℓ. The interconnection scheme has to be such that the elements n and $N-n+1$ are connected. This is shown for an array of $N=4$ elements in Fig. 1.3a where $\ell = \ell_{14} = \ell_{23}$. Given the incident wave from (1.7), we obtain a retransmitted field at the n-th element of our ULA which reads

$$\begin{aligned}\vec{E}_{\mathrm{r}}(z_n\vec{e}_z, t) &= \vec{E}_0{}' \cos\left(\omega\left(t - \frac{\ell}{c}\right) + \delta_{N-n+1}(\theta)\right) \\ &= \vec{E}_0{}' \cos\left(\omega\left(t - \frac{\ell}{c} - \frac{z_N\cos\theta}{c_0}\right) - \delta_n(\theta)\right),\end{aligned} \tag{1.10}$$

where c is the speed of waves in the transmission line and $\vec{E}_0{}'$ is the EM field amplitude produced by our array elements. It can be seen that the van Atta array achieves phase conjugation while introducing a time delay which depends on the transmission line length, the incident direction and the array size. Since the time delay is independent of the frequency ω, the van Atta array is well suited for high bandwidth signals. Moreover, since superposition applies, it is capable to simultaneously retransmit multiple impinging EM waves.

1.1.4 The phase-conjugating mixer

Another possibility to achieve phase conjugation was proposed by Pon in 1964 [11] and is depicted in Fig. 1.3b. Each antenna is connected to a frequency diplexer consisting of two bandpass filters. We select the two filters such that their center frequencies are in the stop band of the other filter. The input bandpass (left) is tuned to the frequency of the incident

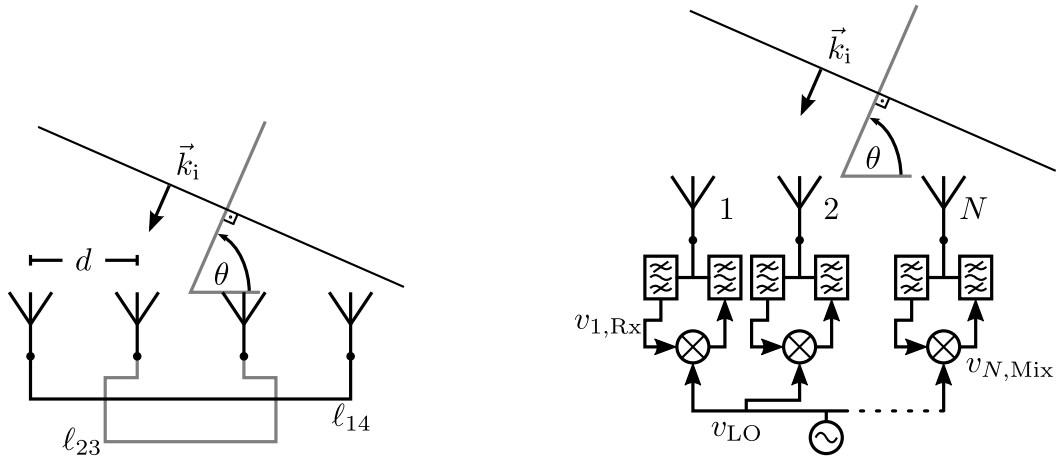

Fig. 1.3: (a) Schematic drawing of a four-element van Atta array with pairwise element connections of equal length. (b) An array using the phase-conjugating mixer technique. The antenna elements can be arbitrarily placed but the LO feed lines have to have the same electrical length.

wave. According to (1.9), the received signal port voltage $v_{n,\mathrm{Rx}}(t)$ at the n-th antenna is proportional to the incident EM field in (1.7). It is multiplied with the sinusoidal local oscillator (LO) signal $v_\mathrm{LO}(t) = \hat{v}_\mathrm{LO}\cos(\omega_\mathrm{LO}t)$. To achieve correct phase conjugation, we have to ensure that the LO signal arrives with equal phase at each multiplier. The resulting mixer output signals are given by

$$v_{n,\mathrm{Mix}}(t) = \frac{1}{2}\hat{v}_\mathrm{Rx}\hat{v}_\mathrm{LO}\left(\cos\left((\omega_\mathrm{LO}+\omega)t+\delta_n(\theta)\right)+\cos\left((\omega_\mathrm{LO}-\omega)t-\delta_n(\theta)\right)\right), \tag{1.11}$$

where $\hat{v}_\mathrm{Rx}$ is the amplitude of the received signals. The LO frequency and the output bandpass (right) are chosen such that the higher frequency term of (1.11) is filtered out while the lower frequency term passes through. Assuming ideal bandpass filters, we obtain the retransmitted signals at the antenna ports reading

$$v_{n,\mathrm{Tx}}(t) = \hat{v}_\mathrm{Tx}\cos(\omega_\mathrm{Tx}t+\varphi_{n,\mathrm{Tx}}) = \frac{1}{2}\hat{v}_\mathrm{Rx}\hat{v}_\mathrm{LO}\cos\left((\omega_\mathrm{LO}-\omega)t-\delta_n(\theta)\right). \tag{1.12}$$

Obviously, the phase term is conjugated but we have to regard the frequency term. If we were able to choose $\omega_\mathrm{LO} = 2\omega$, we would arrive at a retransmitted wave similar to that of the van Atta array in (1.10). However, since the receiver (Rx) and transmitter (Tx) frequencies have to be different, we can only approximate this result. Let us assume $\omega_\mathrm{LO} = 2\omega + \Delta\omega$. Inserting this into (1.12) and expanding the phase term leads to

$$v_{n,\mathrm{Tx}}(t) = \hat{v}_\mathrm{Tx}\cos\left((\omega+\Delta\omega)t-\frac{\omega d}{c_0}(n-1)\cos\theta\right), \tag{1.13}$$

where $\delta_n(\theta) = \frac{\omega d}{c_0}(n-1)\cos(\theta)$ has been substituted. We can see from this expression that for $\Delta\omega \neq 0$ the resulting EM wave will not have its maximum strength in the incident direction.

This is because the phase term is valid for the Rx frequency ω but not the one altered by $\Delta\omega$ [12]. The phase would have to be multiplied by the correction factor

$$\epsilon_\delta = \frac{(\omega + \Delta\omega)}{\omega} = \frac{\omega_{\mathrm{Tx}}}{\omega_{\mathrm{Rx}}}, \tag{1.14}$$

to obtain the correct pointing. However, the regarded system architecture does not permit to include such a correction. Therefore, the resulting pointing error of the phase-conjugating mixer array is

$$\Delta\theta = \theta - \arccos\left(\frac{\omega}{\omega + \Delta\omega}\cos\theta\right). \tag{1.15}$$

Due to this so called array squint, the difference between Rx and Tx frequency must be kept small. In comparison to the van Atta array, this method achieves phase conjugation at each antenna element individually. Therefore, arbitrary array geometries can be realized and malfunction of individual antennas is automatically mitigated.

We have seen that retro-directivity offers desirable properties for communication systems. Especially the self-tracking ability, i.e. the automatic re-direction of the transmitted signal towards an incident wave, is of great interest. As we have shown, the phase conjugation operation can be implemented with analog components. This leads to less complexity and power consumption compared to arrays using digital signal processing (DSP) techniques because they require analog-to-digital conversion for every antenna in the array.

1.2 Satellite communication applications

Satellite communication is ubiquitous in modern societies today [13]. Satellites provide dedicated services like television (TV), telephone networks e.g. Iridium and Globalstar, Internet access, Earth observation and other scientific missions. With the advent of low-cost cube satellites, we can expect an even further increase in the demand for satellite communications. Any space object needs to be controlled from ground which calls for individual communication links for telemetry, tracking, and command (TT&C) as well as data up- and download. In the following, we will discuss different requirements that every satellite communication system has to fulfill.

1.2.1 Frequency allocations

Due to the internationality of space and high demand, there are strict regulations concerning frequency usage for satellite communication links. The European Table of Frequency Allocations [14] lists the permitted bands for different applications including broadcast satellite service (BSS), fixed satellite service (FSS) and mobile satellite service (MSS). A few examples are listed in Table 1.1. We can see that the frequency bands for uplink and downlink are always separated. This is to avoid interference between different services, but also self-interference from the transmitters to the receivers of a satellite when they are working in the same frequency band. Any satellite communication transceiver must therefore be able to operate in the designated bands.

Table 1.1: Exemplary up- and downlink frequency bands

Frequency band	Usage	Uplink	Downlink
VHF	MSS	148 – 150 MHz	136 – 138 MHz
S-band	MSS	1.98 – 2.01 GHz	2.17 – 2.20 GHz
C-band	FSS	5.73 – 6.70 GHz	6.70 – 7.08 GHz
Ku-band	BSS, TV	14.5 – 14.8 GHz	11.7 – 12.2 GHz
Ku-band	FSS	17.3 – 18.1 GHz	10.7 – 11.7 GHz
Ka-band	FSS	27.5 – 31.0 GHz	17.3 – 21.2 GHz
Ka-band	MSS	30.0 – 31.0 GHz	20.1 – 21.2 GHz

1.2.2 Link budget considerations

All radio communication bases on the transfer of energy from a transmitter to a receiver. The link budget captures the influence of the involved system parts and the environment on this process. On satellites, the available power and space for payload systems is limited. Therefore, we have to pay special attention to the link budget. The Friis transmission equation gives the received power of a communication link as [15]

$$P_{\mathrm{R}} = \frac{g_{\mathrm{T}}\eta_{\mathrm{T}}g_{\mathrm{R}}\eta_{\mathrm{R}}}{l_{\mathrm{p}}}P_{\mathrm{T}}, \tag{1.16}$$

where P_{T} is the transmitter power and $g_{\mathrm{T}}, g_{\mathrm{R}}$ are the gains of the transmit and receive antennas towards each other w.r.t. an isotropic reference antenna. $\eta_{\mathrm{T}}, \eta_{\mathrm{R}}$ are the efficiencies of the transmitter and receiver systems. These include losses from impedance mismatch and antenna polarization.

l_{p} denotes the propagation loss which is defined as the power transferred between two isotropic antennas separated by a distance R. The power radiated by an isotropic antenna spreads spherically, i.e. the power density at distance R from the transmitter is given by

$$S = \frac{P_{\mathrm{T,iso}}}{4\pi R^2}. \tag{1.17}$$

The ratio between power at the receiving antenna port and power density of the field is called the effective area of the antenna which is given by

$$A_{\mathrm{eff}} = \frac{P_{\mathrm{R,iso}}}{S} = \frac{\lambda^2}{4\pi}, \tag{1.18}$$

for an isotropic radiator [6, c.6]. Combining the last two expressions, we arrive at the free-space propagation loss

$$l_{\mathrm{p}} = \frac{P_{\mathrm{T,iso}}}{P_{\mathrm{R,iso}}} = \left(\frac{4\pi R}{\lambda}\right)^2. \tag{1.19}$$

Regarding (1.16) for satellite communication, we can make the following qualitative statements: l_{p} is considerably higher than for terrestrial radio links due to the large distances that have to be bridged. On the satellite, P_{T} can not be arbitrarily increased due to the limited available power. Since efficiencies $\eta_{\mathrm{T}}, \eta_{\mathrm{R}}$ cannot exceed 1, the antenna gains are the only

possibility to increase received power and thus improve the link budget. Therefore, high gain antennas are usually required in satellite communications. Since the beamwidths of such antennas are narrow, continuous mechanical or electrical steering of the antenna beam is necessary if one of the communication terminals moves. Automatic Tx beam pointing as exhibited by retro-directive antennas (RDAs) would be an advantage. However, the classic RDA architectures introduced in section 1.1 do not make use of the Rx array gain because the antenna elements receive their signals independently. That is one of the reasons why RDAs are not used in satellite communications yet.

1.3 Contribution

In this thesis, we propose a system architecture which makes retro-directivity applicable to satellite communications. The presented approach achieves phase conjugation while avoiding array squint. It offers automatic self-tracking of the communication terminals and makes use of the antenna gain on both the receiver and the transmitter side. The proposed architecture is analyzed from a system theoretic perspective. The concept is then proven by time domain simulations of the critical components. Additionally, we implement the core system in digital hardware and validate it in combination with analog components using antenna measurement techniques. The rest of the thesis is arranged as follows:

Chapter 2: Discussion of the existing literature on RDA systems. The chapter is organized in sections dedicated to different system architecture types. We regard purely passive approaches as well as active systems using analog and digital components. The achievements and limitations of each contribution are discussed. The chapter concludes with an overview of the qualitative characteristics of the found system architecture types.

Chapter 3: We give the desired properties of a RDA system suitable for satellite communications. From this, the high-level architecture of the proposed system is deduced. We then analyze the receiver path of the system in detail: After introducing the necessary component models, we derive the system output signals and phase transfer functions analytically. Design goals and optimization techniques are also discussed. The receiver part is numerically simulated in the time domain whereby the phase detection and intermediate frequency (IF) signal performance is evaluated. At the end of the chapter, we discuss the applicability of the proposed architecture to the case of multiple simultaneous users.

Chapter 4: In order to realize the proposed RDA architecture, we transfer the analog system to the discrete time domain. By parallel design of an analog and a digital system with the same parameters, we analyze the similarities and differences between the two. This analysis is done first in terms of phase transfer functions and system poles. After that, we compare time domain simulation results for both the analog and the digital implementation. From this we obtain the expected phase detection accuracy. Finally, we implement the discrete time system on a commercial field-programmable gate array (FPGA) platform and validate the simulation results experimentally.

Chapter 5: We build a complete RDA demonstrator system. It consists of the digitally implemented RDA system from the previous chapter, an eight element dual-band antenna array working in C-band and suitable RF front-ends. We use this demonstrator for experimental validation of the retro-directive properties of the system architecture in a compact test range (CTR). The system performance is assessed in terms of monostatic and bistatic measurements. Eventually, we compare the retro-directive performance with results from the open literature.

Chapter 6: We summarize the findings of the thesis, its main contributions and publication impact. We also specify the remaining challenges which have to be overcome to make the suggested RDA system into a commercial product.

2 State-of-the-art

This chapter deals with the existing literature on RDA systems. The contributions are sorted according to the underlying phase conjugation principle or architecture type. The focus lies on active RDA systems, employing analog and/or digital components, but for completeness, also passive approaches are discussed briefly.

2.1 Purely retro-reflective systems

As discussed in section 1.1, an RDA system is purely retro-reflective if it just retransmits an incoming EM wave. Such architectures consist solely of passive physical structures like metal plates, transmission lines, passive antenna elements, etc. Additionally, they may contain active components like amplifiers for signal regeneration.

2.1.1 Corner reflectors

Corner reflectors are the most simple retro-directive systems. Robertson showed their use in enhancing the radar cross section (RCS) of a target for navigation purposes [16]. Different geometric forms of metallic reflectors are analyzed in this work. The functional principle is the same as for the optical reflex reflector shown in 1.1. Analytic formulas of the reflection diagram were published by Lewin [17]. A recent study by Stasny et al. [18] demonstrates the use of corner reflectors to detect wooden ships from space with synthetic aperture radar (SAR).

Another application of corner reflectors is in constructing reflector antennas. This was analyzed in 1940 by Kraus [19] where a dipole was used as feed for a V-shaped structure of parallel metal rods. Neff and Tillman [20] published mathematical expressions to facilitate the design of such antennas. While previously only two-dimensional structures were used, the concept was also analyzed for three-dimensional structures, e.g. in [21]. Recently, Jusoh et al. used the corner reflector principle for a reconfigurable plasma antenna [22]. In these applications however, the reflector is always used in combination with an active feed and no retro-directive performance is obtained.

2.1.2 Van Atta arrays

As mentioned in section 1.1, van Atta reflectors are named after their inventor and are characterized by the use of true time-delay for phase conjugation which makes them very broadband. The functional principle is described in [10], a patent which can be seen as the foundation of RDA systems.

One of the first publications describing a van Atta reflector implementation with dipoles was published by Sharp and Diab in 1960 [23]. In this paper, formulas for the RCS are given

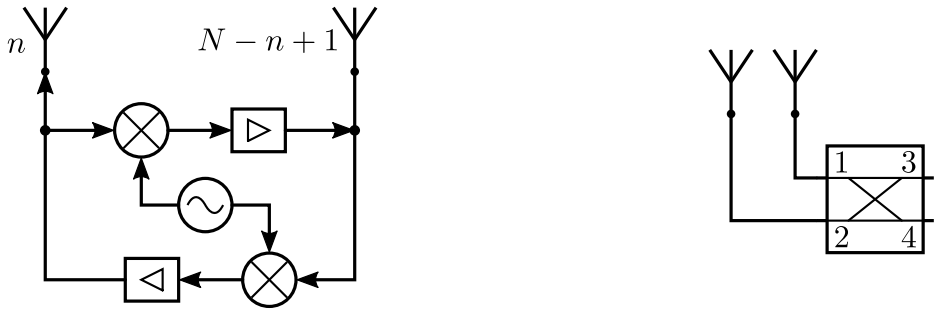

(a) (b)

Fig. 2.1: (a) Bidirectional interconnection scheme for an active van Atta array as proposed in [24]. (b) A passive retro-directive array with two elements which uses a single 90°-hybrid with open port termination.

along with the interconnections for a two-dimensional array. Radiated power and gain are given in terms of standard antenna theory equations. The calculated RCS corresponds well with the measured results up to ±30° from boresight. Thus the performance is better than that of a corner reflector.

Davies [24], as well as Andre and Leonard [25] introduced active components to the van Atta array. The first paper describes the use of bidirectional circuits consisting of amplifiers and mixers between interconnected antenna pairs. It thus retains the functional principle of the van Atta array but regenerates the received signal levels and allows a frequency shift. In the second paper, unilateral amplifiers are employed and the array is divided into a receiving and a transmitting sub-array of equal geometry. The use of additional mixers is proposed which allows regeneration and modulation of the retransmitted signals. Thus, these two publications deliver the basic building blocks for signal regeneration, frequency change and the retransmission of a different communication message. In [26], the architecture from [24] is used and retro-directive operation with a generated frequency offset is successfully demonstrated. The paper reports beam pointing errors between 4 and 8° due to array squint.

Another early active van Atta array is demonstrated by Withers [27]. He uses separate Rx and Tx arrays with a slight frequency difference realized by a mixer. Thus, it is possible to use high gain unilateral amplifiers for signal regeneration. Array squint is mitigated by choosing the same relative spacing between the elements of both arrays.

Vitaz et al. employed retro-directivity for radio frequency identification (RFID) tag detection in a cluttered environment [28]. The proposed architecture consists of interconnected dual polarization antennas which retransmit a cross-polarized signal. Low-noise amplifiers (LNAs) are used to boost one of the polarizations. By interrogating the RDA with two orthogonally polarized signals, it is possible to distinguish the tag response from clutter. The amplifier can thereby be used to additionally modulate the signal. The presented system is clearly not aimed at communication. Nevertheless, it shows an interesting application of RDA systems in Ka-band.

In [29], another recent van Atta array implementation at 30 GHz is shown. Longitudinal slot antennas and substrate integrated waveguides are thereby used. The structure is completely passive and aims at increasing RCS which is proven by monostatic measurements.

The proposed system has no possibility to connect additional components. It therefore can only be used as a passive RCS enhancing device.

Van Atta arrays have the advantage of a simple functional principle which can be implemented as a completely passive system or with some active components for signal regeneration or even modulation. Moreover, the bandwidth of a passive array is limited only by the antenna elements, as long as true time delay is utilized. This is the case if interconnections have the same physical length, not just the same electrical length which limits the error-free usability to a single frequency. With active components, van Atta arrays allow frequency translation between Rx and Tx. However, the resulting array squint can only be overcome by using separate Rx and Tx arrays. Moreover, the array gain is only used for transmitting while on receiving, all elements pick up incoming signals individually. Although being an interesting and simple technique, the van Atta array is not suitable for the communication scenarios addressed in this work. Besides the above mentioned lack of Rx gain, the received signals are not easily accessible and duplex operation is difficult to realize.

2.1.3 Waveguide structures

Phase conjugation of an incoming signal can also be achieved by using passive waveguide structures. Hsieh and Chu [30] propose a RDA based on 90°-hybrids and delay lines acting as fixed phase shifters. The basic building blocks are 90°-hybrids which are four-ports and can be described by their scattering parameter matrix

$$S = \frac{1}{\sqrt{2}} \begin{bmatrix} 0 & 0 & e^{-j\frac{\pi}{2}} & e^{-j\pi} \\ 0 & 0 & e^{-j\pi} & e^{-j\frac{\pi}{2}} \\ e^{-j\frac{\pi}{2}} & e^{-j\pi} & 0 & 0 \\ e^{-j\pi} & e^{-j\frac{\pi}{2}} & 0 & 0 \end{bmatrix}. \tag{2.1}$$

A single hybrid is sufficient for a two element retro-directive array as depicted in Fig. 2.1b. The antennas are connected to ports 1 and 2 of the 90°-hybrid, the other ports remain open. An input signal at port 1 appears at ports 3 and 4 with a phase shift of $\frac{\pi}{2}$ and π, respectively. Due to the open condition at these ports, the signals are reflected and appear again at ports 1 and 2 where they superimpose. In the shown configuration, we can describe the antennas with attached 90°-hybrid as a two-port, i.e.

$$S_{\mathrm{RDA}} = \begin{bmatrix} 0 & 1 \\ 1 & 0 \end{bmatrix} e^{-j\frac{3\pi}{2}}. \tag{2.2}$$

Thus, the hybrid realizes the interconnection scheme of a van Atta array, i.e. an S-parameter matrix with equal anti-diagonal elements. Besides the case of two elements, [30] also considers larger arrays. Thereby, multiple hybrids and additional delay lines have to be used to achieve the necessary connections. For an array of $2N$ elements, it takes N stages to achieve phase conjugation for all channels. Each stage hereby consists of N or $N+1$ components, i.e. either 90°-hybrid or delay line. Therefore, the scalability of the proposed approach is an issue as the component count increases quadratically with the number of antenna elements. This also has an effect on the necessary printed circuit board (PCB) size. Additionally, it is challenging to achieve reproducible performance for all hybrids. In contrast to the van Atta array, the system has to be optimized for a single frequency due to the use of phase

shifters and the tuning of delay line lengths. The paper demonstrates the technique with all structures realized in microstrip technology for an operation frequency of 2.9 GHz and up to six array elements.

Tsai et al. [31] show a phase-conjugating structure in microstrip technology with different behavior in two frequency bands. In the lower band, the behavior is similar to that of the previously discussed system, i.e. retro-directivity is achieved through reflection. In the higher band, the implemented RDA works like a van Atta array, i.e. it realizes a pairwise interconnection scheme. Thus, the result is a RDA system working independently in two frequency bands. However, the received signals are simply reflected back on the same frequency. The system is completely passive and can be seen as a dual-band phase conjugator. The paper presents an implementation, showing simultaneous retro-directive behavior around 2.0 and 3.7 GHz. A similar architecture is developed by the same group and presented in [32]. Limitations of these systems are similar to those seen in [30].

A different approach to constructing a RDA system is the use of Rotman lenses, shown by Christie et al. [33]. The Rotman lens is a passive multiport structure realized in microstrip technique which maps incoming EM waves from N antenna ports onto M beam ports. The mapping is done by wave reflection inside the structure which makes it suitable also for broadband signals. According to its incident direction, an EM wave appears mostly at a certain beam port. The lens thus realizes fixed beams which can be used for retro-directive action by leaving the beam ports open circuited. Incoming waves are thus reflected at the beam port and re-radiated into the direction-of-arrival (DoA). The paper shows design, simulation, and measurement results for an 8 to 12 GHz RDA. Using fixed beams is certainly a limitation of the Rotman lens approach. In [33] a 12-element ULA with 13 beam ports was used, yielding beams with 8.3° separation. Increasing the resolution would ask for more beam ports, resulting in a more complex structure, higher ohmic, dielectric, and spillover losses.

2.2 Active analog retro-directive systems

In this section, we present RDAs where active components are an integral part of the phase conjugation. We begin with the phase-conjugating mixer already mentioned in section 1.1.4 where at least an LO signal generator is needed. From this we move on to phase-locked loop (PLL) based approaches and finally discuss systems which employ direct phase detection at RF.

2.2.1 Phase-conjugating mixer

The phase-conjugating mixer technology was introduced by Pon in 1964 [11]. The phase conjugation circuit is schematically shown for a single antenna element in Fig. 2.2a. In contrast to Fig. 1.3b and the original paper, instead of two bandpass filters a RF circulator is used [34]. As described in section 1.1, the idea is to mix the received signal with a LO signal of twice the Rx frequency. This generates a Tx signal of equal frequency as the received one but with conjugated phase. A general problem hereby is spillover between the Rx and Tx paths. If the Rx and Tx frequencies are exactly the same, low isolation or excessive amplification leads to retransmission towards the Snell's angle of the Rx direction,

a problem described in [35]. This is commonly solved by introducing a small frequency gap between Rx and Tx. It needs to be sufficiently small that the resulting array squint given in (1.15) does not compromise the desired pointing accuracy.

Also in 1964, Skolnik and King [36] proposed a so-called self-phasing antenna which was demonstrated in [37]. Similar to the design by Pon, it consists of individual antenna elements with phase conjugation networks. The respective circuitry is schematically depicted in Fig. 2.2b: The received signals are fed to a circulator and are mixed down to an IF. On the IF, the signal can be amplified and is eventually mixed up to the original frequency again. Via the circulator, the conjugated Tx signal is fed to the antenna and re-radiated. In contrast to the approach by Pon, the mixing signals are generated by using the sum and difference of two oscillators, one with the Rx frequency, the other with the desired IF. Thus, the architecture eliminates the necessity of having an LO of twice the Rx frequency. However, this is achieved at the cost of performing two mixing operations on the received signal per antenna element. Skolnik and King state in [36] that Tx to Rx crosstalk is the main problem of the architecture. Isolation is provided solely by the circulator which achieves up to 50 dB. Poor isolation may lead to a self-oscillation of the device and must be mitigated by pulsed operation or a frequency shift.

The research in phase-conjugating mixers after these fundamental papers from 1964 can be divided into two categories: First, those who follow Pon's idea in [11] and use one mixing operation with a LO frequency which is about twice the Rx frequency. Second, those who adopt the approach of Skolnik and King [36], conjugating the phase on a lower IF at the cost of two mixing operations. Both techniques offer the possibility to use arbitrary array geometries, as phase conjugation is performed individually. This also means that the RDA still works if individual elements fail or do not receive an incident signal, e.g. due to shadowing. Shared disadvantages are the array squint and the necessary high isolation of Rx, Tx and LO signals. Also the Rx array gain cannot be used which follows directly from the independently working individual antenna elements. In the following, we will first present developments using Pon's approach. Afterwards, works about the two mixer technique are discussed.

Single mixer type architectures

Chang et al. [38] presented a practical implementation of the phase-conjugating mixer proposed by Pon at 10.24 GHz in 1998. Using separate antennas for receiving and transmitting, the authors circumvent the isolation problem and are able to use amplifiers for signal regeneration. The paper considers the problem of delivering the necessary 20.48 GHz LO signal to each antenna element with equal phase. The authors propose the use of optical fibers to distribute a laser signal among the array elements. The technique is successfully demonstrated whereby the advantage of using an optical signal is seen mainly in reduced weight of conductors and interconnections.

In 2001, Miyamoto et al. [39] proposed a new phase conjugator to attain higher isolation between Rx, Tx and LO signals. The received signal is split behind each antenna and fed to two active mixers whereby one signal path induces a 90° phase shift to the Rx signal. The split Rx signal is individually mixed with an LO signal of twice the Rx frequency. The resulting Tx signals are sent back to the antenna via the same transmission lines used for receiving. This leads to the following situation at the antenna port: Any LO signal leakage

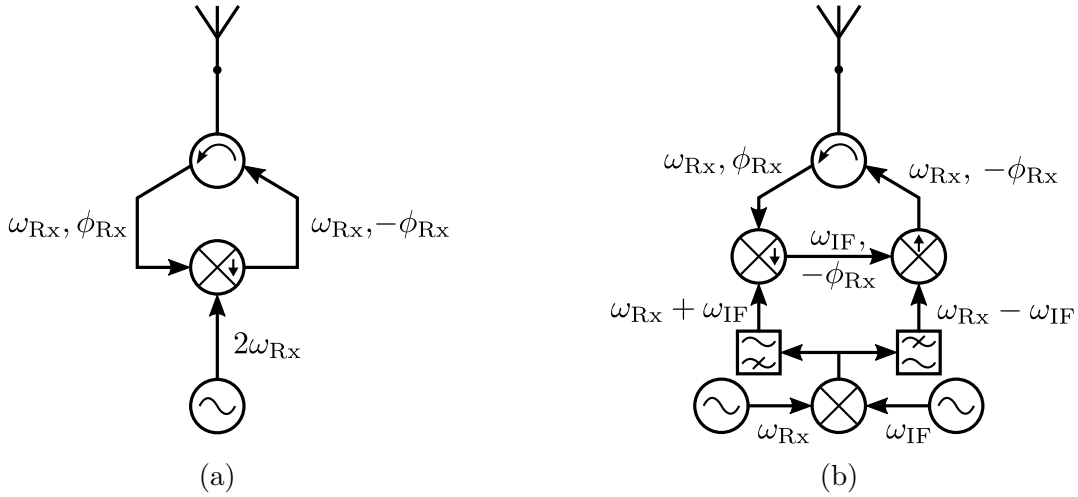

Fig. 2.2: (a) Single phase-conjugating mixer circuit as proposed by Pon [11]. It requires a LO signal of $\omega_{\mathrm{LO}} \approx 2\omega_{\mathrm{Rx}}$. The down-mixer eliminates the higher mixing product. (b) Heterodyne phase-conjugating mixer circuit proposed by Skolnik and King [36]. It avoids a high frequency LO at the cost of multiple mixing operations.

through the mixers arrives with 180° phase shift from the delayed transmission line and thus cancels out. Likewise, any reflection of the Rx signals from the mixers arrives with a $2 \cdot 90°$ phase shift on the delayed transmission line. Thus, only the wanted Tx signal is radiated by the antenna as it adds up constructively at the antenna port. The demonstrated isolation values are better than 20 dB and the system offers a bandwidth of 30 MHz. Although the isolation is improved, the achieved values would not be sufficient to allow a high-power Tx signal.

Another approach proposed by Shiroma [40] in 2003 uses self-oscillating mixers (SOMs) at each antenna element for phase conjugation. The authors claim that they thus avoid the phase aligned distribution of a centrally generated LO signal over a large array. The paper demonstrates a two-dimensional RDA with strongly coupled SOMs at twice the Rx frequency. However, a stable external signal is required to keep the circuits in phase lock and reduce the individual phase noise. According to the paper, the RF circuitry is rather complex and very sensitive to design variations. Due to the necessary external signal, the proposed architecture still needs to distribute a high frequency phase aligned signal. The distribution of LO signals to the individual antenna elements can be simplified by using several PLLs driven by the same low frequency (LF) input signal. Such an approach appears more promising than the suggested solution with SOMs.

In the following year, Leong et al. presented full-duplex capable retro-directive systems [41]. The authors use a Rx signal with amplitude modulation (AM). The received signals are split after the antenna. One branch is used for demodulation, the other for phase conjugation. The LO signal is generated by doubling the frequency of one of the Rx signals. A separate antenna array is used for transmission. Tx signal modulation is done via the LO signal. Measurement results for a 5.8 GHz system are presented with 10 Mbit/s data rate. The use of AM signals is well suited for the radio detection and ranging (RADAR) scenario described in the paper but is not applicable for mobile communication systems where signal amplitudes already vary due to movement.

A very efficient approach in terms of component count was taken by Goshi in 2007 [42]. Using a sparse four element array, only a single phase conjugation circuit is used. RF switches are employed to sequentially connect the array elements to the phase-conjugating mixer. Retro-directive beamforming can be seen when the transmitted signal is integrated over a whole switching cycle. However, from the paper, it is difficult to evaluate the performance of the switching strategy. This is because the authors use a sparse array of four elements which introduces considerable side-lobes. The presented retro-directive patterns are not very pronounced. If this is due to sparsity or the switching operation cannot be judged. Anyway, due to the simple phase-conjugating mixer, the system will suffer from array squint for large frequency gaps.

Dual mixer type architectures

In 2001, Brabetz et al. [43] adopted the IF phase-conjugating mixer technique proposed by Skolnik and King in [36]. By using two balanced harmonic mixers, retro-directive behavior is demonstrated with an LO signal close to the Rx frequency. Phase conjugation is achieved by mixing the Rx signal twice with the same LO which is an improvement over the original design which required two LOs. To increase RF to IF and LO to IF isolation, a stripline rat-race coupler is used. Thus the signals cancel out at unwanted ports yielding isolation values of up to 36 dB. A drawback is that high losses are introduced by the balanced mixers which leads to an overall conversion loss of 12 to 16 dB.

Chen et al. [44] built a RDA using two LO mixing stages and three bandpass filters (BPFs) between two patch antennas in 2012. Phase conjugation takes place on the IF and works in both directions, leading to a bidirectional, dual-frequency RDA. Operation is demonstrated using two four element arrays at 2.44 and 6.0 GHz, respectively. To avoid array squint, the two arrays have the same relative spacing. This also eliminates the isolation problem between Rx and Tx. The authors state that full-duplex communication is possible as the LO signals could be modulated to transmit information. A problem of the proposed system is again conversion loss which is simulated to be around 12 dB. Broadband bidirectional amplifiers would be necessary to mitigate this. In addition, any message modulated onto the Tx signal by the LOs would be sent in both directions. It is not clear, how full-duplex operation could be achieved. Additionally, the proposed system consists of two separate arrays with different physical spacing.

2.2.2 PLL based retro-directive systems

The idea to electronically steer the beam of a Rx array using PLLs was introduced in 1989 by Brennan [12]. The so called self-phased array receiver presented there is schematically shown in Fig. 2.3a. We mention the system here although it is not retro-directive. However, this type of receiver has strongly influenced later RDA designs. The principle is to multiply the received signals of an antenna array with phase shifted mixing signals. These are generated by an individual PLL per antenna element. The down-mixed signal is further down-converted with a LO signal and compared to a common local reference of frequency ω_{ref} whereby a phase detector is used. Thus, all received signals become phase aligned to this reference. The feedback structure of the PLL leads to an automatic beamforming of the Rx array towards the source. Beam correction due to movement of the source also occurs automatically.

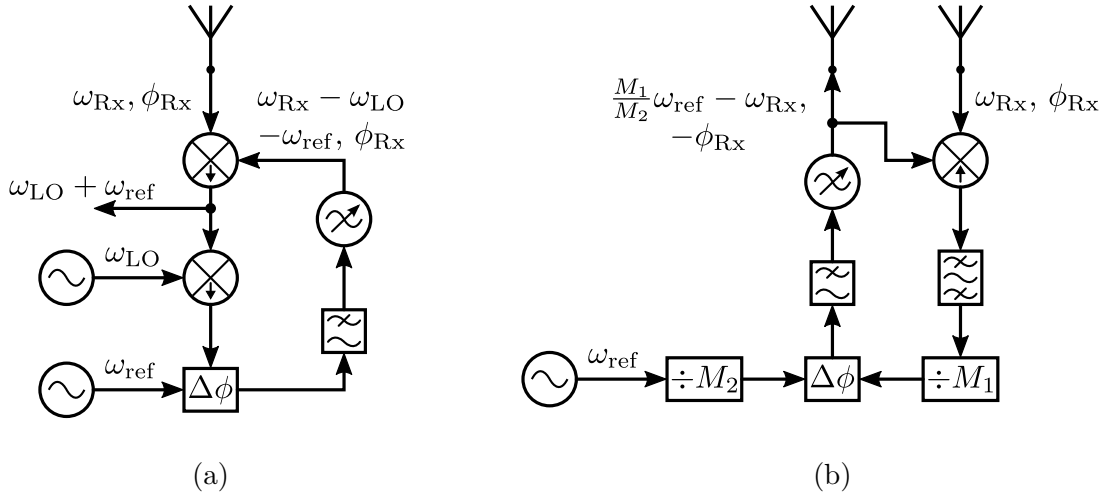

Fig. 2.3: (a) A PLL based receiver as proposed by Brennan [12]. Two down-mixers, i.e. multipliers with adjacent lowpass filters are used to shift the received signal to a LF on which it is compared to a reference signal. The error of this comparison is used to adapt the frequency of the first down-mix signal. (b) Phase conjugation module proposed by Fusco et al. [46]. An up-mixer consisting of a multiplier and a highpass filter is used on the received signal which is then bandpass filtered and frequency divided. A phase comparison is made using a frequency divided reference signal. The result is used to steer the LO and Tx signal.

In [12], a pilot signal is used for tracking. The focus of the paper lies on the tracking performance, retransmission is only marginally regarded. In a multipath situation, the self-phased array forms multiple beams, with their gain proportional to signal power from the respective direction. This is analyzed in more detail in [45], written by the same author. One of the main findings is, that phase lock between the different signals is necessary for the PLL structure to work as intended. The paper describes many of the principles used in later RDA implementations with PLLs. It already shows important performance characteristics like capture probability, Doppler error, pointing error due to frequency offset, and behavior under multipath conditions.

In 2005, Fusco et al. presented a PLL based architecture for a RDA system [46]. It is schematically depicted in Fig. 2.3b and consists of two separate antennas which are coupled by a PLL and synchronized by a common local reference signal of frequency ω_{ref}. The voltage-controlled oscillator (VCO) output of the PLL thereby has two functions: It is used to generate the transmit signal with conjugated phase term $-\phi_{\mathrm{Rx}}$ and to up-mix the received signal to a higher IF. The IF signal is filtered, frequency divided and fed to a phase detector which compares it to the reference. Thus, the multiplied received signals are phase aligned across the whole array, while the VCO signals are shifted. In order to use the VCO signals directly, the Rx signals are actually up-mixed. This could be a problem for high frequency applications. The proposed system architecture does not allow modulation of the retransmitted signal or access to the received signals. Many additional calculations concerning a non-linear mixer model are given in the appendix of [46]. The usefulness of these calculations however is not made clear, as the utilized mixer is idealized at the same time. Whether the given detailed formulas apply in reality is not demonstrated.

The same group of researchers shows a phase conjugation architecture in 2009 [47]. Two PLLs and two mixers are used to implement IF phase conjugation as suggested by Skolnik and King [36]. The carrier of the incoming signal is regenerated using a high Q bandpass filter and a tracking PLL. Additionally, the authors use an I/Q modulator on the Tx signal. The paper thus shows a PLL based phase conjugator which is suitable for duplex communication. RDA operation is demonstrated with an input frequency of 2.4005 GHz and an output frequency of 2.4095 GHz. In [48], the same architecture is presented as a dual mode system. By using only one PLL and the I/Q modulator, basic phased array functionality is achieved. The presented architecture shows retro-directive behavior in a field-of-view (FoV) of $\pm 40°$ around boresight with a 10-element array. System complexity is higher due to the use of three PLLs per channel but enables modulation and individual phase conjugation. The demonstrated frequency gap is small. Since the same antenna elements are used for Rx and Tx, this avoids array squint in the measurements.

In 2016, Buchanan et al. presented a 3×3 element RDA for L-band communication [49]. As in previous work by the authors, PLLs are used to generate LO signals. These are used to phase align the received array signals and to generate phase conjugated Tx carrier signals. The system is successfully demonstrated at Rx and Tx frequencies of 1.55 and 1.65 GHz. Although the realized frequency gap is small, the paper shows that satellite communication with RDAs is feasible.

The tracking ability of PLLs can be used in a receiving array system to steer the Rx antenna beam towards an incoming wave. For RDAs, this technique offers a way to utilize the Rx gain of the array, something which cannot be achieved with the van Atta array or the phase-conjugating mixer.

2.2.3 Architectures using direct phase detection

The detection of phase differences between RF signals is the key to retro-directive operation. Phase detectors are known for many decades and are widely used especially for PLL circuits. However, until recent years, the operation frequency of integrated phase detectors was below the gigahertz region. New developments, e.g. [50, 51] allow direct phase detection also on RF signals.

Shiroma et al. [52] proposed the use of phase detectors for an Rx signal in 2006. The detector output is thereby used for two purposes: First, to steer phase shifters on the Rx side and thus make use of the Rx array gain by phase shifting the received signals. Second, on the Tx side to do retro-directive beamforming. A constant correction factor is applied to the phase detector output which depends on the array element spacings and frequencies. The paper shows measurement results for a 1.425 GHz Rx and a 2.85 GHz Tx array of two elements each. The described architecture decouples Rx and Tx paths completely by using separate arrays and independent Tx signal generation. This allows for high Rx/Tx isolation and arbitrary frequency shifts. Naturally, the performance of the phase detectors employed after the Rx antennas directly influences phase detection accuracy and thus retro-directive behavior. A certain signal-to-noise ratio (SNR) must be ensured at the antenna ports for the system to operate as intended. Any signal modulation would have to be removed before the direct phase detection.

Buchanan and Fusco [53] introduced a phase conjugation circuit which works with a LF phase detector. The Rx signals are thereby fed to a frequency divider to create a 10 MHz

signal. The rising edge of this signal triggers a sample-and-hold circuit to store the current value of a sawtooth reference signal of the same frequency. The stored value is inverted and then compared to another sawtooth signal. The comparator output defines the rising edge of the Tx signal which is phase conjugated with regard to the Rx signal. This principle is demonstrated using 960 MHz input and output signals. A main difficulty in realizing this system is the frequency division of the Rx signal such that it has the same periodicity as the sawtooth reference. In a real application, this may be difficult. Additional circuitry would be needed to ensure frequency stability which is necessary for the architecture to work properly.

2.3 Digital retro-directive systems

Following an often cited definition by Miyamoto [54], RDAs do not employ sophisticated DSP. This may be one reason why there is not much research on digital or digitally enhanced retro-directive systems.

Di Domenico and Rebeiz introduced a digital RDA system in 2001 [55]. All received signals from a circular antenna array are thereby sampled and processed on a FPGA. The paper focuses on signals modulated with binary phase shift keying (BPSK) and how to separate geometric phase information and data. Phase conjugation is achieved before sampling by mixing the Rx signal with a LO of a higher frequency. In the digital domain, the signal modulation is removed by squaring the received signals. A digital PLL is used to regenerate the received carrier signals. The phase shifts between the recovered carriers hold the conjugated geometric phase information of the incoming wave. The regenerated carriers are digitally modulated, converted into analog signals and up-mixed to the desired Tx frequency. Thus the system is capable of duplex operation. The proposed architecture is demonstrated using antenna arrays with six separate elements for Rx and Tx. The realized data rate is 78.125 kbit/s and a bit error rate (BER) smaller than 10^{-6} is demonstrated. The system can cope with small shifts in Rx frequency e.g. through Doppler effects. The paper states that it is possible to have several hundred processing channels on a contemporary FPGA.

In 2005, Goshi et al. proposed a RDA which can retransmit to a selected signal source while suppressing retransmission towards unwanted directions [56]. The work addresses the problem that RDAs respond to any incoming signal which makes them susceptible for interference. The presented system uses sub-arrays of two antenna elements with individual digitally controlled phase shifters. The phase shifters are used to produce a null of the sub-array pattern in the direction of an unwanted signal. The actual retro-directive array is composed of several sub-arrays. The paper does not give much detail about the employed DSP. It is used to estimate the DoA of the incident signal sources from the down-mixed signals of the sub-arrays. With the DoA information, the DSP steers the phase shifters such that a null is located in the unwanted signal source direction. The technique is demonstrated in simulation and measurement using four sub-arrays for receiving and a four element array for transmitting. The authors do not disclose details about the utilized algorithms. Especially, it is not stated how DoA estimation was done. Moreover, it is not clear how the unwanted signal is discerned from the wanted one. Given the chosen sub-array approach at the receiver side, the use of separate arrays for Rx and Tx is necessary. Whether the presented system can be used for a relevant application is doubtable.

2.4 Multi-user and multipath environments

A passive RDA which is interrogated by several transmitters of equal frequency was analyzed by Fusco in [57] in terms of S-parameters. The paper demonstrates that the retransmitted signals show the same power distribution as the received signals. This means that the power of the Tx signal is proportional to the received Rx signal power which is the expected behavior e.g. of a reflector. The paper proves that it is not possible to distribute Tx power arbitrarily between all interrogators. The behavior is explained through the RDA having no knowledge of where the received power at each element comes from. The findings of this work are valid for any RDA system which has direct coupling between the Rx and Tx side. It would be necessary to identify the number of interrogators and their DoA. With this information, the Tx beamforming could be altered such that more power is allocated towards one specific signal source.

Karode and Fusco use an RDA system as a multipath sensor [58]. The utilized RDA is a phase-conjugating mixer presented in detail in [26]. Two parallel reflector plates are used to create two multipath signals besides the line of sight (LoS) path. The authors introduce an effective array factor which is calculated by adding individual array factors for each signal source, i.e. two multipath and one LoS components. The presence of multipath signals is detected by comparing the current pattern of the RDA to its previously measured monostatic radiation pattern. The detection of multipath presented in this work requires the measurement of the array pattern. Thus it is only applicable in static scenarios where the necessary time for the measurement and evaluation is given.

From the existing literature we draw the conclusion that any RDA system to which the superposition principle applies is capable of simultaneously retransmitting multiple impinging signals. Especially, this is true for the retro-reflective systems from section 2.1 and the phase-conjugating mixer architectures from section 2.2. The power distribution of the retransmitted signal is thereby proportional to that of the incident waves. This however is not ideal for communication applications where we would like to transmit more power towards a weak signal source. With the exception of [45], other RDA architectures are not analyzed with regard to their ability to serve multiple users. This indicates that they are not suited for multi-user operation. We will investigate this topic more closely in section 3.5.

2.5 Textbooks and overview articles

Although focusing on large scale arrays with several wavelengths inter-element distance, Hansen gives a good overview of retro-directive or self-phasing antennas in [59, c.5]. The book treats passive and active van Atta arrays, heterodyne phase conjugation circuits as well as PLL based approaches. The building blocks of modern RDA systems are already described in this work. When the book was published in 1966, it was not imaginable that RDAs could be built on the scale of a wavelength. However, the concepts and findings are still valid and often occur in later publications, sometimes without proper reference.

An overview article which received much attention in the last years was written by Miyamoto and Itoh [54]. It describes the development of RDAs over time and gives an overview on recent developments done by different research groups. Especially the already discussed works in [38, 39, 43, 55] are mentioned.

Table 2.1: Qualitative overview of system architecture characteristics

Requirement	Van Atta array	Phase-conjugating mixer	PLL based architectures	Full digital approach
Frequency translation Rx / Tx	-	o	+	+
Array squint correction	-	-	+	+
Different Rx and Tx signals	o	o	+	+
Access to received signal	-	-	o	+
Duplex operation	-	-	+	+
Use of Rx array gain	-	-	+	+
Use of Tx array gain	o	o	o	+
Self-tracking	+	+	+	-
Low complexity	+	+	o	-
Low power consumption	+	+	o	-
Scalability	o	+	+	o
Realizable signal bandwidth	+	+	+	o

2.6 Summary

In the previous sections, we have seen various concepts and realizations of RDAs. In chapter 1, we have discussed the challenges in applying the retro-directive principle to satellite communication. Table 2.1 sums up the advantages and drawbacks of the main concepts presented above, namely the van Atta array, phase-conjugating mixer and PLL based approaches. For comparison, we also include a full digital system architecture. This means that every channel of the Rx antenna array is down-mixed, sampled and digitally processed. On the Tx side, one digital-to-analog converter (DAC) per array element is used to produce the transmitted signals. This approach offers maximum flexibility in terms of signal processing but is complex to realize and power hungry [60]. The evaluation in Table 2.1 is qualitative and shows either +, o, or - for good, intermediate or bad fulfillment of the respective requirement. In the following, we shall discuss the different table entries in more detail.

Frequency translation Rx / Tx means the ability to transmit on a different frequency than the received one. This is an essential property for satellite communication to avoid feedback of the high power Tx signals into the sensitive Rx hardware [1]. As we have seen before, the van Atta array cannot realize this functionality directly but needs additional mixers. The phase conjugation mixer on the other hand can slightly alter the Tx frequency compared to the Rx signal. However, it then suffers from array squint, which means that no arbitrary frequency translation can be realized. For PLL based systems, only small frequency gaps have been demonstrated, but the technique should work also for larger gaps. Since Rx and Tx paths are separated for digital implementations, arbitrary frequency translation can be achieved.

Array squint correction is the capability to counteract pointing errors as described by (1.15). These result from using the same physical array geometry for different Rx and Tx

frequencies. If mixers are used in an active van Atta array as in [27], separate Rx and Tx arrays with different geometry are needed. Phase conjugation mixers are not able to correct the squint since they perform individual phase conjugation at each antenna element. PLL based techniques and also the full digital approach can correct squint errors.

Different Rx and Tx signals means that the signals which are received and transmitted by the system carry different information. Obviously, this is important for communication systems. With active components, the van Atta array can modulate the received signals before retransmitting them. This could be done by using variable gain amplifiers or mixers. For the phase conjugation mixer, data can be modulated onto the transmit signals by changing the common LO signal. In both cases, the arrays then operate in an RFID like fashion. That means, either the received signal is just a carrier or its modulation has to be removed prior to retransmission. The PLL based approach and the fully digital solution natively offer the possibility to transmit an independent return signal.

Access to received signal evaluates how difficult it is to obtain the information encoded in the received signal. Being a retro-reflective system, the van Atta array is not meant to supply received signal information. With additional components like directional couplers and amplifiers, it may be possible to achieve this. A similar approach would be necessary for the phase-conjugating mixer. The PLL based approach generates down-mixed versions of the received signals. These would need to be combined in order to obtain a single output. In the fully digital approach, the received signals can be easily combined as necessary.

Duplex operation is the capability of the system to receive and transmit different communication signals at the same time. As mentioned above, the van Atta array and the phase-conjugating mixer work in an RFID like fashion when they transmit a different return signal. Therefore, duplex operation is difficult to realize. The PLL based architectures only create a carrier signal which can be arbitrarily modulated. A digitally generated Tx signal also offers full flexibility. Thus, the last two concepts offer duplex capability.

Use of Rx array gain means that the system uses array beamforming to receive signals. This is not possible for the van Atta array and the phase-conjugating mixer. Their antenna elements are receiving the incoming signal separately. In contrast to this, the PLL based approach creates phase aligned versions of the received signals. If these are combined, they add up constructively which corresponds to steering the Rx array electronically towards the DoA of the Rx signal. The digital architecture can of course implement arbitrary Rx beamforming algorithms.

Use of Tx array gain is the ability to transmit directively towards the received signal source. This property is fulfilled by all presented architectures. However, it should be noted that the fully digital approach gives much more flexibility in terms of beamforming. While the other architectures operate in a phased array manner, DSP can use advanced techniques. Amplitude tapering for sidelobe level control and null-steering are two examples.

Self-tracking is the ability of the system to automatically track a moving signal source with the retransmitted signal. This is a key feature of retro-directive systems and is therefore fulfilled by the first three architectures. A fully digital system can implement tracking of moving sources e.g. by means of adaptive beamforming. However, this is not the automatic self-tracking we are looking for and comes at the expense of additional DSP load.

Low complexity assesses the number of active and passive components necessary to realize the given system architecture. Since it only needs an interconnection network, the van Atta array scores in this category. The phase-conjugating mixer is slightly more complex as it needs some passive components plus a LO network. The PLL approach requires more parts and some of these have to be active. For the digital approach, complexity is highest as we need individual front-ends for each Rx and Tx channel, an analog-to-digital converter (ADC) or DAC, and the digital processor itself.

Low power consumption is a key requirement for satellite systems. Architectures which use only passive components are best rated in this category. Since power consumption of ADCs and DACs rises with resolution and sample rate, the digital system has a disadvantage here. The PLL based approach is somewhat better as it employs some active components but their power consumption should be in the range of the front-ends needed for the digital solution. The given rating in Table 2.1 is taken from [49] which shows a comparison of different architectures and their power consumption.

Scalability means how easily the system can be expanded in terms of array size. The complexity of the interconnection network for the van Atta array increases greatly. Especially if all interconnects have equal physical length and/or the array is two-dimensional. Since the phase-conjugating mixer achieves individual phase conjugation at each element, it offers good scalability. PLL based systems also have good scalability as they employ individual PLL architectures on each array channel. The digital architectures scale well as long as all processing can be handled on a single FPGA. If the required processing power calls for more signal processing units working together, overhead for synchronization is introduced. Digital systems shown in the literature offer up to eight channels [61]. In [62], FPGA designs for antenna arrays of up to 256 elements have been presented. However, these are meant for 1 bit quantization and have not been demonstrated yet.

Realizable signal bandwidth assesses how easy it is to increase the bandwidth the system can process. In terms of realizable bandwidth, the digital system is restricted by the sample rates of its ADCs. Analog parts like antennas, amplifiers, mixers, etc. can be made with large bandwidths. Therefore, system architectures based on analog hardware have an advantage over sample based ones. There are ADCs with sample rates in the GHz range, e.g. shown in [63]. However, such high data rates call for sophisticated signal processing on the FPGA like multirate techniques. Moreover, their high power consumption discourages the use in satellite systems at the moment.

3 Analog/digital hybrid system concept

In chapter 1, we have discussed reasons why the retro-directive principle is not widely used in communication applications. Additionally, in chapter 2, we have seen the main system architectures for RDAs with section 2.6 summarizing their advantages and drawbacks. From this, we can deduce the requirements for an ideal retro-directive array transceiver to be used in satellite communications. It should

Req. 1: Receive a modulated RF signal of center frequency f_{Rx} and transmit a signal centered around $f_{\mathrm{Tx}} \neq f_{\mathrm{Rx}}$,

Req. 2: Mix down the received signal to an IF from which the contained information can be decoded,

Req. 3: Combine the individually received signals constructively to obtain a single Rx signal and utilize the Rx antenna array gain,

Req. 4: Use the phase differences between the received signals to direct the Tx signal towards the incident direction,

Req. 5: Allow full duplex operation, i.e. the Rx and Tx signals are received and transmitted simultaneously and carry different information,

Req. 6: Use the same physical array geometry to receive and transmit in order to have a compact and scalable system without array squint,

Req. 7: Offer high communication signal bandwidth,

Req. 8: Avoid computationally demanding DSP.

In this chapter, we will introduce and analyze an analog/digital hybrid RDA system architecture which realizes the above characteristics. We shall start with a general overview of the proposed system in section 3.1. The most innovative part is the receiver path whose architecture is described in section 3.2. In section 3.3, we discuss strategies to parameterize the system which we validate by time domain simulation in section 3.4. A discussion of the multi-user capability of the proposed architecture in section 3.5 concludes the chapter.

3.1 System overview

A high-level block diagram of the proposed RDA system is depicted in Fig. 3.1. Bold arrows mark signals carrying information and thus requiring high bandwidths. The thin arrows stand for slowly varying information and control signals. In contrast to classic RDA systems, we separate the data carrying Rx and Tx paths. This is necessary in order to use

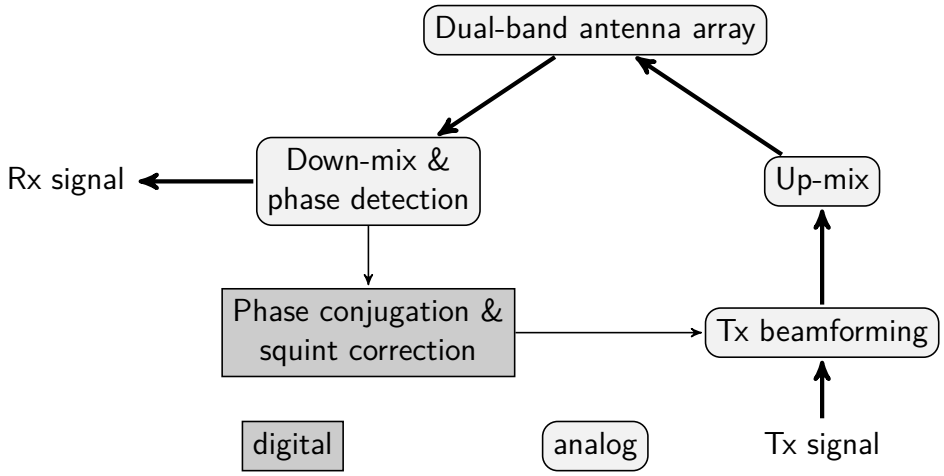

Fig. 3.1: Block diagram of the hybrid system architecture. Bold arrows denote data carrying signals with high bandwidths while slowly changing information and control signals are marked by thin arrows.

the system as a communication transceiver in duplex mode as stated in Req. 5. It allows us to access the Rx signal and to input an independent Tx signal. Rx and Tx paths are coupled such that phase difference information between array elements is extracted from the Rx side and used to steer the Tx beam. Thus retro-directive behavior can be achieved as described in Req. 4. We are thereby able to use different frequency bands which is a key requirement for satellite communication [1]. An important concept behind this architecture is that all information carrying signals are processed by analog components. These can readily provide high bandwidths, as postulated in Req. 7. Digital components are used only to process slow changing information, i.e. the phase differences between array elements, and thus require low data rates. In the following, we shall discuss the individual system parts shown in Fig. 3.1 in more detail and regard their contribution to fulfilling the system requirements.

Dual-band antenna array: We use an array of N identical antenna elements capable to receive and transmit in the desired frequency bands around f_{Rx} and f_{Tx}. This means that the phase centers of the Rx and Tx elements have the same physical spacing. This can be achieved by either a broadband or a dual-band antenna design. In this constellation, array squint as described in (1.15) occurs due to the frequency difference. The dual-band array fulfills Req. 1 and Req. 6.

Down-mix & phase detection: This block receives the incoming signals from the antenna array and performs the following tasks:

1) Mix down the Rx signals to an IF,
2) Output IF signals which carry the information of the received RF signal,
3) Phase align the IF signals among all array channels, combine them constructively and supply them at a single output,
4) Extract the phase differences between the individual Rx signals for phase conjugation.

All functionality can be achieved by analog signal processing. The down-mix and phase detection block is the core unit of the proposed system. It implements Req. 2, Req. 3 and contributes to the fulfillment of Req. 4 and Req. 8. A detailed description and analysis is conducted in section 3.2, section 3.3 and section 3.4.

Phase conjugation & squint correction: The unit receives the phase detection result, i.e. the phase differences between the individual Rx array channels. The phase differences are then conjugated and the correction factor from (1.14) is applied to avoid array squint. The thus computed phase shifts are used for beamforming on the Tx side, fulfilling Req. 4. Due to the necessary computations, this part uses DSP. It should be noted that the Rx phase differences solely depend on the signal incident direction θ. Therefore, they will change on a much slower rate compared to a modulated communication signal. The utilized DSP unit can therefore be optimized for low power consumption.

Tx beamforming: The Tx input signal is processed in the analog domain by digitally controlled phase shifters and variable gain amplifiers (VGAs). This is used to apply analog beamforming as demanded in Req. 4.

Up-mix: This unit coherently mixes the beamformed Tx signals up to the desired transmit frequency. The up-mixed signal is then fed to the dual-band array for transmission. According to Req. 1, the Tx frequency band is different from the Rx band to avoid feedback.

In the following sections, we will analyze the down-mix and phase detection block of the receiver part in Fig. 3.1. We will start with an overview of the receiver channel architecture from which we create an analytic model. Simulations are used to prove that the proposed system is suitable for retro-directive operation.

3.2 Receiver channel architecture and modeling

The proposed RDA system in Fig. 3.1 consists of N Rx and Tx channels, one for each antenna element in the array. A single channel of the down-mix and phase detection block is depicted in Fig. 3.2. The circuit is a nested PLL structure: The phase-frequency detector (PFD) d_1, loop filter h_1 and the VCO V_1 constitute the forward path of an outer PLL [64]. In its feedback path, we find a frequency synthesizer, i.e. a PLL whose output frequency is M times higher than its input frequency. The feedback path of the outer PLL is closed by the mixer and lowpass h_{LP} whose output signal is on an IF.

3.2.1 Qualitative working principle

As we have seen in chapter 2, PLLs can be employed to phase-align signals to a local reference and are widely used for this purpose e.g. in [12, 46, 65, 66]. This principle is exploited in our proposed receiver architecture: The RF signal received by the n-th Rx antenna is multiplied with the PLL synthesizer output signal $v_{\mathrm{V2},n}$. The lowpass h_{LP} removes the resulting higher mixing product. Thus $v_{\mathrm{IF},n}$ is a down-mixed version of the RF signal. It is compared to a

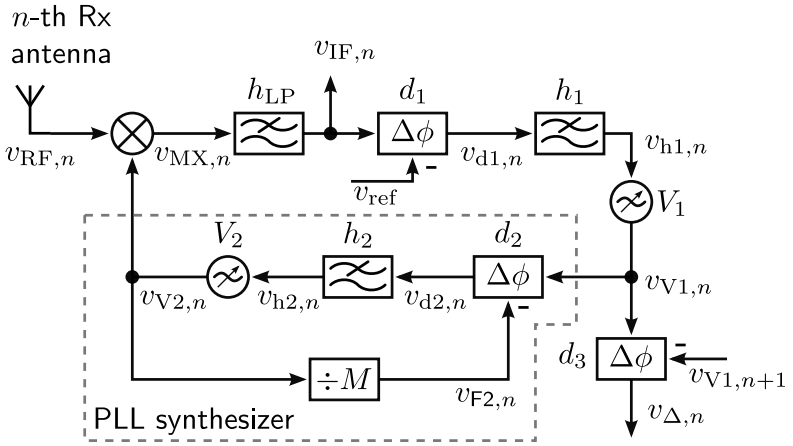

Fig. 3.2: Block diagram of a single receiver channel. Inputs are the RF and the reference signals. The receiver has an IF output, yielding a down-mixed version of the RF input which is phase-aligned to the reference signal. The VCO V_1 output signal carries the RF signal phase information and is compared to that of the neighboring channel.

local reference signal v_{ref} in the PFD d_1. Under the condition that the feedback loop is stable, the system will adapt until the phase difference between $v_{\mathrm{IF},n}$ and v_{ref} is zero. Qualitatively, the system behavior is as follows

- The PFD d_1 compares v_{ref} and v_{IF}; the result steers the VCO V_1;
- The output signal of this VCO generates the mixing signal $v_{\mathrm{V2},n}$ at the output of the frequency synthesizer;
- Through a feedback loop, the system adapts until the IF signal v_{IF} resulting from the filtered multiplication of $v_{\mathrm{RF},n}$ and $v_{\mathrm{V2},n}$ appears in phase with the reference signal v_{ref}.

Using the same reference signal for all channels, we obtain a phase aligned IF version of each received RF signal. Combining all IF signals, we make use of the Rx array gain. In the following, we shall analytically describe the receiver channel and quantitatively analyze its behavior.

3.2.2 System component modeling

When modeling PLL circuits, we have to observe some peculiarities: The input and output signals of a PLL are periodic and are described by harmonic functions. The purpose of the PLL however is to compare the phase terms of two signals and to generate an output signal according to this difference. Therefore, we are mainly interested in the arguments of the harmonic time signals, i.e. their phase terms. In the following, we shall introduce the signal and system models underlying our analysis of the receiver channel. As is common in PLL literature [64, 67, 68, 69], we shall later describe the dynamic behavior of the PLL circuits in terms of phase transfer functions. In preparation of this later analysis in section 3.2.3, we will point out the relevant phase terms in this section.

Array signal reception model

Let us assume that we use a ULA of N identical antenna elements with spacing d as depicted in Fig. 1.2. As in section 1.1.2, we further assume that the ULA is located in the far field and that the narrowband assumption holds. Thus, we have an incident plane wave impinging on the array under angle θ as described in (1.7). According to (1.9), the resulting excitation at the n-th antenna port can then be described as

$$v_{\mathrm{RF},n}(t) = \hat{v}_{\mathrm{RF},n}(\theta)\cos(\underbrace{\omega_{\mathrm{RF}}t + \varphi_{\mathrm{RF}}(t) + \delta_n(\theta)}_{:=\Psi_{\mathrm{RF},n}(t,\theta)}), \tag{3.1}$$

with $n \in 1,\ldots,N$. $\hat{v}_{\mathrm{RF},n}(\theta)$ is the voltage amplitude. The dependency on θ reflects the directional characteristic of the antenna element. ω_{RF} is the carrier frequency, $\varphi_{\mathrm{RF}}(t)$ is the momentary phase of the impinging wave which may be used for modulation, and δ_n is the geometry induced phase term at each antenna element. For our ULA with element $n = 1$ located at the origin, this term reads

$$\delta_n(\theta) = 2\pi(n-1)d_r\cos(\theta), \tag{3.2}$$

where $\theta = 90°$ is the boresight direction, i.e. perpendicular to the array extension, and we have used the relative element spacing

$$d_r = \frac{d}{\lambda_{\mathrm{RF}}} = d\frac{\omega_{\mathrm{RF}}}{2\pi c_0}. \tag{3.3}$$

λ_{RF} and c_0 denote the free-space wavelength of the RF signal and the speed of light in vacuum, respectively. Since retro-directivity requires phase conjugation of the individual phase term of the n-th received signal, the system needs to extract $\delta_n(\theta)$ from (3.1) and apply its conjugated and squint corrected value to a Tx signal.

Down-mixer

As depicted in Fig. 3.2, the down-mixer consists of a multiplier and a subsequent lowpass filter. Let us assume that the two input signals of the multiplier are harmonic signals of the form

$$v_i(t) = \hat{v}_i\cos(\underbrace{\omega_i t + \varphi_i}_{:=\Psi_i(t)}), \quad i \in 1,2, \tag{3.4}$$

with $\varphi_i \in [0,\ldots,2\pi[$. Multiplying these signals and using the product-to-sum identities of sinusoidal functions [70, p.182], we obtain the mixer output to be

$$v_{\mathrm{MX}}(t) = \frac{1}{2}\hat{v}_1\hat{v}_2\Big[\cos(\underbrace{(\omega_1-\omega_2)t + \varphi_1 - \varphi_2}_{\Psi_1(t)-\Psi_2(t)}) - \cos((\omega_1+\omega_2)t + \varphi_1 + \varphi_2)\Big]. \tag{3.5}$$

The resulting signal has a difference and a sum frequency component. We choose the lowpass filter such that it will eliminate the sum frequency part. The remaining signal after the filter thus contains only the frequency difference term and is used as IF signal in our receiver. We assume the lowpass filter to behave ideally. That means, it completely eliminates the frequency sum term in (3.5) and does not introduce any distortion to the remaining term. The output signal after the ideal lowpass filter therefore is

$$v_{\mathrm{IF}}(t) = \frac{1}{2}\hat{v}_1\hat{v}_2\cos(\Psi_1(t) - \Psi_2(t)). \tag{3.6}$$

Linear phase detector

The phase detector is an essential part of any PLL [64]. It compares two periodic signals of approximately equal frequency and outputs a voltage which is proportional to their phase difference. If we assume two harmonic input signals as in (3.4) but with $\omega_1 = \omega_2$, the output voltage of an ideal phase detector is

$$v_{\mathrm{d,ideal}}(t) = K_{\mathrm{d}} \left(\Psi_1(t) - \Psi_2(t)\right) = K_{\mathrm{d}}(\varphi_1 - \varphi_2), \tag{3.7}$$

with K_{d} being the gain of the detector in V/rad. We can approximate this linear behavior by a PFD implementation with flip-flops [64]. Appendix A.2 contains a detailed model of such a PFD which has been published in [71]. (A.10) shows that the device outputs a stream of pulses whose time average is proportional to the desired phase difference. That means, we have to use the mean of the output signal, $\bar{v}_{\mathrm{d}}(t)$, i.e. the time integral of the pulse stream, to obtain the ideal output described by (3.7). In contrast to a pure phase detector, a PFD can also detect frequency differences between its input signals. The sign of the PFD output signal indicates which of the two input frequencies is higher. We can write the expected value of the mean output voltage as

$$E\left[\bar{v}_{\mathrm{d}}\right] = \begin{cases} K_{\mathrm{d}}(\varphi_1 - \varphi_2) & \text{if } \omega_1 = \omega_2 \\ K_{\mathrm{d}}(-1)^{f-1}\left(1 - \dfrac{\omega_s}{2\omega_f}\right) & \text{else} \end{cases}, \tag{3.8}$$

where $f, s \in 1, 2$ and $f \neq s$ are the indices of the faster and slower harmonic signal, respectively. For the receiver channel model, we will use the ideal phase detector described by (3.7). This is justified if the frequencies of the input signals of the PFD are equal. For a stable PLL system, this is the case in the steady state.

Loop filter

In a PLL, the loop filter processes the phase detector output signal. It thus influences the dynamic behavior of the PLL [69]. We require the filter to have lowpass characteristic. This is necessary to capture the desired output of the phase detector which becomes constant in the steady state. Moreover, a lowpass acts as an integrator on its input signal which allows us to use the flip-flop based PFD realization described above. Although filters can be represented in the time domain, it is more convenient to use the Laplace transform of their transfer functions. In general, we can describe a filter in the Laplace domain by

$$h_i(s) = \frac{N_{hi}(s)}{D_{hi}(s)} = \frac{b_{i,0} + b_{i,1}s + \ldots + b_{i,L_{i,\mathrm{N}}}s^{L_{i,\mathrm{N}}}}{1 + a_{i,1}s + \ldots + a_{i,L_{i,\mathrm{D}}}s^{L_{i,\mathrm{D}}}}, \tag{3.9}$$

with $L_{i,\mathrm{D}} \geq L_{i,\mathrm{N}}$. The order of the filter thereby is $L_{i,\mathrm{D}}$. To obtain lowpass behavior, we have to make sure that $b_{i,0} \neq 0$.

Voltage controlled oscillator

A VCO generates a sinusoidal signal whose frequency depends on the input voltage $v_{\mathrm{h}i}(t)$. In the time domain, we can write the VCO output as [64]

$$v_{\mathrm{V}i,n}(t) = \sin\Bigg(\underbrace{\omega_{\mathrm{q}i}t + \int_0^t K_{\mathrm{V}i} v_{\mathrm{h}i,n}(\tau)d\tau}_{:=\Psi_{\mathrm{V}i,n}(t)}\Bigg), \tag{3.10}$$

where $\omega_{\mathrm{q}i}$ is the quiescent frequency of the oscillator and $K_{\mathrm{V}i}$ is the VCO sensitivity in Hz/V. We can see that the VCO acts as an integrator on its input signal. Therefore, even without a loop filter, i.e. $h_i(s) = 1$, the PFD output signal $v_{\mathrm{d}i,n}$ is integrated over time. That means we can assume the ideal PFD behavior in (3.7) when using the flip-flop based implementation described in appendix A.2.

Frequency divider

As the name suggests, this device divides down the frequency of a periodic input signal by a factor $M \in \mathbb{N}$. Although there are analog realizations which use mixers and feedback loops [72, 73], frequency dividers are commonly realized with logic circuits [74]. A digital frequency divider counts the edges of its input signal, by registering sign changes. It is described in [69] and schematically shown in Fig. B.3. After M sign changes have occurred, the output of the circuit is toggled from negative to positive or vice versa. Thus we generate an output square wave whose rising and falling edges are M sign changes of the input signal apart. Obviously, this device is non-linear. Let us regard the Fourier series of the output square wave of the frequency divider which is given by

$$v_{\mathrm{F}}(\Psi_{\mathrm{F,out}}(t)) = \hat{v}_{\mathrm{F}}\frac{4}{\pi}\sum_{m=1}^{\infty}\frac{\sin\left((2m-1)\Psi_{\mathrm{F,out}}(t)\right)}{2m-1}, \tag{3.11}$$

where we used the phase term $\Psi_{\mathrm{F,out}}(t) = \omega_{\mathrm{F,out}}t + \varphi_{\mathrm{F,out}}$ with $\omega_{\mathrm{F,out}}$ and $\varphi_{\mathrm{F,out}}$ being the fundamental frequency and phase.

From the frequency divider description above we can see that the output signal in (3.11) will be generated by any periodic input signal which has M sign changes during the period $1/\omega_{\mathrm{F,out}}$. That means, if the input signal is composed of harmonic waves, e.g. a sinusoid, triangular, sawtooth or square wave, its fundamental phase term must be $\Psi_{\mathrm{F,in}}(t) = M\Psi_{\mathrm{F,out}}(t)$. Although the frequency divider itself is non-linear, the relation between the fundamental phase terms of input and output signals can thus be described by the linear equation

$$\frac{\Psi_{\mathrm{F,out}}(t)}{\Psi_{\mathrm{F,in}}(t)} = \frac{1}{M}. \tag{3.12}$$

3.2.3 Receiver signal model

Having introduced all individual component models, we will now derive the relations between input and output signals of the complete receiver channel depicted in Fig. 3.2. As we have seen previously, the components of our system except the loop filter are non-linear. However, the signals v_{ref}, $v_{\mathrm{RF},n}$, $v_{\mathrm{IF},n}$, $v_{\mathrm{V}i,n}$ and $v_{\mathrm{F2},n}$ are periodic and composed of harmonic waves.

Moreover, we have seen that the down-mixer (3.6), PFDs (3.7) and frequency divider (3.12) have a linear behavior with respect to the phase terms of harmonic input signals. Finally, according to (3.10), the relation between the VCO input signal and its output phase term is also linear. Under the condition that we regard the phase terms of the fundamental harmonics only, this allows us to regard the whole system as linear. We are therefore able to conduct the analysis in the Laplace domain which is convenient since we are dealing with feedback systems.

We will start the following system analysis with the inner feedback loop, i.e. the PLL synthesizer. Then we shall regard the outer PLL and establish the phase transfer function from the RF input to VCO V_1 output. Afterwards, we examine the phase detection output $v_{\Delta,n}$ and finally show the constructive superposition of the IF signals.

PLL synthesizer

This part of our receiver system is a classic PLL as described and analyzed in [64] or [69] among others. We can find the relation between input and output signal phase of the PLL synthesizer by taking the Laplace transform of the VCO phase term in (3.10). It reads

$$\Psi_{\mathrm{V}i}(s) = \frac{\omega_{\mathrm{q}i}}{s^2} + \frac{K_{\mathrm{V}i}}{s} v_{\mathrm{h}i,n}(s) = \frac{\omega_{\mathrm{q}i}}{s^2} + \frac{K_{\mathrm{V}i}}{s} h_i(s) v_{\mathrm{d}i,n}(s), \tag{3.13}$$

where we used the filter transfer function from (3.9) and the PFD output signal from (3.7). Inserting the input signal phase term $\Psi_{\mathrm{V1},n}$ and using (3.12), we obtain the output phase term of the VCO V_2 as

$$\Psi_{\mathrm{V2},n}(s) = \frac{\omega_{\mathrm{q2}}}{s^2} + \frac{K_{\mathrm{V2}}}{s} h_2(s) K_{\mathrm{d2}} \left(\Psi_{\mathrm{V1},n}(s) - \frac{1}{M} \Psi_{\mathrm{V2},n}(s) \right) = \frac{\frac{\omega_{\mathrm{q2}}}{s} + K_2 h_2(s) \Psi_{\mathrm{V1},n}(s)}{s + \frac{K_2}{M} h_2(s)}, \tag{3.14}$$

with $K_2 = K_{\mathrm{V2}} K_{\mathrm{d2}}$. Two observations can be made here: First, (3.14) is not a phase transfer function because we cannot write it in the form $\Psi_{\mathrm{V2},n}/\Psi_{\mathrm{V1},n}$. To arrive at such an expression, we would have to eliminate the quiescent frequency of the VCO, i.e. $\omega_{\mathrm{q2}} = 0$. This is the usual approach in the PLL literature [64, 69]. It is justified by the assumption that only small variations around the quiescent frequency will occur. However, in our analysis, we shall keep the quiescent frequency in order to see its influence on the output signals. Second, we observe that the order of the polynomial in the denominator of (3.14) directly depends on the filter order of h_2 and amounts to $L_{2,\mathrm{D}} + 1$. This shows the influence of the loop filter on the dynamic behavior of the PLL synthesizer. We will discuss this influence in more detail in section 3.3.

Outer PLL

Referring to Fig. 3.2, we see that the PLL synthesizer output signal and the RF signal from the n-th antenna are both fed to the down-mixer. From (3.6), we know that the resulting IF signal phase term in the Laplace domain is given by

$$\Psi_{\mathrm{IF},n}(s) = \Psi_{\mathrm{RF},n}(s) - \Psi_{\mathrm{V2},n}(s). \tag{3.15}$$

The IF signal is the feedback signal of the outer PLL while the actual input is the local reference signal given by

$$v_{\mathrm{ref}}(t) = \cos \underbrace{(\omega_{\mathrm{ref}} t)}_{:=\Psi_{\mathrm{ref}}(t)} . \tag{3.16}$$

Inserting this into (3.13) and using (3.7) again, we arrive at the output signal phase term of VCO V_1 which is

$$\Psi_{\mathrm{V1},n}(s) = \frac{\omega_{\mathrm{q1}}}{s^2} + \frac{K_1}{s} h_1(s) \left(\Psi_{\mathrm{IF},n}(s) - \Psi_{\mathrm{ref}}(s)\right). \tag{3.17}$$

Inserting (3.14) and (3.15), we arrive at

$$\Psi_{\mathrm{V1},n}(s) = \frac{N_{\mathrm{V1},n}(s)}{D_{\mathrm{V1}}(s)}, \quad \text{with} \tag{3.18}$$

$$D_{\mathrm{V1}}(s) = s^2 + s\frac{K_2}{M} h_2 + K_1 K_2 h_1 h_2, \tag{3.19}$$

$$N_{\mathrm{V1},n}(s) = \omega_{\mathrm{q1}} + \frac{1}{s}\left(\frac{K_2}{M} h_2 \omega_{\mathrm{q1}} - K_1 h_1 \omega_{\mathrm{q2}}\right) + K_1 h_1 \left(s + \frac{K_2}{M} h_2\right) \left(\Psi_{\mathrm{RF},n} - \Psi_{\mathrm{ref}}\right), \tag{3.20}$$

where we have omitted the dependency of the phase terms and filter transfer functions on s for better readability. It should be noted that the denominator $D_{\mathrm{V1}}(s)$ is independent of the array channel n. Assuming a constant RF signal phase φ_{RF} and inserting the Laplace transforms $\Psi_{\mathrm{ref}}(s) = \mathcal{L}\{\Psi_{\mathrm{ref}}\} = \frac{\omega_{\mathrm{ref}}}{s^2}$ and $\Psi_{\mathrm{RF},n}(s) = \mathcal{L}\{\Psi_{\mathrm{RF},n}\} = \frac{\omega_{\mathrm{RF}}}{s^2} + \frac{\varphi_{\mathrm{RF}} + \delta_n(\theta)}{s}$, we expand the last term into

$$\begin{aligned} N_{\mathrm{V1},n}(s) =& \frac{1}{s^2}\left(\frac{K_1 K_2 h_1 h_2}{M}(\omega_{\mathrm{RF}} - \omega_{\mathrm{ref}})\right) + \frac{1}{s}\left(\frac{K_2 h_2}{M}\omega_{\mathrm{q1}} + K_1 h_1(\omega_{\mathrm{RF}} - \omega_{\mathrm{ref}} - \omega_{\mathrm{q2}})\right. \\ &\left. + \frac{K_1 K_2 h_1 h_2}{M}\left(\varphi_{\mathrm{RF}} + \delta_n(\theta)\right)\right) + \omega_{\mathrm{q1}} + K_1 h_1 \left(\varphi_{\mathrm{RF}} + \delta_n(\theta)\right). \end{aligned} \tag{3.21}$$

We observe that the phase term of the VCO V_1 output signal depends on the input frequencies of the system, $\omega_{\mathrm{ref}}, \omega_{\mathrm{RF}}$ as well as on the inner frequencies $\omega_{\mathrm{q1}}, \omega_{\mathrm{q2}}$. Besides that, it carries the RF phase information φ_{RF} and the geometric phase $\delta_n(\theta)$ which both are of interest for us: The former to obtain the information modulated on the RF carrier, the latter for phase conjugation and DoA estimation.

Phase detection output signal

The PFD d_3 in Fig. 3.2 compares the output signal of VCO V_1 to that of the neighboring channel. Setting $K_{\mathrm{d3}} = 1/(2\pi)$ V/rad and using (3.7) and (3.18), we can find the time average of the output signal of this PFD to be

$$\bar{v}_{\Delta,n}(s) = \frac{\Psi_{\mathrm{V1},n}(s) - \Psi_{\mathrm{V1},n+1}(s)}{2\pi} = \frac{N_{\mathrm{V1},n(s)} - N_{\mathrm{V1},n+1}(s)}{2\pi D_{\mathrm{V1}}(s)}, \tag{3.22}$$

$n \in 1, \ldots, N-1$. Inserting (3.19) and (3.21) we arrive at the PFD output voltage

$$\bar{v}_{\Delta,n}(s) = \frac{K_1 h_1}{2\pi s} \frac{\left(s + \frac{K_2 h_2}{M}\right)\left(\delta_n(\theta) - \delta_{n+1}(\theta)\right)}{s^2 + s\frac{K_2}{M} h_2 + K_1 K_2 h_1 h_2} = \frac{K_1 h_1}{s} \frac{\left(s + \frac{K_2 h_2}{M}\right)\left(-d_r \cos(\theta)\right)}{s^2 + s\frac{K_2}{M} h_2 + K_1 K_2 h_1 h_2}, \tag{3.23}$$

where (3.2) has been used to get the final expression. By evaluating the difference of two signal phase terms $\Psi_{\mathrm{V1},n}$, we have eliminated all summands independent of n from the numerator. Since our goal is to detect the geometric phase differences which are changing slowly, we are interested in the long term behavior of the output. This is obtained by applying the final value theorem to (3.23) which yields

$$\bar{v}_\Delta(\theta) = \lim_{t\to\infty} \bar{v}_{\Delta,n}(t) = \lim_{s\to 0} s\bar{v}_{\Delta,n}(s) = \frac{\delta_n(\theta) - \delta_{n+1}(\theta)}{2\pi M} = -\frac{d_r \cos(\theta)}{M}. \tag{3.24}$$

That means the output signals of the VCOs V_1 of all channels have a phase difference with respect to the neighboring channel which is proportional to that of the respective RF signals. The proportionality constant is $1/M$. Since we are using a ULA, the $N-1$ phase detection outputs yield the same result. The phase difference between the RF signals of two neighboring array elements can be found by

$$\Delta\delta(\theta) = (2\pi M \bar{v}_\Delta(\theta)) \bmod (2\pi), \tag{3.25}$$

where $a \bmod b$ denotes the modulo division defined in (A.1). This computation is necessary to resolve the ambiguity introduced by the division factor M: Let the RF phase difference be within the range $\Delta\delta \in [0, \ldots, 2\pi[$. Due to the chosen gain K_{d3}, the phase detection output voltage can then be in the range $\bar{v}_\Delta \in]-1\,\mathrm{V}, \ldots, 1\,\mathrm{V}[$. There are now several $\bar{v}_\Delta$ values for the same $\Delta\delta$, which are given by

$$\bar{v}_\Delta(\theta) = \frac{m}{M} K_{\mathrm{d3}} \Delta\delta(\theta), \quad m \in [-M+1, \ldots, -1, 1, \ldots, M-1]\,. \tag{3.26}$$

After applying (3.25) and multiplying with the array squint correction factor from (1.14), we can use the obtained phase difference information to steer the retro-directive Tx signal beam. If desired, we can additionally obtain an estimate of the incident direction of the RF signal from the output signal of PFD d_3 by

$$\hat{\theta} = \arccos\left(-\frac{\Delta\delta(\theta)}{d_r}\right). \tag{3.27}$$

Intermediate frequency output signal

In Req. 3, we have postulated that the RDA system is able to make use of the gain of the Rx antenna array. To check the fulfillment of this requirement, we have to analyze the IF output signal in Fig. 3.2. Starting from (3.15), we insert (3.14) and (3.17) to arrive at

$$\Psi_{\mathrm{IF},n}(s) = \Psi_{\mathrm{RF},n}(s) - \frac{\frac{\omega_{\mathrm{q2}}}{s} + K_2 h_2(s)\left(\frac{\omega_{\mathrm{q1}}}{s^2} + \frac{K_1 h_1(s)}{s}(\Psi_{\mathrm{IF},n}(s) - \Psi_{\mathrm{ref}}(s))\right)}{s + \frac{K_2 h_2(s)}{M}} \tag{3.28}$$

$$= \frac{s\left(s + \frac{K_2 h_2(s)}{M}\right)\Psi_{\mathrm{RF},n}(s) - \omega_{\mathrm{q2}} + K_2 h_2(s)\left(\frac{\omega_{\mathrm{q1}}}{s} - K_1 h_1(s)\Psi_{\mathrm{ref}}(s)\right)}{s\left(s + \frac{K_2 h_2(s)}{M}\right) + K_1 K_2 h_1(s) h_2(s)}. \tag{3.29}$$

Inserting the previously used Laplace transform of the RF and reference signals, we can evaluate the last expression to

$$\Psi_{\mathrm{IF},n}(s) = \frac{N_{\mathrm{IF},n}(s)}{s^2 + s\frac{K_2 h_2(s)}{M} + K_1 K_2 h_1(s) h_2(s)}, \quad \text{with} \tag{3.30}$$

$$\begin{aligned} N_{\mathrm{IF},n}(s) = &\left(s + \frac{K_2 h_2(s)}{M}\right)(\varphi_{\mathrm{RF}} + \delta_n(\theta)) + \omega_{\mathrm{RF}} - \omega_{\mathrm{q2}} \\ &+ \frac{K_2 h_2(s)}{s}\left(\frac{\omega_{\mathrm{RF}}}{M} - \omega_{\mathrm{q1}}\right) + \frac{K_1 K_2 h_1(s) h_2(s)}{s^2}\omega_{\mathrm{ref}}. \end{aligned} \tag{3.31}$$

For all IF signals to be phase aligned, their mutual differences need to vanish. Let us examine the IF signals of channels n and m with $n \neq m$. We take the difference

$$\Delta\Psi_{\mathrm{IF},nm}(s) = \Psi_{\mathrm{IF},n}(s) - \Psi_{\mathrm{IF},m}(s) = \frac{\left(\frac{K_2 h_2}{M} + s\right)(\delta_n(\theta) - \delta_m(\theta))}{s^2 + s\frac{K_2 h_2}{M} + K_1 K_2 h_1 h_2}, \tag{3.32}$$

where we inserted (3.30) and (3.31). Again, we are interested in the steady-state behavior of the output signal. Applying the final value theorem to the last expression leads to the desired result

$$\lim_{t\to\infty} \Delta\Psi_{\mathrm{IF},nm}(t) = \lim_{s\to 0} s\Delta\Psi_{\mathrm{IF},nm}(s) = 0. \tag{3.33}$$

This means that the mutual difference between the IF signals becomes zero over time. Thus, any two IF output signals are phase-aligned and add up constructively when combined. Summing the IF signals of all channels increases signal amplitude by a factor of N at most which means we make use of the Rx array gain.

In this section, we have introduced the individual components of our receiver channels. We have motivated the use of phase transfer functions and deduced the relation between RF input signal phase term, phase detection output and IF output signal phase term. Referring to the requirements made at the beginning of this chapter, we have shown that the proposed system architecture is able to down-mix a received signal to an IF (Req. 2) and make use of the antenna array gain on receive (Req. 3). Moreover, we have seen that the phase detection result can be used for DoA estimation and retro-directive beamforming on different frequencies, thus fulfilling Req. 4.

3.3 Receiver design and dynamic behavior

Up to now, we have analyzed the steady state, i.e. long term behavior of the proposed retro-directive receiver. In the following, we will investigate the dynamic behavior of the receiver channel more closely. We have to know how the system reacts to input signal phase changes. These may be due to movement of the signal source, affecting $\delta_n(\theta)$ in (3.1), or due to phase modulation resulting in a change of $\varphi_{\mathrm{RF}}(t)$. For the latter case, the dynamic behavior shows the capability of our receiver to deal with modulation. This is especially important for the targeted satellite communication applications.

3.3.1 General phase transfer functions

Previously, we have looked at the phase terms of the output signals in order to find the phase detection result and to show that the IF output signals are phase aligned. To analyze system dynamics, we have to work with phase transfer functions. Especially, we are interested in how the RF signal phase influences the output of VCO V_1 and the IF signal. For this, we need functions of the form $\Psi_{\mathrm{V1},n}/\Psi_{\mathrm{RF},n}$ and $\Psi_{\mathrm{IF},n}/\Psi_{\mathrm{RF},n}$. However, regarding (3.18), (3.20) and (3.29), we see that it is not possible to establish such forms. Therefore, we have to make the following assumptions: First, the regarded feedback systems have to be stable. This also means that the PFD outputs attain constant values if the input of the system does not change. If that is the case, the output frequencies of both VCOs, V_1 and V_2 in Fig. 3.2, are stable. Second, we assume that only small phase changes around the stable VCO output frequencies occur. This means that we can neglect the frequency terms in our previously deduced signal model, i.e. $\omega_{\mathrm{RF}} = \omega_{\mathrm{ref}} = \omega_{\mathrm{q1}} = \omega_{\mathrm{q2}} = 0$. These assumptions are widely used in PLL analysis [64, 69]. We show their validity in appendix A.3 by investigating the receiver channel in the time domain and derive the steady state for purely sinusoidal excitation in (A.37) and (A.38).

To avoid confusion, we shall mark the phase terms with the above simplifications by a small circle. Under the mentioned assumptions, the phase transfer function for the outer PLL from (3.18) reads

$$\begin{aligned} G_{\mathrm{V1},n}(s) = \frac{\mathring{\Psi}_{\mathrm{V1},n}(s)}{\mathring{\Psi}_{\mathrm{RF},n}(s)} &= \frac{sK_1h_1 + \frac{K_1K_2}{M}h_1h_2}{s^2 + s\frac{K_2}{M}h_2 + K_1K_2h_1h_2} \\ &= \frac{sK_1N_{h1}D_{h2} + \frac{K_1K_2}{M}N_{h1}N_{h2}}{s^2D_{h1}D_{h2} + s\frac{K_2}{M}N_{h2}D_{h1} + K_1K_2N_{h1}N_{h2}}, \end{aligned} \tag{3.34}$$

where we have inserted the general filter transfer functions from (3.9). Similarly, we can rewrite the IF phase transfer function from (3.29) as

$$\frac{\mathring{\Psi}_{\mathrm{IF},n}(s)}{\mathring{\Psi}_{\mathrm{RF},n}(s)} = \frac{s + \frac{K_2}{M}h_2}{s^2 + s\frac{K_2}{M}h_2 + K_1K_2h_1h_2} = \frac{sD_{h1}D_{h2} + \frac{K_2}{M}N_{h2}D_{h1}}{s^2D_{h1}D_{h2} + s\frac{K_2}{M}N_{h2}D_{h1} + K_1K_2N_{h1}N_{h2}}. \tag{3.35}$$

Regarding the last two equations, we see that the phase transfer functions of our receiver channels depend on the loop filters h_1 and h_2 as can be expected. From (3.9) we know that $N_{hi}(s)$ and $D_{hi}(s)$ are polynomials of order $L_{i,N}$ and $L_{i,D}$, respectively. The poles of a transfer function define the dynamic behavior of the system and its order. The denominator of both (3.34) and (3.35) is the same and the system order is $L_{1,D} + L_{2,D} + 2$. For further characterization of the system we have to make assumptions regarding the actual filter order.

3.3.2 Fourth order system

From now on, we will use first order lowpass filters with one pole and one zero for h_1 and h_2. A realization of such a filter with passive components is depicted in Fig. A.3. Using the formulation in (3.9), we can write the respective transfer function as

$$\breve{h}_i(s) = \frac{\breve{N}_{hi}(s)}{\breve{D}_{hi}(s)} = \frac{1 + s\tau_{2i}}{1 + s(\underbrace{\tau_{1i} + \tau_{2i}}_{:=\tau_{12i}})}, \tag{3.36}$$

whereby the time constants must fulfill $\tau_{1i}, \tau_{2i} > 0$ and thus $\tau_{12i} > \tau_{2i}$. We have chosen this filter type because it is widely used in PLL design to build second order loops [64]. The use of higher order filters is of course possible. However, using (3.36), the receiver becomes a fourth order system which already makes design and optimization of the dynamic behavior challenging as we shall see in the following.

Let us analyze the output phase term of the VCO V_1. By inserting the filter transfer functions from (3.36) into (3.34), we obtain

$$\begin{aligned} G_{\mathrm{V1},n}(s)|_{h_i(s)=\check{h}_i(s)} &= K_1 \frac{s^3\tau_{122}\tau_{21} + s^2\left(\tau_{21}+\tau_{122}+\frac{K_2}{M}\tau_{21}\tau_{22}\right) + s\left(1+\frac{K_2}{M}(\tau_{21}+\tau_{22})\right)+\frac{K_2}{M}}{s^4\tau_{121}\tau_{122} + s^3\left(\tau_{121}+\tau_{122}+\frac{K_2\tau_{22}\tau_{121}}{M}\right) + s^2\Bigg(\frac{K_2}{M}(\tau_{22}+\tau_{121}) \\ &\qquad + K_1K_2\tau_{21}\tau_{22}+1\Bigg) + s\left(\frac{K_2}{M}+K_1K_2(\tau_{21}+\tau_{22})\right)+K_1K_2} \\ &= \frac{K_1}{\tau_{121}\tau_{122}} \frac{\left(s^2\tau_{122}+s\left(1+\frac{K_2}{M}\tau_{22}\right)+\frac{K_2}{M}\right)(s\tau_{21}+1)}{s^4 + s^3\left(\frac{1}{\tau_{122}}+\frac{1}{\tau_{121}}+\frac{K_2}{M}\frac{\tau_{22}}{\tau_{122}}\right) + s^2\Bigg(\frac{K_2}{M}\left(\frac{\tau_{22}}{\tau_{121}\tau_{122}}+\frac{1}{\tau_{122}}\right) \\ &\qquad + K_1K_2\frac{\tau_{21}\tau_{22}}{\tau_{121}\tau_{122}}+\frac{1}{\tau_{121}\tau_{122}}\Bigg) + s\frac{K_2}{\tau_{121}\tau_{122}}\left(\frac{1}{M}+K_1(\tau_{21}+\tau_{22})\right)+\frac{K_1K_2}{\tau_{121}\tau_{122}}}. \end{aligned} \tag{3.37}$$

The denominator of this expression is the characteristic polynomial of our system and is equivalent to the one found by time domain analysis in (A.39). The poles of the transfer function can be found numerically for a given set of parameters K_1, K_2, M and filter time constants. Although there is an algebraic solution to the problem of finding the roots of a fourth order polynomial, its usage does not make much sense here for the following reasons: The solution includes substitutions and the introduction of auxiliary variables. This leads to large and complicated terms which do not allow to identify e.g. the pole with the largest real part. Moreover, the location of every pole is dependent on all our system parameters. Thus, the algebraic solution does not help to deduce a strategy on how to set the parameters in order to achieve a certain system behavior.

3.3.3 Second order approximations

In the following, we shall investigate possible second order systems to approximate the system behavior described in (3.37). As we shall see, second order systems are easier to parameterize and stability is usually fulfilled. However, the validity of the approximations and the stability of the approximated fourth order system has to be checked separately.

Neglecting loop filter influence

We obtain a second order system if we omit the loop filters, i.e. $h_i(s) = 1$. Referring to (3.36), this approximation is valid if

$$\tau_{1i} \ll \tau_{2i} \quad \text{or} \tag{3.38a}$$

$$|\tau_{12i}s| \ll 1. \tag{3.38b}$$

From (3.34), we get the simplified phase transfer function

$$\check{G}_{\mathrm{V1},n}(s) = G_{\mathrm{V1},n}(s)|_{h_i(s)=1} = K_1 \frac{s+\frac{K_2}{M}}{s^2 + s\frac{K_2}{M} + K_1K_2}, \tag{3.39}$$

which describes a second order system. We see that the denominator has the form of a harmonic oscillator, which is commonly written in the Laplace domain as

$$s^2 + 2\zeta\omega_0 s + {\omega_0}^2 = 0. \tag{3.40}$$

It is defined by its natural frequency ω_0 and its damping ratio ζ. Comparing the coefficients with the denominator of (3.39) yields the respective quantities for the second order system as

$$\omega_0 = \sqrt{K_1 K_2}, \tag{3.41}$$

$$\zeta = \frac{1}{2M}\sqrt{\frac{K_2}{K_1}}. \tag{3.42}$$

The poles of (3.39) are given by

$$s_{1,2} = -\omega_0\zeta\left(1 \pm \sqrt{1 - \frac{1}{\zeta^2}}\right). \tag{3.43}$$

Since ω_0 and ζ are positive quantities, the real part of the poles always fulfills $\Re\{s_{1,2}\} < 0$. This means that the system is unconditionally stable. There are two real poles if $\zeta > 1$, a double real pole at $-\omega_0\zeta$ for $\zeta = 1$ and a complex pole pair with a real part of $-\omega_0\zeta$ otherwise.

The system is parameterized by K_1, K_2 and M as we can see from (3.41) and (3.42). Therefore, as long as (3.38) is fulfilled, the dynamic behavior is governed by these quantities. The error function $\Delta\breve{G}_{\mathrm{V1},n}(s)$, i.e. the deviation from the fourth order system for this approximation is given in (A.41).

Infinite synthesizer gain

In the previous section, we have completely neglected the influence of the loop filters to obtain a second order system. Our goal now is to find a second order approximation which takes the influence of the outer loop filter $h_1(s)$ into account. Since our receiver channel is a nested feedback system, we make the following assumption: The inner feedback loop, i.e. the PLL synthesizer, should settle considerably faster than the outer feedback loop. That means we assume that the output of the synthesizer always corresponds to its steady state output. We take the phase transfer function from (3.14) and approximate

$$G_{\mathrm{V2},n}(s) = \frac{\mathring{\Psi}_{\mathrm{V2},n}(s)}{\mathring{\Psi}_{\mathrm{V1},n}(s)} = \frac{K_2 h_2(s)}{s + \frac{K_2}{M}h_2(s)} = \frac{N_{h2}(s)}{s\frac{D_{h2}(s)}{K_2} + \frac{N_{h2}(s)}{M}} \approx M, \tag{3.44}$$

which holds as long as $K_2 \gg |sD_{h2}(s)|$. Consequently, we can see that the approximation becomes exact for $s = 0$ and $K_2 \to \infty$. Given that the assumption holds, the approximated VCO V_1 output signal phase from (3.17) becomes

$$\tilde{\mathring{\Psi}}_{\mathrm{V1},n}(s) = \frac{K_1}{s}h_1(s)\left(\mathring{\Psi}_{\mathrm{RF},n}(s) - M\mathring{\Psi}_{\mathrm{V1},n}(s)\right) = \frac{K_1 h_1(s)}{s + K_1 h_1(s) M}\mathring{\Psi}_{\mathrm{RF},n}(s). \tag{3.45}$$

Inserting (3.36), we arrive at the approximated phase transfer function

$$\frac{\tilde{\mathring{\Psi}}_{\mathrm{V1},n}(s)}{\mathring{\Psi}_{\mathrm{RF},n}(s)} = \tilde{G}_{\mathrm{V1},n}(s) = \frac{K_1}{\tau_{121}} \frac{1 + s\tau_{21}}{s^2 + s\left(\frac{1}{\tau_{121}} + K_1 M \frac{\tau_{21}}{\tau_{121}}\right) + \frac{K_1 M}{\tau_{121}}}. \tag{3.46}$$

The deviation between this expression and the true phase transfer function from (3.34) is given in (A.44). We see that the denominator of the phase transfer function again has the form of an harmonic oscillator as in (3.40). This time the natural frequency and damping factor are given by

$$\omega_{01} = \sqrt{\frac{K_1 M}{\tau_{121}}}, \tag{3.47}$$

$$\zeta_1 = \frac{1}{2}\left(\sqrt{\frac{1}{K_1 M \tau_{121}}} + \sqrt{\frac{K_1 M}{\tau_{121}}}\tau_{21}\right), \tag{3.48}$$

and the location of the poles of (3.46) are again found by (3.43). We see that this approximated system is also unconditionally stable for positive filter time constants. The loop filter now allows us to influence natural frequency and damping factor. Alternatively, we can choose the filter time constants for our system to achieve a certain ω_{01} and ζ_1. Reformulating the above equations we arrive at

$$\tau_{121} = \frac{K_1 M}{{\omega_{01}}^2}, \tag{3.49}$$

$$\tau_{21} = \frac{2\zeta_1}{\omega_{01}} - \frac{1}{K_1 M}. \tag{3.50}$$

Since $\tau_{21} \geq 0$, the last equation imposes a restriction on the maximum realizable natural frequency, i.e.

$$\omega_{01,\max} \geq 2\zeta_1 K_1 M. \tag{3.51}$$

Additionally, $\tau_{121} > \tau_{21}$ must be fulfilled from which we obtain the relation

$$K_1 M - 2\zeta_1 \omega_{01} + \frac{1}{K_1 M}{\omega_{01}}^2 > 0. \tag{3.52}$$

This yields the additional condition for the natural frequency if $\zeta_1 \geq 1$:

$$\omega_{01} = \alpha_1 \cdot \omega_{01,\max} \quad \text{with} \begin{cases} \frac{1}{2}\left(1 + \sqrt{1 - \frac{1}{\zeta_1^2}}\right) < \alpha_1 \leq 1 \\ 0 < \alpha_1 < \frac{1}{2}\left(1 - \sqrt{1 - \frac{1}{\zeta_1^2}}\right) \end{cases}. \tag{3.53}$$

As we can see, if ζ_1 becomes large, ω_{01} will approach $\omega_{01,\max}$ or 0. Regarding the filter constants in (3.49) and (3.50), choosing $\omega_{01} = \omega_{01,\max}$ means that $\tau_{21} = 0$, i.e. the loop filter transfer function has no zero anymore. Approaching the lower limit for ω_{01} in the first case of (3.53) leads to $h_1(s) \to 1$.

Under the condition in (3.44), we thus obtain another second order approximation of our receiver system, which can be parameterized within the boundaries specified above. By using the parameters ω_{01} and ζ_1, we get a more intuitive insight of the approximated

system behavior compared to using filter time constants. Additionally, we restrict the valid parameter space. The PLL synthesizer of our receiver system can be similarly characterized as a harmonic oscillator. This is shown in appendix A.5. From these considerations, we have the following approximations to design the fourth order system $G_{\mathrm{V1}}(s)$ described in (3.34):

1) $\check{G}_{\mathrm{V1}}(s)$: second order system model from (3.39) which neglects the loop filter influence and only depends on K_1, K_2 and M,

2) $\tilde{G}_{\mathrm{V1}}(s)$: second order system model from (3.46) which includes loop filter h_1 but assumes that the inner PLL synthesizer adjusts to changes immediately; also depends on K_1, K_2, M, and additionally on τ_{21}, τ_{121} or alternatively ζ_1 and ω_{01},

3) $G_{\mathrm{V2}}(s)$: second order model of the PLL synthesizer from (A.46) which depends on K_2, M and loop filter h_2 which can be parameterized by τ_{22}, τ_{122} or alternatively ζ_2 and ω_{02}.

We will use the second and third option in combination and compare the designed system to the first approximation as well as to the fourth order system.

3.3.4 Design goals

As we have previously seen, the fourth order system can be adjusted by the parameter set

$$\mathbf{p} = [\zeta_1, \omega_{01}, \zeta_2, \omega_{02}]^T. \tag{3.54}$$

In order to find suitable parameter sets, we have to clarify the goals we want to achieve when designing the fourth order system. Referring to the analysis of the phase transfer functions, our design goals are related to the location of its poles $s_{\mathrm{p}i}, i \in 1, \ldots, 4$. Our parameter set $\mathbf{p}$ shall

1) Ensure system stability; this requires all poles of the phase transfer function of the fourth order system to be on the left half plane of the s domain, i.e.

$$\Re\{s_{\mathrm{p}i}\} < 0 \ , \ \forall i. \tag{3.55}$$

   Since the second order approximations are unconditionally stable, stability needs to be checked using the fourth order phase transfer function.

2) Minimize the real part of the pole or pole pair closest to the $j\omega$-axis; the closer a pole is to the axis the slower the system response will. Therefore, we want to find the parameter set

$$\mathbf{p}_{\mathrm{opt}} = \arg\min_{\mathbf{p}} \left[\max\left(\Re\{s_{\mathrm{p}i}\}\right)\right]. \tag{3.56}$$

The first goal is necessary for the receiver to work as expected. However, there will be multiple $\mathbf{p}$ resulting in a stable system. The second goal restricts the solution to the system which we expect to have the fastest transient response.

Table 3.1: Example system base parameters

Parameter	Symbol	Value
Received signal RF	f_{RF}	5.8 GHz
Desired output IF	f_{IF}	100 MHz
Reference oscillator frequency	f_{ref}	100 MHz
VCO V_1 sensitivity	K_{V1}	2.0 MHz/V
PFD D_1 gain	K_{d1}	$2.5/2\pi$ V/rad
VCO V_1 quiescent frequency	f_{q1}	100 MHz
VCO V_2 sensitivity	K_{V2}	63.0 MHz/V
VCO V_2 quiescent frequency	f_{q2}	5.7 GHz
PFD D_2 gain	K_{d2}	$2.5/2\pi$ V/rad
Frequency division factor	M	57

3.3.5 C-band example system

We have seen that it is not possible to generally analyze the system stability because it depends on the actual set of parameters, including K_1, K_2 and M. Let us therefore regard an example system in C-band which is one of the relevant satellite communication bands listed in Table 1.1. We would like to receive signals at $f_{\mathrm{RF}} = 5.8\,\mathrm{GHz}$ and these should be down converted to an IF of 100 MHz. The base parameters of the example system are listed in Table 3.1. The VCO sensitivity and PFD gain values were taken from PLL components offered by Analog Devices [75, 76].

Initial system design

To define the loop filter time constants, we use the phase transfer functions in (3.46) and (A.46). For the initial design to be stable, we aim at fulfilling the condition in (3.38a). From the previous discussions we know that this occurs if we chose $\zeta_1, \zeta_2 > 1$ and ω_{01}, ω_{02} close to the allowed minimum value. The resulting parameter choice for the example system is detailed in Table 3.2. We calculate the location of the fourth order system poles and zeros numerically in MATLAB. Table 3.3 lists these locations along with the poles and zeros of the approximated phase transfer functions. Foremost, we see that the designed fourth order system is stable since $\Re\{s_{1\mathrm{p}i}\} < 0, \forall i$ with the pole pair closest to the $j\omega$-axis being $s_{1p3/4}$. We expect $\check{G}_{\mathrm{V1}}(s)$ to better model this behavior since $s_{2\mathrm{p}1/2}$ is much closer to $s_{1\mathrm{p}3/4}$ than the poles of $\tilde{G}_{\mathrm{V1}}(s)$. It should be noted that except $s_{1\mathrm{z}1} = s_{3\mathrm{z}1}$, the poles and zeros of the second order models are different from those of the fourth order system. The largest poles of $G_{\mathrm{V1}}(s)$ and $\tilde{G}_{\mathrm{V1}}(s)$ are close. The pole at $s_{1\mathrm{p}2}$ however is not represented in the second order models.

The phase transfer function of the resulting fourth order system along with the approximations and the respective deviations are plotted in Fig. 3.3 over the frequency of input phase changes. We can see that for low frequencies all phase transfer functions take a value of $-17.559\,\mathrm{dB}$ corresponding to $\frac{1}{M}$. That means the phase of the input signal appears at the output divided by the factor M. This is the expected result which we have seen in (3.24). All phase transfer functions in Fig. 3.3 hold this value up to a frequency of about 100 kHz.

Table 3.2: Initial system and filter parameters

Parameter	Symbol	Calculation	Value
Approx. system damping factor	ζ_1		2.0
Maximum approx. system natural freq.	$\omega_{01,\max}$	(3.51)	$181.4 \cdot 10^6 \cdot 2\pi\,\mathrm{rad/s}$
Chosen natural frequency	ω_{01}	$0.94 \cdot \omega_{01,\max}$	$170.6 \cdot 10^6 \cdot 2\pi\,\mathrm{rad/s}$
Combined time constants	τ_{121}	(3.49)	$2.4819 \cdot 10^{-10}\,\mathrm{s}$
Time constant 2	τ_{21}	(3.50)	$2.2396 \cdot 10^{-10}\,\mathrm{s}$
PLL damping factor	ζ_2		2.0
Maximum PLL natural frequency	$\omega_{02,\max}$	(A.51)	$1.759 \cdot 10^6 \cdot 2\pi\,\mathrm{rad/s}$
Chosen PLL natural frequency	ω_{02}	$0.94 \cdot \omega_{02,\max}$	$1.654 \cdot 10^6 \cdot 2\pi\,\mathrm{rad/s}$
Combined time constants	τ_{122}	(A.49)	$2.5599 \cdot 10^{-8}\,\mathrm{s}$
Time constant 2	τ_{22}	(A.50)	$2.3100 \cdot 10^{-8}\,\mathrm{s}$

Table 3.3: Poles and zeros of example system and its models

	Poles	Zeros
$G_{\mathrm{V1}}(s)$	$s_{1\mathrm{p}1} = -4.0292 \cdot 10^9$	$s_{1\mathrm{z}1} = -4.4650 \cdot 10^9$
	$s_{1\mathrm{p}2} = -4.0223 \cdot 10^7$	$s_{1\mathrm{z}2} = -3.8774 \cdot 10^7$
	$s_{1\mathrm{p}3/4} = -6.5900 \cdot 10^5 \pm j2.7648 \cdot 10^7$	$s_{1\mathrm{z}3} = -2.7839 \cdot 10^6$
$\check{G}_{\mathrm{V1}}(s)$	$s_{2\mathrm{p}1/2} = -1.3816 \cdot 10^6 \pm j2.8028 \cdot 10^7$	$s_{2\mathrm{z}1} = -2.7632 \cdot 10^6$
$\tilde{G}_{\mathrm{V1}}(s)$	$s_{3\mathrm{p}1} = -3.9993 \cdot 10^9$	$s_{3\mathrm{z}1} = -4.4650 \cdot 10^9$
	$s_{3\mathrm{p}2} = -2.8713 \cdot 10^8$	

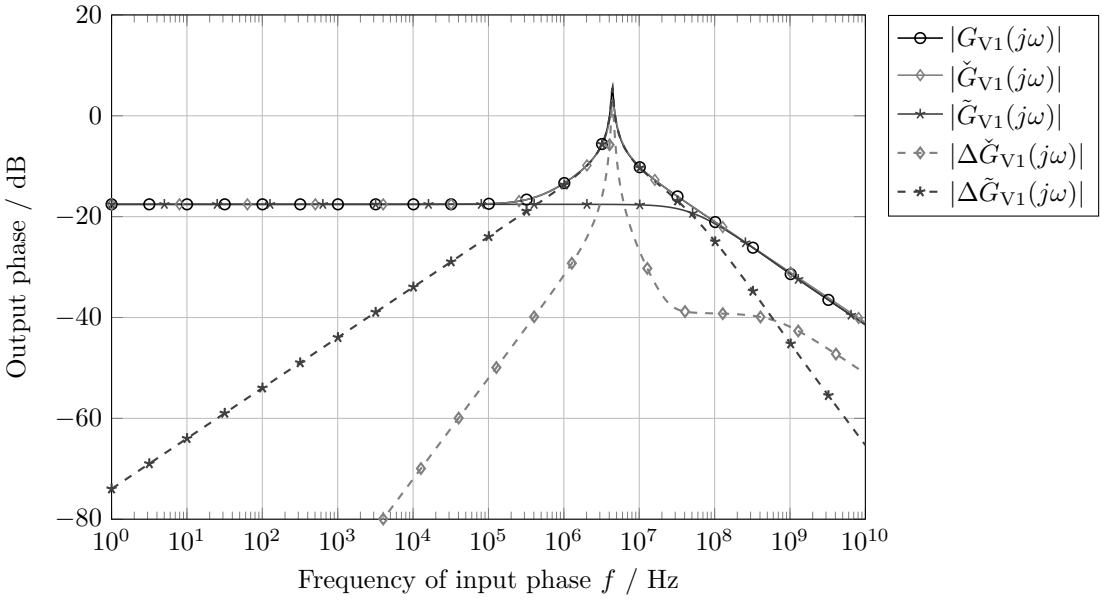

Fig. 3.3: Exact and approximate phase transfer functions of the example system.

Beyond this point, the fourth order system exhibits a pronounced resonance which is well modeled by $\check{G}_{\mathrm{V1}}$. This can also be seen when we regard the error plots $\Delta\check{G}_{\mathrm{V1}}$ and $\Delta\tilde{G}_{\mathrm{V1}}$: The deviation of $\Delta\check{G}_{\mathrm{V1}}$ from the true phase transfer function is below $-20\,\mathrm{dB}$ over most of the plotted frequency range. Above 600 MHz, the error of $\Delta\tilde{G}_{\mathrm{V1}}$ becomes lower. However, at this point the absolute errors are already smaller than $-40\,\mathrm{dB}$. That means, we can use $\check{G}_{\mathrm{V1}}$ to model this specific fourth order system over the plotted frequency range with reasonably small error. This was intended by our initial parameter choice. It is apparent, that it would be desirable to design the system such that it behaves more like the model $\tilde{G}_{\mathrm{V1}}$ which exhibits a much lower deviation from the desired output $\frac{1}{M}$ over a wider frequency range. This however is only achievable by increasing the gain K_2 of the inner loop.

Parameter influence

Since the effect of the filter parameters on the location of the system pole closest to the $j\omega$-axis cannot be described analytically, we will use a numeric approach to visualize the parameter influence. Starting from the stable base system described in Table 3.2, we vary the design parameters in $\mathbf{p}$ separately and observe the resulting movement of the fourth order system poles. Hereby, we have different strategies to variate the damping factors and the natural frequencies: We take $L_{\mathrm{var}} \in \mathbb{N}$ different values $\hat{\zeta}_i$ for each damping factor which are in the range

$$\frac{1}{a}\zeta_i \leq \hat{\zeta}_i \leq a\zeta_i, \quad a > 1. \tag{3.57}$$

For $\zeta_i \leq 1$, the respective natural frequency is altered in L_{var} linear steps such that $0 < \hat{\omega}_{0i} < \omega_{0i,\max}$. In the case of $\zeta_i > 1$, the valid natural frequencies ω_{0i} are given by (3.53) and (A.53), respectively. We then use the parameter ranges

$$0 < \hat{\alpha}_i \leq \frac{1}{2}\left(1 - \sqrt{1 - \frac{1}{\zeta_i^2}}\right) \quad \text{and} \quad \frac{1}{2}\left(1 + \sqrt{1 - \frac{1}{\zeta_i^2}}\right) \leq \hat{\alpha}_i < 1, \tag{3.58}$$

where we discretized the lower range with $\lfloor L_{\mathrm{var}}/2 \rfloor$ and the higher range with $\lceil L_{\mathrm{var}}/2 \rceil$ points. $\lfloor\cdot\rfloor$ and $\lceil\cdot\rceil$ denote the floor and ceil operations, respectively.

The effect of parameter variation on the poles closest to the $j\omega$-axis is shown in Fig. 3.4. The squares indicate the two complex poles $s_{1\mathrm{p}3/4}$ of the initial example system while the diamond shaped markers represent the poles of the system approximation without loop filters, $\check{G}_{\mathrm{V1}}(s)$. The star- and cross-shaped markers indicate the pole locations for the lowest and highest parameter value respectively. The X-shaped markers represent the actual poles at each step of the parameter variation.

We can see that our system becomes unstable if we decrease the damping factors ζ_1, ζ_2. Varying ω_{01} does not influence the location of the regarded poles much. However, our choice of ω_{02} heavily influences stability. Regarding the plots, it becomes clear that we obtain maximum stability if we choose ω_{02} close to the inner limits of the parameter range in (3.58). At these points we have $\tau_{122} = \tau_{22}$ which is equivalent to eliminating the loop filter of the PLL synthesizer. Moreover, for this parameter choice, the depicted poles of our fourth order system get very close to those of the second order model $\check{G}_{\mathrm{V1}}(s)$ as can be expected.

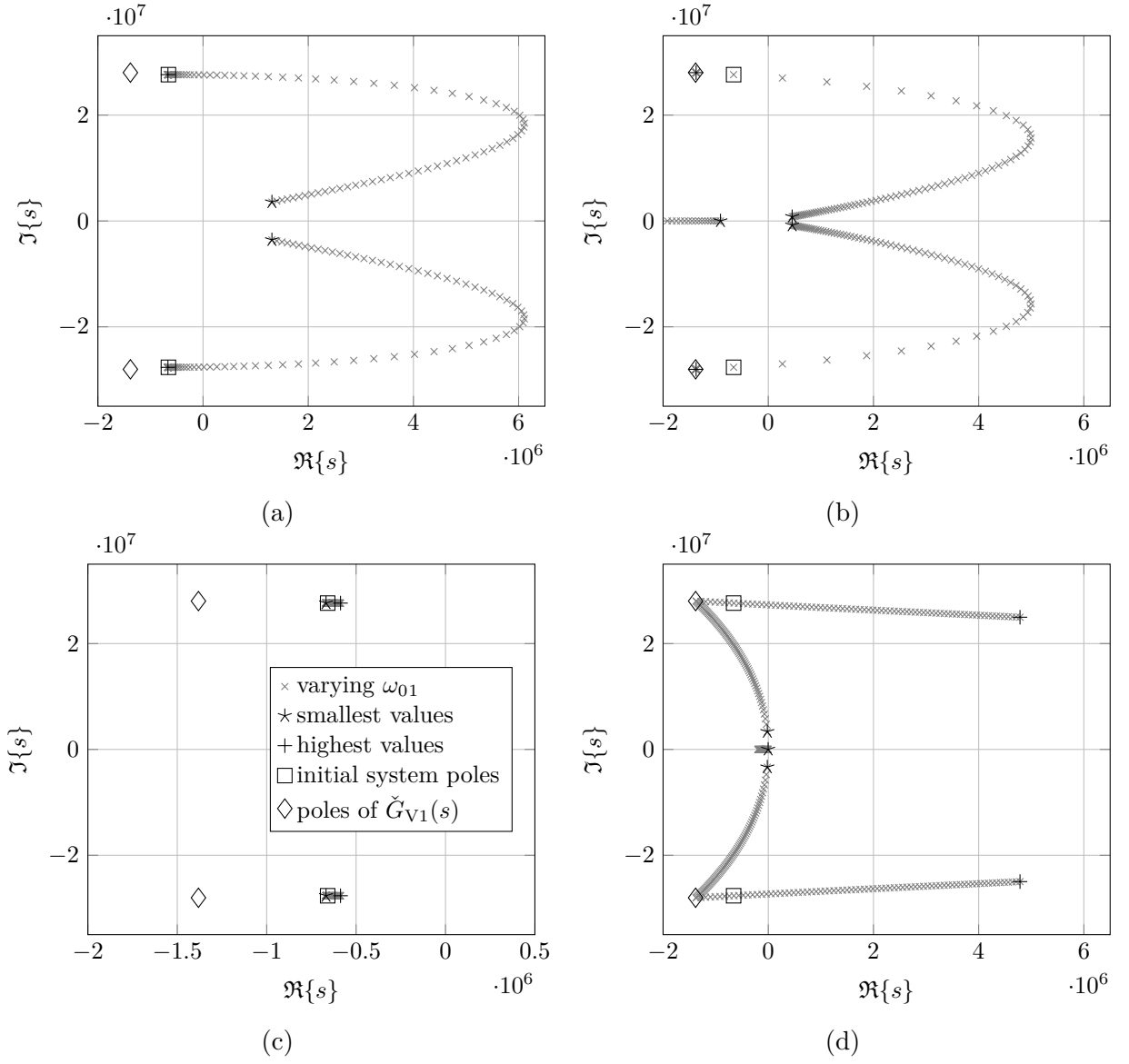

Fig. 3.4: Poles of the fourth order system if parameters are varied around the initial parameter settings in Table 3.2. The plots show variations of (a) ζ_1, (b) ζ_2, (c) ω_{01} and (d) ω_{02}. Each parameter was varied over $L_{\text{var}} = 151$ points and the damping factor range was $a = 200$. The plot legend is shown only in (c) but is analogously valid for the remaining graphs.

Table 3.4: Adjusted system and filter parameters for G'_{V1}

Parameter	Symbol	Calculation	Value
PLL damping factor	ζ_2		2.0
Maximum PLL natural frequency	$\omega_{02,\max}$	(A.51)	$1.7591 \cdot 10^6 \cdot 2\pi\,\mathrm{rad/s}$
Chosen PLL natural frequency	ω_{02}	$0.9330 \cdot \omega_{02,\max}$	$1.6412 \cdot 10^6 \cdot 2\pi\,\mathrm{rad/s}$
Combined time constants	τ_{122}	(A.49)	$2.5984 \cdot 10^{-8}\,\mathrm{s}$
Time constant 2	τ_{22}	(A.50)	$2.5984 \cdot 10^{-8}\,\mathrm{s}$

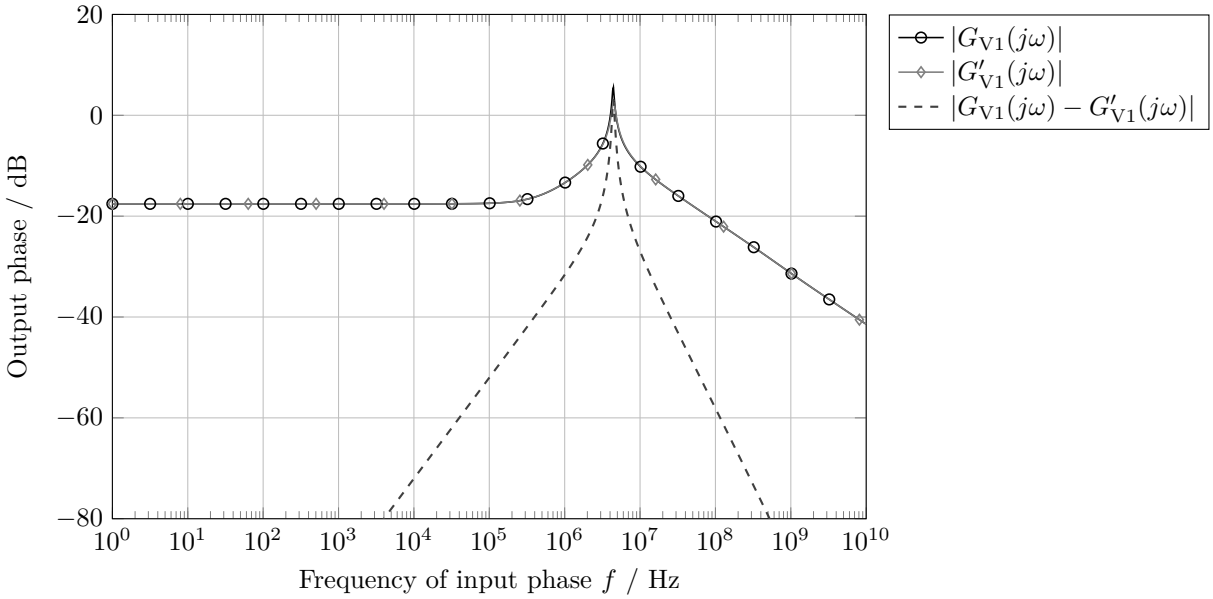

Fig. 3.5: Comparison between fourth order systems with initial and adjusted parameter set. The dashed curve marks the deviation between the two.

Adjusted system design

Referring to our system design goals, we find the best parameter set by varying ω_{02}. To analyze the effect of the optimization, we design a fourth order system with the adjusted parameters for the PLL synthesizer as listed in Table 3.4. We changed the natural frequency ω_{02} to the value giving us the lowest real part for the pole pair closest to the $j\omega$-axis. We did not alter the remaining parameters. The resulting phase transfer function G'_{V1} is plotted in Fig. 3.5 along with the initial fourth order system and the difference between the two. As we can see, this is not significant. When we apply the previously done sequential variation of the system parameters to G'_{V1}, we obtain the locations of the poles closest to the $j\omega$-axis depicted in Fig. 3.6. As we can see, there is no possibility to shift the poles of the adjusted system further left by varying a single design parameter. That means, we have found a locally optimum solution in terms of minimizing the real part of the largest pole.

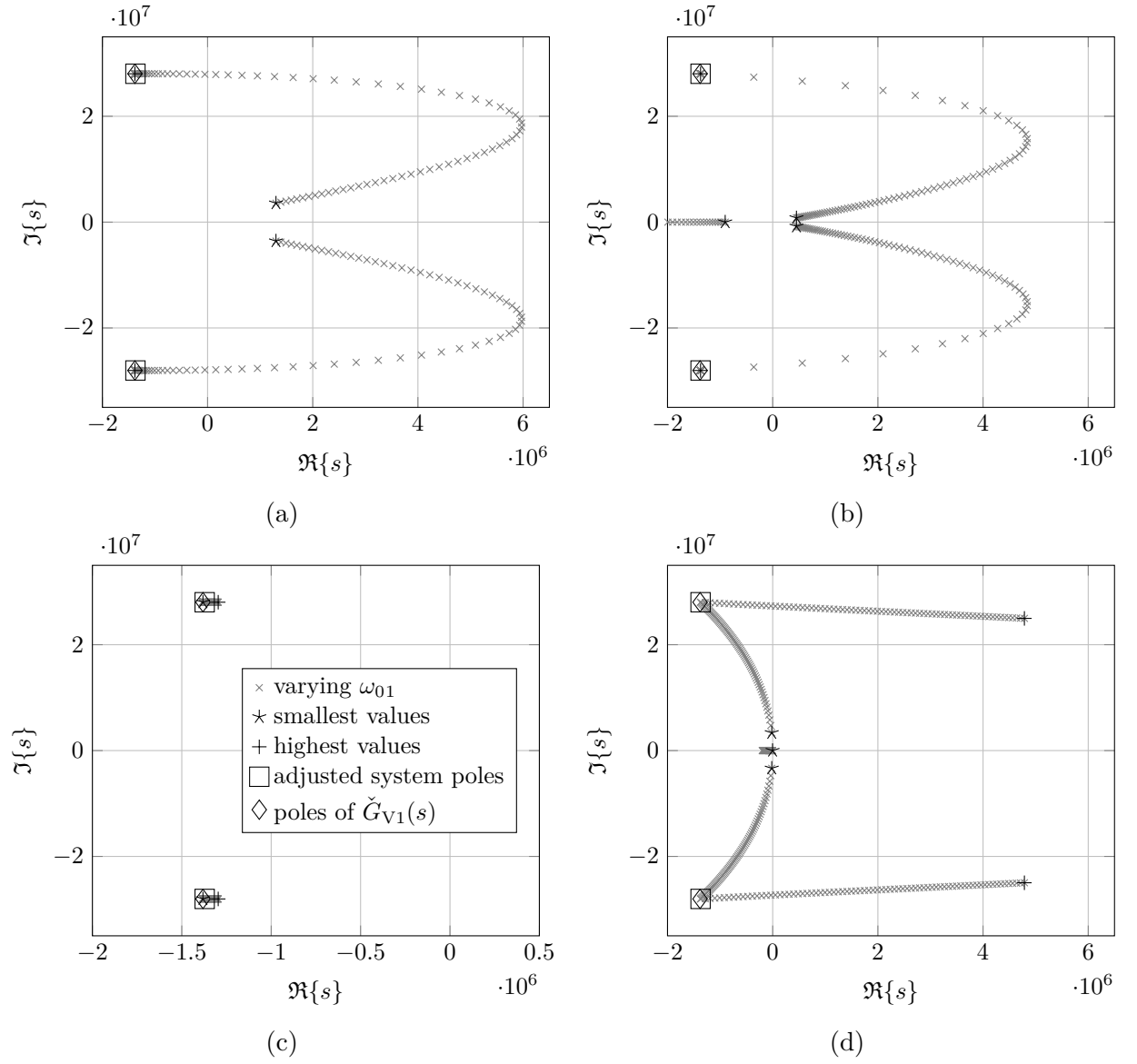

Fig. 3.6: Poles of the fourth order system when parameters are varied around the adjusted parameter settings. The plots show variations of (a) ζ_1, (b) ζ_2, (c) ω_{01} and (d) ω_{02}. Number of points and choice of values for the variation was identical to that in Fig. 3.4.

Table 3.5: Optimized system and filter parameters of G''_{V1}

Symbol	Calculation	Value
ζ_1		6.1230
$\omega_{01,\max}$	(3.51)	$555.47 \cdot 10^6 \cdot 2\pi\,\mathrm{rad/s}$
α_1	(3.58)	0.9933
ω_{01}	$\alpha_1 \cdot \omega_{01,\max}$	$551.75 \cdot 10^6 \cdot 2\pi\,\mathrm{rad/s}$
τ_{121}	(3.49)	$2.3714 \cdot 10^{-11}\,\mathrm{s}$
τ_{21}	(3.50)	$2.3667 \cdot 10^{-11}\,\mathrm{s}$
ζ_2		1.7194
$\omega_{02,\max}$	(A.51)	$1.5123 \cdot 10^6 \cdot 2\pi\,\mathrm{rad/s}$
α_2	(A.53)	0.9067
ω_{02}	$0.9067 \cdot \omega_{02,\max}$	$1.3712 \cdot 10^6 \cdot 2\pi\,\mathrm{rad/s}$
τ_{122}	(A.49)	$3.7223 \cdot 10^{-8}\,\mathrm{s}$
τ_{22}	(A.50)	$3.7223 \cdot 10^{-8}\,\mathrm{s}$

Optimization by parametric search

As we have discussed in section 3.3.2 and the subsequent sections, it is not possible to directly find an optimum solution for the choice of the parameters of the fourth order system. In order to find the best solution for the specific system discussed in this chapter, we apply a parametric search over all plausible values of the parameter space $\mathbf{p}$. Since this is a brute force method, the necessary computation time increases exponentially with the number of parameters and the chosen resolution of the parameter grid. For our analysis we have chosen to use a grid of $L_{\mathrm{var}} = 101$ points for each parameter resulting in $101^4 = 104\,060\,401$ runs. This computation takes around 9 h on a year 2013 laptop computer. We use the following parameter variation strategy:

1) The ζ_i are varied in L_{var} logarithmic steps between 0.01 and 8,

2) For ω_{0i}, we vary the factors α_i from (3.53) and (A.53). The chosen range thereby depends on the actual ζ_i:
   a) For $\zeta_i \leq 1$, we use linear steps in the range $\alpha \in \left[\frac{1}{L_{\mathrm{var}}+1}, \ldots, \frac{L_{\mathrm{var}}}{L_{\mathrm{var}}+1}\right]$,
   b) For $\zeta_i > 1$, we use the range specified in (3.58) with linear steps.

According to our design goals stated in section 3.3.4, the primary objective is to obtain a stable system. Therefore, we ignore any parameter set which yields an unstable fourth order system. For the second design goal which is to minimize the real part of the largest system pole, we numerically calculate the system poles for each variation. Afterwards, we identify the one closest to the $j\omega$-axis. Thus, we arrive at a unique solution whose transfer function we denote by G''_{V1}. It is detailed in Table 3.5.

The location of poles and zeros for the adjusted and optimized system parameter sets are listed in Table 3.6 for comparison. The resulting phase transfer functions and their difference to the second order model $\breve{G}_{\mathrm{V1}}(j\omega)$ are plotted in Fig. 3.7. We can see that optimizing the location of the largest pole leads to a negligible difference between the fourth order system

Table 3.6: Poles and zeros of the adjusted and optimized systems

System	Poles	Zeros
$G'_{\mathrm{V1}}(s)$	$s_{4\mathrm{p1}} = -4.0292 \cdot 10^9$	$s_{4\mathrm{z1}} = -4.4650 \cdot 10^9$
	$s_{4\mathrm{p2}} = -3.8486 \cdot 10^7$	$s_{4\mathrm{z2}} = -3.8486 \cdot 10^7$
	$s_{4\mathrm{p3/4}} = -1.3720 \cdot 10^6 \pm j2.8029 \cdot 10^7$	$s_{4\mathrm{z3}} = -2.7632 \cdot 10^6$
$G''_{\mathrm{V1}}(s)$	$s_{5\mathrm{p1}} = -4.2169 \cdot 10^{10}$	$s_{5\mathrm{z1}} = -4.2252 \cdot 10^{10}$
	$s_{5\mathrm{p2}} = -2.6865 \cdot 10^7$	$s_{5\mathrm{z2}} = -2.6865 \cdot 10^7$
	$s_{5\mathrm{p3/4}} = -1.3816 \cdot 10^6 \pm j2.8028 \cdot 10^7$	$s_{5\mathrm{z3}} = -2.7632 \cdot 10^6$

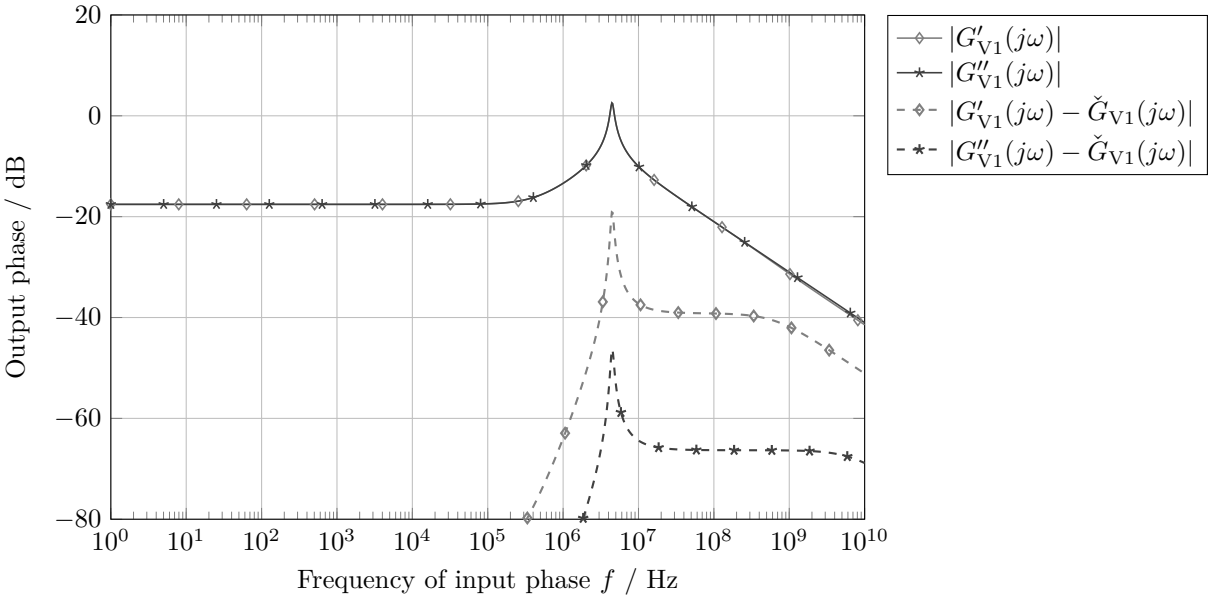

Fig. 3.7: Phase transfer functions for the optimized systems.

G''_{V1} and the second order model. This is due to the largest pole $s_{5\mathrm{p}3/4}$ being identical to the poles of $\check{G}_{\mathrm{V1}}$. Since the real part of the next pole $s_{5\mathrm{p}2}$ is more than one order of magnitude further away from the $j\omega$-axis, its influence on the transfer function is negligible. In section 3.4 we will investigate the dynamic behavior of the adjusted initial system and of the optimized system in the time domain.

3.3.6 Summary

In section 3.3, we have laid out strategies to design and optimize a receiver channel of the proposed retro-directive system. For this, we have introduced an alternative parameterization: The loop filter time constants τ_{1i}, τ_{2i} have to be positive but are otherwise unbounded. The resulting parameter space is thus not well suited for discretization. Therefore we have regarded the inner and outer PLLs as two separate second order loops which can be characterized by their natural frequencies ω_{0i} and damping factors ζ_i, $i \in \{1, 2\}$. As can be seen in (3.51), (3.53), (A.51) and (A.52), ω_{0i} are bounded by the chosen ζ_i. Even though the damping factor $\zeta_i > 0$ itself is unbounded, values $\zeta_i \gg 1$ strongly restrict the valid range of ω_{0i} as stated in (3.58) and (A.53). Thus, the parameter space $\mathbf{p}$ given by (3.54) can be discretized better than the original one defined by the filter time constants, i.e. $[\tau_{11}, \tau_{21}, \tau_{12}, \tau_{22}]$.

We have used the alternative system parameters to optimize the location of the pole closest to the $j\omega$-axis. We have seen that we can find local optima in the solution space by sequentially varying individual parameters. However, to find a global optimum, we have to relate to a full parametric search over $\mathbf{p}$. We have also found that the poles of the second order approximation without loop filters, $\check{G}_{\mathrm{V1}}(s)$, equal those of the found optimum. Since the dynamic behavior is dominated by the poles with the largest real part, this approximation is a suitable model of the fourth order system. This also means that the system behavior is mainly defined by the loop gains K_1, K_2 and the division factor M. The loop filters have only a minor influence which can also be seen in the similarity of the phase transfer functions depicted in Fig. 3.7.

3.4 Verification by time domain simulation

In the previous section, we have designed our fourth order system with the help of phase transfer functions. This approach is useful to ensure stability and to predict the dynamic behavior. Our next step is to prove that the suggested system can actually be used for phase detection, IF signal phase alignment and phase modulated RF signals. For this, we create a Simulink model of the receiver to simulate its behavior in the time domain. Thereby, we shall use the system parameters derived in the previous section. These simulations shall also serve as a proof of concept for the previously introduced system component models.

The simulation setup used for the following investigations is shown in Fig. 3.8. It consists of two RF signal generators which are modulated by the same BPSK signal but have a phase shift δ to model the RF incident direction. Details about the signal generator model can be found in appendix B.1.1 and Fig. B.4. The generated RF signals are subject to additive white Gaussian noise (AWGN) realizing a given SNR. They are fed to two identical receivers with the architecture shown in Fig. 3.2. Details about the Simulink receiver model are given in appendix B.1. The IF outputs of the channels are summed and appear at the IF_sum

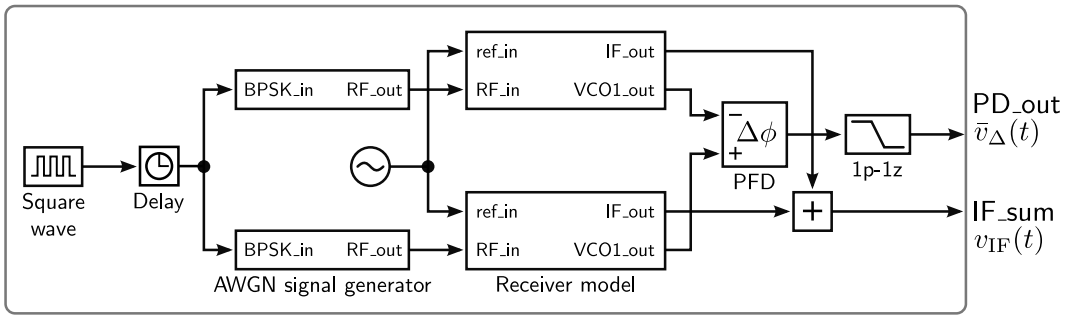

Fig. 3.8: Simulink simulation setup for the dual channel receiver.

port of the model. We denote the respective signal by $v_{\mathrm{IF}}(t)$. The VCO V_1 output signals are compared by a PFD and are lowpass filtered afterwards. The resulting signal is the time averaged phase detection output $\bar{v}_\Delta(t)$ from (3.22) which appears at the PD_out port.

For the following simulations, we use both the adjusted system parameterization $G'_{\mathrm{V1}}(s)$ and the optimized system design $G''_{\mathrm{V1}}(s)$ from Tables 3.4 and 3.5. To assess the performance of the phase detection, we generate input signals which have a constant phase difference δ. The BPSK modulation is used later in section 3.4.3 for the analysis of the attainable phase modulation rate.

3.4.1 Phase detection performance

We perform several simulation runs with various phase differences δ and SNR values denoted by $\mathrm{SNR}_{\mathrm{RF}}$. The phase differences are set to $\delta \in [0, \pi/12, \ldots, 23/12\pi]$. The simulation time for each run is 20 µs. We are mainly interested in the final value of $\bar{v}_\Delta(t)$ to assess the phase detection ability. Nevertheless, also the initial behavior of $\bar{v}_\Delta(t)$ has to be regarded to see when the output becomes steady and the final values have been reached.

Fig. 3.9a shows the initial phase detection output voltage $\bar{v}_\Delta(t)$ for different RF phase shifts δ. The shown results are from the adjusted system design $G'_{\mathrm{V1}}(s)$. We can see that after an initial adaption, the voltage approaches a steady value which is proportional to δ. The curves in this plot are the results of individual simulations. During each simulation run, δ was held constant. The expected final values are given by (3.24) and are reached after approximately 5 µs.

For the evaluation of the phase detection error, we calculate mean and standard deviation of the phase detection output signal as

$$\bar{\bar{v}}_\Delta = \frac{1}{T_2 - T_1} \int_{T_1}^{T_2} \bar{v}_\Delta(t) dt, \tag{3.59}$$

$$\sigma_{\mathrm{PD}} = \sqrt{\frac{1}{T_2 - T_1} \int_{T_1}^{T_2} \left(\bar{\bar{v}}_\Delta(t) - \bar{v}_\Delta \right)^2 dt}, \tag{3.60}$$

with $T_1 = 10$ µs and $T_2 = 20$ µs. We obtain the phase detection result $\Delta\delta$ from the mean phase detection output using (3.25). Fig. 3.9b shows mean and standard deviation bars of

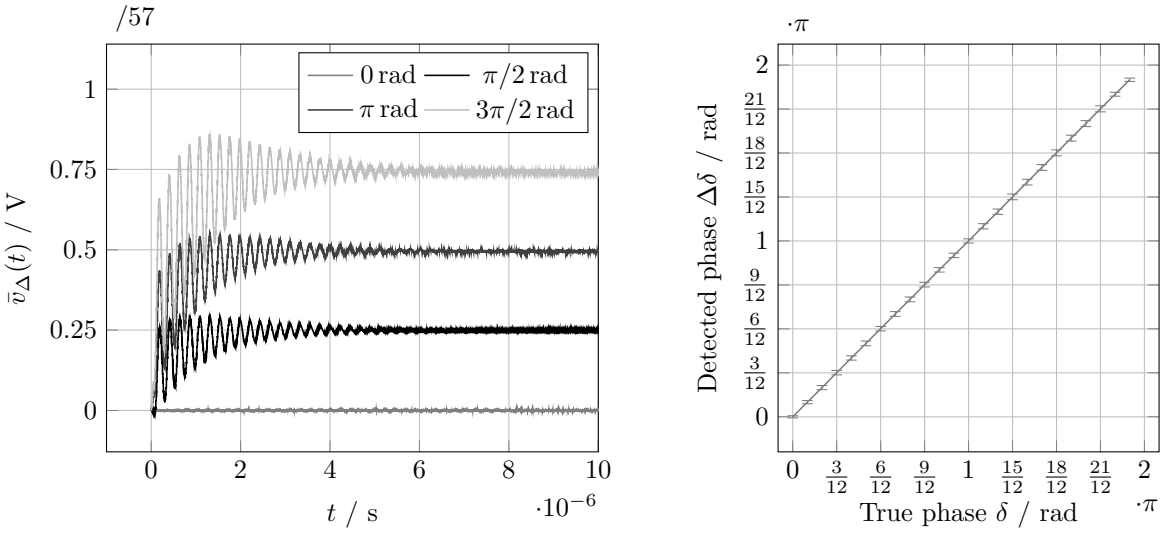

Fig. 3.9: (a) Initial phase detection output for various phase differences δ and 40 dB SNR. (b) Mean value and standard deviation bars of the phase detection output for 40 dB SNR over the final 10 µs of the simulation for all regarded phase differences.

the phase detection output voltage over the last 10 µs of each simulation at 40 dB SNR. We can see that the phase detection results are accurate and the standard deviation is low.

To assess the overall phase detection performance and its susceptibility to noise, we repeat the above simulation for SNR values from 40 to 0 dB. To obtain a single figure of merit for each RF SNR value, we use the following metric: For every input phase difference δ, we calculate the mean (3.59) and standard deviation (3.60) of $\bar{v}_\Delta(t)$ for the final 10 µs of the simulation. Using the true phase difference, we obtain the mean phase detection error by

$$e_\delta = \delta - \Delta\delta(\bar{\bar{v}}_\Delta). \tag{3.61}$$

Using the same value range of δ as before, we obtain 24 mean errors e_δ. We then take the ensemble mean over all simulated phase differences of e_δ and σ_{PD}. The figures of merit thus are the mean values of all e_δ and all σ_{PD}, denoted by $\bar{e}_\delta$ and $\bar{\sigma}_{\mathrm{PD}}$, respectively. These are shown in Fig. 3.10.

Although $\bar{e}_\delta$ in Fig. 3.10a does not decrease monotonically for higher SNR values, a corresponding trend is observable. Since we are using AWGN on the RF signals, we may expect that the mean error remains stable even for low SNR values as the noise influence is averaged out. However, as detailed in appendix B.1, we use Schmitt triggers at the input of the PFD d_1 in order to avoid multiple subsequent signal sign changes due to noise fluctuations around 0 V. If the noise amplitude becomes large enough, it still can toggle the Schmitt trigger multiple times. In this case, the phase detection result becomes erroneous. The increase in the mean error curve for low SNRs is caused by this phenomenon. For these SNR values, the standard deviation of the noise in (B.2) is in the order of the trigger thresholds of ±0.2 V. That means, we need to ensure a certain SNR at the RF input for the system to be able to perform correct phase detection. Alternatively, the Schmitt trigger threshold could be increased. Down to 5 dB SNR we observe a mean phase detection error $\bar{e}_\delta$ below 0.01 rad,

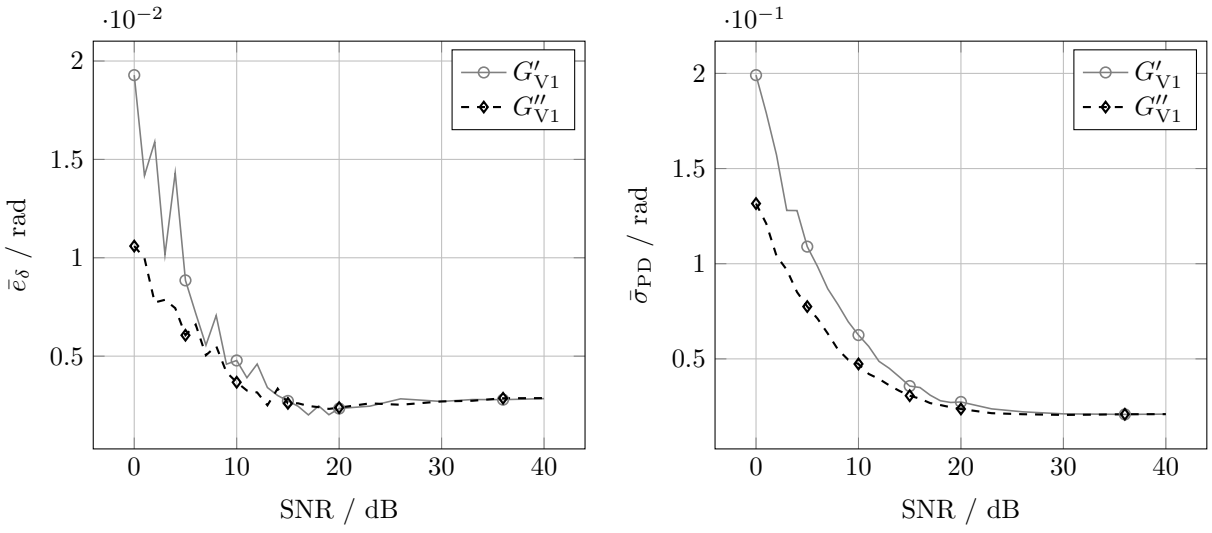

Fig. 3.10: Mean of the mean errors and standard deviations of the phase detection output for different SNRs.

corresponding to 0.57° for G'_{V1}. For the optimized system, we obtain such low mean errors down to 1 dB SNR. This mean error level is sufficiently low for the desired phase conjugation and DoA estimation.

Regarding the mean of the phase error standard deviations over SNR in Fig. 3.10b, we see that for lower SNRs the standard deviation of our phase detection result rises. This can be expected since it is a measure of the uncertainty of the phase detection result which is strongly influenced by noise. Down to 6 dB SNR, the standard deviation is below 0.1 rad or 5.73° for the adjusted system design. The optimized system can keep this low standard deviation down to 3 dB SNR. Given the involved division factor of $M = 57$ in the detected phases, this is a promising result. It shows that phase detection is still possible with good accuracy even for relatively high noise levels. The results also show that the optimization of the system parameters has a positive effect on the performance.

3.4.2 Intermediate frequency signal time constant

One distinct advantage of the proposed receiver over classic RDAs is its ability to make use of the antenna array gain for the received signal. This implies that all channel IF output signals are in phase. Thus, their sum is a down-mixed version of the RF signal whose amplitude is ideally N-times that of a single channel IF output, i.e.

$$v_{\mathrm{IF}}(t) = \sum_{n=1}^{N} v_{\mathrm{IF},n} \approx N v_{\mathrm{IF},1}(t). \tag{3.62}$$

We want to know, if the receiver can attain this IF signal amplitude. Moreover, we are interested in the time it takes to reach it, i.e. in the time constant of the IF response which we denote by τ_{IF}. Since the IF signal is oscillating, we need to obtain the signal envelope $\hat{v}_{\mathrm{IF}}(t) \geq 0$ to measure its time constant. Let us assume the IF signal to be sinusoidal as

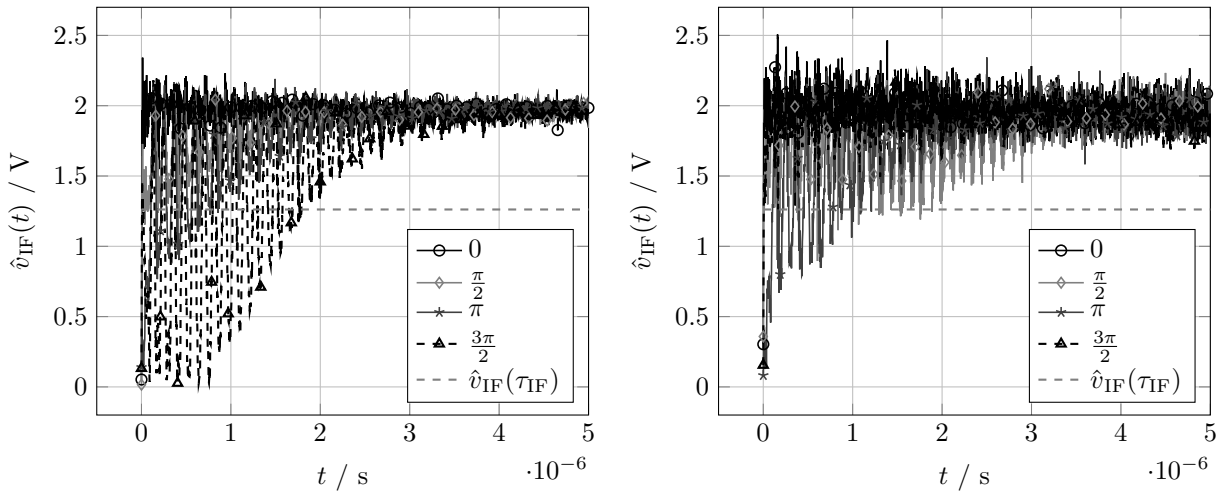

(a) (b)

Fig. 3.11: Initial rise of the IF signal envelope for different phase differences δ using (a) 20 dB and (b) 6 dB SNR.

defined in (3.4) but with variable amplitude.

$$v_{\mathrm{IF}}(t) = \hat{v}_{\mathrm{IF}}(t) \cos\left(\omega_{\mathrm{IF}} t + \varphi_{\mathrm{IF}}\right). \tag{3.63}$$

This assumption is justified since the individual IF signals $v_{\mathrm{IF},n}$ are sinusoids of equal frequencies in the steady state. Using the Hilbert transform $H(\cdot)$ and the identity $H(\cos(x)) = \sin(x)$ [77, p.453], we can obtain the envelope of such a signal as

$$\hat{v}_{\mathrm{IF}}(t) = \left| v_{\mathrm{IF}}(t) + jH(v_{\mathrm{IF}}(t)) \right|. \tag{3.64}$$

We then define the time constant of the IF signal envelope by

$$\tau_{\mathrm{IF}} = \max_t \left[t \;\middle|\; \hat{v}_{\mathrm{IF}}(t) \leq \left(1 - e^{-1}\right) M \hat{v}_{\mathrm{IF},1} \right], \tag{3.65}$$

where e is Euler's number. In other words, for all $t > \tau_{\mathrm{IF}}$ the signal envelope is larger than 62.3 % of its maximum value. This corresponds to the definition of time constants e.g. for RC circuits. Using (3.65), we obtain a measure for the dynamic behavior of the system. However, the obtained value τ_{IF} will be dependent on the actual phase difference δ as this influences the adaption process of the PLLs in the receiver. This can be seen in Fig. 3.11 where the initial development of the IF sum signal envelope is shown for different δ and SNRs of 20 and 6 dB. We can see strong variations in the beginning but eventually the signal envelopes approach the expected final value from (3.62). In our case, the nominal IF signal amplitude of a single channel is 1.0 V and $N = 2$. The plots in Fig. 3.11 also show the threshold associated with τ_{IF}. As expected, the measured time constants vary for different δ values.

The duration of the adaption process cannot be predicted. From both Fig. 3.11a and Fig. 3.11b, we see that the largest τ_{IF} is not caused by the largest phase difference which would be $\delta = \pi$. In order to obtain a more general figure of merit for the adaption speed,

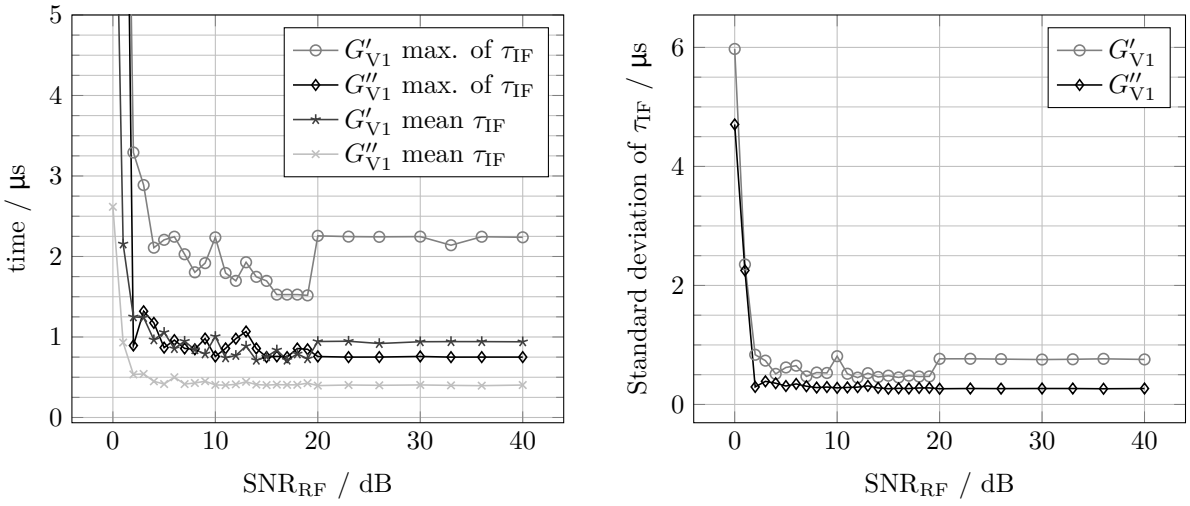

(a) (b)

Fig. 3.12: (a) Mean and maximum values, (b) standard deviation of the IF sum signal envelope time constant τ_{IF} for simulation runs with different SNR_{RF}.

we simulate the two channel case again with $\delta \in [0, \pi/12, \ldots, 23/12\pi]$ and SNRs from 0 to 40 dB. As prior, we do not use the BPSK modulation shown in Fig. 3.8 during these simulations. The result is shown in Fig. 3.12 where we plot the maximum, mean, and standard deviation of the occurring τ_{IF} over SNR for both the adjusted system design G'_{V1} and the optimized parameter set G''_{V1}. For low SNRs, the maximum τ_{IF} goes towards the simulation time of 20 µs. This means that the signal envelope does not stay above the threshold value. Such behavior can be expected and is caused by the high noise level which leads to large fluctuations in the envelope signal. This is confirmed by the significant rise in the standard deviation of τ_{IF} for the lowest SNR values. For higher SNRs, we see that the curves are relatively stable, given the limited amount of data points. We also observe that the measured time constants of the optimized system are smaller than those of G'_{V1} which again shows the influence of the system pole locations.

3.4.3 Phase modulation rate

Finally, we want to show that the IF sum signal contains the phase modulation of the RF signal. As shown in Fig. 3.8, we use a square wave generator to BPSK modulate the RF signal. We thereby alter the signal phase by π with a frequency of f_{BPSK}. This can be thought of as a worst case scenario because phase changes occur as often as possible. Due to the square wave modulation, the phase changes also occur abruptly.

To demodulate the IF signal, we multiply it with the reference signal and filter the result, i.e.

$$v_{demod}(t) = (v_{IF}(t) \cdot v_{ref}(t)) * h_{LP}(t), \tag{3.66}$$

where $*$ denotes the convolution and $h_{LP}(t)$ is the impulse response of a lowpass filter suitable to eliminate the frequency $2\omega_{ref}$. Since the IF and reference signals are phase aligned, (3.66) will be close to $\frac{1}{2}(\hat{v}_{IF} \cdot \hat{v}_{ref})$ in the steady state. Due to an occurring phase shift by π, (3.66)

will momentarily drop to zero before rising again towards the steady state level. Thus, a RF signal phase change can be detected in the demodulated signal.

For this analysis we regard the optimized system only. The results for the adjusted system are very similar and are not given since they do not offer additional insights. For the simulations, we use the parameters from Table B.1 with the following exceptions:

- Longer simulation time of $t_{\mathrm{sim}} = 100\,\mu\mathrm{s}$ in order to have a significant amount of phase changes,
- Different BPSK rates, $f_{\mathrm{BPSK}} \in \{100, 400, 700, 1000\,\mathrm{kHz}\}$.

The BPSK modulation starts after 10 µs to allow the receiver to initially reach its steady state.

The resulting demodulated IF signals can be seen in Fig. 3.13. We see that up to 700 kHz BPSK modulation rate, the system is capable of demodulating the IF sum signal: Each flank of the BPSK signal is marked by a considerable drop in the amplitude of $v_{\mathrm{demod}}(t)$ which is recovered shortly afterwards. We shall consider the detection of a phase jump successful, if

- $v_{\mathrm{demod}}(t)$ drops below 36.79 % of its expected maximum amplitude after the jump and
- recovers to more than 63.21 % of its expected maximum amplitude before the next phase jump.

In Figs. 3.13a and 3.13b, the signal returns to the steady state amplitude after each phase change. The occurring phase changes can thus be detected without difficulties. At 700 kHz, the signal amplitude can not completely recover before the next phase change arrives as can be seen in Fig. 3.13c. Nevertheless, demodulation according to the definition above is still possible. If we increase the modulation rate further, we will arrive at a point, where the phase changes are too fast. Fig. 3.13d shows a decrease in the maximum amplitude of $v_{\mathrm{demod}}(t)$ compared to the other cases. The detection of phase jumps is no longer possible.

Since we perform a complete time domain system simulation, it is not feasible to simulate several thousand BPSK symbols over different RF SNRs. The necessary computation time would be several weeks. However, such a simulation would be necessary to create enough data for a BER over SNR plot. Moreover, we would need a more sophisticated phase modulator with a random symbol generator and pulse shaping filter along with a suitable demodulator. While the shown results do not have the same argumentative impact as a BER curve, they still demonstrate the principal ability of the system to demodulate BPSK signals up to a certain modulation rate.

3.4.4 Receiver proof-of-concept

In section 3.4, we have proven the properties of the receiver proposed in section 3.2 by time domain simulations in MATLAB/Simulink. We have demonstrated the phase detection ability and used the ensemble mean of both the mean phase error and its standard deviation over time as figures of merit. We have shown that the receiver is able to perform phase detection on RF signals of SNRs down to 6 dB with a mean error smaller than 0.01 rad and standard deviation of less than 0.1 rad. Thus, our receiver is able to meet Req. 4 as it

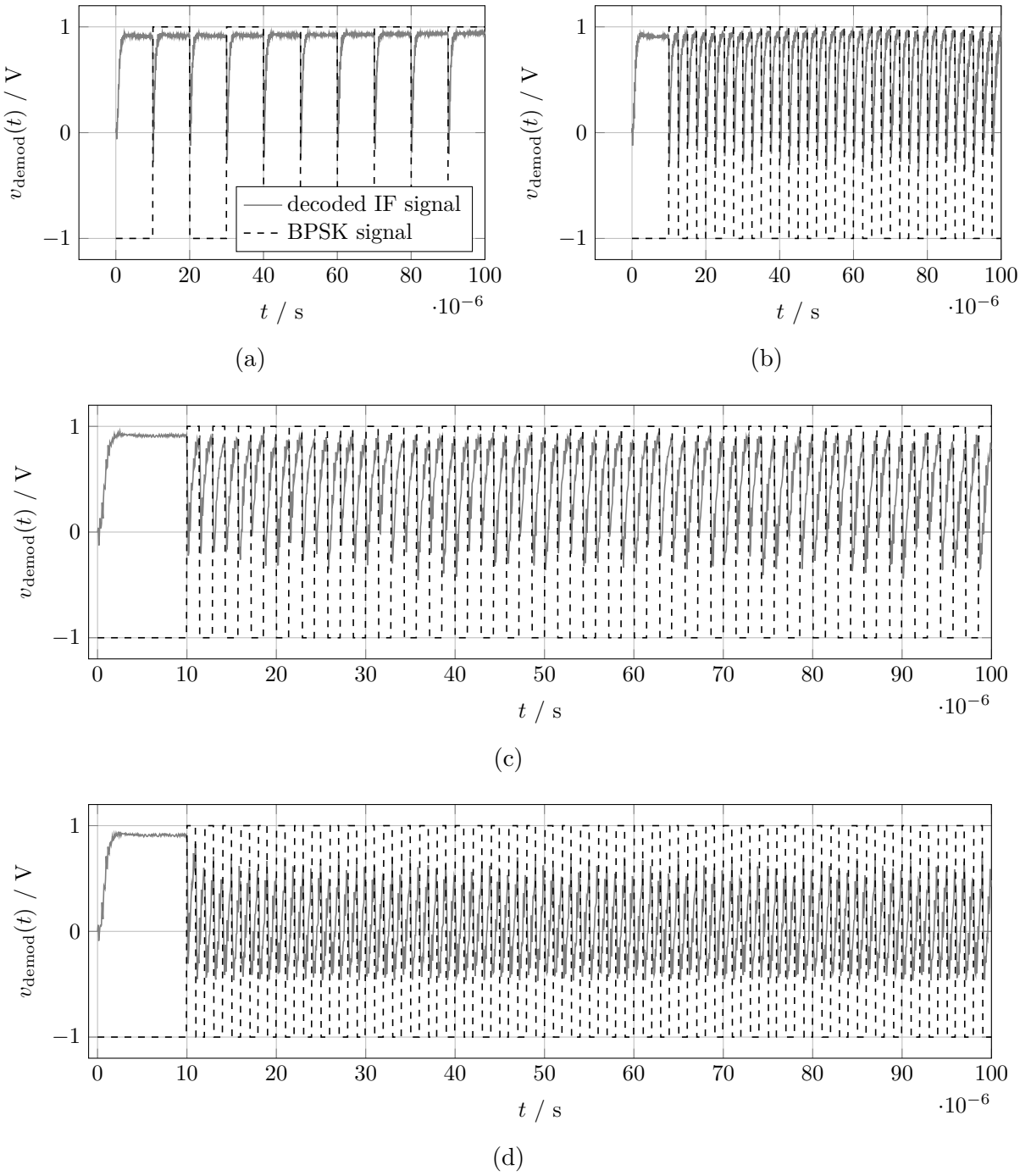

Fig. 3.13: Demodulated IF sum signals for BPSK modulation rates of (a) 100 kHz, (b) 400 kHz, (c) 700 kHz and (d) 1000 kHz.

extracts the Rx phase differences between neighboring antenna elements which can then be used to direct a Tx beam toward the incident direction.

Moreover, we have shown that the receiver makes use of the Rx antenna array gain by constructive superposition of the IF signals, thereby meeting Req. 3. For this, we have used the time constant τ_{IF} of the IF sum signal envelope as figure of merit. The results show that this time constant varies with the RF signal phase difference. By taking the mean and maximum values of τ_{IF} over multiple SNRs, we have shown that the adaption speed does not vary significantly down to 3 dB SNR. In this SNR range, τ_{IF} does not exceed 2.5 µs for our example system. As could be expected, we have seen an improvement in τ_{IF} for the optimized system $G''_{\mathrm{V1}}(s)$ where we minimized the real part of the largest pole of the phase transfer function.

Finally, we have demonstrated how BPSK-like phase shifts of the RF signal can be identified in the IF sum signal. We have seen that demodulation becomes more difficult for higher modulation rates. The time domain simulation employed in our analysis is not suitable to obtain BER over SNR curves, as the necessary simulation time for enough BPSK symbols would be too long. Nevertheless, we have shown that the receiver can fulfill Req. 2, i.e. decode the information modulated on the received RF signal.

3.5 Multiple user capability

In this section we shall investigate if the proposed RDA system is suitable for simultaneous operation with multiple users. This is of interest because simpler system architectures like the van Atta array or the phase-conjugating mixer have this property [36, 37, 57], [59, c.5].

3.5.1 Signal model for multiple users

Starting from our received signal model for a single source in (3.1), let us assume that K planar wave fronts from different directions θ_k impinge on our ULA. The voltage at the n-th antenna port due to the k-th user signal will then be

$$v_{k,n}(t) = \hat{v}_k(\theta_k)\cos(\underbrace{\omega_{\mathrm{RF}}t + \delta_n(\theta_k) + \varphi_k(t)}_{:=\Psi_{\mathrm{RF}\,k,n}(t)}), \tag{3.67}$$

with $k \in 1, \ldots, K$. Since superposition is valid for the incident EM waves and the antenna port voltages are linear dependent on them, we assume that the port voltages of multiple users linearly superimpose. Thus the resulting antenna port voltage is given by

$$v_n(t) = \sum_{k=1}^{K} v_{k,n}(t). \tag{3.68}$$

Since all of the summed signals are of equal frequency, this can again be written as a harmonic wave of the form

$$v_n(t) = V_n(t) \cdot \cos(\underbrace{\omega_{\mathrm{RF}}t + \Delta_n(t)}_{:=\Psi_{\mathrm{RF},n}(t)}), \tag{3.69}$$

with

$$V_n^2(t,\theta_k) = \sum_{k=1}^{K}\sum_{l=1}^{K} \hat{v}_k(\theta_k)\hat{v}_l(\theta_l) \cdot \cos\left(\delta_n(\theta_k) - \delta_n(\theta_l) + \varphi_k(t) - \varphi_l(t)\right), \tag{3.70}$$

$$\Delta_n(t,\theta_k) = \operatorname{atan2}\left(\sum_{k=1}^{K} \hat{v}_k(\theta_k)\sin\left(\delta_n(\theta_k) + \varphi_k(t)\right), \sum_{k=1}^{K} \hat{v}_k(\theta_k)\cos\left(\delta_n(\theta_k) + \varphi_k(t)\right)\right), \tag{3.71}$$

where $\operatorname{atan2}(y,x)$ denotes the arctangent with two arguments as defined in appendix A.1.3. This alters the numerator of the VCO V_1 output in (3.20) as follows

$$\begin{aligned} N_{\mathrm{V1},n}(s) =& \frac{1}{s^2}\left(\frac{K_1K_2h_1h_2}{M}(\omega_{\mathrm{RF}} - \omega_{\mathrm{ref}})\right) + \frac{1}{s}\left(\frac{K_2h_2}{M}\omega_{\mathrm{q1}} + K_1h_1(\omega_{\mathrm{RF}} - \omega_{\mathrm{ref}} - \omega_{\mathrm{q2}})\right. \\ &\left. + \frac{K_1K_2h_1h_2}{M}\Delta_n(s,\theta_k)\right) + \omega_{\mathrm{q1}} + K_1h_1\Delta_n(s,\theta_k). \end{aligned} \tag{3.72}$$

Inserting this into (3.22), we arrive at the phase detection output of our proposed receiver

$$\bar{v}_{\Delta,n}(s) = K_1h_1\frac{\left(s + \frac{K_2h_2}{M}\right)\left(\Delta_n(s,\theta_k) - \Delta_1(s,\theta_k)\right)}{s^2 + s\frac{K_2}{M}h_2 + K_1K_2h_1h_2}, \tag{3.73}$$

which in contrast to (3.23) does not yield the phase differences $\delta_n(\theta_k)$ directly. Additionally, the phase terms $\varphi_k(t)$ do not cancel out.

To obtain a phase detection result, we have to assume that the $\varphi_k(t) = \varphi_k$, i.e. vary slowly over time such that they can be assumed constant until the phase detection output has converged. This eliminates the time dependency of (3.71) and allows us to rewrite the last expression as

$$\bar{v}_{\Delta,n}(s) = \frac{K_1h_1}{s}\frac{\left(s + \frac{K_2h_2}{M}\right)\left(\Delta_n(\theta_k) - \Delta_1(\theta_k)\right)}{s^2 + s\frac{K_2}{M}h_2 + K_1K_2h_1h_2}, \tag{3.74}$$

which lets us apply the final value theorem to obtain

$$\lim_{t\to\infty}\bar{v}_{\Delta,n}(t) = \lim_{s\to 0}s\bar{v}_{\Delta,n}(s) = \frac{\Delta_n(\theta_k) - \Delta_1(\theta_k)}{M}. \tag{3.75}$$

We have to find out under which conditions it is possible to extract the DoA information for the K users from this term. From (3.71), we can see that $\Delta_n(\theta_k)$ contains $3K$ unknowns, namely φ_k, θ_k, and $\hat{v}_k(\theta_k)$, with $k \in 1,\ldots,K$.

3.5.2 Two-user case with isotropic antennas

To narrow down the problem, we make the following additional restrictions:

1) We know that the number of signal sources is $K = 2$,
2) We use an array of isotropic antennas and
3) We assume that both user signals arrive with identical signal strength at our array, i.e. $\hat{v}_k(\theta_k) = \hat{v}$.

Under these strong assumptions, we can rewrite (3.71) as

$$\Delta_n(\theta_1,\theta_2) = \operatorname{atan2}\left(\sin\left(\Sigma_n(\theta_1,\theta_2)\right)\cos\left(\Pi_n(\theta_1,\theta_2)\right), \cos\left(\Sigma_n(\theta_1,\theta_2)\right)\cos\left(\Pi_n(\theta_1,\theta_2)\right)\right), \tag{3.76}$$

where addition theorems [70, c. 2.5] and the following identities have been used

$$\Sigma_n(\theta_1,\theta_2) = \frac{1}{2}\left(\delta_n(\theta_1)+\delta_n(\theta_2)+\varphi_1+\varphi_2\right) = \frac{\pi z_n}{\lambda}\underbrace{\left(\cos\theta_1+\cos\theta_2\right)}_{:=\gamma(\theta_1,\theta_2)}+\frac{\varphi_1+\varphi_2}{2}, \tag{3.77}$$

$$\Pi_n(\theta_1,\theta_2) = \frac{1}{2}\left(\delta_n(\theta_1)-\delta_n(\theta_2)+\varphi_1-\varphi_2\right) = \frac{\pi z_n}{\lambda}\underbrace{\left(\cos\theta_1-\cos\theta_2\right)}_{:=\beta(\theta_1,\theta_2)}+\frac{\varphi_1-\varphi_2}{2}. \tag{3.78}$$

In the final expressions, we make use of the position of the n-th array element z_n from (1.5). With this notation and the definitions of atan2 (A.3) and sgn (A.2) functions, and by using (A.55), we can rewrite (3.76) as

$$\Delta_n = \Sigma_n + \frac{\pi}{2}(\operatorname{sgn}(\cos(\Sigma_n)\cos(\Pi_n)) - 1) + 2\pi m, \tag{3.79}$$

with $m \in \mathbb{Z}$ being chosen such that Δ_n lies within the range $[-\pi, \pi[$. We have omitted the angle dependence of Σ_n and Π_n for better readability. It should be noted that (3.79) is valid for all cases except when

$$\cos(\Sigma_n)\cos(\Pi_n) = 0, \tag{3.80}$$

which are singular points in our variable space. Using (3.79), we can rewrite the phase differences from (3.75) as

$$M \lim_{t\to\infty} \bar{v}_{\Delta,n}(t) = \Sigma_n - \Sigma_1 + \frac{\pi}{2}\left[\operatorname{sgn}\left(\cos\Sigma_n\cos\Pi_n\right) - \operatorname{sgn}\left(\cos\Sigma_1\cos\Pi_1\right)\right] + 2\pi m \tag{3.81}$$

$$= \frac{\pi z_n}{\lambda}\gamma(\theta_1,\theta_2) + \frac{\pi}{2}\left[\operatorname{sgn}\left(\cos\Sigma_n\cos\Pi_n\right) - \operatorname{sgn}\left(\cos\Sigma_1\cos\Pi_1\right)\right] + 2\pi m. \tag{3.82}$$

$\gamma(\theta_1,\theta_2)$ is a linear combination of the cosines of the two incident angles. Thus the term is ambiguous, i.e. there are several value pairs of θ_1 and θ_2 leading to the same $\gamma(\theta_1,\theta_2)$. In order to solve this ambiguity, we have to use the second summand in (3.82) which can either be 0 or $\pm\pi$. This term can be interpreted as binary information for each of the $N-1$ phase differences.

Since the first array element is located at $z_1 = 0$, we can write

$$\operatorname{sgn}\left(\cos\Sigma_1\cos\Pi_1\right) = \operatorname{sgn}\left(\cos\left(\frac{\varphi_1+\varphi_2}{2}\right)\cos\left(\frac{\varphi_1-\varphi_2}{2}\right)\right), \tag{3.83}$$

which is constant. Therefore, the first term in brackets in (3.82) defines whether the whole expression becomes 0 or $\pm\pi$ for the n-th array element. Since the sign changes of the cosine functions occur at $\{\Sigma_n, \Pi_n\} = \frac{1}{2}\pi + m\pi, m \in \mathbb{Z}$, the expression is constant within regions whose borders are given by

$$\hat{\gamma} = \left(\frac{1}{2} + m - \frac{\varphi_1+\varphi_2}{2\pi}\right)\frac{\lambda}{z_n}, \tag{3.84}$$

$$\hat{\beta} = \left(\frac{1}{2} + m - \frac{\varphi_1-\varphi_2}{2\pi}\right)\frac{\lambda}{z_n}, \tag{3.85}$$

derived from the notation of γ and β in (3.77) and (3.78).

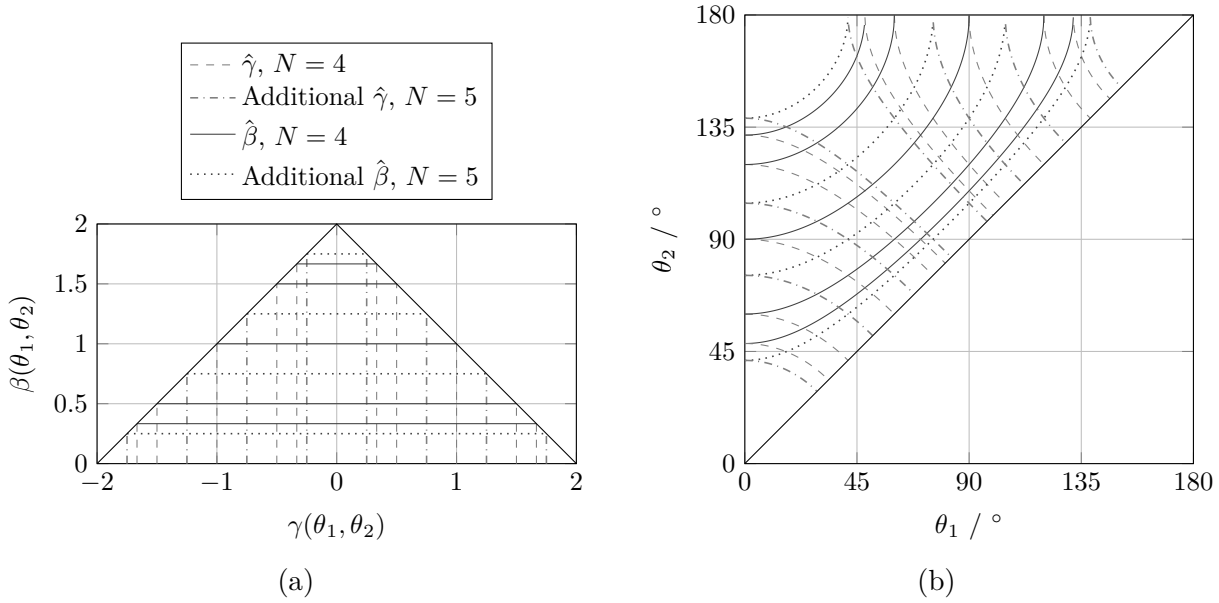

(a) (b)

Fig. 3.14: (a) (γ, β) and (b) (θ_1, θ_2) solution spaces with borders shown for a 4-element ULA. The dotted lines represent the additional borders for an array of 5 elements.

DOA performance with uniform linear arrays

For linear arrays, we regard incident angles in the range $\theta_i = 0°, \ldots, 180°$. To avoid ambiguities between the two incident directions, we define without loss of generality $\theta_1 < \theta_2$. It follows that $\gamma(\theta_1, \theta_2) \in]-2, \ldots, 2[$ and $\beta(\theta_1, \theta_2) \in]0, \ldots, 2[$. Fig. 3.14 shows the borders defined in (3.84) and (3.85) for a ULA of four elements with 0.5λ spacing. It should be noted that both Fig. 3.14a and Fig. 3.14b are two different representations of the same solution space. The $\theta_1 = \theta_2$ line in Fig. 3.14b for example is identical to $\beta = 0$ in Fig. 3.14a. Additionally, the $\gamma = 0$ line in Fig. 3.14a corresponds to $\theta_1 = 180° - \theta_2$, i.e. a diagonal from $(\theta_1, \theta_2) = (0°, 180°)$ to $(90°, 90°)$ in Fig. 3.14b.

Both plots in Fig. 3.14 also show the additional borders introduced when a ULA of five elements is used. The phase values in this example are $\varphi_1 = \varphi_2 = 0$. We can see the difference between the (γ, β) and the (θ_1, θ_2) solution spaces: While the former exhibit straight borders $\hat{\gamma}$ and $\hat{\beta}$, the latter show the actual position of these borders in the DoA solution space. When we regard an array of four elements, there are three equations (3.82), $n \in \{2, 3, 4\}$. The common $\gamma(\theta_1, \theta_2)$ term which is present in all these equations, restricts the solution space in Fig. 3.14 to a line. This line is parallel to the $\hat{\gamma}$ borders. From the combination of $\pm\pi$ phase jumps in the three equations, we can narrow down the solution space to a line segment between two of the $\hat{\beta}(\theta_1, \theta_2)$ borders. However, we cannot determine the exact location of the correct solution, i.e. there remains an uncertainty about the true DoA of the impinging signals.

To assess the quality of this solution space discretization, we have to introduce a figure of merit which represents how well we are able to estimate the two DoA. Also, the figure of merit should be an upper bound for the estimation errors that are to be expected. Thus it makes sense to compare the projections on the θ axes of all possible γ curve segments created by neighboring $\hat{\beta}$ borders. The figure of merit is then the longest occurring θ span

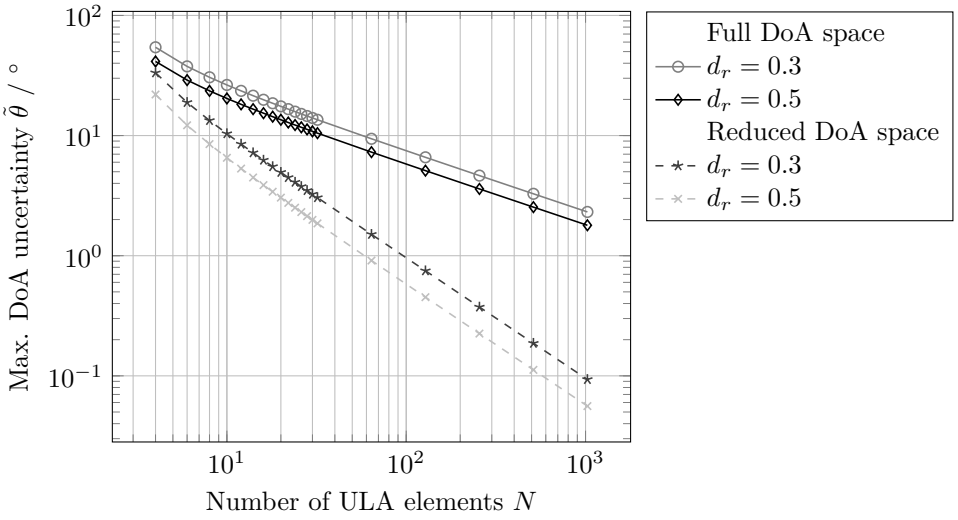

Fig. 3.15: Maximum DoA uncertainty for ULAs of different size and spacing. The dashed lines are valid for a restricted range of incident angles $\theta_i \in [30°, \ldots, 150°]$.

representing the largest region within whom the exact (θ_1, θ_2) solution is located. Due to the symmetry of the solution spaces, it is enough to regard the projections onto the θ_1-axis. We define the maximum DoA uncertainty in the following way:

$$\tilde{\theta} = \max(|\theta_1' - \theta_1''|), \tag{3.86}$$

with

$$\theta_1' = \arccos\left(0.5(\gamma + \hat{\beta}')\right), \tag{3.87}$$

$$\theta_1'' = \arccos\left(0.5(\gamma + \hat{\beta}'')\right), \tag{3.88}$$

where β' and β'' denote any two adjacent $\hat{\beta}$ borders and θ_1', θ_1'' are the start and end points of the projections of all γ line segments.

For the ULA with four elements, the maximum DoA uncertainty is 41.41°. There are two γ curve segments whose projections exhibit this range. Their starting points (θ_1', θ_2') are $(0°, 90°)$ and $(0°, 120°)$, respectively. Due to the symmetry of the solution space, the same uncertainty result can be obtained for θ_2, whereby the respective γ lines start at $(60°, 180°)$ and $(90°, 180°)$. If we use a ULA with five elements, the maximum DoA reduces to 28.96°.

We can see the influence of the array geometry on the maximum uncertainty from (3.86) in Fig. 3.15. The solid lines show $\tilde{\theta}$ for ULAs with different relative spacing and number of elements for the complete solution space, i.e. $\theta_i \in [0°, \ldots, 180°]$. N was computed for the value range $[4, 6, \ldots, 32, 64, 128, \ldots, 1024]$. The figure shows that larger relative element spacing reduces uncertainty. In any case, we need a ULA of 64 elements or more for a maximum uncertainty below 10°.

However, if we are able to restrict our solution space to incident angles around the array boresight, i.e. $\theta_i \in [30°, \ldots, 150°]$, we obtain the dashed curves in Fig. 3.15 which exhibit considerably lower maximum uncertainties. This means that by adding more ULA elements, the discretization of the reduced solution space improves more than for the excluded angles

which are far from boresight. For the reduced incident angle range, we obtain a maximum uncertainty below 10° already with 8 array elements.

Even if we can reduce the range of incident angles as described above, we need to aim at a DoA uncertainty much better than 10° if the system shall be suitable for satellite communication applications. Fig. 3.15 shows that for an uncertainty below 1°, we would require a ULA with over 100 elements. From (3.84), (3.85) and Fig. 3.14, we see that increasing the size of our ULA leads to an irregular discretization of the solution spaces. The reason for this is that the lowest $\hat{\beta}$ border is defined by the position of the last element z_N and $k = 0$ giving

$$\hat{\beta}_{\text{min,ULA}} = \frac{1}{2d_r(N-1)}, \tag{3.89}$$

i.e. it decreases inversely proportional with the number of elements. In the following, we shall analyze if a different array geometry yields better DoA uncertainty results.

DOA performance with non-uniform linear arrays

A straight forward strategy to improve the solution space discretization would be to postulate that adding one antenna element to the array should halve the γ line sections in the (γ, β) solution space. With the first element still located at $z_1 = 0$, this can be achieved by arranging the array elements at the positions

$$z_n = 2^{n-2} d_r \quad \text{for} \quad n \in 2, \ldots, N, \tag{3.90}$$

which increases the inter-element spacing exponentially and leads to the lowest $\hat{\beta}$ border reading

$$\hat{\beta}_{\text{min,EXP}} = \frac{1}{d_r 2^{N-1}}. \tag{3.91}$$

The respective discretized solution spaces of a four element array with $d_r = 0.5$ are shown in Fig. 3.16. The figure also shows the additional borders for an exponentially spaced array of $N = 5$ elements. We can see the more regular discretization of the (γ, β) solution space compared to the ULA in Fig. 3.14. From this we expect a lower maximum DoA uncertainty.

This is demonstrated in Fig. 3.17 where $\tilde{\theta}$ is plotted for exponentially spaced linear arrays of up to $N = 24$ elements. It should be kept in mind that due to the element spacing in (3.90), an array of N elements has the same physical size as a ULA of $2^{N-2} + 1$ elements, $N \geq 4$. Comparing to Fig. 3.15, we see that the attained maximum DoA uncertainty for these two cases is the same. This shows that the position of the lowest borders $\hat{\beta}_{\text{min}}$ in (3.89) and (3.91) mainly defines the figure of merit $\tilde{\theta}$. This position is related to the largest distance between two elements in the array and thus its physical size. It follows that the exponentially spaced linear array is better suited for DoA estimation since it has fewer elements than the ULA but offers the same precision at equal dimensions.

3.5.3 General multiple user case

In general, it is not possible to find a unique DoA solution for the case of multiple users from (3.75) and (3.71). As we have seen, we can narrow down the solution space by using the strong assumptions listed in section 3.5.2. However, especially the presence of two signals

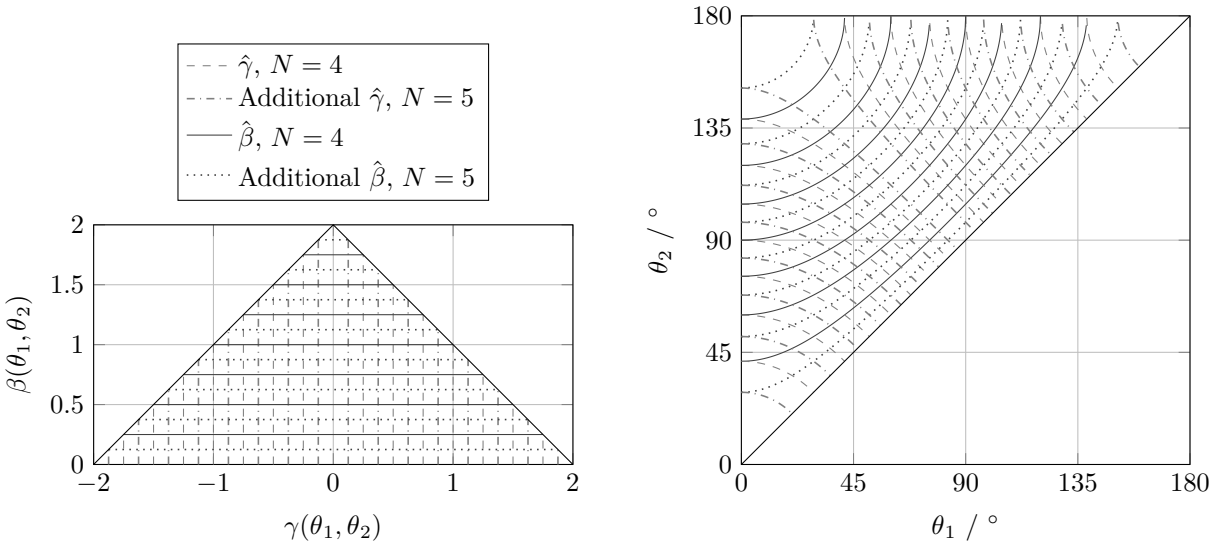

Fig. 3.16: (a) (γ, β) and (b) (θ_1, θ_2) solution spaces with borders shown for a 4-element exponentially spaced array. The dotted lines represent the additional borders for an array of 5 elements.

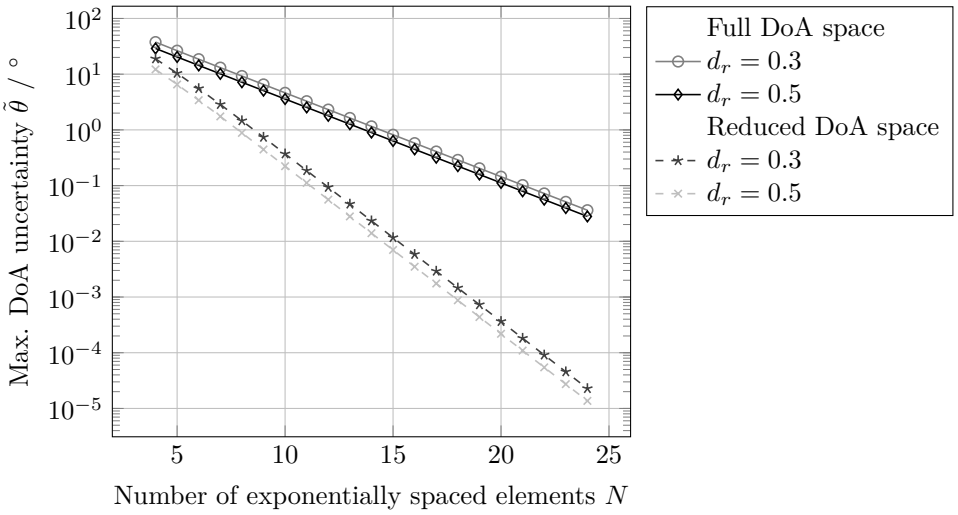

Fig. 3.17: Maximum DoA uncertainty for exponentially spaced arrays of different size. The dashed lines are valid for a restricted range of incident angles $\theta_i \in [30°, \ldots, 150°]$.

of equal power is difficult to motivate in communication scenarios. It is also usually not the case for multipath scenarios where we have strong LoS and weak reflected signal paths.

Leaving this aside, our analysis in the previous section looks promising as we can obtain very small DoA uncertainties with a reasonable number of array elements. However, we based the investigation on the assumption of perfect knowledge of the absolute signal phases φ_1, φ_2. This means that both signal sources are phase locked, which is not a suitable assumption for a communication scenario with multiple users. If the phases are unknown, the solution space borders defined in (3.84) and (3.85) are shifted. The $\pm\pi$ jumps in the detected phases (3.82) cannot be matched to a $\gamma(\theta_1, \theta_2)$ line segment and DoA estimation is no longer possible in the way outlined before.

Our investigation shows that it is in general not possible to detect the DoA of multiple incident signals from the received phases only. This also means that phase conjugation alone is not sufficient to achieve retro-directive behavior in a multi-user scenario. It is also necessary to preserve the amplitude information at the individual antenna elements in (3.70). A van Atta array or a phase conjugation mixer scale the signal amplitudes linearly. In this case, superposition applies if multiple signal sources are present and each signal is individually phase conjugated and retransmitted [37, 59, 78]. In contrast, we can say that any RDA which makes use of phase information only is in general not capable of serving multiple users in parallel. These findings are in line with the work of Brennan in [45] where the necessity of amplitude information is stressed if a second signal is impinging on a PLL based self-phasing array.

4 Digital system implementation

At the beginning of chapter 3, we have introduced the architecture of our RDA system. Afterwards, we have focused on the receiver part and have shown its functional principle analytically and by continuous time simulations. In this chapter, we shall realize the complete retro-directive transceiver as a discrete time system. As stated in chapter 3, the proposed transceiver is meant to be implemented with analog components. However, we will see that the discrete time system is closely related to the analog one presented before. Our goal is to realize the discrete time transceiver on a FPGA for an experimental validation of the whole RDA architecture. We have chosen a digital implementation due to its better reconfigurability. Additionally, the digital approach allows us to directly include the necessary processing of the phase differences and the Tx beamforming which has not been addressed in detail yet. Thus, we can realize the complete transceiver functionality. The system will be designed for lower signal frequencies than in chapter 3 which is due to the limitation of clock rates available for customizable digital circuits.

We begin the chapter by introducing the discrete time receiver design in section 4.1. Thereby, we draw parallels to the analog system described in section 3.2. To underline the similarity, we compare the analog and digital phase transfer functions using an identical parameterization. In section 4.2, we evaluate the digital receiver by discrete time simulations using ModelSim. We also compare the initial IF signal behavior and phase detection performance to continuous time simulations of the respective analog system. After that, we explain in section 4.3 how the complete transceiver can be realized in digital hardware. We thereby target a system with eight Rx and Tx channels. Additionally, we present a method to arrive at a single phase estimate and show how it is implemented on the FPGA. We conclude the chapter by running the proposed transceiver on a FPGA development platform and assess its phase detection performance experimentally.

4.1 Receiver design

To draw parallels to the previously described system architecture, we replicate the analog receiver shown in Fig. 3.2 as closely as possible in the discrete time domain. This will allow us to do the parameterization in the analog domain and transfer it to discrete time. A receiver channel with discrete time components and quantization is depicted in Fig. 4.1. The parallels to Fig. 3.2 and to the Simulink model shown in Fig. B.1 can be clearly seen. In contrast to the analog receiver, the signal values are quantized. The word width w of each signal is written next to the respective connection. All signals are signed integer numbers with a value range $[2^{w-1}, \ldots, 2^{w-1} - 1]$.

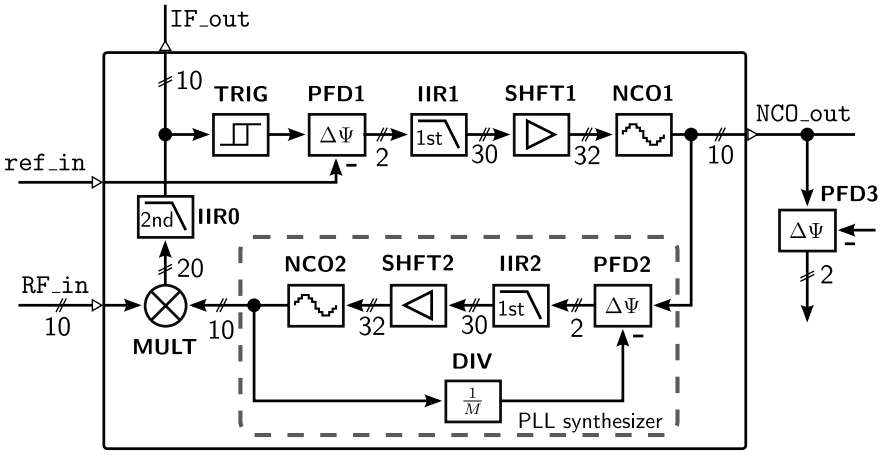

Fig. 4.1: Digital implementation of a single receiver channel. Numbers next to the connections represent the word width of the respective signal. Blank lines mark the propagation of a single bit. The structure closely resembles the analog receiver channel shown in Fig. 3.2.

4.1.1 Details of digital components

In this section, we will introduce the discrete time components used within the receiver and their difference equations. Input signals are thereby noted by x, output signals by y. In order to obtain phase transfer functions and draw parallels to the analog system design, we use the z-transform.

Down-mixer

As in the analog design, this part is used to mix down the input RF signals. It consists of a multiplier and a subsequent lowpass to eliminate higher mixing products. We hereby use a second order Butterworth filter and choose the coefficients according to the frequency plan of the receiver. Similar to (3.6), the phase transfer function of the down-mixer is approximately

$$\Psi_{\mathrm{IF}}(z) = \Psi_1(z) - \Psi_2(z). \tag{4.1}$$

We hereby denote the two mixer input signal phase values by $\Psi_i, i \in \{1, 2\}$. We assume that the discrete time frequencies of these signals fulfill $\Omega_1 > \Omega_2$.

Schmitt trigger

The Schmitt trigger is a comparator with hysteresis. We can write its output signal as

$$y_{\mathrm{trig}}(n) = \begin{cases} y_{\mathrm{trig}}(n-1) & \text{if} \quad |x_{\mathrm{trig}}(n)| < x_{\mathrm{th}} \\ 0 & \text{if} \quad x_{\mathrm{trig}}(n) \geq x_{\mathrm{th}} \\ 1 & \text{if} \quad x_{\mathrm{trig}}(n) \leq -x_{\mathrm{th}} \end{cases}, \tag{4.2}$$

with x_{th} being the threshold signal amplitude. The binary output represents the sign bit of the input signal x_{trig} whereby the influence of small amplitude fluctuations, e.g. from noise and residual higher mixing products, are eliminated by the hysteresis. We thus ensure that

the sign changes at the subsequent PFD input are caused solely by the IF signal. Regarding the phase transfer function, we will assume that the Schmitt trigger introduces a unit delay, i.e. z^{-1}.

Phase-frequency detector

Since we work with discrete time components, the flip-flop based PFD is directly realized as shown in appendix A.2 and Fig. A.1. Only the output stage is altered: We use logic gates to map the flip-flop outputs q_1, q_2 to a 2 bit signal which can take the values $y_{\mathrm{PFD}} \in \{-1, 0, 1\}$. This output signal forms the expected pulse train with sign and duty cycle according to the phase difference of the input signals.

In accordance with the considerations in (3.8) and appendix A.2, we assume the time average of the discrete time PFD output signal to be

$$\bar{y}_{\mathrm{PFD}}(n) = K_{\mathrm{d}} \left(\Psi_{\mathrm{in},1}(n-1) - \Psi_{\mathrm{in},2}(n-1) \right). \tag{4.3}$$

The z-transform of the average PFD output then reads [64, c.4]

$$\bar{y}_{\mathrm{PFD}}(z) = K_{\mathrm{d}} z^{-1} \left(\Psi_{\mathrm{in},1}(z) - \Psi_{\mathrm{in},2}(z) \right). \tag{4.4}$$

Due to the given output signal range, the PFD gain is fixed to $K_{\mathrm{d}} = 1/(2\pi)$ in our case.

IIR loop filter

In order to allow a direct comparison between analog and digital implementation, we use first order infinite impulse response (IIR) filters in our digital receiver design. The filter output signal in the discrete time domain is given by [69, p.281]

$$y_{\mathrm{IIR}}(n) = -\frac{a_1}{a_0} y_{\mathrm{IIR}}(n-1) + \frac{b_0}{a_0} x_{\mathrm{IIR}}(n) + \frac{b_1}{a_0} x_{\mathrm{IIR}}(n-1). \tag{4.5}$$

with a_i, b_i being the filter coefficients, $i \in \{0, 1\}$. We find the z-transform of this filter to be

$$h(z) = \frac{b_0 + b_1 z^{-1}}{a_0 + a_1 z^{-1}}, \tag{4.6}$$

which corresponds to the form of the analog loop filter with one pole and one zero in (3.36). To obtain the correct filter coefficients, we use the following procedure: An analog filter with the desired time constants is designed. Then we apply the bilinear transform [79, p.504] to it. Using the approximate substitution

$$s = 2F_s \frac{z-1}{z+1}, \tag{4.7}$$

we obtain the digital filter coefficients by

$$a_0 = 1 + 2\tau_{12} F_s, \tag{4.8a}$$
$$a_1 = 1 - 2\tau_{12} F_s, \tag{4.8b}$$
$$b_0 = 1 + 2\tau_2 F_s, \tag{4.8c}$$
$$b_1 = 1 - 2\tau_2 F_s, \tag{4.8d}$$

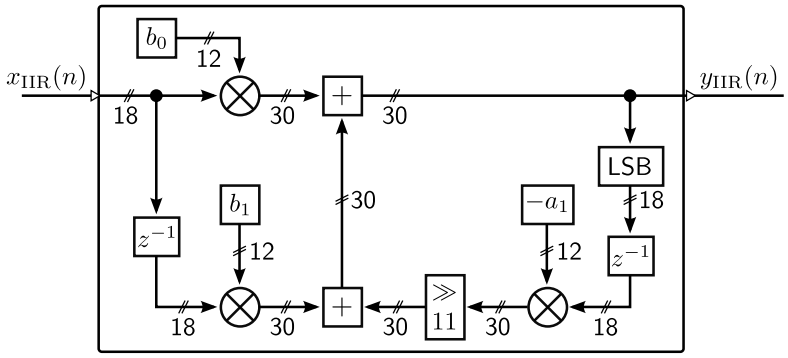

Fig. 4.2: Implementation of the first order discrete time IIR filter. All coefficients are normalized to $a_0 = 2^{11}$.

whereby F_s denotes the sample frequency of the discrete time system. The bilinear transform ensures stability for the resulting digital filter under the condition that the analog filter was stable.

The digital implementation of the first order IIR filter is shown in Fig. 4.2. For the coefficients, we choose a word width of $w_{\mathrm{IIR}} = 12\,\mathrm{bit}$ which corresponds to the width of the hardware multipliers in our implementation. Since a_0 in (4.8a) is always the largest coefficient, we set it to $a_0 = 2^{11} = 2048$. The remaining coefficients from (4.8) are mapped to the range $[-2048, \ldots, 2047]$ and multiplied with the respective forward or feedback signals. Using this normalization, we save the multiplier for coefficient a_0. Instead, we only need an arithmetic bit shifter in the feedback path of a_1.

The thus realized filter has a gain of a_0. Since the filter input signal is the PFD output, its value range is $\{-1, 0, 1\}$, as written above. Due to this bounded input, the 30 bit outputs of the multipliers and adders in the filter design are not fully used. This oversizing is necessary in order to avoid loss of information when we truncate the filter output signal to its 18 least significant bits (LSBs) in the feedback path of the filter.

Bit shifter

To adjust the PLL forward gain, we use arithmetic bit shifters after the loop filters. The input signal is thereby up or down shifted by d_{SHFT} bits. The arithmetic shifter hereby preserves the sign of the input signal. As long as the output signal is not truncated, the difference equation of the shifter is given by

$$y_{\mathrm{SHFT}}(n) = 2^{d_{\mathrm{SHFT}}} x_{\mathrm{SHFT}}(n-1), \tag{4.9}$$

with $d_{\mathrm{SHFT}} \in \mathbb{Z}$. The z-transform thus reads

$$h_{\mathrm{SHFT}}(z) = 2^{d_{\mathrm{SHFT}}} z^{-1}. \tag{4.10}$$

Numerically controlled oscillator

A discrete time oscillator is implemented as a lookup table with 2^{w_φ} entries where w_φ is the word width of the phase accumulator [64, c.9.7.2]. The table entries are equally spaced

amplitude samples of a single period of a sinusoid. We find the quantized digital oscillator output signal to be

$$y_{\mathrm{osc}}(n) = \left\lfloor 2^{w_{\mathrm{osc}}-1} \sin\left(2\pi \frac{\varphi_{\mathrm{inc}}}{2^{w_\varphi}} n\right) \right\rfloor, \tag{4.11}$$

with w_{osc} denoting the word width of the signed signal amplitude and $\varphi_{\mathrm{inc}} \in \mathbb{N}$ the phase increment. The physical frequency of the oscillator depends on the sample rate F_s and is given by

$$f_{\mathrm{osc}} = \frac{\varphi_{\mathrm{inc}}}{2^{w_\varphi}} F_s. \tag{4.12}$$

A numerically controlled oscillator (NCO) is a quantized digital oscillator with a frequency modulation (FM) input. We find its output signal to be

$$y_{\mathrm{nco}}(n) = \left\lfloor 2^{w_{\mathrm{nco}}-1} \sin \underbrace{\left(2\pi \frac{\varphi_{\mathrm{inc}} n + \sum_{l=0}^{n-1} x_{\mathrm{nco}}(l)}{2^{w_\varphi}}\right)}_{:=\Psi_{\mathrm{nco}}(n)} \right\rfloor, \tag{4.13}$$

where $x_{\mathrm{nco},i}(n)$ is the NCO input signal. The parallel to the VCO output signal from (3.10) is obvious. We can rewrite the NCO output phase term as

$$\Psi_{\mathrm{nco}}(n) = \Psi_{\mathrm{nco}}(n-1) + 2\pi \frac{\varphi_{\mathrm{inc}} + x_{\mathrm{nco}}(n-1)}{2^{w_\varphi}}. \tag{4.14}$$

Neglecting the constant phase increment φ_{inc}, the z-transform of this expression reads [64, c.4.2.3]

$$\frac{\Psi_{\mathrm{nco}}(z)}{x_{\mathrm{nco}}(z)} = \frac{2\pi}{2^{w_\varphi}} \frac{z^{-1}}{1 - z^{-1}}, \tag{4.15}$$

where the first term is the sensitivity $K_{\mathrm{V}} = 2\pi/2^{w_\varphi}$ of the NCO. We see that the NCO translates the input signal into the phase term of a periodic signal similar to the VCO in (3.10).

Frequency divider

The frequency divider is implemented in the same way as described in section 3.2.2 and shown in Fig. B.3 for the Simulink model. It consists of a counter which increments with each input signal sign change. Since the input signal of the divider is the quantized output of a NCO, it is sufficient to regard its sign bit. After M input signal sign changes, the frequency divider toggles its output signal.

Under the assumption that the input signal frequency remains constant over M periods, the phase transfer function of the frequency divider reads

$$\Psi_{\mathrm{div}}(z) = \frac{z^{-1}}{M} \Psi_{\mathrm{nco}}(z). \tag{4.16}$$

4.1.2 Receiver phase transfer function

Having described all necessary system components, we can obtain the phase transfer function of the inner PLL. Using (4.15) and inserting (4.6), (4.4) and (4.16), we arrive at

$$\begin{aligned}\Psi_{\mathrm{NCO2}}(z) &= K_{\mathrm{V2}}\frac{z^{-1}}{1-z^{-1}}h_2(z)K_{\mathrm{d2}}z^{-1}\left(\Psi_{\mathrm{NCO1}}(z)-\frac{\Psi_{\mathrm{NCO2}}(z)}{M}z^{-1}\right)\\ &= \frac{K_2h_2(z)z^{-2}}{1-z^{-1}+\frac{K_2}{M}h_2(z)z^{-3}}\Psi_{\mathrm{NCO1}}(z).\end{aligned} \tag{4.17}$$

From this, we can derive the phase transfer function of the whole receiver from RF and reference inputs to the outer NCO output. Once again, we take (4.15) and insert (4.1), (4.6), (4.4) and (4.17) which yields

$$\begin{aligned}\Psi_{\mathrm{NCO1}}(z) &= K_{\mathrm{V1}}\frac{z^{-1}}{1-z^{-1}}h_1(z)K_{\mathrm{d1}}z^{-1}\left(\left(\Psi_{\mathrm{RF}}(z)-\Psi_{\mathrm{NCO2}}(z)\right)z^{-T_d}-\Psi_{\mathrm{ref}}(z)\right)\\ &= \frac{K_1h_1(z)z^{-2}\left(1-z^{-1}+\frac{K_2}{M}h_2(z)z^{-3}\right)\left(\Psi_{\mathrm{RF}}(z)z^{-T_d}-\Psi_{\mathrm{ref}}(z)\right)}{(1-z^{-1})\left(1-z^{-1}+\frac{K_2}{M}h_2(z)z^{-3}\right)+K_1K_2h_1(z)h_2(z)z^{-4-T_d}}.\end{aligned} \tag{4.18}$$

T_d denotes the delay introduced by the mixing and filtering operations between the RF and NCO output signals and by the Schmitt trigger. To determine zeros and poles of the phase transfer functions (4.17) and (4.18), we have to insert the filter transfer functions from (4.6). The respective expressions can be found in appendix B.2. With first order filters, the order of the phase transfer function (4.18) is $6+T_d$ which inhibits an analytical calculation of the system poles. To check system stability for a given realization, we therefore have to obtain the poles numerically again. We will use the above system phase transfer function later in section 4.1.4 to compare the discrete time system performance to that of the analog one.

4.1.3 Phase detection

As can be seen in Fig. 3.8, we have obtained the phase detection results for our continuous time simulations by feeding the VCO 1 outputs of two channels to a PFD and lowpass filtering its output. The lowpass filter thereby averages the PFD output signal over time, thus leading to a smooth phase detection result. In the digital implementation, we will again obtain the phase differences between two receiver channels by comparing their NCO 1 outputs from Fig. 4.1 using a PFD. The averaging however will be done differently: As described above, our digital PFD has a 2 bit output signal. The most significant bit (MSB) thereby determines the sign of the PFD output, while the LSB denotes if a pulse is present or not. In order to obtain the phase difference of the two input signals, we have to determine sign and duty cycle of the PFD output signal. For this, we use a duty cycle counter (DCC) whose structure is depicted in Fig. 4.3. It consists of two counters: The lower one acts as reference. It counts upwards on every clock cycle and we use its overflow signal to update the DCC output register. With the counter output word width w_{cnt}, the overflow is triggered every $2^{w_{\mathrm{cnt}}}$ clock cycle. The upper counter keeps track of the arriving pulses. For this, we use the MSB, i.e. the sign of the pulse to decide if the counter counts up- or downward. With the LSB, we enable the counter such that it is only counting if a pulse is present. The

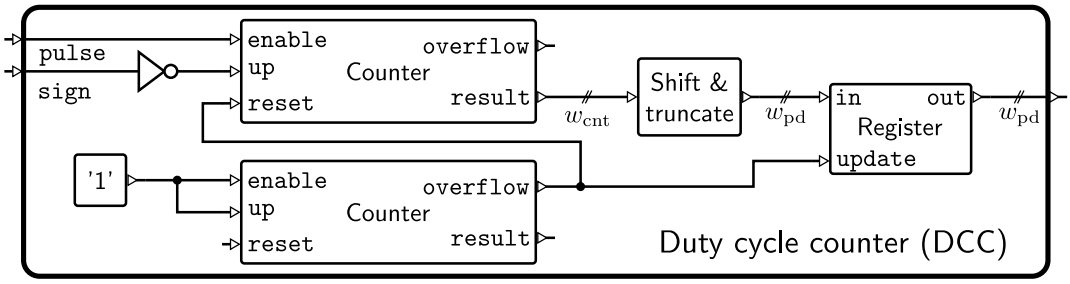

Fig. 4.3: Block diagram of the digitally implemented DCC used to extract the duty cycle of a PFD output signal.

ratio between the two counter outputs is proportional to the duty cycle of the input pulse train.

To arrive at the desired phase differences, we have to implement the computation of (3.25), i.e. remove the factor $1/M$ and apply the modulo operation. Therefore, we select the word width of the counters according to

$$w_{\mathrm{cnt}} = w_{\mathrm{pd}} + \log_2(M) + b_{\mathrm{s}}, \tag{4.19}$$

where w_{pd} is the desired word width of the phase detection output and M must be a power of 2. b_{s} is a number of additional bits used to increase the averaging time of the phase detection and thus smooth the result. We hereby implement the necessary multiplication by M because we are counting over M-times more clock periods. The modulo division is realized by shifting down the counter output by b_{s} and then truncating to the w_{pd} LSBs. At the DCC output, we thus obtain an averaged estimate for the duty cycle of the input pulse train. The phase detection output maps the possible phase differences $[0, \ldots, 2\pi[$ between two PFD input signals to the available integer range $[0, \ldots, 2^{w_{\mathrm{pd}}} - 1]$. Due to the described DCC structure based on counters, we obtain the time between phase detection output updates to be

$$t_{\mathrm{upd,pd}} = \frac{2^{w_{\mathrm{cnt}}}}{f_{\mathrm{clk,pd}}}, \tag{4.20}$$

where $f_{\mathrm{clk,pd}}$ is the clock of the phase detection circuitry. We see that enlarging the counter word width leads to a better granularity of the phase detection but also exponentially increases update time.

Besides the quantization of the phase detection result by the output word width w_{pd}, we have to observe that the pulse widths of the PFD output signal are also quantized. This is because the PFD is a clocked device and its output can only change from one clock cycle to the next. Thus we obtain a pulse train whose duty cycles are integer multiples of the PFD clock which we also set to $f_{\mathrm{clk,pd}}$. Each of the two PFD input signals is the output from a NCO 1. In the steady state, they will have an equal frequency f_{N1} and the minimum detectable phase difference between the input signals is

$$\Delta\delta_{\min} = 2\pi M \frac{f_{\mathrm{N1}}}{f_{\mathrm{clk,pd}}} = 2\pi \frac{f_{\mathrm{RF}} - f_{\mathrm{ref}}}{f_{\mathrm{clk,pd}}}, \tag{4.21}$$

where f_{RF} and f_{ref} are the RF and reference frequency of our receiver, respectively. We see that it would be desirable to have a high $f_{\mathrm{clk,pd}}$ in order to minimize $\Delta\delta_{\min}$ and thus increase

Table 4.1: Digital example system base parameters

Parameter	Symbol	Value
Main clock frequency	f_{clk}	100 MHz
Received signal RF	f_{RF}	13.28 MHz
Reference oscillator frequency	f_{ref}	781.25 kHz
Expected output IF	f_{IF}	781.25 kHz
NCO phase accumulator width	w_{φ}	32 bit
Loop filter gain	K_{h}	2^{11}
PFD 1 gain	K_{d1}	$1/2\pi$ V/rad
Bit shifter 1 distance	d_{SHFT1}	4 bit
NCO 1 quiescent frequency	f_{q1}	781.25 kHz
PFD 2 gain	K_{d2}	$1/2\pi$ V/rad
Bit shifter 2 distance	d_{SHFT2}	16 bit
NCO 2 quiescent frequency	f_{q2}	12.5 MHz
Frequency division factor	M	16
DCC phase detection output width	w_{pd}	8 bit
DCC number of smoothing bits	b_{s}	1 bit
DCC counter word width	w_{cnt}	13 bit
Phase detection clock frequency	$f_{\mathrm{clk,pd}}$	200 MHz
DCC update time	$t_{\mathrm{upd,pd}}$	40.96 µs
Minimum detectable phase difference	$\Delta\delta_{\mathrm{min}}$	$1/8\pi$ rad

the phase resolution. This also decreases the DCC update time in (4.20). However, for a real implementation, the attainable clock speeds are limited by the chosen FPGA device.

4.1.4 Parameterization

Previously, we have introduced all necessary components for the receiver in the discrete time domain. From that, we have derived the system phase transfer function in (4.18) and have introduced the phase detection circuitry. In order to assess the performance of the receiver, we have to choose its parameterization. Similar to the analog receiver channel designed in section 3.3, the discrete time system is characterized by the following parameters:

- Loop gains K_1, K_2, incorporating the gain values of PFD, filter, arithmetic bit shifter and NCO,
- Divider factor M,
- Filter time constants τ_{2i}, τ_{12i} which can be converted to IIR filter coefficients using (4.8).

Due to the parallels between continuous and discrete time systems, we are able to compare their phase transfer functions and the locations of poles. For this analysis, we use the discrete time example system detailed in Table 4.1. Compared to the analog receiver parameters from Table 3.1, we see the following differences: The signal frequencies are much lower which is

Table 4.2: Filter parameters for digital implementation

Parameter	Initial	Optimized
τ_{121}	0.2768 µs	9.2827 µs
τ_{21}	0.2763 µs	1.0373 µs
a_{11}	−1975	−2046
b_{01}	2044	230
b_{11}	−1971	−228
τ_{122}	0.526 61 µs	10.805 µs
τ_{22}	0.526 60 µs	9.3884 µs
a_{12}	−2009	−2046
b_{02}	2048	1780
b_{12}	−2009	−1778

due to the digital implementation. From previous experience with digital systems [80, 81], we aim at a clock frequency of $f_{\text{clk}} = 100\,\text{MHz}$ for the digital implementation. All occurring frequencies in the design have to fulfill the sampling theorem [82]. The RF has to be chosen such that the higher mixing product after the down-mixer in Fig. 4.1 can be filtered out. We have chosen the IF frequency to be $\frac{1}{128} f_{\text{clk}}$ which directly yields the available phase resolution for the IF and NCO 1 output signals. As detailed above, the division factor M was chosen to be a power of 2 in order to do the necessary modulo division from (3.25) with the presented DCCs. While the NCO sensitivity is fixed in the digital approach by the width of the phase accumulator, we can adjust the loop gains by changing the bit shifter distances. We see that for the chosen parameterization, the gain of the inner PLL is by a factor of 2^{12} higher than that of the outer PLL.

In general, the discrete time receiver channel shall mirror the behavior of the analog one. Therefore, our design goals are the same as stated in section 3.3.4, i.e. ensure system stability and minimize the real part of the pole closest to the $j\omega$-axis in the Laplace domain. For the discrete time system, stability is achieved when all poles of the phase transfer function in (4.18) lie within the unit circle. We have to check this condition by numerically calculating the pole locations of (4.18) for each parameter set.

In order to apply the optimization technique introduced in section 3.3.4, we have to transfer the discrete time system to the Laplace domain. As for the IIR filters, we apply the bilinear transform to the phase transfer function in (4.18). In the following, we regard two different sets of loop filter parameterization which are detailed in Table 4.2:

1) Initial: The filter coefficients taken from the analog design in section 3.3,

2) Optimized: The coefficients found by a full parametric search fulfilling (3.56), whereby we use the actual values of K_1, K_2 and M from Table 4.1.

Both parameter sets lead to stable systems but differ considerably. We see this in the time constants which are an order of magnitude apart. Moreover, we observe that for the initial parameterization, the second loop filter is eliminated for the digital system design. We shall compare the two parameter sets in terms of phase transfer function and system poles.

Table 4.3: Poles of the initial and optimized system designs

Parameter set	Poles (analog)	Poles (digital, quantized)
Initial	$-3.6123 \cdot 10^6$	$-3.6291 \cdot 10^6$
	$-1.8989 \cdot 10^6$	$-1.9226 \cdot 10^6$
	$-1.6671 \cdot 10^5$	$-1.6741 \cdot 10^5$
	$-2.8603 \cdot 10^4$	$-2.8624 \cdot 10^4$
Optimized	$-1.6796 \cdot 10^5$	$-1.5512 \cdot 10^5$
	$-1.0568 \cdot 10^5$	$-1.2382 \cdot 10^5$
	$-4.8169 \cdot 10^4 \pm j1.8923 \cdot 10^4$	$-4.3424 \cdot 10^4 \pm j2.2002 \cdot 10^4$

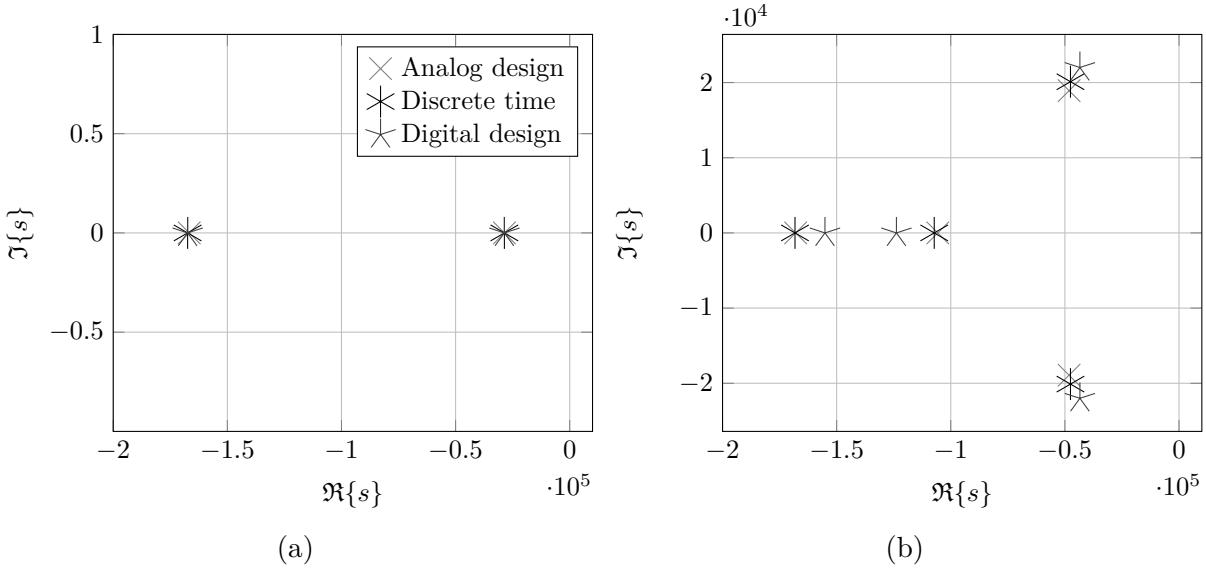

Fig. 4.4: Poles of the receiver with (a) initial and (b) optimized parameter set. It can be seen that the influence of filter coefficient quantization is larger for the optimized set.

The locations of the poles in the Laplace domain are listed in Table 4.3 and the poles closest to the $j\omega$-axis are shown in Fig. 4.4. The plots show the location of system poles for three cases: First, we use the phase transfer function in (3.46), i.e. we have an analog system from whose transfer function we obtain the poles directly in the Laplace domain. We denote this as the analog design. Second, we use the discrete time phase transfer function in (4.18) with double precision, i.e. unquantized filter coefficients and apply the bilinear transform to obtain the phase transfer function in the Laplace domain. From this we obtain the poles numerically. We call this the discrete time system. Third, we use the same procedure but quantize the filter coefficients to integer values as in Table 4.2. This represents an actual hardware implementation and we denote it as the digital design. As shown in (B.4), the discrete time phase transfer functions are of order $6 + T_d$. The additional system poles are not listed because their real parts are smaller than $-1.5 \cdot 10^8$ and thus are located orders of magnitude farther from the $j\omega$-axis than the listed poles. Therefore, they will not influence the dynamic system behavior significantly.

Regarding Table 4.3 and comparing the plots in Fig. 4.4, we see that the optimization leads to multiple changes: First, the real pole closest to the $j\omega$-axis becomes a complex pole pair. While its real part is smaller due to the chosen optimization, the presence of an imaginary part will cause oscillations in the system response. Additionally, the optimized analog system has all four poles close to the $j\omega$-axis with the farthest being at $\Re\{s\} = -1.6796 \cdot 10^5$. For the initial system we find the pole farthest from the $j\omega$-axis to be located at $\Re\{s\} = -3.6123 \cdot 10^6$. That means, although the optimization decreased the real part of the pole closest to the $j\omega$-axis, it increased the real part of the remaining poles such that all four are within the same order of magnitude. This may have a negative influence on the dynamic behavior. We have to see from time domain simulations if the chosen optimization method yields an improvement in this case.

Analyzing the effect of the bilinear transform and quantization, we see in Fig. 4.4a that the location of the poles is the same for all three cases. That means, we can layout the discrete time system using the analog system design approach and expect similar behavior. Finally, we observe that the influence of quantization is negligible in this case since the pole locations do not differ visibly. Regarding the poles for the optimized parameter set in Fig. 4.4b, we see good agreement between the analog and the discrete time system. However, the influence of quantization is recognizable and we observe that the rightmost pole pair is closer to the $j\omega$-axis for the digital design. We therefore expect differences in the dynamic behavior.

A comparison of the phase transfer functions in the Laplace domain is depicted in Fig. 4.5. The figure shows the curves for the analog and the digital designs. The respective curves for the discrete time systems are not shown as they are very similar to the ones from the digital design. We observe that the phase transfer functions of analog and digital design agree well for both cases although slight differences can be seen for the optimized parameter set. Strong deviations occur only close to the Nyquist frequency of the discrete time system. These are caused by the bilinear transform. However, we do not expect any major influence on the system behavior from this.

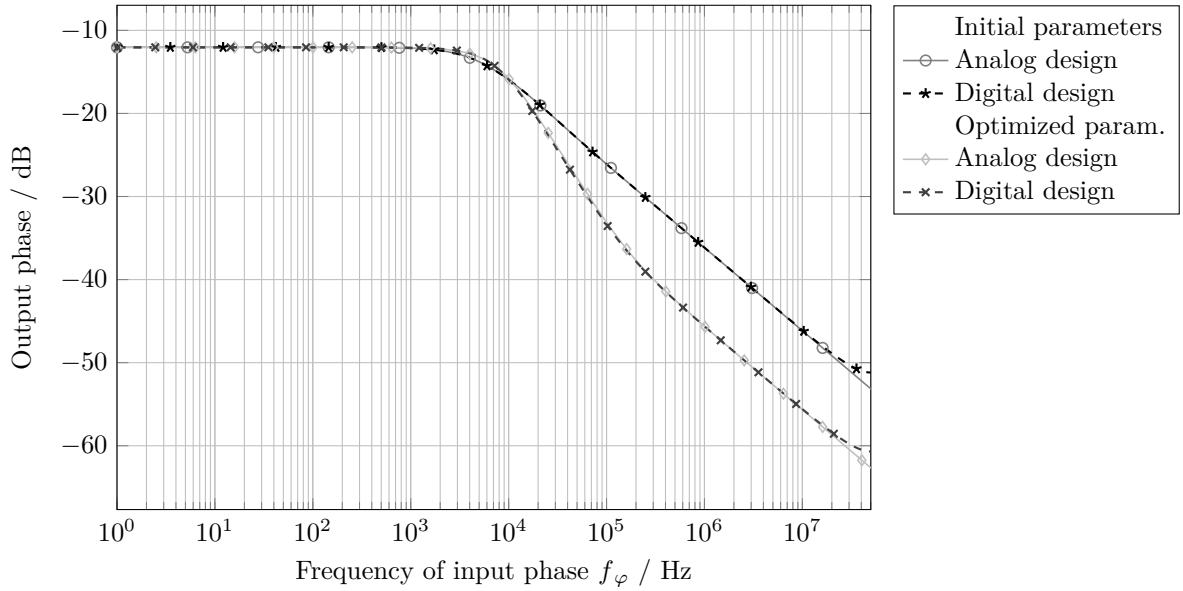

Fig. 4.5: Phase transfer functions comparing the analog design and the result of the bilinear transform applied to the digital design. We use two parameter sets: the initial set taken from chapter 3 and the result of the parameter optimization using the correct values of K_1, K_2 and M in Table 4.1.

4.2 Receiver hardware simulations

Previously, we have obtained the phase transfer function for the discrete time system and have compared it to that of the continuous time version. In this section, we simulate an eight channel receiver with the parameters listed in Table 4.1 and both sets of filter coefficients in Table 4.2. We will thereby use two different simulation methods

1) An eight channel Simulink model for continuous time domain simulations which is detailed in appendix B.1.2,

2) An eight channel receiver written in VHSIC hardware description language (VHDL) for discrete time simulation in ModelSim.

The first is an expansion of the dual channel receiver used in section 3.4. The latter is an implementation using the discrete time receiver channels and DCCs described in section 4.1.

4.2.1 Initial IF sum signal behavior

Fig. 4.6 shows the initial behavior of the IF sum signal envelope of the Simulink runs for various phase differences in steps of $\pi/2\,\mathrm{rad}$. The plots are both for the initial system parameter set and the optimized one. We see that the finally achieved amplitudes are equal and differences in adaption speed are small. In Fig. 4.7, we see the initial behavior of the IF sum signal envelope obtained by discrete time simulation with ModelSim. It should be noted that the time scales of the two depicted plots are different. Compared to the continuous time simulations, we observe the following differences: The adaption speed differs considerably between the parameter sets with the initial one converging much faster. This is due to the

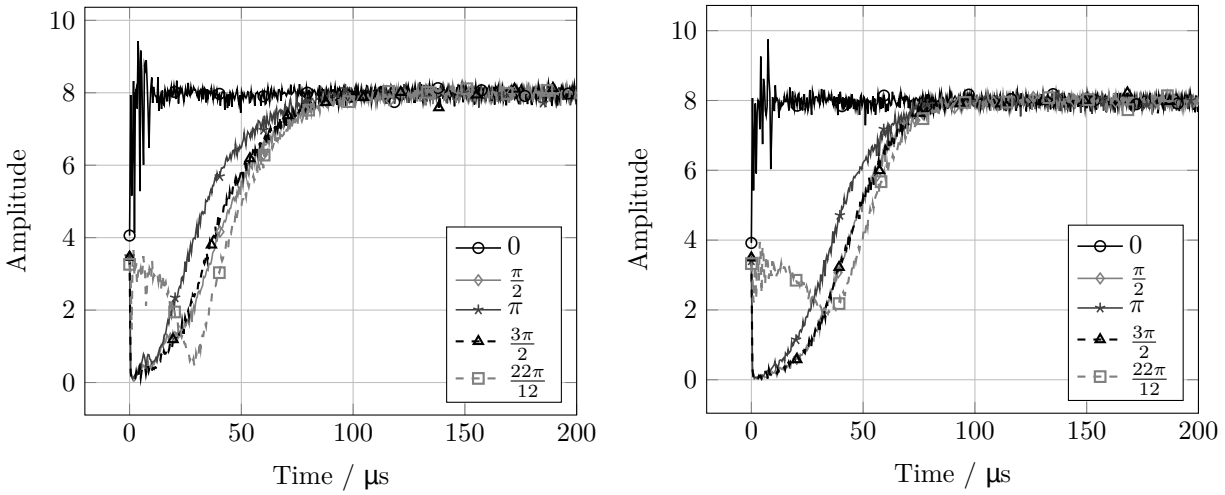

Fig. 4.6: IF sum signal envelope from Simulink simulation runs using (a) the initial and (b) the optimized parameter sets on different time scales. The last curve in each plot represents the case with the largest measured time constant.

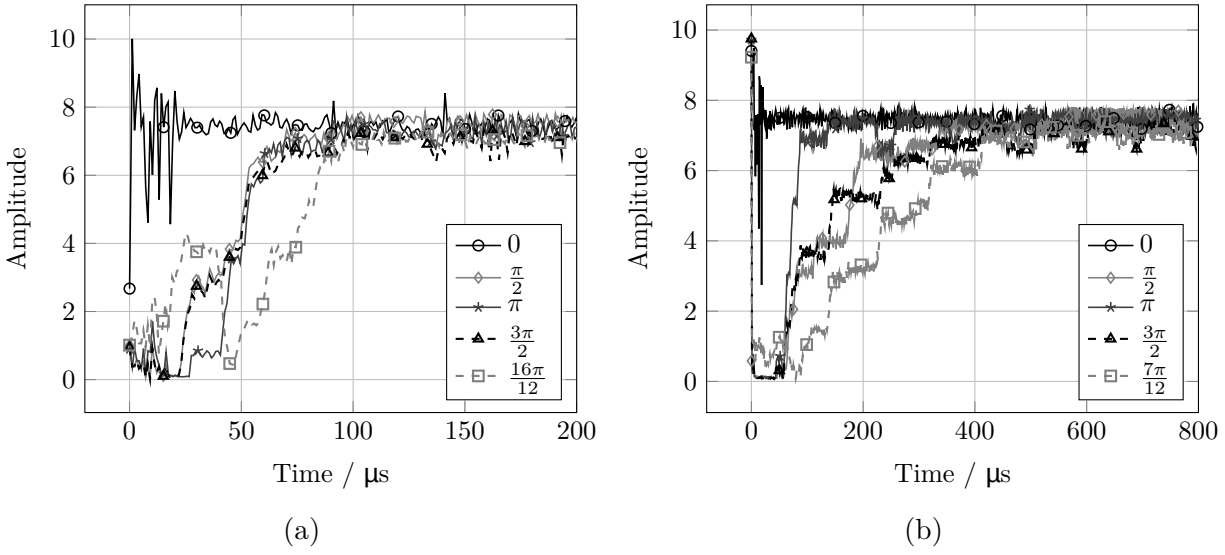

Fig. 4.7: IF sum signal envelope for ModelSim simulation runs with (a) initial and (b) optimized parameter set. It can be seen that the optimization does not improve the initial behavior.

Table 4.4: Measured IF sum signal envelope time constants

Simulation tool	Simulink		ModelSim	
Parameter set	Initial	Optimized	Initial	Optimized
Mean time constant / µs	37.25	45.67	54.19	178.53
Standard deviation / µs	13.12	15.85	15.44	82.52
Maximum time constant / µs	52.14	54.93	81.25	315.65
According phase difference / rad	$\frac{22}{12}\pi$	$\frac{22}{12}\pi$	$\frac{16}{12}\pi$	$\frac{7}{12}\pi$

previously discussed change in the location of the system poles and the additional negative effect of the filter coefficient quantization.

We also notice that for both parameter sets the attained amplitude level is lower than the theoretical maximum of 8. Moreover, the changes in the envelope levels happen in distinctive steps. This is caused by the time and level discretization of the PFD outputs inside the PLLs of our receivers. The steps in the envelope are caused by a change in the phase detection output signal of one or more channels which causes a jump in NCO frequency. Due to constant changes of the NCO frequencies between the channels, a perfect phase alignment of all eight IF output signals is not achieved. Therefore, we also do not obtain the optimum envelope amplitude of 8.

Table 4.4 lists the measured time constants obtained from all simulations above. For the Simulink runs, we see that the mean, standard deviation and maximum time constant are very close. However, we cannot observe an improvement of the optimized system over the initial one. On the contrary, we see a slight increase in the measured time constants. The reason for this is the significantly diminished distance of the remaining poles to the $j\omega$-axis already discussed in section 4.1.4.

The decrease in performance is even more pronounced in the case of the discrete time simulations. While the initial parameter set leads to time constants similar to the continuous time cases, the optimized parameter set yields significantly worse results. This illustrates the above mentioned influence of the discretization of the filter coefficients on the system pole locations.

We conclude that the optimization of the system phase transfer function with respect to the location of the pole closest to the $j\omega$-axis does not always lead to improved system behavior. If the remaining system poles are drawn closer to the $j\omega$-axis and are located in the vicinity of the optimized pole, the overall system phase response may become slower. Comparing to the optimization result obtained in section 3.3.5, we see that there was no similar influence on the leftmost poles. That means, there were no additional poles in the vicinity of the $j\omega$-axis after optimization. Thus the optimized system yielded better results than the initial one as can be seen in Fig. 3.12. In conclusion, we see that the result of the proposed optimization technique has to be carefully regarded. Since we cannot obtain the time constants directly from the system phase transfer function, an optimization criterion which takes all pole locations into account would be necessary. However, a detailed analysis on how to choose the cost function of such an optimization which minimized the time constants of a high order system is beyond the scope of this thesis. Finally, the IF signal envelope time constants from the two Simulink simulations in Table 4.4 are relatively

close although the filter time constants from both parameter sets differ considerably. This hints at a limited influence of the loop filters on the dynamic system behavior. As we have already seen in chapter 3, the behavior is rather dependent on the loop gains of the PLLs. Moreover, the system in ModelSim with the initial parameter set performs equally well as the respective Simulink model. We observe large deviations only when the pole locations of continuous time and digital design differ considerably. Therefore, we can see this as an indication of inferior performance.

4.2.2 Phase detection output

Besides the initial adaption of the IF sum signal envelope, we are interested in the achieved phase detection performance. In contrast to the dual channel receiver regarded in section 3.4, if we are simulating N channels we obtain $N-1$ phase difference estimates. In order to arrive at a single phase difference, we calculate the mean over all estimates by

$$\hat{\delta} = \frac{1}{N-1} \sum_{i=1}^{N-1} \Delta\delta_i, \tag{4.22}$$

where $\Delta\delta_i$ denotes the phase detection outputs from (3.25). This method is also applied for the discrete time implementation where the $\Delta\delta_i$ are the DCC outputs. The result $\hat{\delta}$ then is an integer number with word width w_{pd}.

From (3.25), we see that the calculation of the $\Delta\delta_i$ involves the modulo operation which has discontinuities. Calculating the mean of several $\Delta\delta_i$ which are close to such discontinuities may lead to an erroneous result. To avoid this, we use two methods to calculate the phase difference estimates, namely

$$\Delta\delta^{\mathrm{u}}(v_\Delta) = (2\pi M v_\Delta(\theta)) \bmod (2\pi), \tag{4.23a}$$
$$\Delta\delta^{\mathrm{s}}(v_\Delta) = (2\pi M v_\Delta(\theta) + \pi) \bmod (2\pi) - \pi, \tag{4.23b}$$

where the first is identical to (3.25) and gives us an unsigned phase value in the range of $[0, \ldots, 2\pi[$. The second yields a signed phase value within $[-\pi, \ldots, \pi[$. For the digital system with phase detection word width of w_{pd}, the different results of (4.23) are achieved by interpreting the DCC outputs either as unsigned or as signed integer numbers before calculating the mean by (4.22). For the following simulations, we will state the method used to obtain the phase detection results. For the realization in actual hardware in section 4.3, we will introduce other methods to decide if the mean of (4.23a) or (4.23b) is used.

The phase detection output signals of the ModelSim simulation with the optimized parameter set are depicted in Fig. 4.8. The plot shows the outputs of 24 simulation runs with $\delta \in [0, \frac{1}{12}\pi, \ldots, \frac{23}{12}\pi]$ whereby we always used (4.23a). We can observe the $t_{\mathrm{upd,pd}} = 40.96\,\mu\mathrm{s}$ update time of the DCCs from (4.20) in the spacing between jumps of the phase detection output curves. We see that the curves eventually approach the correct values in all cases. As listed in Table 4.1, the phase detection output word width is $w_{\mathrm{pd}} = 8\,\mathrm{bit}$. The output signal amplitude is therefore discretized in steps of $\pi/128$ which can be observed in the small fluctuations of the final values. The phase detection outputs of the Simulink simulations are not given as they are similar to those given in section 3.4. In Fig. 4.8, we show the results for the optimized parameter set. Thus we can prove that although the initial IF sum signal

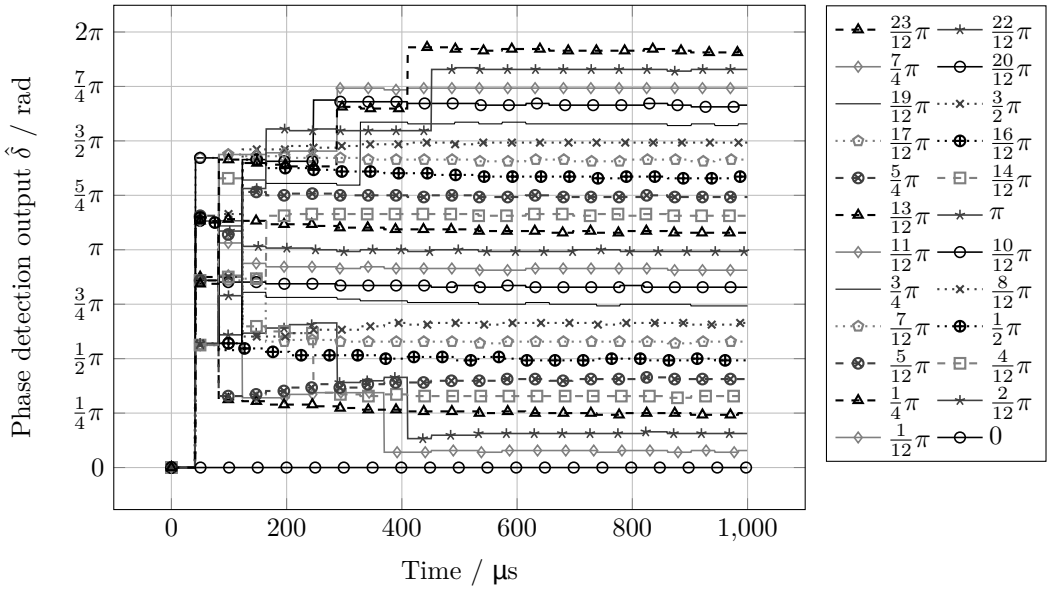

Fig. 4.8: Phase detection output of the discrete time system simulation in ModelSim over time using the optimized parameter set.

convergence is worse for this parameterization, the phase detection does still work. That means the actual filter coefficients do not influence the final phase detection result.

Fig. 4.9 shows the average phase detection errors of the Simulink and ModelSim simulation runs for the 24 input phase differences. We have thereby averaged the phase detection output $\hat{\delta}$ over the final 500 µs of the respective simulation, i.e.

$$\bar{\delta} = \frac{1}{T_2 - T_1} \int_{T_1}^{T_2} \hat{\delta} dt, \tag{4.24}$$

with $T_1 = 500\,\mu s$ and $T_2 = 1000\,\mu s$. For the Simulink case, we have used (4.23b) and it can be seen that for $\delta = \pi$ the plot shows no value. This is because the mean error is much higher than the graph scale in this case, but this is caused by the discontinuity of the modulo operation. We can see that the continuous time simulation yields much more accurate results: The errors for both the initial and the optimized parameter set are below $1.7\pi \cdot 10^{-4}$ rad or 0.03°. In the discrete time simulation, we attain larger errors which lie below $1.2\pi \cdot 10^{-2}$ rad or 2.16°. These differences are caused by the quantization and time discretization effects of the ModelSim simulation. As mentioned before, the phase is represented by 8 bit words and can only change at distinct points in time. Taking the mean of the output signal therefore does not reduce the error as effectively as in the continuous time case. Moreover, the PFD output pulse width is discretized by the sample time which lowers the accuracy even further.

As can be expected, the phase errors of the discrete time model are larger than those in the continuous time simulation. Nevertheless, we see that phase detection is also possible using the discrete time system. The achieved accuracy should be sufficient for the purposes of phase conjugation and DoA estimation. With these results, we can go one step further and implement the simulated discrete time receiver in actual digital hardware.

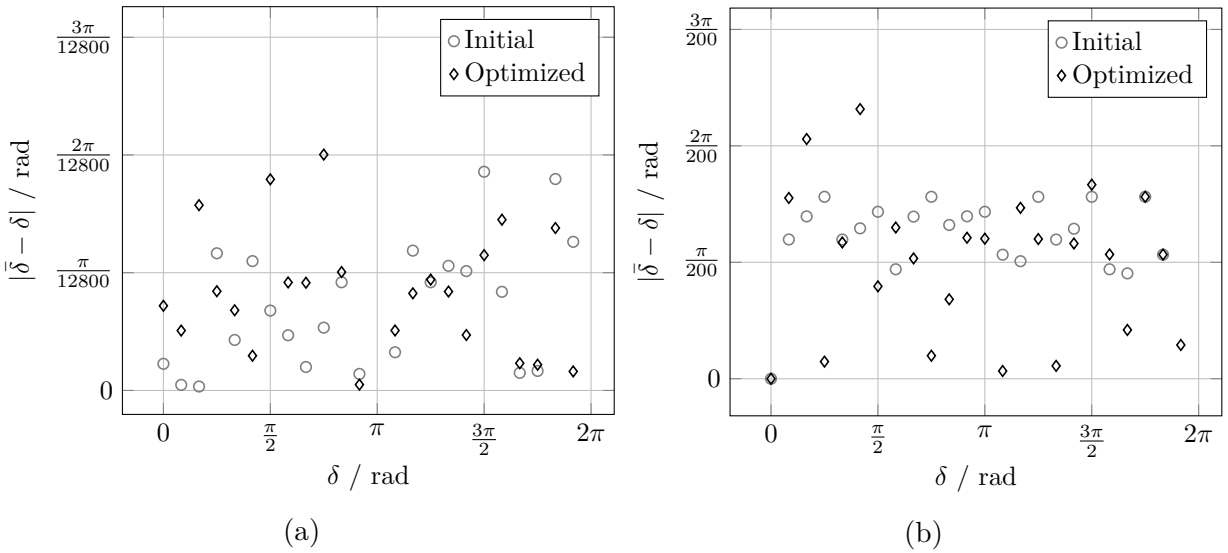

Fig. 4.9: Average final phase detection errors for (a) continuous time Simulink and (b) discrete time ModelSim simulations.

4.3 Transceiver hardware implementation

In the following, we show how the retro-directive transceiver can be realized in digital hardware. Regarding the system architecture in Fig. 3.1, we shall implement all blocks except the dual band antenna array on a FPGA. It should be noted that the digital implementation presented here is made to experimentally proof the system concept. Working with digital hardware allows us perfect similarity between channels and easier adjustment of system parameters. For the target application of satellite communications, the data carrying system blocks shall be realized with analog components as described in chapter 3.

4.3.1 Functional description

The complete digital implementation of the retro-directive transceiver with eight channels is depicted schematically in Fig. 4.10. It is written in VHDL. On the left hand side, we see the eight receiver inputs. The arriving RF signals are sampled by ADCs and fed to individual digital receiver channels which have been described previously in section 4.1. All channels share a common reference NCO. The IF outputs of the receiver channels are summed up and the result appears as IF sum signal at the DAC 9.

In the design, we see the two clock sources specified in Table 4.1: The main system clock f_{clk} drives most of the sub-systems while the faster $f_{\mathrm{clk,pd}}$ is used only for the receiver output NCOs and the subsequent PFDs and DCCs in order to increase phase detection accuracy as shown in (4.21). The DCCs are designed as presented in section 4.1.3.

The DCC output signals are processed in the block labeled Channel mean where (4.22) is calculated with both versions of (4.23). As mentioned above, we have to find means to decide whether we use the unsigned or the signed version of the mean phase difference estimation. This is done in the Time average & variance unit which is schematically depicted in Fig. 4.11. The block takes the phase difference estimations $x_{\mathrm{EST}}(n)$ as input. In the upper branch, we calculate the time average by storing the last 2^L input values in a first-in, first-out (FIFO)

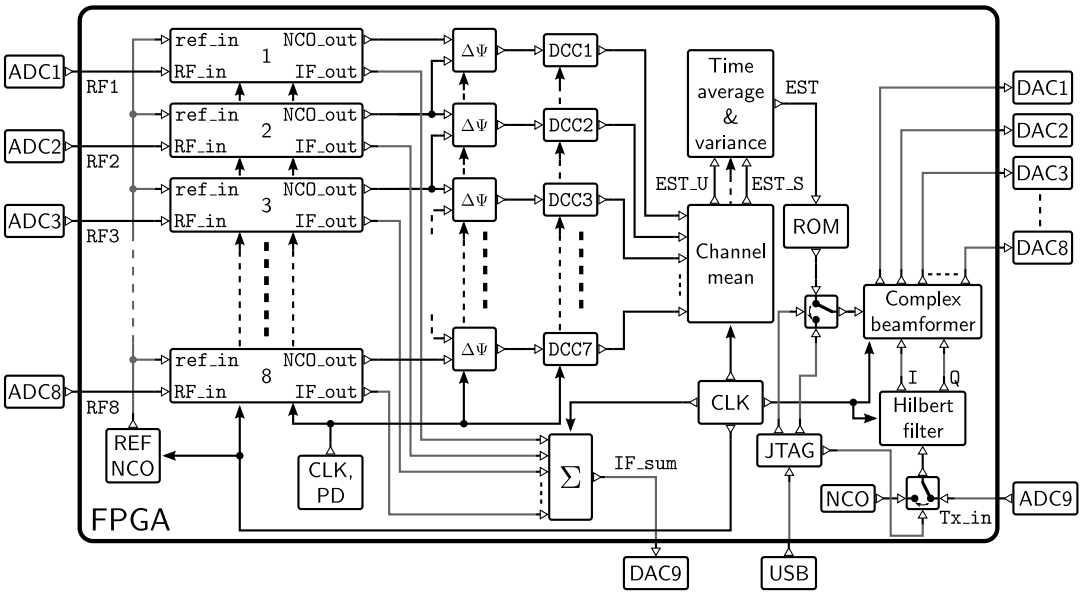

Fig. 4.10: Block diagram of the FPGA program of an eight channel transceiver configured for retro-directive operation with an external Tx input signal. RF signals with progressive phase shifts and common phase modulation are expected at the inputs of the eight identical receiver channels. The phase shift is detected and used for Tx beamforming. A down-converted and constructively superposed version of the RF signals appears at the IF sum output.

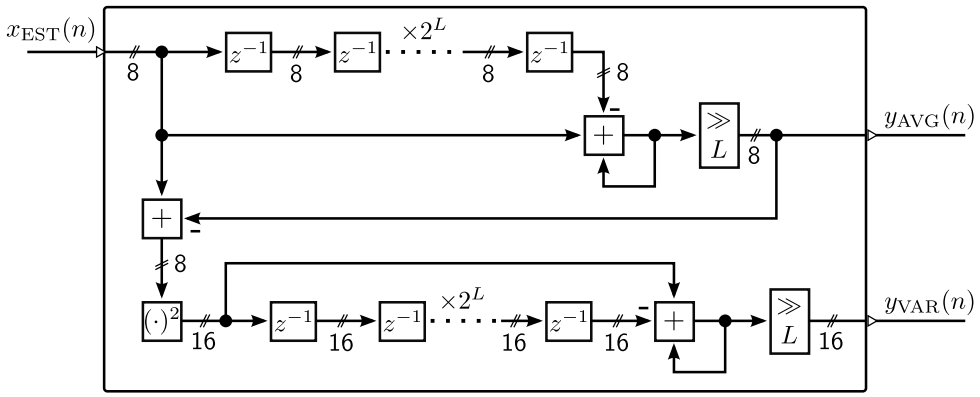

Fig. 4.11: Implementation of the time average and variance calculation for the phase difference estimates.

delay line. The moving average output is given by

$$y_{\mathrm{AVG}}(n) = \left\lfloor \frac{1}{2^L} \sum_{k=0}^{2^L-1} x(n-k) \right\rfloor . \tag{4.25}$$

The floor operation $\lfloor \cdot \rfloor$ is hereby achieved by the bit shifter. At the same time, we obtain the variance of the phase difference estimates in the lower branch of the structure in Fig. 4.11. By subtracting the current average value from the input estimate and squaring the result, we calculate the variance of the current phase estimate. We use the same FIFO delay line structure as above to calculate a moving variance of the phase estimates as

$$y_{\mathrm{VAR}}(n) = \left\lfloor \frac{1}{2^L} \sum_{k=0}^{2^L-1} \left(x_{\mathrm{EST}}(n-k) - y_{\mathrm{AVG}}(n-k)\right)^2 \right\rfloor . \tag{4.26}$$

It should be noted that this calculation works only if there are no short term variations in the input phase differences δ of the receiver. The average output y_{AVG} used for the calculation of the current y_{VAR} is always 2^L samples old. If the input phases are changing significantly within this time, the resulting variance output is not valid. Using (4.20) and the length of the FIFO we can compute the time for a complete cycle of the moving average filter by

$$t_{\mathrm{MA}} = 2^L \frac{2^{w_{\mathrm{cnt}}}}{f_{\mathrm{clk,pd}}}. \tag{4.27}$$

Using $L = 8$ and $w_{\mathrm{cnt}} = 13$, we obtain $t_{\mathrm{MA}} = 10.5\,\mathrm{ms}$. That means, the input phase differences should be steady for at least this amount of time in order to get a valid time average. For a valid variance output, the phase differences have to remain steady twice as long.

Calculation of time average and variance are done simultaneously for the unsigned and signed phase estimates. We then choose the estimate which has lower variance. If both estimates have the same variance value, we use the signed one. This is because we rather expect phase differences centered around $\delta = 0$ which corresponds to signals coming from boresight, i.e. $\theta = 90°$.

As can be seen in Fig. 4.10, the chosen phase estimate is used to select Tx beamforming coefficients which are stored in a read-only memory (ROM). The coefficients are chosen such that they perform phase conjugation and correct for array squint. The selected coefficients are then used as weights for a complex beamformer. We get the Tx input signal for the beamformer from the ADC 9 at the `Tx_in` port. We use a Hilbert filter to obtain a complex signal with which we can do beamforming. At the output of the beamformer, we get eight individually weighted versions of the Tx input signal. These are fed to DACs whose outputs can be used to feed an antenna array.

Alternatively, the FPGA program allows us to set the Tx beamforming coefficients externally. This is done via a universal serial bus (USB) connection which controls a standardized Joint Test Action Group (JTAG) interface on the FPGA. A multiplexer before the complex beamformer is used in Fig. 4.10 to switch the source of the beamforming weights. Additionally, we can choose if the Tx signal comes from an external source via the ADC 9 or from an internal NCO. We will use the external beamforming option in combination with the internal signal generator for the following hardware loop tests.

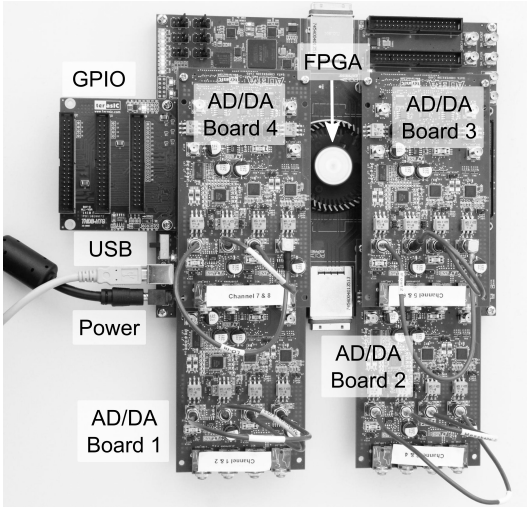

Fig. 4.12: Experimental setup for hardware loop validation consisting of an FPGA (located under the fan) and four extension cards each with two ADCs and two DACs. Input signals are generated internally and sent to the DACs. Via SubMiniature version A (SMA) cables, the signals are fed to the ADCs and used as inputs to the eight channel receiver. The USB connection serves to control and monitor the system and to extract phase detection results.

4.3.2 Hardware loop experiments

We use the transceiver design shown in Fig. 4.10 to validate our retro-directive system concept with digital hardware. The platform for this evaluation is the commercially available TR4 FPGA development board produced by terasIC [83]. It incorporates an Altera Stratix IV FPGA [84]. The evaluation board can be equipped with proprietary expansion cards, each providing two ADC and two DAC channels [85].

The FPGA board with four such expansion cards is shown in Fig. 4.12. The FPGA is located under the fan. Besides the AD/DA cards, we have connected a general-purpose input/output (GPIO) card which allows us to control external components. We will use this functionality for the measurements in chapter 5. The FPGA board also has a USB connection to a host PC which lets us to program the FPGA. Additionally, we can record signal snippets from the digital design during runtime using the JTAG interface. We use this functionality in the following experiments to obtain phase detection results.

In Fig. 4.12, the FPGA board is shown in a loop configuration. That means each DAC output is connected to an ADC input by a short SMA cable. We will use this loop setup to test our receiver with defined input signals. To create these signals, we control the beamformer and the internal NCO for Tx signal generation in Fig. 4.10 directly using the USB connection.

Steady state phase detection performance

In this experiment, we let the DACs generate eight input signals of frequency f_{RF} with progressive phase shifts. This corresponds to the signals we expect if the ULA receives a signal from a given direction θ. We then observe the phase estimates at the output of the

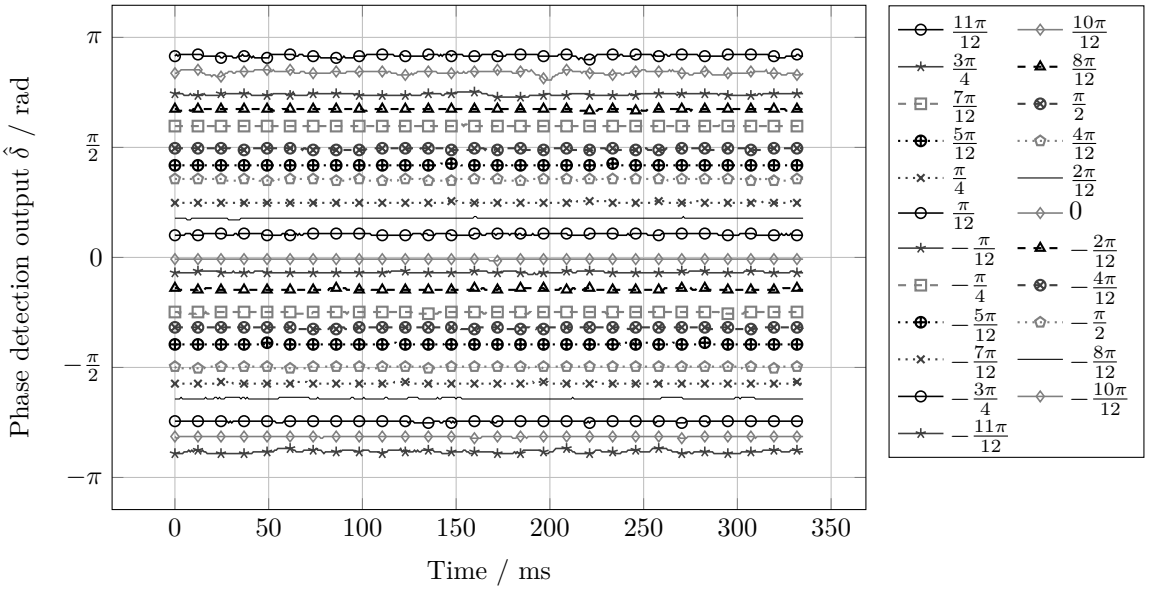

Fig. 4.13: Steady state phase detection output signals over time for stable progressive input phase differences measured during hardware loop tests.

time average & variance block in Fig. 4.10 and evaluate the phase estimation error. Via the JTAG interface, we record one data point each time the DCC outputs are updated, i.e. every 40.96 µs as shown in (4.20). The FPGA stores 8192 data points such that we can analyze the phase estimation outputs over 335.5 ms. We expect a result similar to that of the ModelSim simulation shown in Fig. 4.8. However, on the FPGA we cannot capture the initial behavior but can analyze the steady state values only.

Fig. 4.13 shows the phase detection estimate for different progressive phase shifts δ in steps of $\frac{1}{12}\pi$. Hereby, we have drawn the curves of several subsequent measurements in one plot. It can be seen that the phase detection outputs are relatively stable over time. We observe some small fluctuations e.g. in the $10/12\pi$ and $-11/12\pi$ curves. Also the spacing of the curves is not perfectly equal as we would expect for the given setup.

To arrive at a concise figure of merit for the phase detection capability, we calculate the mean of the detected phase values over time. The result is shown in Fig. 4.14a while Fig. 4.14b depicts the mean error and the standard deviation of the phase detection output over time for all simulation runs. We can see that the obtained mean errors are below $0.0272 \cdot \pi$ rad or 4.9°. The standard deviations are smaller than $0.0082 \cdot \pi$ rad or 1.5°. Compared to the results of the ModelSim simulation in section 4.2, we see that the maximum phase error is more than twice as high. Reasons for this increase are differences in the analog signal paths consisting of DACs, cables and ADCs. Moreover, in contrast to the simulations, there is noise in the received signals. Nevertheless, the results show that the proposed digital implementation of our retro-directive receiver is able to perform phase detection with physical input signals. The performance is better than those reported in [30] and [46] where phase conjugation errors up to 15° occurred for systems with six channels. The errors shown here form a base line for the phase detection and DoA estimation performance of our receiver when it is used in combination with RF hardware and an actual antenna.

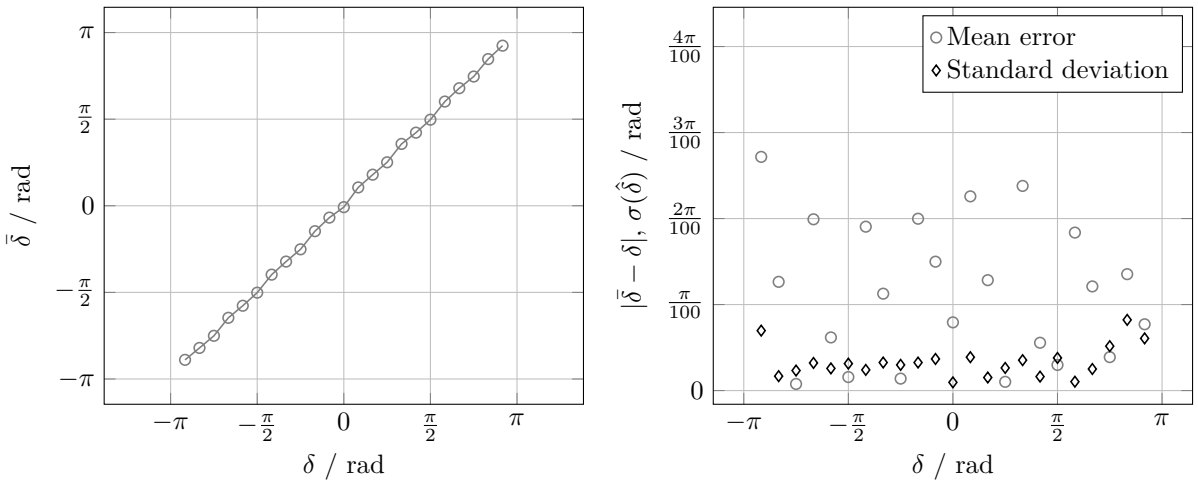

(a) (b)

Fig. 4.14: Result of the static phase detection experiment. (a) Average of the estimated phases over time and (b) absolute error of the average values and standard deviation of the detected phases over time.

Detection performance for time-varying phase differences

In order to show the ability to track a moving signal source, we use the same hardware loop setup shown in Fig. 4.12. In this experiment however, we vary the input signal phases over time. We thereby cover the range of $\delta \in [-\pi, \ldots, \pi[\,\text{rad}$. During the experiment, we change the progressive phase difference between the input signals by an amount of $\pi/90\,\text{rad/s}$. Thus we sweep over the whole range of δ within 180 s. Before and after the phase sweep, the phase difference is set to 0.

The progressive phase difference of the input signal over time is plotted in Fig. 4.15a along with the phase detection result $\hat{\delta}$ of our receiver. We see that the estimate is accurate except for the phase jumps and differences close to $\pm\pi\,\text{rad}$. However, as we have discussed previously, such phase differences are not likely to occur in the target application because they represent incident angles far from boresight. Fig. 4.15b shows the absolute phase detection error whereby we have plotted only the lower error range. During the phase jumps, errors go up to $\pi\,\text{rad}$. However, within the region of linear phase changes, we see that the error stays below $\pi/32\,\text{rad}$ most of the time.

Fig. 4.15c and Fig. 4.15d are plots from the same data base but show how the phase differences from the experiment translate into DoA. For this we use (3.27) and assume an array with relative spacing of $d_r = 0.5$. In Fig. 4.15c we can see the arcsine shape of the estimated DoA. As can be expected from the phase detection results, the DoA estimate has only small errors during most of the experiment. The pointing error in Fig. 4.15d shows that we obtain an accuracy better than 3.0° over the largest part of the phase difference range. We can conclude that the digitally implemented receiver is able to track a moving signal source in a FoV of ±60° around boresight.

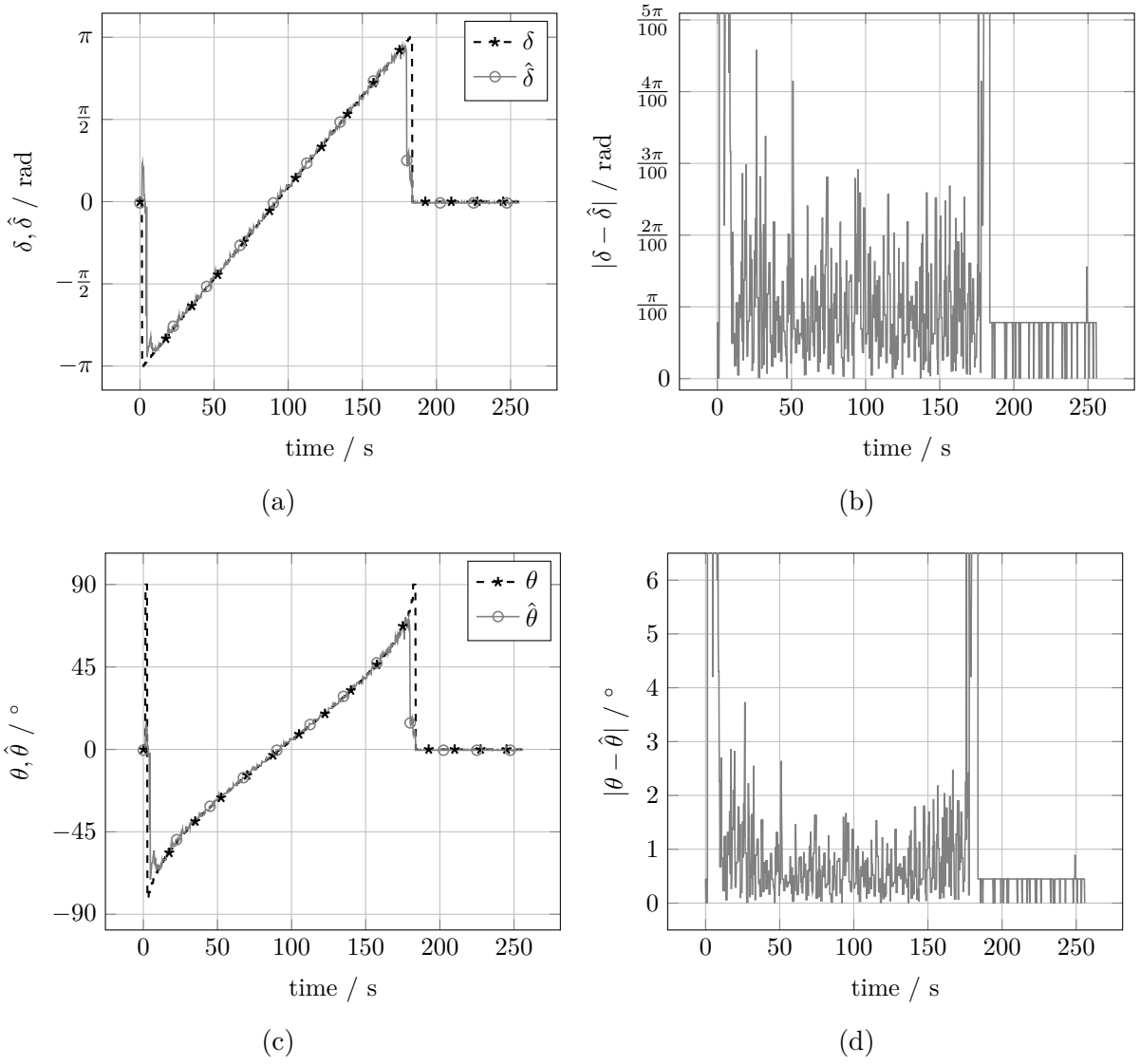

Fig. 4.15: Result of the loop test with varying progressive input phase difference δ. (a) shows the true and estimated signal phases over time, (b) the absolute phase estimation error. (c) plots the corresponding true and estimated DoA with $d_r = 0.5$ array element spacing. (d) shows the DoA estimation error.

4.4 Summary

In this chapter, we have transferred the analog continuous time receiver introduced in chapter 3 to the discrete time domain. For that, we have defined suitable representations for the previously used analog components. Additionally, we have demonstrated how the phase detection output signals can be processed in a digital system using DCCs for time averaging instead of lowpass filters. After that, we have compared the analog system design with the respective discrete time representation in terms of pole locations and phase transfer functions. We have been able to show, that the discrete time system is in good agreement with its continuous time counterpart. However, we have also observed a distinct influence of quantization on the location of the system poles.

In time domain simulations using Simulink and ModelSim, we have analyzed the dynamic behavior of both analog and digital receiver designs. We have thereby used the time constants of the IF output envelope signals to characterize the initial behavior. We have seen that the optimization technique used in chapter 3 did not improve system behavior. This is explained by the influence of the algorithm on the system poles which are not targeted by the optimization. The phase detection accuracy of the digital system has been determined to be better than 2.16° in the steady state.

In the last part of this chapter, we have presented the digital implementation of the complete retro-directive transceiver. It comprises down-mix, phase detection and IF processing on the Rx side as well as squint correction and respective beamforming on the Tx side. We have validated the design by hardware loop experiments on an actual FPGA board where the Rx input signals have been generated by the Tx outputs of the design. We have thereby demonstrated a phase detection accuracy of 4.9°. Using a dynamic scenario, we have additionally shown the expected DoA accuracy of the system to be better than 3.0° over a FoV of ±60°.

5 Experimental validation

In the previous chapter, we have demonstrated the capability of our digitally implemented transceiver to perform phase detection and DoA estimation. However, the utilized hardware loop setup does not allow us to demonstrate retro-directive behavior since we use the Tx path of our system to generate the Rx input signals. In this chapter, we shall deliver the experimental proof of our transceiver architecture using antenna measurement techniques. For this, we need to interface the digital hardware presented in chapter 4 with an antenna array using suitable analog front-ends. Additionally, we have to create a measurement setup which allows us to assess the performance of an active antenna system.

Our demonstration targets satellite communication in the C-band. Therefore the RDA system shall receive signals at 5.8 GHz and transmit at 7.0 GHz. We will present the additional hardware for the experiments and show how it is installed in an anechoic antenna measurement chamber, a so called CTR. After that, we will introduce the measurement methods to characterize a RDA system. We will then present results for DoA estimation with the receiver path and retro-directive operation using the whole transceiver. We also draw a comparison to results from systems in the open literature. Finally, we recap the system requirements set in chapter 3 and discuss in how far they are fulfilled by the presented demonstrator system.

5.1 Demonstrator measurement setup

In this section, we introduce the necessary setup to measure the transceiver as a RDA system in a CTR facility. Besides the additional system hardware components, i.e. front-ends and antenna array, this also comprises LO generation and distribution, power supply as well as the measurement devices. We give a comprehensive overview over all system parts, their interaction and the applied measurement techniques in the following.

5.1.1 Analog signal processing

Since our digital hardware works with low frequencies as detailed in Table 4.1, we need to interface it to C-band signals. This is done by analog RF signal processing and comprises the front-ends for Rx and Tx which are the interfaces to our ADCs and DACs, respectively. The front-ends are connected to a dual-band antenna array which represents the interface to free space. These individual demonstrator parts are described in detail in appendix C. We will mention only the most important properties here.

The dual-band antenna has been developed by Deutsches Zentrum für Luft- und Raumfahrt e.V. (DLR) for the required center frequencies of 5.8 and 7.0 GHz. It is a ULA of eight antenna elements. Each element consists of a rectangular patch. The dual-band capability is achieved by tuning the lengths of the rectangle sides and by the placement of the feed points.

The antenna is linearly polarized and the two frequency bands have orthogonal polarization. The relative spacing of the antenna elements in the ULA is $d_{r,\mathrm{Tx}} = 0.5$ for 7.0 GHz. This corresponds to $d_{r,\mathrm{Rx}} = 0.414$ for 5.8 GHz. More details can be found in appendix C.1.

The utilized Tx front-ends have been developed at DLR by students from our partners at Universidade Federal do Pampa (UNIPAMPA). The design concept and measurement data can be found in appendix C.2. Each front-end consists of two PCBs: First, a beamforming unit which mixes its input signal up to an IF of 1.9 GHz and features a digitally controlled phase shifter and a VGA. Second, an upconverter unit which mixes the IF signal to the desired Tx frequency of 7.0 GHz. The beamforming capability is used to calibrate the eight Tx paths. That means, we adjust the phases and gains such that they exhibit equal amplitude and phase at all antenna input ports. Details on the calibration of the Tx paths are given in appendix C.5.

The development of the Rx front-ends was done within the scope of this thesis. Details can be found in appendix C.3. The front-ends perform a down-conversion of the received signals at 5.8 GHz to an IF of 113 MHz. A LO signal of 5.687 GHz is thereby used. The front-ends have an adjustable gain between 30.0 and 60.0 dB. The gain setting is chosen such that the subsequent ADCs are not clipping the signal. The ADCs are clocked with 100 MHz and thus perform bandpass sampling which results in 13 MHz input signals for the digital hardware which corresponds to the values listed in Table 4.1.

5.1.2 Compact test range setup

The block diagram of the complete measurement setup for the CTR is depicted in Fig. 5.1. The system is distributed between three locations which can also be seen in the photograph of the measurement chamber in Fig. 5.3: First, some devices are located in the control room of the measurement facility. This comprises the VNA, measurement antenna, and host PC. Second, we place heavy devices like signal generators on the base of the antenna positioner. Third, we have equipment on the positioner head of the facility where the antenna-under-test (AUT) is placed for measurement. We shall describe the respective system parts in the following.

Control room

The central part of the measurement setup is the VNA. It is connected to one port of a dual-feed antenna to receive the 7.0 GHz Tx signal from our retro-directive demonstrator. A corresponding output signal from the VNA is sent to the positioner base over an installed RF cable. This signal is used as input for the AUT.

The second port of the dual-feed antenna is connected to a signal generator running at 5.8 GHz. Thus we generate an incident Rx signal for our AUT. By using a dual-feed antenna, we make sure that the Rx signal comes from the same direction where the measurement antenna is placed.

Finally, we set up the host PC for our digital hardware in the control room. Using a USB over ethernet adapter, we connect it to the FPGA board on the antenna positioner. Thus, we can control system parameters and take signal snapshots from the FPGA without entering the measurement chamber.

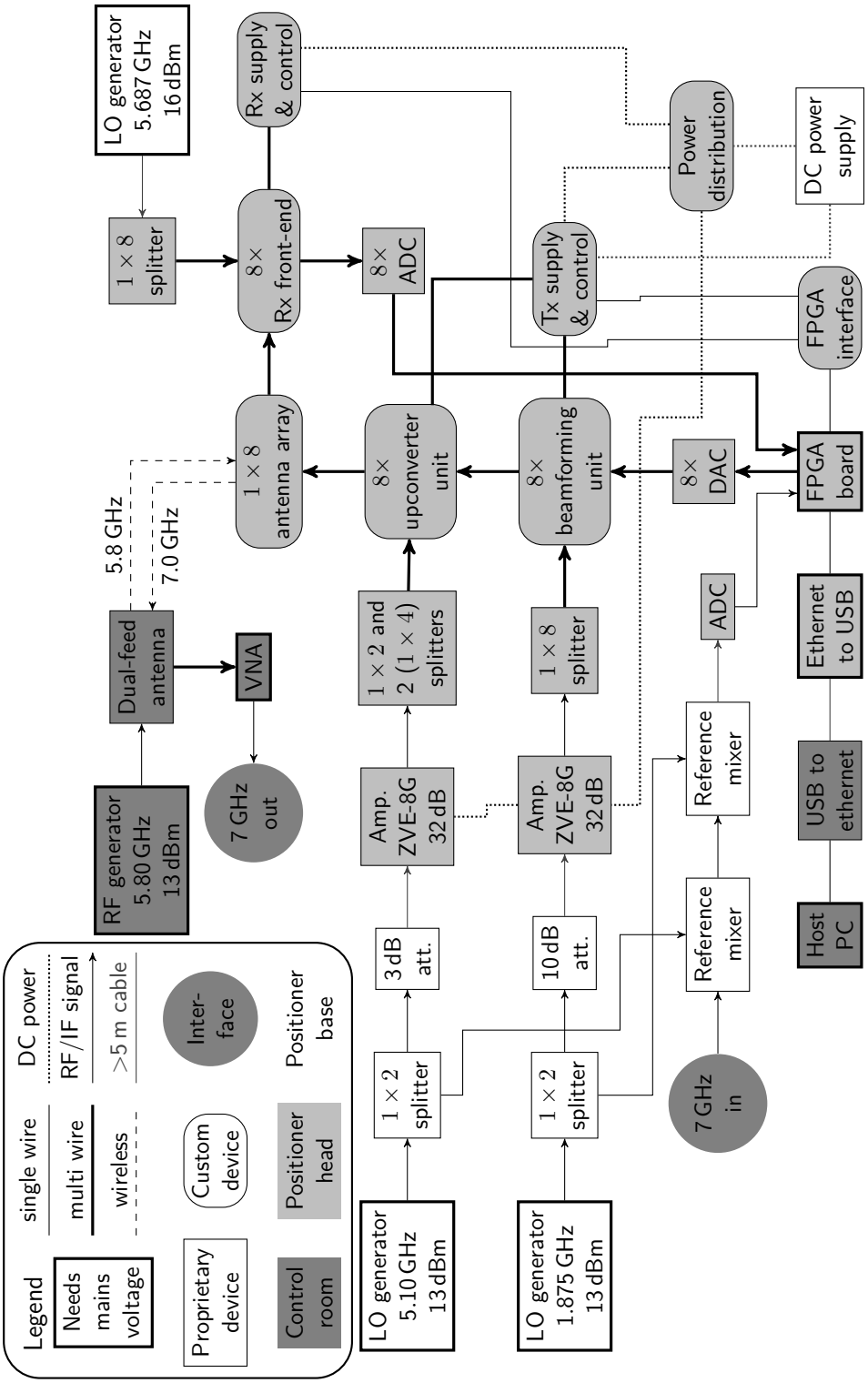

Fig. 5.1: Block diagram of the measurement setup in the CTR.

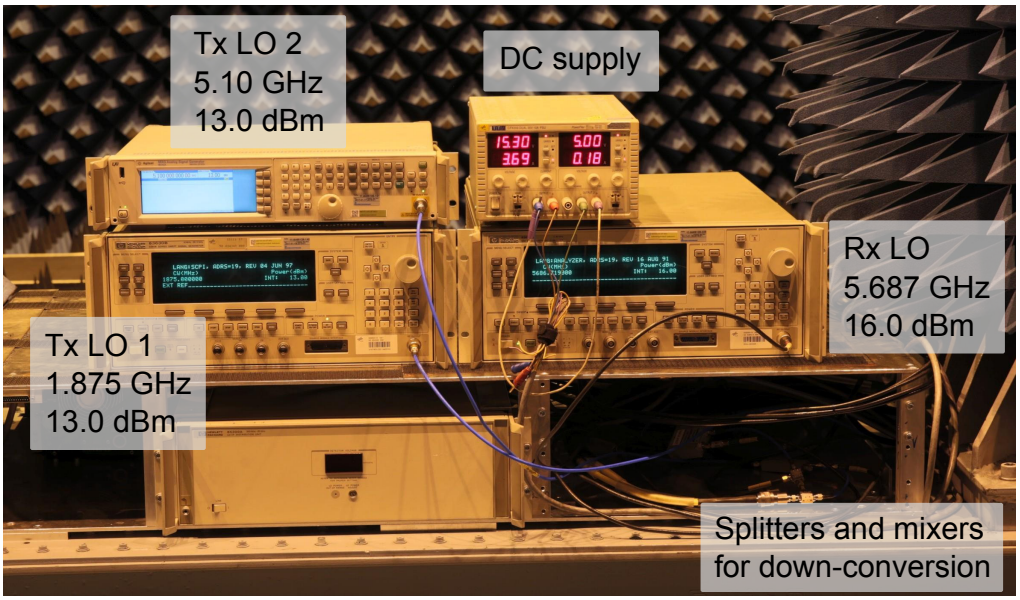

Fig. 5.2: Devices on the base of the antenna positioner: Direct current (DC) power supply and three LO signal generators. The splitters and mixers for the down-conversion of the vector network analyzer (VNA) signal were placed in the empty rack on the right.

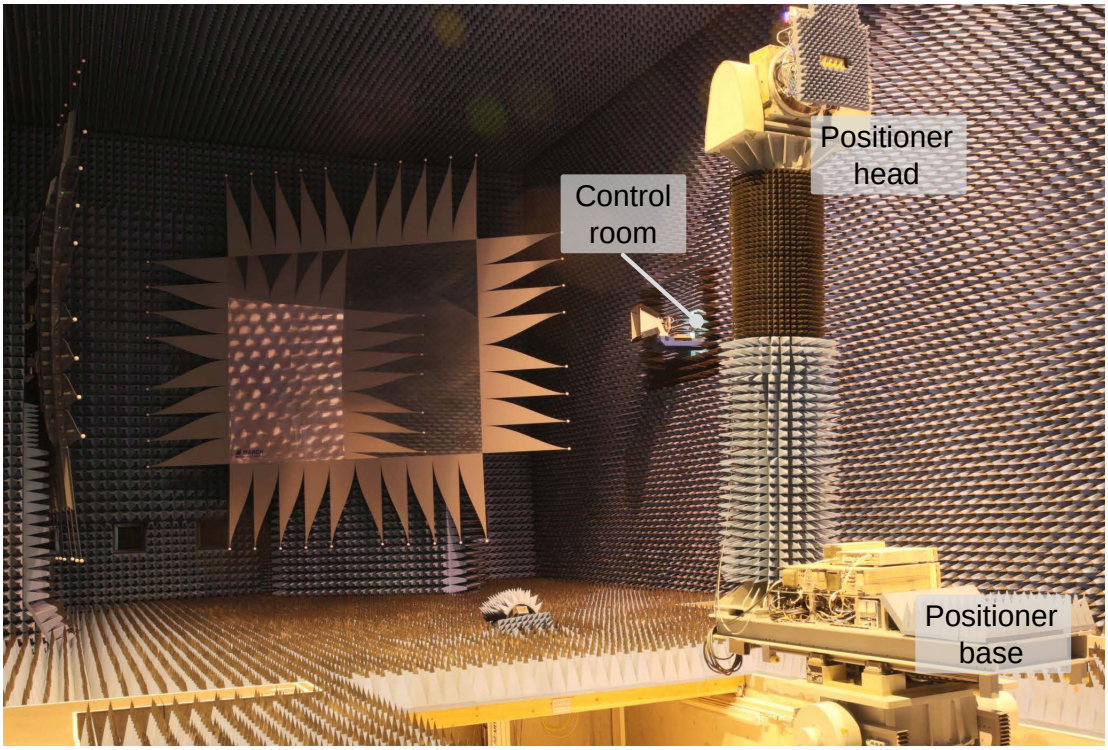

Fig. 5.3: Demonstrator measurement setup in the CTR. The main system parts are mounted on the positioner head and covered with RF absorbers. Heavy devices are placed at the positioner base. The whole system can be steered from the control room.

Positioner base

As can be seen in Fig. 5.1, we have a DC power supply and three generators for the necessary LO signals on the base of the positioner. The arrangement of these devices can be seen in Fig. 5.2. Additionally, we use the two Tx LO signals to mix down the 7.0 GHz output signal from the VNA to 25 MHz. Two commercial 1-by-2 splitters and reference mixers are employed for this. We use the resulting low frequency signal as Tx input to our digital hardware, as shown in Fig. 4.10. Thus, we obtain phase-lock between the VNA output and the 7.0 GHz signals transmitted by our AUT. Phase-lock between the sent and received signals of the VNA is a prerequisite for valid antenna measurements.

From the positioner base, we need the following connections to the RDA on the positioner head:

1) 230 V mains voltage,

2) DC voltages for 15 V and −5 V,

3) Three SMA cables for the LO signals,

4) An additional SMA cable for the 25 MHz Tx signal,

5) An Ethernet cable to establish the USB connection between host PC and FPGA board.

The respective connections for signals and DC power are marked in Fig. 5.1 as >5 m cables. The two LO signals for the Tx path are attenuated. This is necessary in order to avoid driving the subsequent amplifiers into saturation which in turn would create unwanted harmonics at the front-end LO inputs.

Positioner head

Fig. 5.4 shows a photograph of the demonstrator hardware rigged on the positioner head in the measurement chamber. The individual components can be identified in the block diagram from Fig. 5.1 and are described in the following.

Receiver path: The dual-band antenna array we use in the setup is a 1×8 ULA. It receives signals at 5.8 GHz which are mixed down by the Rx front-ends. As described above, the 5.687 GHz LO signal comes from the positioner base. To achieve coherent down-mix, we distribute the signal via an 1-to-8 splitter to all front-ends. The 113 MHz IF signals are sampled by the eight ADCs of our digital hardware platform. On the FPGA, we use the signal processing described in section 4.3 and depicted in Fig. 4.10.

Each Rx front-end is attached to the supply and control PCB via a ribbon cable. Over this connection we obtain the necessary DC voltages of 3.3 V and 5.0 V which are generated on the power distribution PCB. Additionally, the Rx supply & control board connects the VGAs of the front-ends to the FPGA. We adjust the VGA settings using a serial peripheral interface (SPI) bus driven by the FPGA and steered by the host PC. For better visibility, the Rx front-ends with the LO distribution and control PCB are depicted on their own in Fig. 5.5. We can see the individual ribbon cable connection for each front-end and the SMA cables carrying the LO signals from the 1-to-8 splitter.

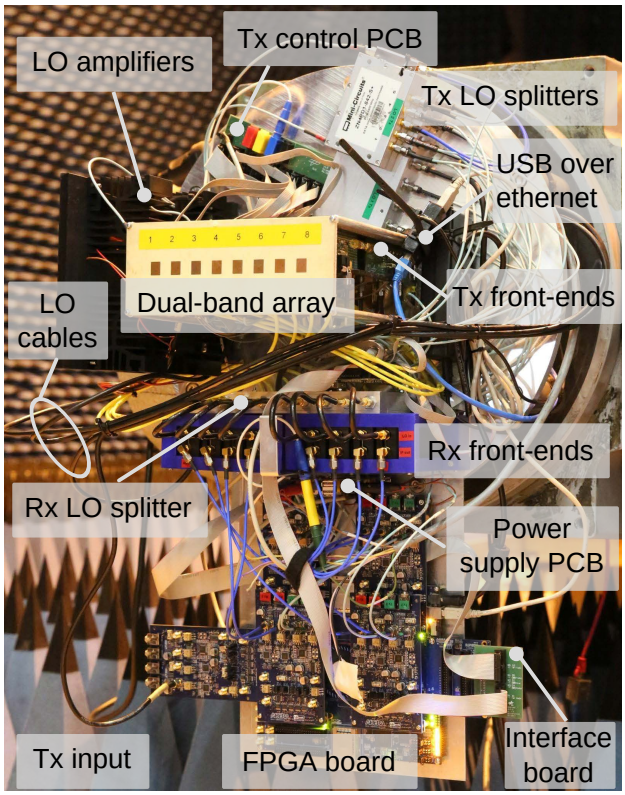

Fig. 5.4: Demonstrator mounted on the positioner in the anechoic measurement chamber at DLR.

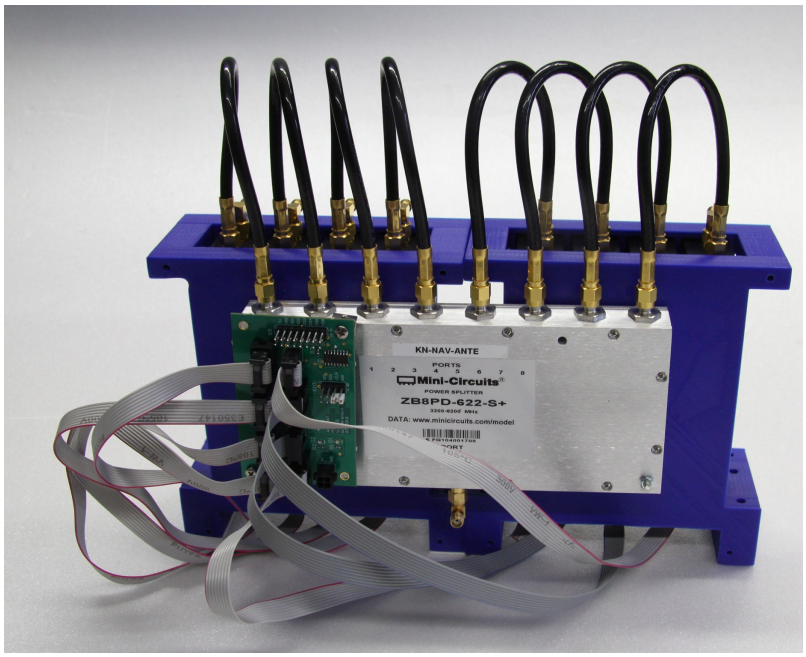

Fig. 5.5: Eight Rx front-ends in individual 3D printed cases (black) put into a common holder (blue). The setup includes the 1-to-8 splitter used for LO signal distribution and the Rx supply & control PCB with individual ribbon cable connection to each front-end.

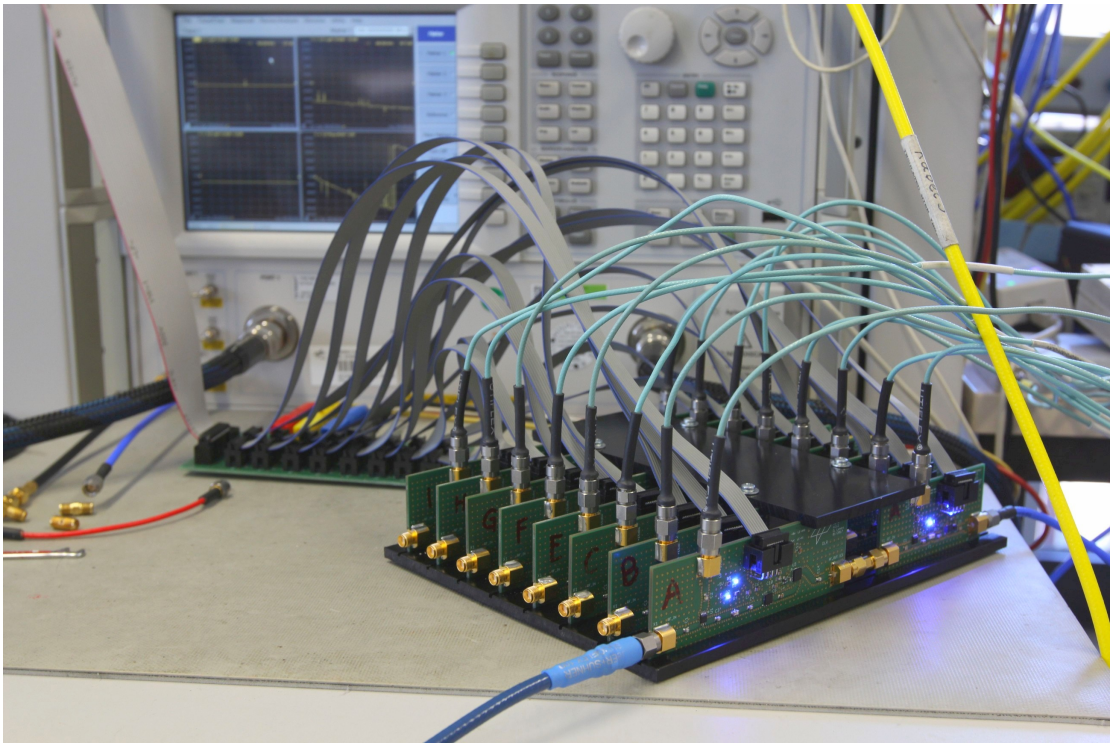

Fig. 5.6: Eight Tx front-ends in common mount during a VNA measurement. The supply & control PCB with the individual ribbon cable connections can be seen in the background. The LO signals are fed to the front-ends through SMA cables from the right.

Digital hardware: As can be seen in Fig. 5.4, we use the FPGA development board depicted in Fig. 4.12. Instead of the loop configuration, the IF outputs of the Rx front-ends are connected to the ADCs. The DACs are feeding the Tx front-end inputs. We have connected the GPIOs of the boards to an interface PCB which distributes command signals from the FPGA to the respective supply & control PCBs for Rx and Tx front-ends. Additionally, the FPGA board features an additional ADC which we use as input for the 25 MHz Tx signal.

Transmitter path: The eight Tx front-ends get their input signals from the DACs of our FPGA platform. The front-end RF outputs are screwed on to the antenna array with direct SMA connectors. The two necessary LO signals are distributed over 1-to-8 splitters such that they arrive with equal phase at each front-end. We use two commercially available amplifiers prior to the splitters to enhance the power of the LO signals. This is done to ensure correct mixer operation which requires a certain LO signal power level. Similar to the Rx front-ends, we have a supply & control PCB for distribution of DC power and steering signals for the phase shifters and VGAs. Fig. 5.6 shows the Tx front-ends without the antenna array. The IF inputs are facing to the front in this picture. In the background, we see the supply PCB with ribbon cable connections to each front-end module. Similarly, we have the LO cables from two RF splitters for 1.9 and 5.1 GHz.

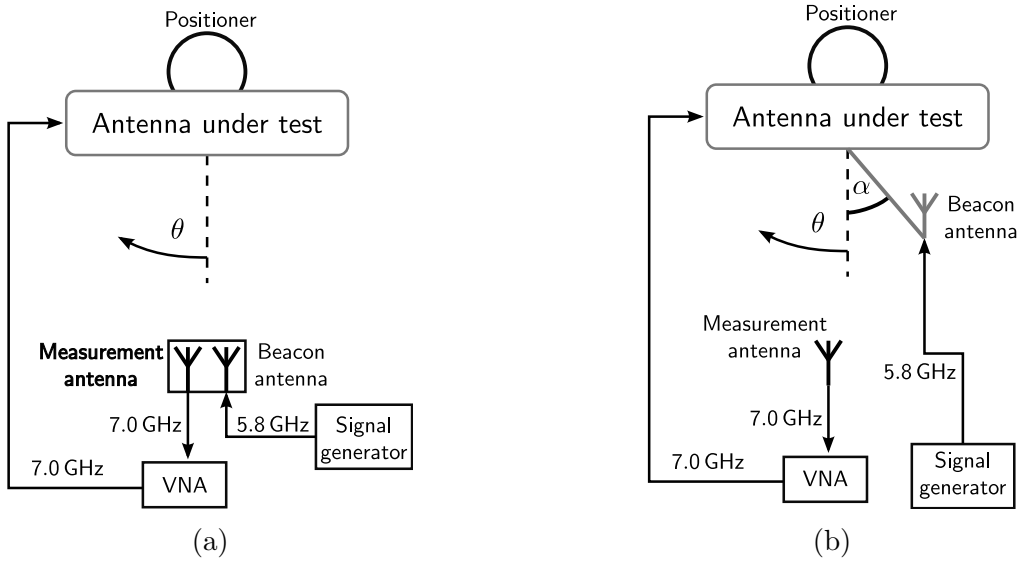

Fig. 5.7: Measurement setups for RDA systems: (a) monostatic setup with beacon and measurement antennas in the same direction, (b) classic bistatic setup with beacon antenna at a fixed angle with respect to the AUT.

5.1.3 Monostatic and bistatic measurements

Mono- and bistatic measurements have been used to characterize the performance of a RDA system and are defined in [86]. We can see the respective measurement setups in Fig. 5.7. In both cases, the AUT is mounted on the positioner and can be rotated by the angle θ with respect to the measurement antenna. Via a RF cable, a VNA excites the AUT with the desired Tx frequency, in our case 7.0 GHz. A receive antenna is connected to another port of the VNA. It picks up the EM waves transmitted from the AUT and allows us to record the antenna pattern, i.e. transmitted power over positioner angle.

The monostatic setup is similar to that of a RCS measurement for RADAR. It characterizes the ability of the RDA to return power into the direction of an incident wave. For this, we transmit power to the AUT with a beacon antenna at a frequency of 5.8 GHz. Simultaneously, we receive power from the AUT with a measurement antenna at 7.0 GHz. Both antennas are hereby very close such that they excite and receive from the same direction. In our case, we use a dual-feed antenna to achieve this. The monostatic characteristic is obtained by rotating the AUT on the positioner and measuring the radiated 7.0 GHz power as shown in Fig. 5.7a. A perfect RDA would have a uniform monostatic characteristic, i.e. it returns the same amount of power towards any incident direction. However as detailed in appendix B.3, real RDAs have a monostatic characteristic which resembles the single antenna element patterns of the array.

In bistatic measurements, we want to see the antenna pattern of our AUT when it is illuminated from a fixed direction. As we can see in Fig. 5.7b, the beacon antenna is now held at a fixed angle with respect to the AUT. The positioner with the AUT and the beacon antenna is then rotated and the power picked up by the measurement antenna is plotted over the rotation angle. A classic bistatic measurement setup requires a fixture for the beacon antenna which is mounted on the positioner. Since in our RDA system, Rx and Tx paths

are separated, we can circumvent such a complicated addition to our setup by using the following procedure:

1) Turn the positioner to the desired signal incident angle α with respect to the beacon antenna,
2) Let the receiver perform an estimation of the Rx phase differences,
3) Freeze the resulting Tx beamforming coefficients,
4) Optionally, switch off the beacon signal,
5) Perform a normal antenna measurement at 7.0 GHz,
6) Repeat the procedure for a different incident angle.

The result of the bistatic measurement is a true antenna pattern. Since the excitation of the array is not changing during the measurement, we obtain the radiated power over angle. The pattern can be integrated to obtain the total radiated power of the array. In contrast, the monostatic characteristic is not an antenna radiation pattern because the excitation of the array changes during the measurement. In other words, for each measurement point of the monostatic characteristic there is a matching bistatic pattern. That means the monostatic curve is composed of single points taken from bistatic patterns.

5.2 Receiver performance

The Rx path of our RDA system with its phase detection and DoA estimation capability is the key innovation of this work. Therefore, we want to see how it performs in combination with actual RF signals. For this, we use the positioner of the measurement chamber to illuminate our AUT with the beacon antenna from known incident angles. On the RDA system, we perform phase detection. The phase detection result is recorded as in the previous experiment in section 4.3.2 and the DoA estimate is calculated offline.

The results are shown in Fig. 5.8. On the left hand side, we see the estimated DoA $\hat{\theta}$ over the true DoA θ. The curve shows the expected linear trend. We can see some deviation at the beginning and end of the curve, i.e. for angles close to the endfire direction. This can also be observed in the plot of the absolute error in Fig. 5.8b: The DoA error is below 2.0° for incident angles $\theta \in [30°, \ldots, 165°]$. For a ULA of eight elements, this accuracy is sufficient since the main lobes of the Tx beams are considerably broader than 2.0° as can be seen in appendix C.6. This experiment confirms the DoA performance predicted in the hardware loop tests in section 4.3.2. The larger DoA errors towards the edges of the incident angle range are increased by the lower gain of the antenna elements in these directions which can also be seen in appendix C.1. Additionally, the array is embedded in an absorber plate which further inhibits reception from these directions.

5.3 Retro-directive system performance

As described in section 5.1.3, the main figures of merit for a RDA system are the monostatic and bistatic measurement results.

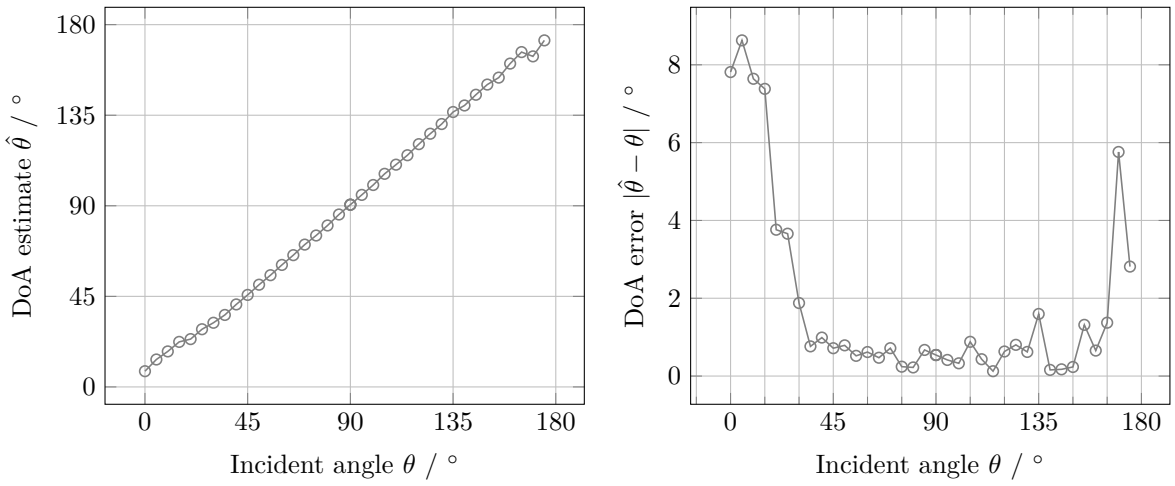

Fig. 5.8: DoA estimation performance of the demonstrator system. (a) DoA estimates in steps of 5° over true incident angle. (b) absolute DoA estimation error.

5.3.1 Monostatic characteristic

The monostatic characteristic of the demonstrator system in the DoA range of $\theta \in [30°, \ldots, 150°]$ is shown in Fig. 5.9. As customary for RDA systems, the curve is normalized to the boresight value. We can see that the monostatic curve is relatively flat around boresight. We achieve gain variations of less than 3 dB over a FoV of 83°, i.e. from 40° to 123°. This is sufficient for the targeted satellite communication applications. We note fluctuations in the gain curve right of boresight direction as well as around 60° and 115°. These are caused by the phase estimation process of the system which continuously runs. Since this means that the Tx beamforming coefficients change during the measurement, it affects the measured gain and thus can be seen in the monostatic curve.

Monostatic patterns are a generally used figure of merit for RDAs. Results from the open literature differ widely in terms of array size, frequencies and phase conjugation methods. Nevertheless, we can still compare the monostatic characteristics since they are independent of the number of elements and spacing as we show in appendix B.3. During monostatic measurements, our system exhibits a coverage of 83° with variations up to 3 dB and a 113° coverage with variations up to 5 dB. For better readability, we shall describe this as a FoV of 83° (3 dB) and 113° (5 dB), respectively. This is slightly better than the result in [52] with 110° (5 dB) for a two element array. [48] shows a monostatic characteristic over 110° (3 dB) using patch antennas at 2.4 GHz. In [87], monostatic curves with approximately 80° (5 dB) are shown with 5.8 GHz patch antenna elements. Using two separate arrays, [44] demonstrates a FoV of 95° (5 dB) with patch antennas for 2.44 and 6.0 GHz. Finally, in [49] a 3×3 patch antenna array is shown which exhibits a 80° (2 dB) FoV and approximately 100° (5 dB). From these results, we see that our RDA demonstrator performs as well as comparable systems with patch antennas found in the open literature.

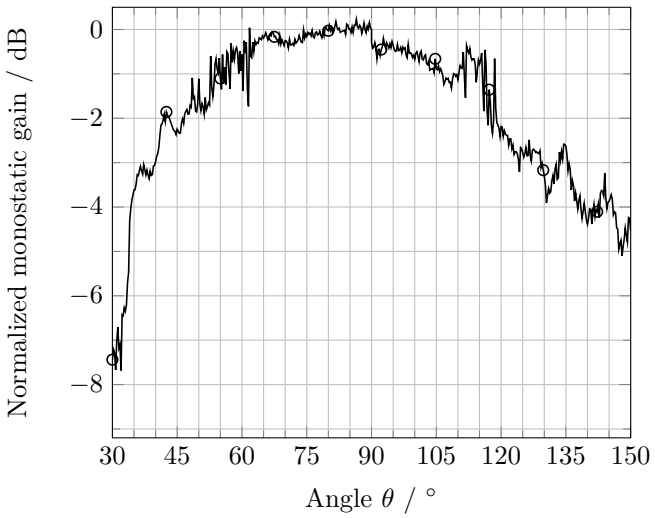

Fig. 5.9: Monostatic characteristic of the system, normalized to the boresight gain.

Table 5.1: Characteristics of bistatic patterns

Incident direction / °	Maximum / dB	Maximum / °	Error / °	Beamwidth (3 dB) / °
60	−0.6	63	3	<15
70	−0.4	72	2	<14
80	−0.1	78	2	<14
90	0.0	89	1	<13
100	0.0	102	2	<14
110	−0.3	110	0	<14
120	−0.4	118	2	<15

5.3.2 Bistatic patterns

We obtain bistatic patterns using the procedure described in section 5.1.3. The patterns for incident directions from 60° to 120° in steps of 10° are shown in Fig. 5.10. The main characteristics of the patterns are listed in Table 5.1. The plotted antenna patterns are normalized to the maximum of the boresight pattern. In this experiment, we used the antenna in a phased array manner. That means, the beamforming coefficients for the patterns shown in Fig. 5.10 have unit magnitude and a progressive phase shift. Since the coefficients are read from a ROM as can be seen from the FPGA program in Fig. 4.10, we could use any synthesizable array pattern. Some examples for pattern shapes that we can realize with the system are detailed in appendix C.6. The measurements have been carried out with an angular resolution of 1.0°. Therefore, we can give all angles only with this accuracy. We can see that the pointing errors are in the range predicted by the DoA experiments from section 5.2. As can be expected, the 3 dB beamwidth increases slightly for angles farther away from boresight. Accordingly, we observe a slight decrease in gain.

The bistatic patterns prove the ability of the demonstrator system to transmit a signal on a different frequency back into the direction of incidence. We can see that the antenna

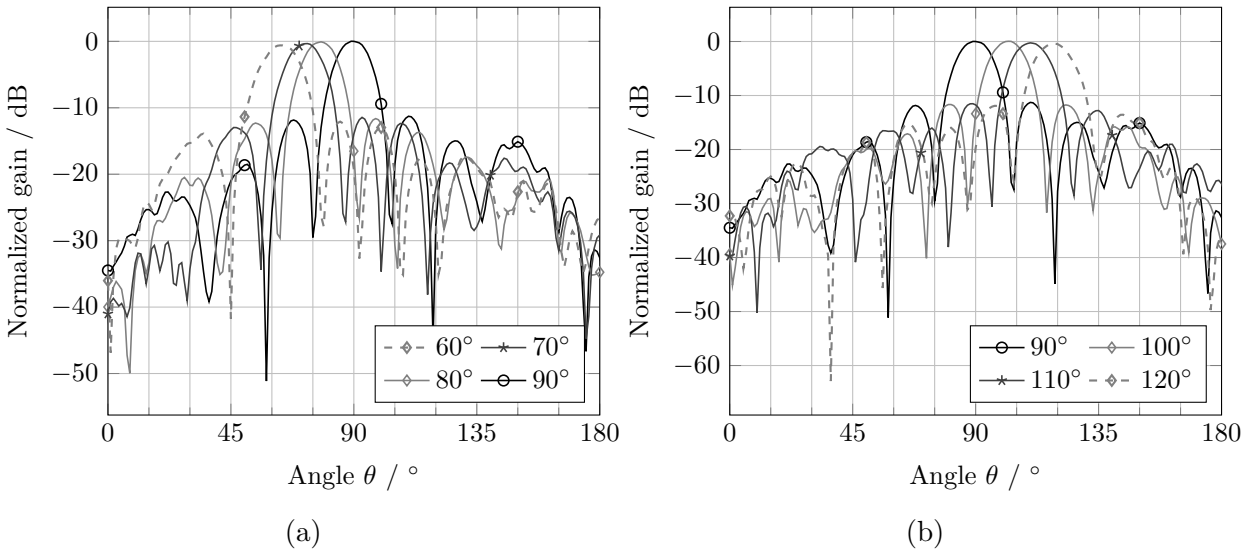

Fig. 5.10: Bistatic patterns of the system for different incident directions, normalized to the boresight pattern, i.e. $\theta = 90°$. (a) incident angles left of boresight, (b) incident angles right of boresight.

array gain is used for the transmission. Side lobe levels are in the range of 12 dB which can be expected for phased array operation.

5.4 Summary

In chapter 3, we have set requirements for the development of our retro-directive system. Already in section 3.1, we have discussed how we plan to meet these specifications with our proposed system architecture. We shall now compare in how far the built demonstrator system fulfills these demands.

Req. 1: Partly fulfilled. We have demonstrated the use of different Rx and Tx frequencies with sinusoidal signals in a measurement chamber. We have not shown the use of modulated signals. This is because it is not possible to use modulated signals for CTR measurements.

Req. 2: Not fulfilled, since no modulated signals were used with the demonstrator. However, we could visualize the presence of a phase modulated signal in the IF output using Simulink simulations in section 3.4.

Req. 3: Completely fulfilled. We have shown that if we successfully detect the phase differences at the antenna elements, our system achieves constructive superposition of the individual IF signals. The demonstrator experiments have been focused on phase detection and DoA estimation. Since these were performed successfully, our demonstrator makes use of the Rx array gain.

Req. 4: Completely fulfilled. We have shown successful back-transmission into the direction of an incident wave by measuring the monostatic characteristic of our demonstrator.

Req. 5: Completely fulfilled. During the measurement of the monostatic characteristic, the system runs in full duplex mode, i.e. it receives and transmits simultaneously.

Req. 6: Completely fulfilled. The utilized array uses a stacked patches architecture with equal physical spacing of the antenna elements in both bands.

Req. 7: Partly fulfilled. The digital hardware offers a bandwidth of several MHz. However, since we have not worked with modulated signals, the bandwidth has not been used.

Req. 8: Not fulfilled, since the system was realized on an FPGA. However, as detailed in section 4.1 the digital design consists of components for whom analog counterparts are available. Although it is therefore possible to realize the system with a high bandwidth using such parts, this was beyond the scope of this thesis.

From this summary, we can see that most of the set requirements for the novel retro-directive architecture could be achieved by our demonstrator. The main shortcoming of the system is that we are not able to use modulated signals. Therefore, we cannot measure the available signal bandwidth or achievable BER. Implementation of these features however has not been in the scope of this thesis. The main goal namely retro-directive behavior using two different carrier frequencies was achieved. That means as long as the carrier of a communication signal can be extracted, the suggested system architecture can be used. In the literature, there are techniques to remove modulation from a carrier, e.g. with Costas loops [88] or similar techniques [66]. Alternatively, Buchanan et al. propose in [49] to use a phase modulated Rx signal e.g. down-mixed from antenna element 1, as reference signal for all other elements in the array. The authors show that the PLLs of their system are then able to track phase modulated input signals although only up to data rates of 8.4 kbit/s. Such methods can also be adapted to the architecture presented in this thesis to enable the use of communication signals.

Using our demonstrator system, we have been able to prove the validity of our system architecture introduced in section 3.1. Especially, we could show the predicted phase detection ability of the novel receiver presented in section 3.2. Moreover, we have demonstrated retro-directive performance which is comparable to that of existing systems. Thus, we could illustrate the complete design cycle from analytical phase transfer functions, over simulations in continuous and discrete time until the actual hardware implementation. The demonstrated DoA estimation accuracy is a promising result for future developments of the proposed system architecture.

6 Conclusion and outlook

We have started this work with an introduction to the retro-directive principle. From that we have seen that retro-directivity offers automatic beamforming towards and thus tracking of moving communication terminals. While these are desirable properties for satellite communications, we have discussed the difficulties in applying the retro-directive principle to such applications. Although RDAs have been suggested for these purposes for many decades, the necessary frequency translation between Rx and Tx turns out to be the largest obstacle. By an extensive literature review, we have shown in chapter 2 that most retro-directive architectures which are in use today cannot solve this problem.

From the vantage point of satellite communications, we have derived requirements for a suitable RDA system in chapter 3. This has led us to a novel analog/digital hybrid retro-directive architecture with a PLL based receiver path. It offers the necessary frequency translation, makes use of the Rx antenna array gain and its data carrying signal paths can be built solely with analog circuitry. Therefore, it solves the most critical issues which have inhibited the wide spread use of RDA systems up to now. We have shown the functional principle of the proposed receiver by means of phase transfer functions. In order to improve dynamic system behavior, we have proposed an optimization methodology based on the location of the slowest system pole. Using a Simulink model of the receiver, we could prove the phase detection ability of the system by time domain simulations. Moreover, we could show that it is possible to receive phase modulated signals with the proposed receiver. We concluded the analysis of the system architecture by regarding the case of multiple incident user signals. We arrived at the conclusion that the proposed RDA system is not able to cope with multiple signal sources. While this is not the case for passive RDA signals, it is a common problem for all PLL based architectures.

To demonstrate the performance of the proposed RDA system, we have transferred the analog receiver to the discrete time domain in chapter 4. By designing the receiver as an analog and a digital system in parallel, we could show similarity in terms of system poles and transfer functions. During continuous and discrete time simulations, differences were observed due to the slower phase detection in digital hardware. Also the phase detection errors of the digital implementation are larger which stems from the time discretization and value quantization. Nevertheless, we could show by simulation of VHDL code that the digital implementation offers sufficient phase detection accuracy for the targeted satellite communication application. We have proven this in hardware loop tests using a FPGA development board and phase shifted analog input signals. We have also shown the ability of the system to track dynamically changing phase differences as they would occur in a mobile scenario.

In the last chapter, we have combined the previously shown digitally implemented system with a 5.8 and 7.0 GHz ULA of eight elements and specifically designed RF front-ends. We have detailed the setup necessary for experiments in a CTR. With mono- and bistatic measurements, we have characterized the system and compared its retro-directive performance

to that of systems in the open literature. Thereby, we have found that the novel architecture performs equally well.

In this thesis, we have identified a research gap in the field of RDA systems, namely their applicability to satellite communications. Motivated by this, we have suggested a novel system architecture and have performed a complete development including

1) Derivation of the necessary requirements to fill the identified research gap,

2) Conceptual design of a RDA system which deals with the challenges,

3) Description of this system by means of analytic transfer functions and their parameterization,

4) Proof-of-concept by continuous and discrete time simulations using Simulink and ModelSim,

5) Realization in a hardware demonstrator and

6) Characterization of the system with monostatic and bistatic measurements.

We have started the research on retro-directive antennas presented in this thesis at DLR in 2012. Together with our partners at Technische Universität München (TUM) and UNIPAMPA, we have been able to enter this research field and make a significant contribution. This can be seen in the published conference and journal articles [71, 89, 90, 91, 92, 93, 94, 95, 96, 97, 98].

There are still some challenges which have to be overcome if the proposed RDA architecture is to be applied for satellite communications. First, we have not been able to show that the system can receive modulated signals. This is mainly because the necessary hardware for modulation and demodulation was not available. Additionally, the measurements in the CTR can only be carried out with a VNA which uses sinusoidal signals. However, since the processing of communication signals is a key aspect, further development of the demonstrator system shall be conducted in this direction. Within this thesis, we have already made suggestions on how to overcome possible difficulties with phase modulated signals. Second, we have only shown the realization of the system in digital hardware. Although the implementation with analog components is straight forward, it is to be expected that issues arise e.g. from fabrication tolerances. Therefore, a considerable amount of development work would be necessary. In the end, it would be beneficial to integrate the analog RDA system on a single chip as it is already done for traditional RF front-ends. Solving these challenges would clear the way for a commercial application of retro-directive systems, 60 years after the first publication on such devices by van Atta.

Appendices

A Function definitions and analytical models

A.1 Definition of mathematical functions

A.1.1 Modulo operator

We define the modulo operator such that the result has the same sign as the divisor, i.e.

$$a \bmod b = a - b \cdot \left\lfloor \frac{a}{b} \right\rfloor , \tag{A.1}$$

where $\lfloor \cdot \rfloor$ is the floor operator.

A.1.2 Sign function

We define the sign function as follows

$$\operatorname{sgn}(y) = \begin{cases} 1 & y \geq 0 \\ -1 & y < 0 \end{cases} . \tag{A.2}$$

A.1.3 Arctangent with two arguments

The arctangent function with two arguments is defined as

$$\operatorname{atan2}(y, x) = \begin{cases} \arctan\left(\frac{y}{x}\right) & x > 0 \\ \arctan\left(\frac{y}{x}\right) + \operatorname{sgn}(y) \cdot \pi & x < 0 \\ \operatorname{sgn}(y) \cdot \frac{\pi}{2} & x = 0, y \neq 0 \\ \text{undefined} & x = y = 0 \end{cases} , \tag{A.3}$$

where we used the sign function in (A.2). The number of cases can be reduced by writing

$$\operatorname{atan2}(y, x) = \begin{cases} \arctan\left(\frac{y}{x}\right) - \frac{1}{2}\left(\operatorname{sgn}(x) - 1\right)\left(\operatorname{sgn}(y) \cdot \pi\right) & x \neq 0 \\ \operatorname{sgn}(y) \cdot \frac{\pi}{2} & x = 0, y \neq 0 \\ \text{undefined} & x = y = 0 \end{cases} . \tag{A.4}$$

A.2 Linear phase-frequency detector assumption

In this section, we shall analyze a flip-flop based phase-frequency detector architecture which is widely used in modern PLL integrated circuits [99] and system designs [100]. Brown [101]

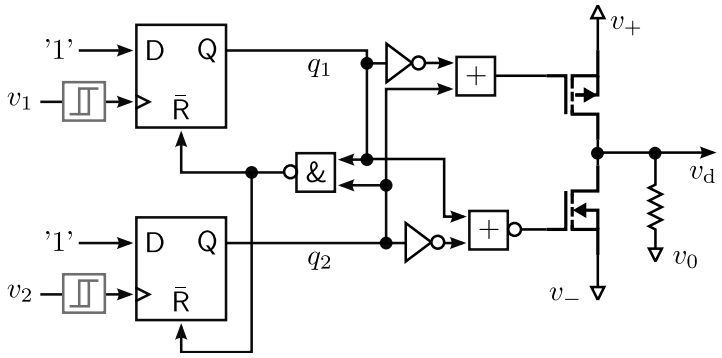

Fig. A.1: Flip-flop based PFD with reset network and CMOS switch at the output.

Table A.1: PFD output voltage states

q_1	q_2	v_d
'0'	'0'	v_0
'0'	'1'	v_-
'1'	'0'	v_+
'1'	'1'	v_0

was the first to use complementary metal oxide semiconductor (CMOS) logic to build a phase detector which is also frequency sensitive. The devices are sometimes called digital, but they are used to compare unquantized continuous time signals. Most of the content in this section was published in [71].

A.2.1 Flip-flop based architecture

The regarded flip-flop based PFD is schematically shown in Fig. A.1. Two input voltage signals v_1, v_2 are fed to the clock inputs of the flip-flops. We may use Schmitt triggers to ensure clear rising edges [102]. The flip-flop data inputs 'D' are always held high. A rising edge of $v_i, i \in 1, 2$ thus causes the respective flip-flop output signal q_i to go high ('1'). If $q_1 = q_2 =$ '1', the output of the NAND gate goes low and both flip-flops are simultaneously reset, i.e. their outputs become '0'. The flip-flop outputs q_i control a CMOS switch which consists of an n- and a p-channel metal oxide semiconductor field effect transistor (MOSFET). If q_1 is high and q_2 is low, the p-channel MOSFET will be in active mode. This causes the PFD output voltage to become $v_d = v_+$. Similarly, when q_2 is high and q_1 is low, the n-channel MOSFET is active causing $v_d = v_-$. If q_1 and q_2 are both low or high, none of the MOSFETs is active and the pull-down resistor will ensure $v_d = v_0$. Table A.1 summarizes the relation between the flip-flop outputs and the PFD output voltage.

We shall now investigate the behavior of the flip-flops. Let us assume that both flip-flop outputs are '0', i.e. $q_1 q_2 =$ '00'. It now depends on which input signal v_1, v_2 has the next rising edge. If this is the case for v_1, the output state will become $q_1 q_2 =$ '10'. This will not change until v_2 exhibits a rising edge which triggers the reset of both flip-flops. Thus the output eventually becomes $q_1 q_2 =$ '00' again. If v_2 exhibits the first rising edge after the

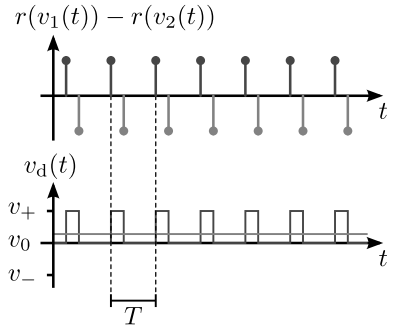

Fig. A.2: Top: Location of rising edges for two input signals of equal frequency. Bottom: PFD output signal and mean value.

initial state, the behavior is similar but the output state is $q_1 q_2 =$ '01' until v_1 has a rising edge.

From this we see an important property of the circuit: It ignores consecutive rising edges of one input signal. Once the output is set to '01' ('10') by a rising edge of v_1 (v_2), it will only go to '00' again if v_2 (v_1) has a rising edge. This is important to detect frequency differences between the two input signals as detailed in [71].

A.2.2 Analytic input signal model

The phase-frequency detector inputs have to be periodic signals with a single rising edge per period. Without loss of generality, we assume sinusoidal input signals of the form

$$v_i(t) = \hat{v}_i \sin(\omega_i t + \varphi_i), \quad i \in 1, 2, \tag{A.5}$$

with $\varphi_i \in [0, \ldots, 2\pi[$. The rising signal edges of v_i clock the flip-flops in Fig. A.1. They occur when the sign of v_i changes from negative to positive. This happens at the time points given by

$$t = \frac{2\pi m_i - \varphi_i}{\omega_i} = T_i \left(m_i - \frac{\varphi_i}{2\pi} \right), \quad m_i \in \mathbb{Z}, \tag{A.6}$$

where $T_i = 2\pi/\omega_i$ denotes the signal period. Marking the rising edges of the input signals $v_i(t)$, we can describe them as a train of Dirac delta distributions $\delta_\Delta(t)$ located at the points given in (A.6). This yields

$$r(v_i(t)) = \sum_{m_i \in \mathbb{Z}} \delta_\Delta \left(t - T_i \left(m_i - \frac{\varphi_i}{2\pi} \right) \right). \tag{A.7}$$

In the following, we shall formulate the phase detector output using the last expression.

A.2.3 Output signal for equal input frequencies

Let us regard the case of two signals with $T_1 = T_2 = T$, i.e. two signals with only a phase difference. Fig. A.2 shows a corresponding example of $r(v_i(t))$ and $v_\mathrm{d}(t)$. In this case, there will always be a rising edge of v_2 between two rising edges of v_1. So in each period T there is exactly one output pulse. We assume an initial state $v_\mathrm{d}(0) = v_0$ and $v_+ = -v_- = \hat{v}_\mathrm{d}$. Then

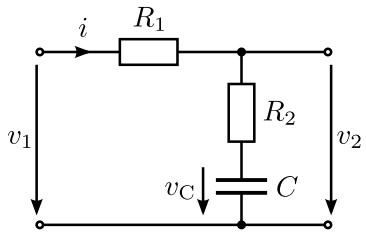

Fig. A.3: Schematic of the loop filter with one pole and one zero.

we obtain the PFD output signal by integrating the difference of the rising edge trains in (A.7), leading to

$$v_{\mathrm{d}}(t) = \hat{v}_{\mathrm{d}} \int_0^t \left(r(v_1(\tau)) - r(v_2(\tau))\right) d\tau \tag{A.8}$$

$$= \hat{v}_{\mathrm{d}} \sum_{m\in\mathbb{N}} \left[u\left(t - T\left(m - \frac{\varphi_1}{2\pi}\right)\right) - u\left(t - T\left(m - \frac{\varphi_2}{2\pi}\right)\right)\right], \tag{A.9}$$

where $u(t)$ denotes the unit step function. To calculate the mean of (A.9) it is sufficient to regard a single period, i.e.

$$\bar{v}_{\mathrm{d}} = \frac{1}{T} \int_{(m-1)T}^{mT} v_{\mathrm{d}}(t)dt = \frac{\hat{v}_{\mathrm{d}}}{T}\left(\Big[t\Big]_{(m-\frac{\varphi_1}{2\pi})T}^{mT} - \Big[t\Big]_{(m-\frac{\varphi_2}{2\pi})T}^{mT}\right) = \hat{v}_{\mathrm{d}}\frac{\varphi_1 - \varphi_2}{2\pi}. \tag{A.10}$$

Thus, the mean of the output pulse train is proportional to the phase difference between the two input signals. We see that the last expression is the desired ideal phase detector output in (3.7) with $K_{\mathrm{d}} = \hat{v}_{\mathrm{d}}/\mathrm{rad}$.

A.3 Time domain model of the fourth order system

In section 3.2, we have used the Laplace representation of our retro-directive receiver channel to describe its behavior. This is advantageous e.g. when formulating the phase transfer functions without specifying the loop filter orders as done in (3.34). Additionally, the Laplace formulations are in general much easier to handle than their time domain counterparts. However, it is possible to find a time domain formulation for any system which can be described in the Laplace domain. In the following, we want to deduce the time domain model for our retro-directive receiver channel under the assumption of loop filters with one zero and one pole, each. The purpose of this derivation is to confirm the characteristic polynomial of the system obtained by the analysis in the Laplace domain.

A.3.1 Analog loop filter

As mentioned in section 3.3, the loop filters used in the regarded retro-directive receiver channel have one zero and one pole. Fig. A.3 shows the schematic of such a filter. In the following, its time domain behavior is analyzed. Using the time constants $\tau_2 = R_2C$ and

$\tau_{12} = (R_1 + R_2)C$, we get

$$i(t) = C\frac{dv_C(t)}{dt}, \tag{A.11}$$

$$v_1(t) = \tau_{12} i(t) + v_C(t), \tag{A.12}$$

$$v_2(t) = R_2 i(t) + v_C(t) = \tau_2 \dot{v}_C(t) + v_C(t), \tag{A.13}$$

where $\dot{v}_C(t)$ denotes the derivative of $v_C(t)$ with respect to time t and reads

$$\dot{v}_C(t) = \frac{1}{\tau_{12}} v_1(t) - \frac{1}{\tau_{12}} v_C(t), \tag{A.14}$$

with the solution

$$v_C(t) = e^{-\frac{t}{\tau_{12}}} v_C(0) + \int_0^t \frac{1}{\tau_{12}} v_1(t') e^{-\frac{t-t'}{\tau_{12}}} dt', \tag{A.15}$$

and the derivative

$$\dot{v}_C(t) = \frac{1}{\tau_{12}} v_1(t) - \frac{1}{\tau_{12}} v_C(0) e^{-\frac{t}{\tau_{12}}} - \frac{1}{\tau_{12}^2} \int_0^t v_1(t') e^{-\frac{t-t'}{\tau_{12}}} dt'. \tag{A.16}$$

We finally arrive at

$$v_2(t) = \left(1 - \frac{\tau_2}{\tau_{12}}\right) v_C(0) e^{-\frac{t}{\tau_{12}}} + \frac{\tau_2}{\tau_{12}} v_1(t) + \frac{1}{\tau_{12}} \left(1 - \frac{\tau_2}{\tau_{12}}\right) \int_0^t v_1(t') e^{-\frac{t-t'}{\tau_{12}}} dt'. \tag{A.17}$$

The filter impulse response is contained in the convolution integral of the last term. It reads

$$h(t) = \frac{1}{\tau_{12}} \left(1 - \frac{\tau_2}{\tau_{12}}\right) e^{-\frac{t}{\tau_{12}}}. \tag{A.18}$$

A.3.2 System equations

We assume the previous signal definitions for the RF (3.1) and reference signals (3.16). The VCO output signals v_{V1} and v_{V2} are defined according to (3.10) and the down-mixer output as shown in (3.6). The output signals of the PFDs and loop filters for the nested PLL structure are given by

$$v_{\mathrm{d1,n}}(t) = K_{\mathrm{d1}} \left[\Psi_{\mathrm{RF},n}(t) - \Psi_{\mathrm{V2},n}(t) - \Psi_{\mathrm{ref}}(t)\right], \tag{A.19}$$

$$v_{\mathrm{d2,n}}(t) = K_{\mathrm{d2}} \left[\Psi_{\mathrm{V1},n}(t) - \frac{1}{M} \Psi_{\mathrm{V2},n}(t)\right], \tag{A.20}$$

$$v_{\mathrm{h}i,n}(t) = \left(1 - \frac{\tau_{2i}}{\tau_{12i}}\right) v_{Ci,n}(t) + \frac{\tau_{2i}}{\tau_{12i}} v_{\mathrm{d}i,n}(t), \tag{A.21}$$

where the output of the ideal PFD in (3.7) has been used. The system is described by the VCO output phases $\Psi_{\mathrm{V}i,n}$ and the voltages across the filter capacitances $v_{Ci,n}$. The state equation of the system can then be written in the form

$$\dot{\mathbf{x}} = \mathbf{A}\mathbf{x} + \mathbf{b}v + \mathbf{C}\mathbf{c}, \tag{A.22}$$

with

$$\mathbf{x} = \left(\Psi_{\mathrm{V1},n}, \Psi_{\mathrm{V2},n}, v_{C1,n}, v_{C2,n}\right)^T, \tag{A.23}$$

$$\mathbf{b} = \left(K_1 \frac{\tau_{21}}{\tau_{121}}, 0, \frac{K_{\mathrm{d1}}}{\tau_{121}}, 0\right)^T, \tag{A.24}$$

$$v = \Psi_{\mathrm{RF},n} - \Psi_{\mathrm{ref}}, \tag{A.25}$$

$$\mathbf{c} = \left(\omega_{\mathrm{q1}}, \omega_{\mathrm{q2}}\right)^T. \tag{A.26}$$

As before, we write $K_i = K_{\mathrm{d}i} K_{\mathrm{V}i}$. The system matrix is given by

$$\mathbf{A} = \begin{pmatrix} 0 & -K_1 \frac{\tau_{21}}{\tau_{121}} & K_{\mathrm{V1}} \left(1 - \frac{\tau_{21}}{\tau_{121}}\right) & 0 \\ K_2 \frac{\tau_{22}}{\tau_{122}} & -K_2 \frac{\tau_{22}}{\tau_{122} M} & 0 & K_{\mathrm{V2}} \left(1 - \frac{\tau_{22}}{\tau_{122}}\right) \\ 0 & -K_{\mathrm{d1}} \frac{1}{\tau_{121}} & -\frac{1}{\tau_{121}} & 0 \\ K_{\mathrm{d2}} \frac{1}{\tau_{122}} & -K_{\mathrm{d2}} \frac{1}{\tau_{122} M} & 0 & -\frac{1}{\tau_{122}} \end{pmatrix}. \tag{A.27}$$

and the constant frequency components are included by choosing

$$\mathbf{C} = \begin{pmatrix} 1 & 0 \\ 0 & 1 \\ 0 & 0 \\ 0 & 0 \end{pmatrix}. \tag{A.28}$$

Equilibrium occurs for $\dot{\mathbf{x}} = 0$, leading to

$$v_{C1,n}(t)_{|\dot{\mathbf{x}}=0} = K_{\mathrm{d1}} \left(\Psi_{\mathrm{RF},n}(t) - \Psi_{\mathrm{V2},n}(t) - \Psi_{\mathrm{ref}}(t)\right), \tag{A.29}$$

$$v_{C2,n}(t)_{|\dot{\mathbf{x}}=0} = K_{\mathrm{d2}} \left(\Psi_{\mathrm{V1},n}(t) - \frac{1}{M} \Psi_{\mathrm{V2},n}(t)\right), \tag{A.30}$$

$$\Psi_{\mathrm{V1},n}(t)_{|\dot{\mathbf{x}}=0} = -\frac{\omega_{\mathrm{q2}}}{K_2} + \frac{\omega_{\mathrm{q1}}}{K_1 M} + \frac{1}{M} \left(\Psi_{\mathrm{RF},n}(t) - \Psi_{\mathrm{ref}}(t)\right), \tag{A.31}$$

$$\Psi_{\mathrm{V2},n}(t)_{|\dot{\mathbf{x}}=0} = \frac{\omega_{\mathrm{q1}}}{K_1 M} + \Psi_{\mathrm{RF},n}(t) - \Psi_{\mathrm{ref}}(t). \tag{A.32}$$

When we insert the last two expressions into the first and second, we see that the voltages over the loop filter capacitances are constant, as expected for the steady state:

$$v_{C1,n}(t)_{|\dot{\mathbf{x}}=0} = K_{\mathrm{d1}} \left(\frac{\omega_{\mathrm{q1}}}{K_1 M}\right), \tag{A.33}$$

$$v_{C2,n}(t)_{|\dot{\mathbf{x}}=0} = K_{\mathrm{d2}} \left(-\frac{\omega_{\mathrm{q2}}}{K_2} + \frac{\omega_{\mathrm{q1}}}{K_1 M} - \frac{\omega_{\mathrm{q1}}}{K_1 M^2}\right), \tag{A.34}$$

A.3.3 Long term system behavior

Constant excitation If $\Psi_{\mathrm{RF},n}(t) = \varphi_{\mathrm{RF}}$, the steady state of the system is

$$\Psi_{\mathrm{V1},n}(t) = \frac{\varphi_{\mathrm{RF}}}{M} - \frac{\omega_{\mathrm{ref}}}{M} t - \frac{\omega_{\mathrm{q2}}}{K_2} + \frac{\omega_{\mathrm{q1}}}{K_1 M}, \tag{A.35}$$

$$\Psi_{\mathrm{V2},n}(t) = \varphi_{\mathrm{RF}} - \omega_{\mathrm{ref}} t + \frac{\omega_{\mathrm{q1}}}{K_1 M}. \tag{A.36}$$

Purely sinusoidal excitation Under $\Psi_{\mathrm{RF},n}(t) = \omega_{\mathrm{RF}} t + \varphi_{\mathrm{RF}}$, the steady state is

$$\Psi_{\mathrm{V1},n}(t) = \frac{\omega_{\mathrm{RF}} - \omega_{\mathrm{ref}}}{M} t - \frac{\omega_{\mathrm{q2}}}{K_2} + \frac{\omega_{\mathrm{q1}}}{K_1 M} + \frac{\varphi_{\mathrm{RF}}}{M}, \tag{A.37}$$

$$\Psi_{\mathrm{V2},n}(t) = (\omega_{\mathrm{RF}} - \omega_{\mathrm{ref}}) t + \frac{\omega_{\mathrm{q1}}}{K_1 M} + \varphi_{\mathrm{RF}}. \tag{A.38}$$

A.3.4 Transient system behavior

From (A.27), we can find the characteristic polynomial of the system to be

$$\begin{aligned} 0 = {} & \lambda^4 + \lambda^3 \left(\frac{1}{\tau_{121}} + \frac{1}{\tau_{122}} + \frac{K_2 \tau_{22}}{M \tau_{122}} \right) \\ & + \lambda^2 \left(\frac{1}{\tau_{121}\tau_{122}} + \frac{K_2}{\tau_{122}} \left(\frac{1}{M} + \frac{\tau_{22}}{\tau_{121} M} + \frac{K_1 \tau_{21} \tau_{22}}{\tau_{121}} \right) \right) \\ & + \lambda \frac{K_2}{\tau_{121}\tau_{122}} \left(\frac{1}{M} + K_1 (\tau_{21} + \tau_{22}) \right) + \frac{K_1 K_2}{\tau_{121}\tau_{122}}, \end{aligned} \tag{A.39}$$

with λ being the Eigenvalues of (A.27). This expression corresponds to the denominator of the phase transfer function from (3.37). It shows that our approach to regard the system in the Laplace domain is valid.

A.4 Error of second order system approximations

We shall start with the approximation error when using (3.39), i.e. neglecting the loop filter influence. The error is given by the difference between approximated and true phase transfer function, which reads

$$\begin{aligned} \Delta \check{G}_{\mathrm{V1},n}(s) &= G_{\mathrm{V1},n}(s)_{|_{h_i(s)=1}} - G_{\mathrm{V1},n}(s) \\ &= K_1 \frac{s + \frac{K_2}{M}}{s^2 + s\frac{K_2}{M} + K_1 K_2} - \frac{\left(s K_1 N_{h1} D_{h2} + \frac{K_1 K_2}{M} N_{h1} N_{h2} \right)}{s^2 D_{h1} D_{h2} + s \frac{K_2}{M} N_{h2} D_{h1} + K_1 K_2 N_{h1} N_{h2}} \end{aligned} \tag{A.40}$$

$$\begin{aligned} &= K_1 \frac{\begin{array}{r} s^3 D_{h2}(N_{h1} - D_{h1}) + s^2 \frac{K_2}{M} (D_{h2} + N_{h2})(N_{h1} - D_{h1}) \\ + s \left(K_1 K_2 N_{h1} (D_{h2} - N_{h2}) + \frac{{K_2}^2}{M^2} N_{h2} (N_{h1} - D_{h1}) \right) \end{array}}{\begin{array}{l} s^4 D_{h1} D_{h2} + s^3 \left(\frac{K_2}{M} (N_{h1} N_{h2} + D_{h1} D_{h2}) \right) \\ + s^2 \left(K_1 K_2 N_{h1} N_{h2} + \frac{{K_2}^2}{M^2} N_{h2} D_{h1} + K_1 K_2 D_{h1} D_{h2} \right) \\ + s \frac{K_1 {K_2}^2}{M} N_{h2} (D_{h1} + N_{h1}) + {K_1}^2 {K_2}^2 N_{h1} N_{h2} \end{array}}. \end{aligned} \tag{A.41}$$

For comparison, we are also interested in the resulting error if we assume a very large loop gain K_2. We start from (3.45) and write the numerator and denominator of the loop filter h_1 explicitly. This yields

$$\tilde{G}_{\mathrm{V1},n}(s) = \frac{\tilde{\mathring{\Psi}}_{\mathrm{V1},n}(s)}{\mathring{\Psi}_{\mathrm{RF},n}(s)} = \frac{K_1 N_{h1}(s)}{s D_{h1}(s) + K_1 N_{h1}(s) M}. \tag{A.42}$$

We obtain the error by subtracting (3.34), i.e.

$$\begin{aligned}\Delta\tilde{G}_{\mathrm{V1},n}(s) &= \tilde{G}_{\mathrm{V1},n}(s) - G_{\mathrm{V1},n}(s)\\ &= \frac{K_1 N_{h1}}{sD_{h1} + K_1 N_{h1} M} - \frac{\left(sK_1 N_{h1} D_{h2} + \frac{K_1 K_2}{M} N_{h1} N_{h2}\right)}{s^2 D_{h1} D_{h2} + s\frac{K_2}{M} N_{h2} D_{h1} + K_1 K_2 N_{h1} N_{h2}} \qquad \text{(A.43)}\\ &= \frac{-s\frac{{K_1}^2 N_{h1}^2 M D_{h2}}{K_2}}{s^3\frac{D_{h1}^2 D_{h2}}{K_2} + s^2\left(\frac{K_1 M N_{h1} D_{h1} D_{h2}}{K_2} + \frac{D_{h1}^2 N_{h2}}{M}\right)} \qquad \text{(A.44)}\\ &\qquad + sK_1 N_{h1} N_{h2}\left(D_{h1} + 1\right) + {K_1}^2 N_{h1}^2 N_{h2} M\end{aligned}$$

As can be expected, the error terms both vanish at $s = 0$.

$$\lim_{s\to 0} \Delta\breve{G}_{\mathrm{V1},n}(s) = \lim_{s\to 0} \Delta\tilde{G}_{\mathrm{V1},n}(s) = 0. \qquad \text{(A.45)}$$

If we assume that the true system is of fourth order, i.e. as described in (3.37), N_{hi} and D_{hi} are first order polynomials. That means the numerator of (A.41) is a fifth order and the numerator of (A.44) is a fourth order polynomial. The denominators of both expressions are sixth order polynomials. Regarding the order of the numerators, we expect that (A.41) will increase faster than (A.44). We may presume that therefore $\tilde{G}_{\mathrm{V1},n}(s)$ is a more suitable approximation for higher s which can also be observed in Fig. 3.3.

A.5 Second order PLL synthesizer

We obtain a second order PLL synthesizer by inserting (3.36) into (3.44) yielding

$$\breve{G}_{\mathrm{V2}}(s) = \frac{K_2\breve{h}_2(s)}{s + \frac{K_2}{M}\breve{h}_2(s)} = \frac{K_2}{\tau_{122}}\frac{1 + \tau_{22}s}{s^2 + s\left(\frac{1}{\tau_{122}} + \frac{K_2\tau_{22}}{M\tau_{122}}\right) + \frac{K_2}{M\tau_{122}}}. \qquad \text{(A.46)}$$

We obtain the characteristic values of the resulting harmonic oscillator as

$$\omega_{02} = \sqrt{\frac{K_2}{M\tau_{122}}}, \qquad \text{(A.47)}$$

$$\zeta_2 = \frac{1}{2}\left(\sqrt{\frac{M}{K_2\tau_{122}}} + \sqrt{\frac{K_2}{M\tau_{122}}}\tau_{22}\right). \qquad \text{(A.48)}$$

However, if we want to design this PLL, we are rather interested in how to choose the time constants to achieve a certain natural frequency ω_{02} and damping factor ζ_2. For this, we can reformulate the last two expressions to

$$\tau_{122} = \frac{K_2}{M\omega_{02}^2}, \qquad \text{(A.49)}$$

$$\tau_{22} = \frac{2\zeta_2}{\omega_{02}} - \frac{M}{K_2}. \qquad \text{(A.50)}$$

Since the time constants need to be non-negative, the last expression gives us the condition

$$\omega_{02} < \omega_{02,\max} = \frac{2K_2\zeta_2}{M}. \qquad \text{(A.51)}$$

Moreover, since $\tau_{122} > \tau_{22}$, we also have to ensure that for $\zeta_2 \geq 1$

$$\omega_{02} < \frac{K_2}{M}\zeta_2\left(1-\sqrt{1-\frac{1}{\zeta_2^2}}\right) \quad \text{and} \quad \omega_{02} > \frac{K_2}{M}\zeta_2\left(1+\sqrt{1-\frac{1}{\zeta_2^2}}\right). \tag{A.52}$$

This defines minimum and maximum values for the achievable natural frequency. We can also express this by

$$\omega_{02} = \alpha_2\omega_{02,\max}, \quad \begin{cases} \frac{1}{2}\left(1+\sqrt{1-\frac{1}{\zeta_2^2}}\right) < \alpha_2 < 1 \\ 0 < \alpha_2 < \frac{1}{2}\left(1-\sqrt{1-\frac{1}{\zeta_2^2}}\right) \end{cases}. \tag{A.53}$$

A.6 Arctangent of sine over cosine

The arctangent of the special case

$$\arctan\left(\frac{\sin(x)}{\cos(x)}\right) = \begin{cases} x+2\pi m & 2\pi l - \frac{\pi}{2} \leq x < \frac{\pi}{2} + 2\pi l, l \in \mathbb{Z} \\ x+(2m+1)\pi & \text{else} \end{cases}, \tag{A.54}$$

with $m \in \mathbb{Z}$ chosen such that the result is within $[-\pi, \ldots, \pi[$ can be reformulated to

$$\arctan\left(\frac{\sin(x)}{\cos(x)}\right) = x + \frac{\pi}{2}\left(\operatorname{sgn}(\cos(x)) - 1\right) + 2\pi m. \tag{A.55}$$

B Details on simulation models

B.1 Simulink receiver model

The utilized Simulink receiver model is depicted in Fig. B.1. Comparing to Fig. 3.2, we can see the following differences: The ideal lowpass filter is replaced by a Butterworth filter of order 4 and a 3 dB bandwidth f_{bwIF}. A gain block is used to multiply the IF signal by 2 to eliminate the factor $\frac{1}{2}$ in (3.6). The PLL synthesizer is depicted as a two-port. We will describe the underlying model below.

The PFD model is shown in Fig. B.2. After the two signal inputs, we employ Schmitt triggers with a threshold voltage $v_{\mathrm{trig},i}$, $i \in \{1, 2, 3\}$. We need these in order to obtain clear signal sign changes in case of noisy input signals. As detailed in section A.2.2, the input signals are used as clock inputs for two D-type flip-flops whose data input is always held high. In contrast to the ideal model, we have to introduce a delay in the flip-flop reset path. Since the flip-flops and the NAND-gate work without delay, an immediate feedback loop between flip-flop outputs and reset inputs would occur which cannot be simulated. These so called anti-backlash delays are denoted as $t_{\mathrm{del},i}$.

The output section of the PFD is modeled with switches rather than MOSFETs. If the input to a switch is '0', its output is 0 V, if the input is '1', the output will be $\pm K_{\mathrm{d}i}$. The output of the switches are summed to form the actual PFD output. Thus we have ensured that the PFD output is 0 V when both flip-flop outputs are high.

Going back to our receiver model in Fig. B.1, the PLL synthesizer block is shown in more detail in Fig. B.3. In this circuit, we have a Schmitt trigger for the input signal followed by a PFD and the loop filter h_2. The time constants of this filter are calculated from damping factor ζ_2 and natural frequency $f_{\mathrm{n}2} = \omega_{02}/(2\pi)$ using (A.49) and (A.50). The output signal Out_sens is again for debugging only. The main output of the PLL is the VCO signal which appears at the VCO_out port. The sinusoidal VCO signal is fed to a Schmitt trigger to get a rectangular signal. This is then used for a counter whose output becomes '1' after M edges at the input. The subsequent JK flip-flop toggles its output state for every '1' at the

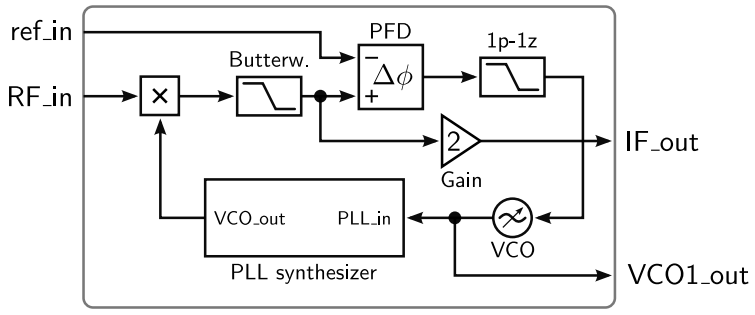

Fig. B.1: Block diagram of the Simulink model of the receiver.

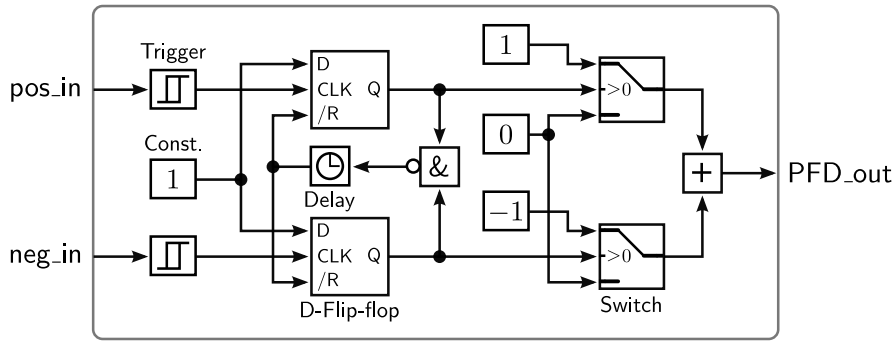

Fig. B.2: Simulink model of the PFD with Schmitt triggers to provide clear input signal sign changes.

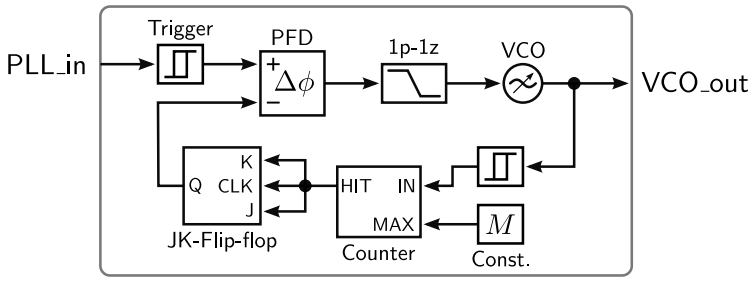

Fig. B.3: Simulink model of the PLL synthesizer within the receiver.

inputs. Thus, we obtain at the flip-flop output a rectangular signal with rising and falling edges spaced $M/2$ periods of the VCO signals apart. The flip-flop output is used as feedback signal and compared to the PLL_in input signal.

B.1.1 Dual channel receiver simulations

The simulation parameters for the dual channel receiver in Fig. 3.8 are listed in Table B.1. If nothing is specified, the default values were used for simulations.

For the dual channel simulations, we need to generate sinusoidal input signals with AWGN. Moreover, we have to have the possibility to change the RF signal phase, i.e. use BPSK modulation. The respective signal generator model is shown in Fig. B.4. It consists of a sine waveform generator which is multiplied with the sign of the BPSK in port. This realizes the

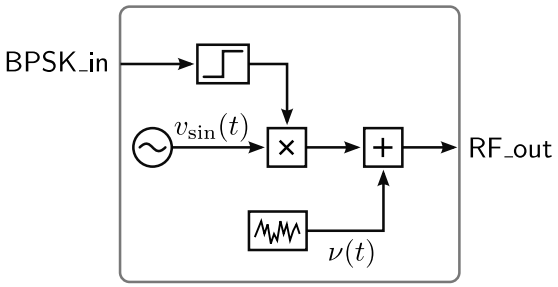

Fig. B.4: Simulink model of the RF signal generator with BPSK modulation and additive noise.

Table B.1: Dual channel receiver simulation parameters

Parameter	Symbol	Default value
System reference frequency	f_{ref}	100 MHz
Reference signal SNR	$\mathrm{SNR}_{\mathrm{ref}}$	40 dB
Noiseless input signal amplitude	v_{RF}	1.0 V
Input signal RF	f_{RF}	5.80 GHz
Input signal SNR	$\mathrm{SNR}_{\mathrm{RF}}$	40 dB
Input signal phase difference	δ	$\pi/2$ rad
Bandwidth of IF filter	f_{bwIF}	500 MHz
VCO V_1 quiescent frequency	f_{q1}	100 MHz
VCO V_2 quiescent frequency	f_{q2}	5.70 GHz
Schmitt trigger threshold voltages	$v_{\mathrm{trig},i}$	0.2 V
Bandwidth of PFD d_3 lowpass filter	f_{bwPD}	200 kHz
Input phase modulation rate	f_{BPSK}	0 Hz
Total simulation time	t_{sim}	20 µs
PFD reset delays	$t_{\mathrm{del},i}$	0.5 ns

desired modulation. Noise is added to the modulated signal and the result appears at the RF_out port. The generated sine waveform is parameterized by

$$v_{\mathrm{gen}}(t) = \mathrm{sgn}(v_{\mathrm{BPSK}}(t))\hat{v}_{\mathrm{sin}} \sin\left(2\pi f_{\mathrm{RF}} t + (i-1)\delta\right) + \nu(t), \tag{B.1}$$

where $v_{\mathrm{BPSK}}(t)$ is the BPSK input signal and $i \in \{1, 2\}$ is the receiver channel number. The noise signal is the output of a random number generator with the properties

$$\nu(t) \sim \mathcal{N}\left(0, \frac{\hat{v}_{\mathrm{sin}}^2}{2} \frac{1}{\mathrm{SNR}_{\mathrm{RF}}}\right). \tag{B.2}$$

The generator for the reference signal is the same except that it is missing the BPSK input and multiplier.

B.1.2 Eight channel receiver simulations

Fig. B.5 shows the block diagram for the eight channel receiver in Simulink. We use a common reference signal generator along with eight individual RF signal generators which realize the progressive phase shifts between the channels. The IF output signals are summed while the VCO outputs are compared pairwise by PFDs. The subsequent signal processing consists of a lowpass filter to obtain the time average of the PFD pulse trains. The result is multiplied by the division factor M and the modulo operation is applied. With this, we implement the computation of (3.25) to obtain the phase difference estimates. Finally, we calculate the mean of all estimates by summing them and dividing by $N-1$. Thus we arrive at a single phase difference estimate which appears at the PD_out output.

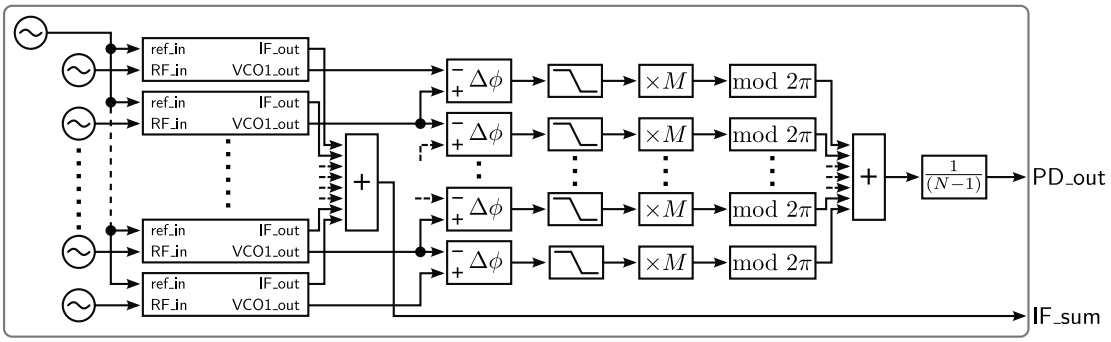

Fig. B.5: Simulink setup for the simulation of an eight channel receiver. It includes IF and phase detection signal processing.

B.2 Discrete time system implementation

In section 4.1.2, we have introduced the phase transfer functions of the discrete time receiver system. In this section, we will insert the first order IIR filter equation into these phase transfer functions to obtain the system order. Let us start with the NCO 2 phase output from (4.17) and insert (4.6). This yields

$$\frac{\Psi_{\mathrm{NCO2}}(z)}{\Psi_{\mathrm{NCO1}}(z)} = \frac{K_2(b_{02}+b_{12}z^{-1})z^{-2}}{a_{02}+(a_{12}-a_{02})z^{-1}-a_{12}z^{-2}+\frac{K_2}{M}(b_{02}+b_{12}z^{-1})z^{-3}}, \tag{B.3}$$

which is a fourth order system. We will do the same for the complete receiver phase transfer function from (4.18). After inserting (4.6), we obtain

$$\begin{aligned}\frac{\Psi_{\mathrm{NCO1}}(z)}{\Psi_{\mathrm{RF}}(z)z^{-T_d}-\Psi_{\mathrm{ref}}(z)} = {} & \\ & K_1 z^{-2}\Big[z^{-5}\tfrac{K_2}{M}b_{11}b_{12}+z^{-4}\tfrac{K_2}{M}(b_{01}b_{12}+b_{11}b_{02}) \\ & +z^{-3}\left(\tfrac{K_2}{M}b_{01}b_{02}-a_{12}b_{11}\right)+z^{-2}(b_{11}(a_{12}-a_{02})-b_{01}a_{12}) \\ & +z^{-1}(b_{11}a_{02}+b_{01}(a_{12}-a_{02}))+b_{01}a_{02}\Big] \\ \hline & z^{-4-T_d}K_1K_2\left(z^{-2}b_{11}b_{12}+z^{-1}(b_{01}b_{12}+b_{02}b_{11})+b_{01}b_{02}\right) \\ & -z^{-6}\tfrac{K_2}{M}a_{11}b_{12}+z^{-5}\tfrac{K_2}{M}\left(b_{12}(a_{11}-a_{01})-a_{11}b_{02}\right) \\ & +z^{-4}\left(\tfrac{K_2}{M}(a_{01}b_{12}+b_{02}(a_{11}-a_{01}))+a_{11}a_{12}\right) \\ & +z^{-3}\left(\tfrac{K_2}{M}a_{01}b_{02}-a_{12}(a_{11}-a_{01})-a_{11}(a_{12}-a_{02})\right) \\ & +z^{-2}((a_{11}-a_{01})(a_{12}-a_{02})-a_{02}a_{11}-a_{01}a_{12}) \\ & +z^{-1}(a_{01}(a_{12}-a_{02})+a_{02}(a_{11}-a_{01}))+a_{01}a_{02}\end{aligned} \tag{B.4}$$

The order of this system is defined by the delay of the down-mixer, filter and Schmitt trigger of the receiver T_d. The minimum order using $T_d = 1$ is seven. The above phase transfer function shows the necessity of evaluating the poles numerically.

B.3 Analytic monostatic array characteristics

Since monostatic measurements are not widely known, we shall introduce them here in more detail. Additionally, we will present analytic results to see monostatic characteristics of

ideal arrays. As described in section 5.1.3, the monostatic characteristic defines, how well a system transmits back towards any incident direction if it is excited from that direction. For a given array, we can thus construct the optimum monostatic characteristic by plotting the maximum field strength which can be transmitted in each direction. Thereby, we follow the approach presented in [103, c.6] to calculate the radiation patterns of ULAs with uniform amplitude excitation. We assume a ULA of identical antenna elements where each has a directivity $D_{\text{ant}}(\theta)$. Assuming a purely linear polarization for simplicity, the electric field generated by such an antenna is

$$\vec{E}_{\text{ant}}(r,\theta) \propto \frac{1}{r}\sqrt{\eta_0 D_{\text{ant}}(\theta)}\vec{e}_y, \tag{B.5}$$

where r is the distance from the antenna and η_0 is the intrinsic impedance of free space. The geometry of the ULA and its excitation define the array factor

$$\text{AF}(\theta,\hat{\theta}) = \sum_{n=1}^{N} e^{j(\delta_n(\theta)-\delta_n(\hat{\theta}))} = \sum_{n=1}^{N} e^{j2\pi d_r(n-1)(\cos(\theta)-\cos(\hat{\theta}))}, \tag{B.6}$$

whereby $\delta_n(\hat{\theta})$ is the phase shift of the excitation that we introduce to point the array mainlobe towards the direction $\hat{\theta}$. According to [103], we can obtain the electric field produced by the beamsteered array from

$$\vec{E}_{\text{array}}(r,\theta,\hat{\theta}) = \text{AF}(\theta,\hat{\theta}) \cdot \vec{E}_{\text{ant}}(r,\theta). \tag{B.7}$$

Since (B.5) is valid for the array also, we can eliminate the dependency on r by regarding the directivity of the array with beamsteering, i.e.

$$D_{\text{array}}(\theta,\hat{\theta}) \propto \text{AF}^2(\theta,\hat{\theta}) \cdot D_{\text{ant}}(\theta). \tag{B.8}$$

We shall use this formulation to calculate the directivity of two ULAs for $\hat{\theta} \in [0°,\ldots,180°]$. The first ULA is made of isotropic antennas, the second of cosine shaped element patterns of the form

$$D_{\text{ant,cos}}(\theta) = \cos(\theta)^{1.2}. \tag{B.9}$$

We obtain the ideal monostatic characteristic by plotting $D(\hat{\theta},\hat{\theta})$ over $\hat{\theta}$. Inserting this into (B.6), we see that the array factor becomes $\text{AF}(\hat{\theta},\hat{\theta}) = N$. Fig. B.6 shows the respective results for different array sizes N. As can be expected for the isotropic element array, the monostatic curves in Fig. B.6a are perfectly flat. This is because for each pointing angle $\hat{\theta}$ we find an excitation which causes constructive superposition of the electric fields transmitted by all antenna elements. In the case of non-isotropic elements, we see a decline in the ideal monostatic curves if we move away from boresight. The dashed curves in both plots are obtained by normalizing the solid curves by their respective maxima. That means, the monostatic characteristic is independent of the number of array elements. Although it is not shown here, the monostatic curves are also independent of the array spacing d_r as long as mutual coupling is neglected.

From these calculations, we see that the normalized monostatic characteristic is independent of array size and spacing. However, it mirrors the single element pattern. Even though the analytic patterns and characteristics shown here are idealized, we can expect a similar behavior when measuring RDA systems.

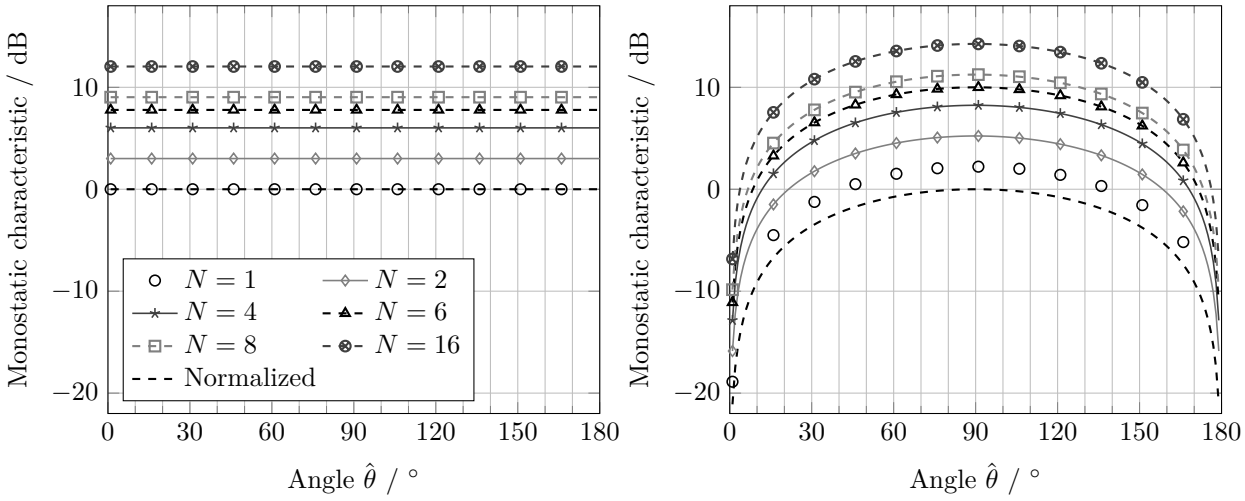

Fig. B.6: Optimum monostatic patterns calculated in MATLAB for ULAs with $d_r = 0.5$ and (a) isotropic radiators as well as (b) elements with $\cos(\theta)^{1.2}$ shaped directivity. The solid curves are for different numbers of elements N, the dashed curve represents the monostatic characteristics normalized to their maximum values.

C Demonstrator system hardware

C.1 Dual-band antenna array

For the RDA demonstrator, we have used a 5.8/7.0 GHz dual-band ULA with eight elements described in section 5.1.1. We have measured the antenna array in two configurations. First, without any additional RF hardware. That means the antenna was placed in an anechoic chamber and measured directly using the antenna ports. This is the classic measurement procedure for a passive antenna. Second, we used the complete Tx path of the retro-directive demonstrator. The measurement signal was thereby fed to the antenna via the FPGA and Tx front-ends. Additionally, absorbers were placed around the antenna in order to shield metallic structures which could cause reflections. From these active measurements, we get the embedded pattern of the array elements, i.e. the pattern as it occurs when the antenna is in its operation environment. Fig. C.1 shows a comparison of the measured passive and active patterns for the corner antenna element 1 and the middle element 4 at 7.0 GHz. We can see the influence of the additional hardware. While this does not impair the phased array beamsteering we use for retro-directive operation, it is interesting to see the influence of the system setup. It means that the passive patterns cannot be used to evaluate beamforming coefficients for the complete Tx system. Instead, it is necessary to measure the active patterns to obtain the installed performance of the antenna.

C.2 Analog transmitter front-ends

The Tx front-ends have been developed by students of our partner UNIPAMPA, Alegrete, Brazil. Some results have been published in [98]. The requirements for the front-ends are

1) Input frequency in the bandwidth of the DACs [104],

2) Output frequency of 7.0 GHz,

3) Tx power >10 dBm.

The developed front-end consists of two modules which are depicted in Fig. C.2: The IF signals from the DAC are first mixed up to 1.9 GHz. This is done on the PCB in Fig. C.2a. At this second IF, we perform analog beamforming using a digitally steerable phase shifter and a VGA. The upconverter module in Fig. C.2b contains a second mixing stage with which we obtain the desired 7.0 GHz output signal. Table C.1 lists details about the link budget of both front-end modules.

Originally, we have planned to use the phase shifters and VGAs to do analog beamforming. However, it has turned out that the two devices do not work independently from each other. That means, if we change the phase shifter setting of a front-end, its gain is also affected by

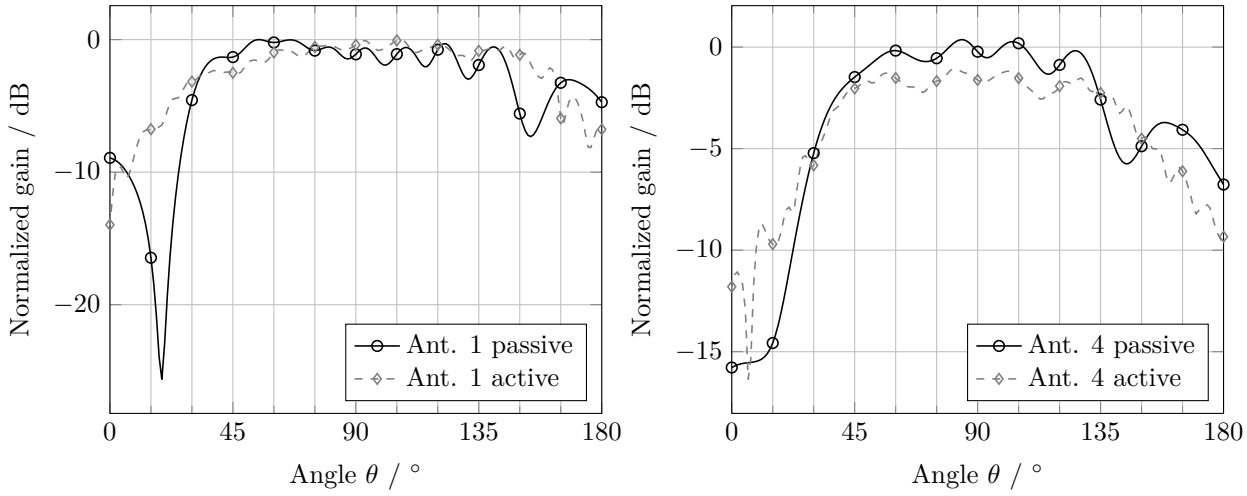

(a) (b)

Fig. C.1: Comparison of the Tx antenna array element patterns at 7.0 GHz. The curves are normalized to the maxima of antenna element 1.

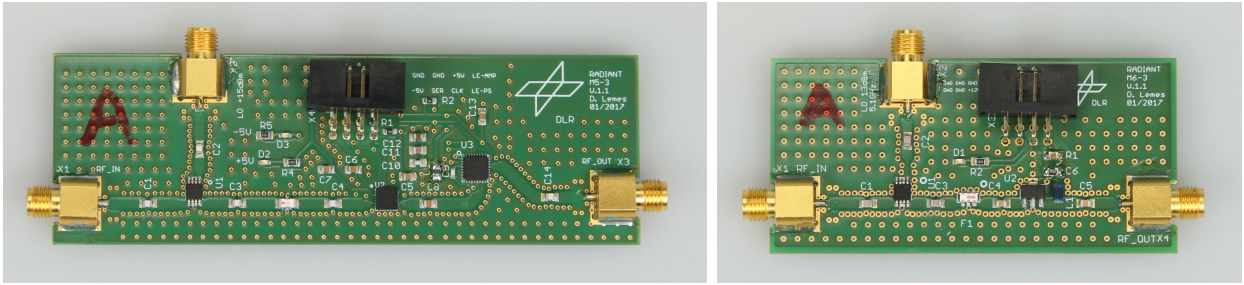

(a) (b)

Fig. C.2: Photograph of assembled Tx front-end modules. (a) Beamforming module with phase shifter and VGA at 1.9 GHz, (b) Upconverter module with 7.0 GHz output frequency.

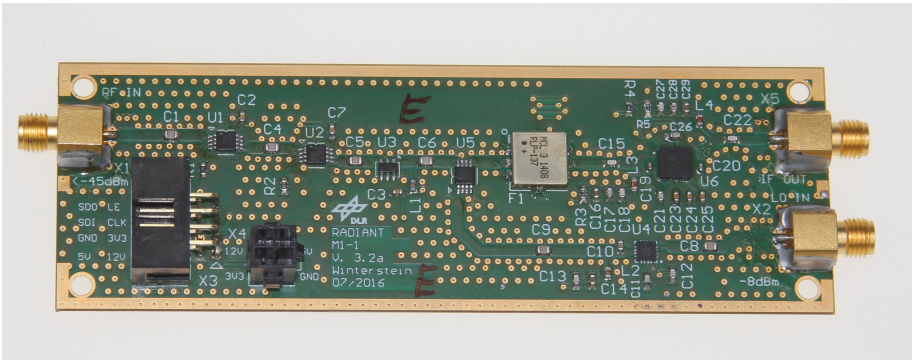

Fig. C.3: Photograph of an assembled Rx front-end. The SMA connectors are for RF input on the left side, IF output and LO input on the right.

Table C.1: Link budget of Tx front-ends

Component		Gain / dB	Link budget / dB
U1	Mixer – HMC316 [105]	-8	-8
F1	Bandpass – BFCN-1945+ [106]	-2	-10
U2	Phase shifter – MAPS-010163 [107]	-5	-15
U3	VGA – ADL-5240 [108]	20	5
U1	Mixer – HMC-218 [109]	-7	-2
F1	Highpass – HFCN-6010+ [110]	-1	-3
U2	Gain block – GALI-2+ [111]	14	11

this change. Moreover, we found the steps of the phase shifters to be not equally spaced as promised in the data sheet.

Thus it is not possible to do e.g. phased array beamforming by simply steering the phase shifter. On the contrary, it would have been necessary to measure all possible combinations of phase shifter and VGA settings for each front-end in order to be able to pick the setting which corresponds to a desired beamforming coefficient. Since this is not feasible, we have decided to use the phase shifters and VGAs of our front-ends only to calibrate the Tx path. Therefore, we found settings which ensure that all Tx paths exhibit the same magnitude and phase at their outputs. The measurement results are depicted in Fig. C.4. On the left hand side, we see magnitude and phase of each front-end before the calibration. All VGAs are set to minimum amplification. It can be seen that the differences are considerably high. On the right hand side, we have the characteristics of all front-ends after calibration. Hereby, the whole Tx signal path including the FPGA is measured. The procedure is detailed in appendix C.5. We see that we could greatly decrease the differences between all Tx channels by adjusting the phase shifter and VGA setting. We have used this calibration for the experimental results shown in chapter 5 and in appendix C.6.

C.3 Analog receiver front-ends

We have developed the Rx front-ends specifically for the RDA system presented in this thesis. Thereby, we have assumed that the system shall be used for measurements in free-space and compact antenna test ranges. Therefore, LoS distances up to 100 m must be bridged. An estimate for the resulting link budget is based on the following considerations:

1) According to (1.19), the expected propagation loss for this distance is approximately $l_{\mathrm{p,Rx}} = 88\,\mathrm{dB}$ at 5.8 GHz,

2) The ADCs have a full scale input power around $P_{\mathrm{RDA,Rx}} = 4\,\mathrm{dBm}$ [112],

3) The available measurement signals from the test facilities can have powers up to $P_{\mathrm{ATR,Tx}} = 20\,\mathrm{dBm}$,

4) The measurement antennas are directional with gain values of at least $g_{\mathrm{ATR}} = 10\,\mathrm{dBi}$,

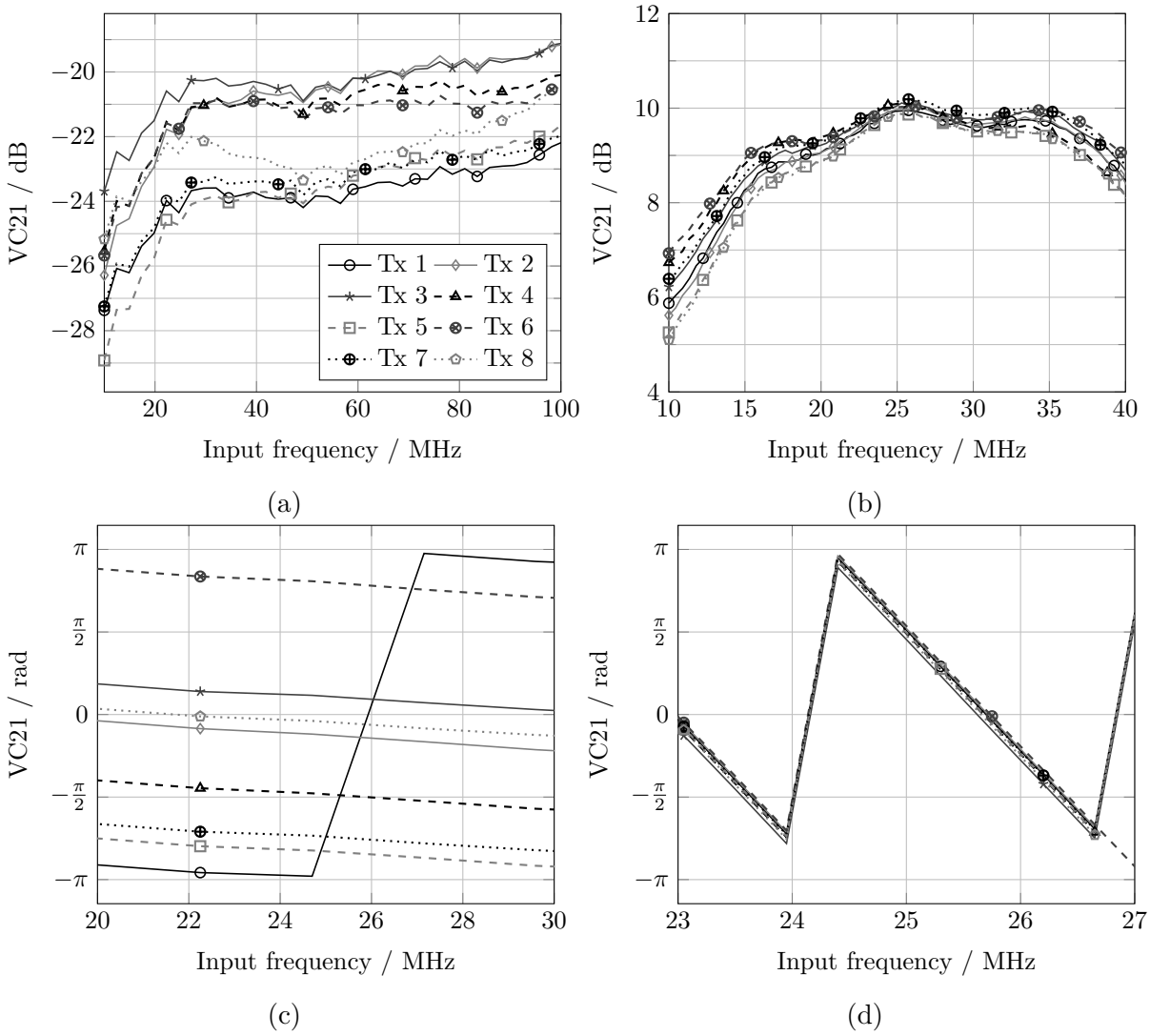

Fig. C.4: VC21 magnitude of the Tx front-ends (a) before and (b) after calibration. (c) and (d) show the respective VC21 phase values.

Table C.2: Link budget of Rx front-ends

Component		Gain / dB	Link budget / dB
U1	LNA 1 – HMC320 [113]	12	12
U2	LNA 2 – HMC320	12	24
U3	Gain block – HMC313 [114]	17	41
U5	Mixer – HMC218 [109]	-7	34
F1	Lowpass filter – RLP-137+ [115]	-1	33
U6	VGA – HMC681ALP5E [116]	45	78

5) The Rx antennas have a small gain which varies over their FoV, so we assume their contribution is 0 dBi.

From this, we obtain an estimate for the required gain of the receiver path to be

$$g_{\mathrm{Rx}} = \frac{P_{\mathrm{RDA,Rx}} \cdot l_{\mathrm{pRx}}}{P_{\mathrm{ATR,Tx}} \cdot g_{\mathrm{ATR}}} = 62\,\mathrm{dB}. \tag{C.1}$$

The requirements for the development of the Rx front-ends are therefore:

1) Input frequency 5.8 GHz,

2) Output frequency within the analog bandwidth of the ADCs, i.e. <400 MHz,

3) Conversion gain >62 dB to enable measurements in the antenna far field.

Fig. C.3 shows a photograph of the final Rx front-end. Eight units are necessary for the complete RDA system. The signal flow is from left to right: The RF signal enters the front-end at the SMA connector X1. We pass the signal through a cascade of two LNAs (U1, U2) and a gain block (U3) to increase signal power. After that, we mix the RF signal down to an IF using U5. The necessary LO signal enters the PCB through SMA connector X2 and is amplified in the high power amplifier (HPA) U4. After the down-mixer, we employ a lowpass filter F1 to eliminate higher mixing products. We adjust the IF signal power by the VGA U6 before it is output at the connector X5. Table C.2 details the components used in the RF to IF path of the front-end. The listed gain values are nominal. For the VGA, we list the maximum gain.

When designing a front-end for RF signals, we expect the circuit to exhibit losses from impedance mismatch at the various transition points between 50 Ω strip lines on the PCB and components. Additionally, losses from the PCB substrate are to be expected. Since, we do not have the necessary software to simulate these losses beforehand, we have included a gain margin in the link budget.

Fig. C.5 shows measurement results obtained for all eight Rx front-ends. In order to measure a down converting circuit with a VNA we need to perform vector-mixer calibration (VMC) measurements. Instead of the standard S-parameters, the measurement result for VMC is the forward conversion gain VC21 of a down-converter.

We see that the measured conversion gain of the eight front-ends is between 61 and 68 dB. This is considerably lower than expected from the nominal gain values of the individual

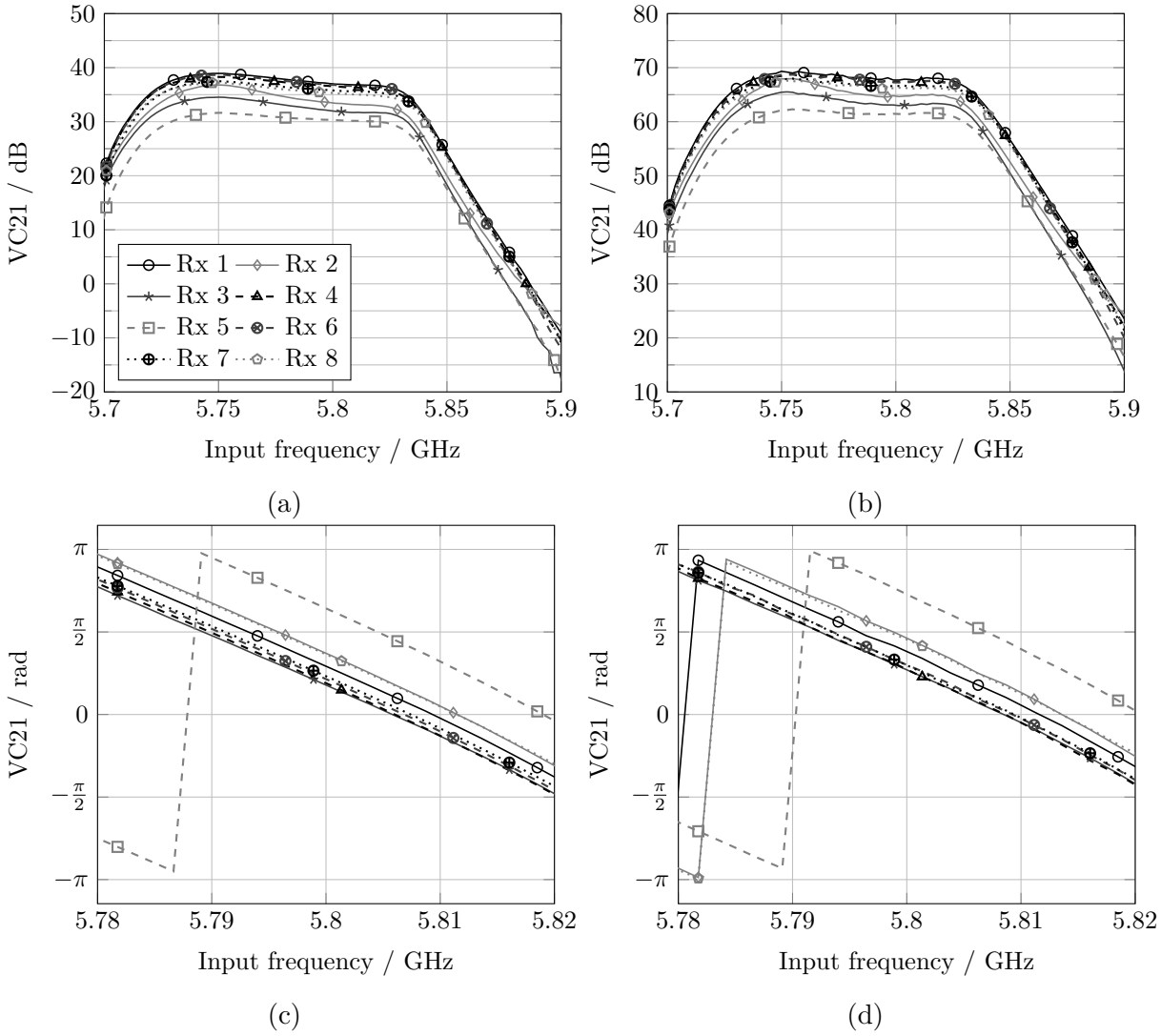

Fig. C.5: Magnitude of conversion gain VC21 for (a) minimum and (b) maximum VGA settings of all eight Rx front-ends. (c) and (d) show the respective phase of VC21.

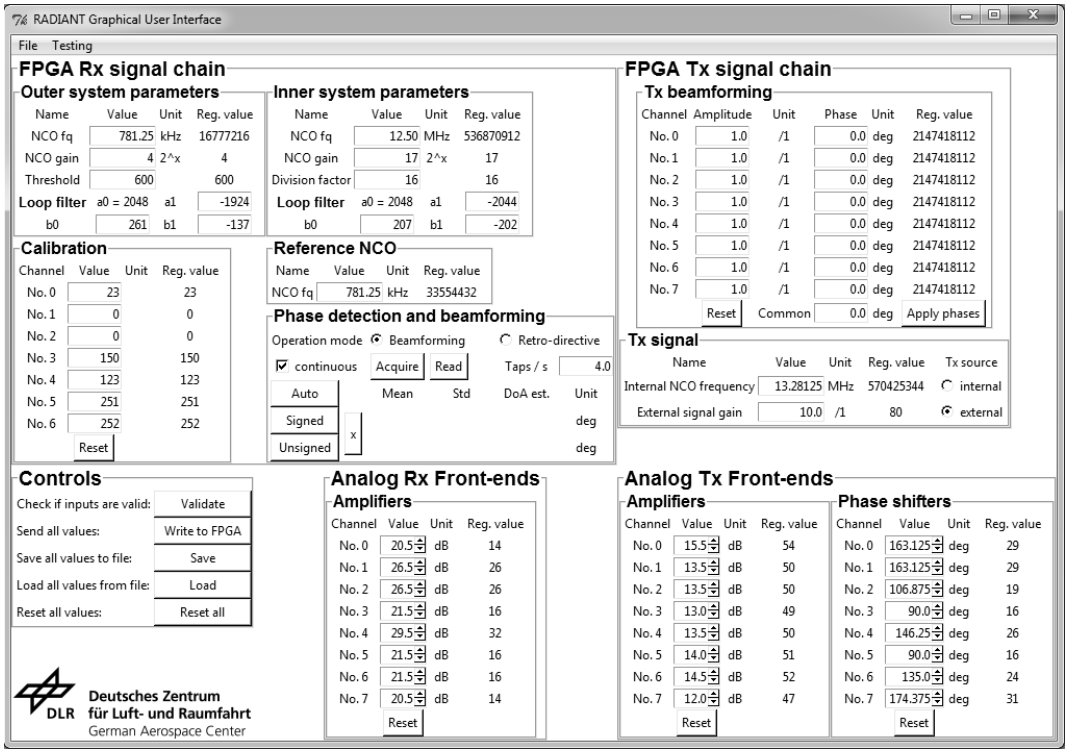

Fig. C.6: Screenshot of the graphical user interface used to control the demonstrator setup. It allows to change parameters of the Rx and Tx paths on the FPGA, but also to control the VGA and phase shifter settings on the analog front-ends.

components in Table C.2 but meets our previously set gain requirement in all but one front-end. However, since we do not require the full scale power at the ADC input, the available gain should be sufficient for the RDA measurements.

C.4 Graphical user interface

In this section, we describe the graphical user interface (GUI) that we use to control the demonstrator system. The program is written in Python and its main window can be seen in Fig. C.6. The back-end of the GUI program communicates via USB with the JTAG interface of the FPGA. Thus it is possible to send data words from the PC to the digital hardware. In the upper left part of the GUI, we can change receiver parameters like loop filter coefficients, quiescent frequencies, etc. The "Calibration" section is used to equalize differences in the Rx phase detection paths. We find the correct settings by receiving a signal from boresight direction and measure the resulting phase detection values. In the middle section, superscribed "Phase detection and beamforming", we can obtain the current phase and DoA estimate from the FPGA. We can also set the operation mode of the system. "Retro-directive" hereby means that the digital beamforming coefficients are taken from the ROM in Fig. 4.10, according to the phase detection values. If we choose "Beamforming", we can set the Tx coefficients manually in the upper right part of the GUI. We use this mode for the hardware loop experiments with the receiver and to test the Tx path alone.

As can be seen in the measurement setup in Fig. 5.1, the FPGA is connected to the Rx and Tx front-end PCBs via an interface card. This connection implements an SPI bus over which we can address the VGAs and phase shifters to adjust their gain settings and phase shifts. The user can access these controls in the lower part of the GUI window.

With the GUI, we are able to change all necessary parameters of our demonstrator system from a single point. This has been especially useful during the CTR measurements because there is no need to repeatedly access the RF hardware in the chamber. Additionally, we have used the GUI in our hardware loop tests in section 4.3.2.

C.5 Transmitter path calibration setup

As mentioned in section 5.1.1, we need to calibrate the Tx signal chains of our RDA demonstrator. The goal of this procedure is to ensure that a single Tx input signal arrives with equal magnitude and phase at all antenna input ports. This is a prerequisite for beamforming since differences in the individual signal paths will lead to a deviation of the generated patterns from the desired ones.

Fig. C.7 shows the hardware setup which we use for Tx calibration. It is identical to the Tx path shown in the complete CTR setup without the antenna. The LO signal chains are the same as for the demonstrator, including cable lengths. This ensures that the LO power and phase are always the same. Also the support devices, i.e. power supply, power distribution and host PC connection are identical to the CTR setup.

The central measurement device is the VNA. It outputs an IF signal to the input ADC of our FPGA board. This signal propagates through the digital beamformer and the eight DACs before it is fed to the Tx front-ends. During calibration, all digital beamforming coefficients are unity. Thus we ensure input signals of equal magnitude and phase for the front-ends. We then subsequently connect each front-end output to the VNA to measure the conversion gain. One front-end setting is thereby taken as a reference. All other front-ends have their VGA gain and phase shifter settings adjusted until they match the reference. The calibration result is shown in Figs. C.4b and C.4d.

It should be noted that the VNA does not perform a standard S-parameter measurement in this procedure but a so called VMC. That means, it measures the conversion gain of an up-mixer in our case with two stages. In order to do this, the VNA needs a reference up-mixer path. This is shown left of the VNA in Fig. C.7: The two reference mixers use the same LO signals as the measured front-ends. This is important since the up-mixed signals in reference and measurement paths need to be coherent in order to yield correct phase differences. To ensure this, the VNA and LO generators are additionally synchronized by a common 10 MHz signal which is not shown in the diagram.

C.6 Transmitter performance

Prior to retro-directive experiments, we have analyzed the transmitter path of the RDA demonstrator alone. Fig. C.8 shows measured antenna patterns with digital beamforming. For the three cases in Figs. C.8a, C.8c and C.8d, we employed the phased array beamforming coefficients which are stored in the ROM in Fig. 4.10 and are used during retro-directive

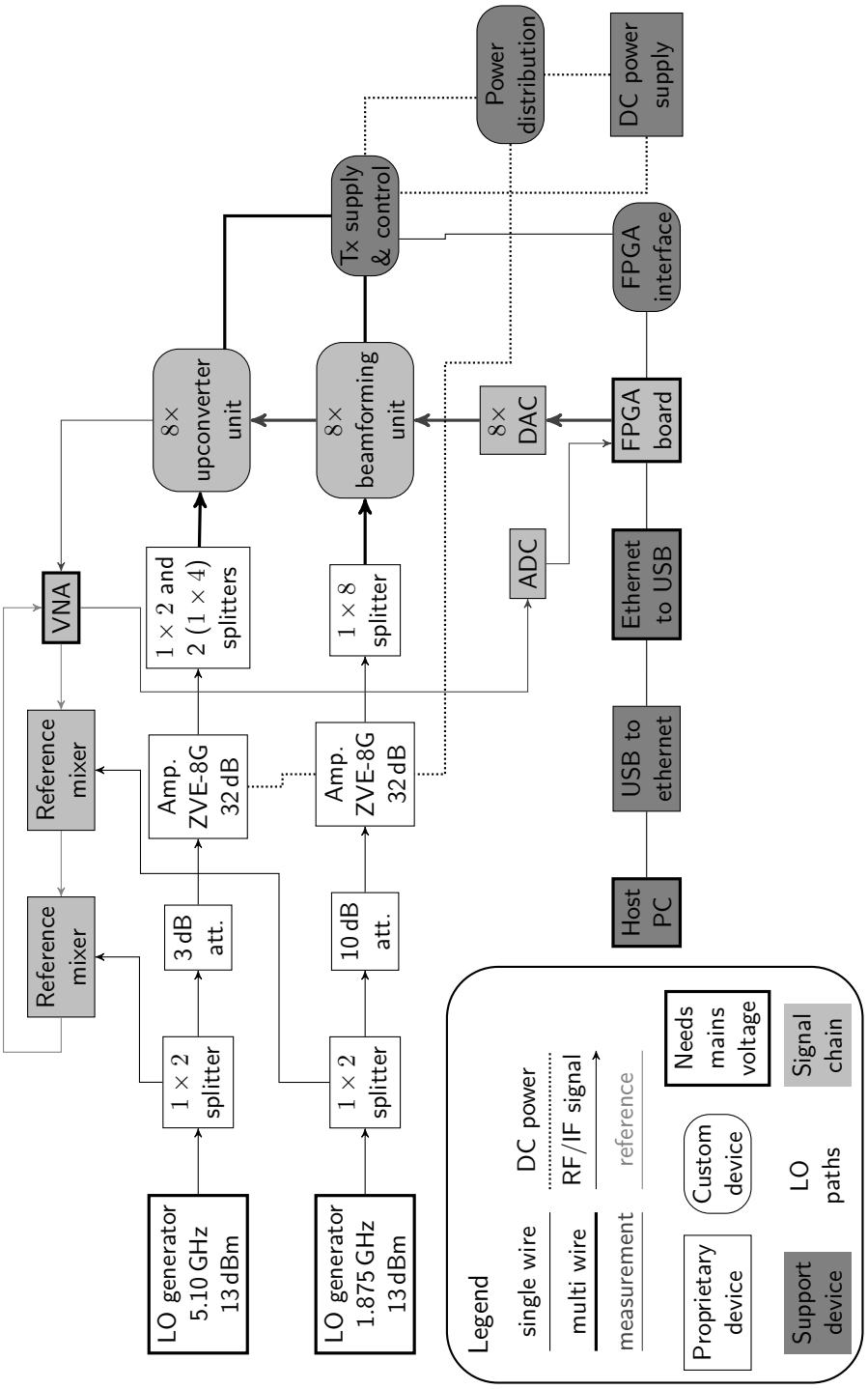

Fig. C.7: Block diagram of the measurement setup for calibration of the demonstrator Tx paths.

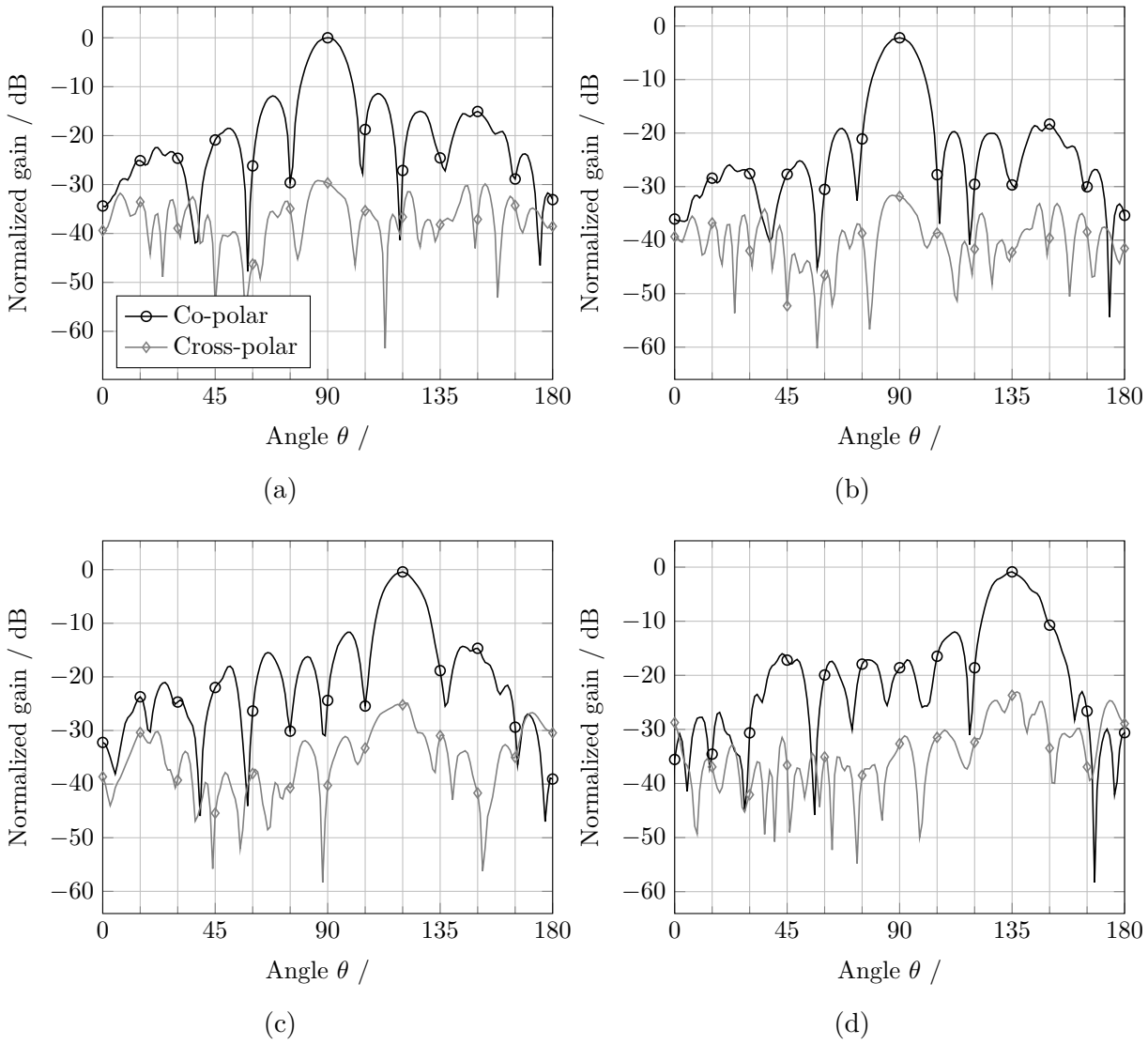

Fig. C.8: Tx beamforming capability of the system. (a) Radiation pattern after calibration, no beamforming, main lobe in boresight direction, i.e. 90°. (b) Chebishev amplitude tapering for boresight direction, theoretical side lobe level −20 dB. (c) Phased array beamsteering towards 120°. (d) Phased array beamsteering towards 135°. The gain curves are normalized to the maximum of (a).

operation. We can see that the main lobes of the patterns are towards the desired directions. A power decrease of about 1 dB can be observed in the main lobe for 135° steering. This is due to the radiation patterns of the antenna array elements which have their maximum approximately in boresight direction.

Of course, digital beamforming gives us more degrees of freedom for the pattern synthesis. As an example, we used Chebishev amplitude tapering to reduce the side lobe level of the boresight looking pattern in Fig. C.8b [103, c.6.7.3]. Although we do not achieve the theoretically predicted value of −20 dB, we still see a considerable improvement over Fig. C.8a The drawback of amplitude tapering is the approximately 3 dB drop in main lobe level.

From these results, we see that the Tx path of the demonstrator with digital beamforming is working as expected. Using phased array steering, we are able to direct the main lobe of the array pattern towards the desired directions. This is a prerequisite for retro-directive behavior.

Acronyms

ADC	analog-to-digital converter. 24, 81, 83–85, 89, 90, 93, 95, 125, 127, 129, 130
AM	amplitude modulation. 16
AUT	antenna-under-test. 90, 93, 96, 97
AWGN	additive white Gaussian noise. 49, 51, 118
BER	bit error rate. 20, 55, 57, 101
BPF	bandpass filter. 17
BPSK	binary phase shift keying. 20, 49, 50, 54–57, 118, 119
BSS	broadcast satellite service. 6, 7
CMOS	complementary metal oxide semiconductor. 108
CTR	compact test range. 9, 89–92, 100, 103, 104, 130
DAC	digital-to-analog converter. 22, 24, 81, 83–85, 89, 95, 123, 130
DC	direct current. 92, 93, 95
DCC	duty cycle counter. 70–73, 76, 79, 81, 85, 88
DLR	Deutsches Zentrum für Luft- und Raumfahrt e.V.. 89, 90, 94, 104
DoA	direction-of-arrival. iii, 14, 20, 21, 23, 33, 35, 52, 58, 60–64, 80, 85–89, 97–101, 129
DSP	digital signal processing. iii, 6, 20, 23–25, 27
EM	electro-magnetic. 2–5, 11, 14, 57, 96
FIFO	first-in, first-out. 81, 83
FM	frequency modulation. 69
FoV	field-of-view. iii, iv, 19, 86, 88, 98, 127
FPGA	field-programmable gate array. iii, 8, 20, 24, 65, 72, 81–85, 88, 90, 93, 95, 99, 101, 103, 123, 125, 129, 130

FSS fixed satellite service. 6, 7

GPIO general-purpose input/output. 84, 95
GUI graphical user interface. 129, 130

HPA high power amplifier. 127

IF intermediate frequency. 8, 15, 17–19, 25–29, 32–36, 41, 49, 52–57, 65, 67, 72, 73, 76–79, 81, 82, 88, 90, 93, 95, 100, 117, 119, 120, 123, 124, 127, 130
IIR infinite impulse response. 67, 68, 72, 73, 120

JTAG Joint Test Action Group. 83–85, 129

LF low frequency. 16, 18, 19
LNA low-noise amplifier. 12, 127
LO local oscillator. 5, 14–20, 23, 24, 89, 90, 92–95, 124, 127, 130
LoS line of sight. 21, 64, 125
LSB least significant bit. 68, 70, 71

MOSFET metal oxide semiconductor field effect transistor. 108, 117
MSB most significant bit. 70
MSS mobile satellite service. 6, 7

NCO numerically controlled oscillator. 69–73, 78, 81, 83, 84, 120

PCB printed circuit board. 13, 90, 93–95, 123, 127, 130
PFD phase-frequency detector. 27, 28, 30–34, 36, 41, 50, 51, 67, 68, 70–72, 78, 80, 81, 108–111, 117–119
PLL phase-locked loop. 14, 16–24, 27, 28, 30, 32, 33, 36–38, 40–43, 45, 49, 53, 64, 68, 70, 73, 78, 79, 101, 103, 111, 114, 117, 118

RADAR radio detection and ranging. 16, 96
RCS radar cross section. 11–13, 96
RDA retro-directive antenna. iii, 8, 9, 11–22, 25, 27, 34, 52, 57, 64, 65, 89, 93, 96–98, 103, 104, 121, 123, 125, 127, 129, 130

RF	radio frequency. 2, 9, 14, 16, 17, 19, 25–29, 32–36, 41, 49–52, 54, 55, 57, 66, 70–73, 81, 82, 85, 89, 90, 92, 95–97, 103, 104, 111, 118, 119, 123, 124, 127, 130
RFID	radio frequency identification. 12, 23
ROM	read-only memory. 83, 99, 129, 130
Rx	receiver. iii, iv, 5, 6, 8, 12–28, 34, 35, 57, 65, 88–90, 93–97, 100, 101, 103, 124, 125, 127–130
SAR	synthetic aperture radar. 11
SLR	satellite laser ranging. 2
SMA	SubMiniature version A. 84, 93, 95, 124, 127
SNR	signal-to-noise ratio. iii, 19, 49–55, 57, 119
SOM	self-oscillating mixer. 16
SPI	serial peripheral interface. 93, 130
TT&C	telemetry, tracking, and command. 6
TUM	Technische Universität München. 104
TV	television. 6, 7
Tx	transmitter. iii, iv, 5, 6, 8, 12–27, 29, 34, 57, 65, 82–84, 88–90, 93, 95–98, 100, 103, 123–126, 129–133
ULA	uniform linear array. iii, 3, 4, 14, 29, 34, 57, 60–62, 84, 89, 90, 93, 97, 103, 121–123
UNIPAMPA	Universidade Federal do Pampa. 90, 104, 123
USB	universal serial bus. 83, 84, 90, 93, 129
VCO	voltage-controlled oscillator. 18, 27, 28, 31–34, 36–38, 41, 50, 58, 69, 70, 111, 117–119
VGA	variable gain amplifier. 27, 90, 93, 95, 123–125, 127–130
VHDL	VHSIC hardware description language. 76, 81, 103
VHF	very high frequency. 7
VMC	vector-mixer calibration. 127, 130
VNA	vector network analyzer. 90, 92, 93, 95, 96, 104, 127, 130

Symbols

$*$	Convolution. 54
$\cdot$	Multiplication sign. 3, 16, 39, 42, 45, 47, 54, 57, 58, 107, 121, 127
Δ	Combined phases. 57–59
Ω	Discrete time frequency. 66
Π	Difference of phase geometric and signal phase terms. 59
Ψ_{IF}	IF signal phase term. 32–34, 36, 66
Ψ_{RF}	RF signal phase term. 32–34, 36, 57, 70, 111–113, 120
Ψ_{V1}	VCO phase term of outer PLL. 32–34, 36, 111–113
Ψ_{V2}	VCO phase term of inner PLL. 32, 111–113
Ψ_{ref}	Phase term of the reference signal. 33, 34, 70, 111, 112, 120
Ψ	Phase term. 29–33, 35, 36, 38, 39, 66, 67, 69, 70, 111, 113, 120
Σ	Sum of geometric and signal phase terms. 59
α	Factor between actual and maximum natural frequency. 39, 43, 47, 115
$\bar{\delta}$	Time average over mean phase estimates. 80
β	Difference of cosines. 59–63
δ_Δ	Dirac delta distribution. 109
δ	Composite phase. 3–5, 29, 33–35, 49–51, 53, 54, 57–59, 71, 72, 79, 80, 83, 85–87, 119, 121
ϵ_δ	Array squint correction factor. 6
η_0	Impedance of free space. 121
η	Efficiency of a receiver or transmitter. 7
γ	Sum of cosines. 59–64
$\hat{\delta}$	Mean phase estimates over all channels. 79, 80, 86
$\hat{\theta}$	Estimated DoA. 34, 97
λ	Eigenvalue. 113
λ	Wave length. 2, 3, 7, 29, 59, 60

ν Noise signal. 119
ω_0 Natural frequency of a harmonic oscillator. 38–47, 49, 114, 115, 117
ω_{IF} IF signal angular frequency. 53
ω_{RF} RF signal angular frequency. 29, 33, 35, 36, 57, 58, 113
ω_{q1} Quiescent frequency of outer VCO. 33–36, 58, 112, 113
ω_{q2} Quiescent frequency of inner VCO. 32–36, 58, 112, 113
ω_{ref} System reference frequency. 17, 18, 33, 35, 36, 54, 58, 112, 113
ω Angular frequency. 2–6, 16, 29–32, 40, 41, 43, 45, 47, 49, 73, 75, 78, 109
ϕ Azimuth angle. 1, 2
π Ratio between a circles circumference and diameter. 2, 3, 7, 13, 29, 31, 33, 34, 50, 53, 54, 59, 60, 64, 67, 69, 71, 78–80, 85, 86, 107, 109, 110, 115, 117, 119, 121
σ Standard deviation. 50, 51
τ_{IF} System response decay time. 52–54, 57
τ Filter time constant. 36, 37, 39, 40, 42, 43, 45, 47, 49, 54, 67, 72, 73, 110–115
θ Elevation angle. 1–6, 27, 29, 33–35, 57–64, 79, 83, 84, 96–98, 100, 121, 122
φ_{RF} RF signal phase. 29, 33, 35, 112, 113
φ Signal phase. 5, 29–31, 53, 57–60, 64, 68, 69, 72, 109, 110
ζ Damping coefficient of a harmonic oscillator. 38–47, 49, 114, 115, 117

$\mathbf{A}$ System matrix. 111, 112
a Factor for minimum and maximum parameter variation. 43, 44
A_{eff} Effective area, also called antenna aperture. 7
AF Array factor. 121
a Feedback digital filter coefficient. 67, 68, 73, 120
atan2 Arcus tangens with two arguments. 58, 59, 107

b Forward digital filter coefficient. 67, 73, 120
b_s Phase detection smoothing bits. 71, 72

c Speed of waves in material medium. 4
c_0 Speed of light in vacuum. 2–5, 29

D Directivity of an antenna. 121
d Array element spacing. 3, 5, 29
$\breve{D}_h$ Denominator of one-pole, one-zero filter transfer function. 36
D_h Denominator of filter transfer function. 30, 36, 38, 113, 114
d_r Relative element spacing. 29, 33, 34, 62, 86, 87, 90, 121, 122
d_{SHFT} Bit shifter distance. 68, 72

E Electric field strength. 2, 4
$\vec{e}$ Unity vector. 1–4, 121
e Exponential function. 2, 13, 53, 111, 121
$\vec{E}_0$ Complex electric field amplitude vector. 2–4
e_δ Phase detection error. 51
$\vec{E}$ Electric field vector. 2–4, 121
E Expected value. 30

f Frequency. 41, 54, 55, 69, 71, 72, 84, 117, 119
f_{clk} Clock frequency. 71–73, 81, 83
f_{Rx} Received signal frequency. 25, 26
F_s Sample frequency. 67–69
f_{Tx} Transmit signal frequency. 25, 26

G System transfer function. 37–43, 45, 47–50, 52, 54, 57, 113, 114
g Antenna gain. 7
g Gain of a component. 125, 127

H Hilbert transform. 53
H Complex conjugation operator (Hermitian). 4
h Filter transfer function. 27, 30–40, 54, 58, 67, 68, 70, 111, 113, 117
$\breve{h}$ Transfer function of analog one-pole, one-zero filter. 36, 37, 114

i Current signal. 111

j Imaginary unit. 2, 13, 40–43, 45, 47–49, 53, 73–75, 78, 121

K Component gain. 30–34, 41, 67, 69, 70, 72, 110–112, 117
K Number of users. 57, 58
$\vec{k}$ Wave vector. 2–4
k User index. 57, 58
K_1 Outer PLL linear forward gain. 33–41, 49, 58, 70, 72, 73, 76, 112–114, 120
K_2 Inner PLL linear forward gain. 32–38, 40, 41, 43, 49, 58, 70, 72, 73, 76, 112–115, 120

$\mathcal{L}$ Laplace transform. 33
L Filter order. 30, 32, 36
l User index. 58
L Length of moving average and variance calculation. 81, 83
l_{eff} Effective length of an antenna. 4
l_{p} Propagation loss. 7, 125, 127
ℓ Length of a transmission line. 4
L_{var} Number of parameter variations. 43, 44, 47

M PLL division factor. 27, 31–41, 43, 49, 52, 53, 58, 59, 69–73, 76, 79, 111–115, 117–120
m Integer number. 31, 109, 110

N Number of array elements. 3, 4, 13, 26, 27, 29, 33–35, 52, 53, 59, 61, 62, 79, 119, 121, 122
n Array element index. 3–5, 27–29, 31–39, 52, 53, 57–60, 62, 111–114, 121
$\breve{N}_h$ Numerator of one-pole, one-zero filter transfer function. 36
N_h Numerator of filter transfer function. 30, 36, 38, 113, 114
n Discrete time. 66–69, 81, 83

P Power. 7, 125, 127
$\vec{p}$ Antenna polarization. 2, 4
$\mathbf{p}$ System parameter vector. 40, 43, 47, 49

R Resistance. 110, 111
$\mathfrak{R}$ Real part. 38, 40, 41, 75
r Radius in spherical coordinate system. 121
$\vec{r}$ Position vector. 2, 4

S Power flux density. 7
S Scattering parameters. 13
s Complex frequency. 30–43, 48–50, 57, 58, 67, 75, 113, 114
sgn Sign function. 59, 107, 115, 119
SNR Signal-to-noise ratio. 50, 54, 119

T Period length. 109, 110
T Conjugate of a vector or matrix. 2, 4, 40, 112
t Continuous time. 2–5, 29–31, 33–35, 50–55, 57–59, 72, 80, 83, 109–113, 117, 119
T_d Discrete time delay. 70, 75, 120
$t_{\mathrm{upd,pd}}$ Update time of the phase detection output. 71, 79

u Heaviside step function. 110

V Voltage. 57, 58
v Voltage signal. 4, 5, 27–33, 52–55, 57, 58, 108–112, 117, 119
v_{d} Phase-frequency detector output voltage. 30, 31, 108–111
v_{IF} Intermediate frequency sum signal voltage. 28, 29, 50, 52–54
v_{Δ} Channel phase detection output voltage. 32, 79
$\bar{v}_{\Delta}$ Time average of the phase detection output voltage. 33, 34, 50, 51, 58, 59
$\bar{\bar{v}}_{\Delta}$ Integrated time average of the phase detection output voltage. 50, 51

w Word width, i.e. number of bits of a digital signal. 65, 68–72, 79, 83

x x-coordinate. 2
x Input signal. 66–69, 81, 83

$\mathbf{x}$ System state vector. 111, 112

y y-coordinate. 2, 121
y Output signal. 66–69, 83

z z-coordinate. 2–4, 59, 62
z Discrete time frequency. 66–70, 120

Bibliography

[1] B. R. Elbert, *Introduction to Satellite Communication*. Norwood, MA 02062: Artech House, 2008.

[2] C. Alley, R. Chang, D. Currie, and S. Poultney, "Laser ranging retro-reflector: Continuing measurements and expected results," *Science*, vol. 167, pp. 458–460, January 1970.

[3] P. L. Bender, D. G. Currie, S. K. Poultney, R. H. Dicke, D. H. Eckhardt, W. M. Kaula, J. D. Mulholland, H. H. Plotkin, E. C. Silverberg, and J. E. Faller, "The lunar laser ranging experiment," *Science*, vol. 182, pp. 229–238, October 1973.

[4] L. Combrinck, *Satellite Laser Ranging*, pp. 301–338. Berlin, Heidelberg: Springer Berlin Heidelberg, 2010.

[5] J. D. Jackson, *Classical Electrodynamics*. New York: John Wiley & Sons, Inc., 1962.

[6] S. A. Schelkunoff and H. T. Friis, *Antennas Theory and Practice*. New York: John Wiley & Sons, Inc., 1952.

[7] J. A. Russer, M. T. Ivrlac, M. Haider, S. Wane, D. Bajon, P. Russer, and J. A. Nossek, "Multiport model of hertzian dipoles coupled in the near-field," in *2017 47th European Microwave Conference (EuMC)*, pp. 1293–1296, Oct 2017.

[8] R. Roy and T. Kailath, "Esprit-estimation of signal parameters via rotational invariance techniques," *IEEE Transactions on Acoustics, Speech, and Signal Processing*, vol. 37, pp. 984–995, July 1989.

[9] R. E. Collin and F. J. Zucker, *Antenna Theory Part 1*, vol. 7 of *Inter-University Electronics Series*. New York: McGraw-Hill, 1969.

[10] L. C. van Atta, "Electromagnetic reflector," October 1959.

[11] C. Y. Pon, "Retrodirective array using the heterodyne technique," *IEEE Transactions on Antennas and Propagation*, vol. 12, pp. 176 – 180, March 1964.

[12] P. V. Brennan, "An experimental and theoretical study of self-phased arrays in mobile satellite communications," *IEEE Transactions on Antennas and Propagation*, vol. 37, pp. 1370–1376, Nov 1989.

[13] V. S. Labrador, *Heavens Fill with Commerce - A Brief History of the Satellite Communications Industry*. Satnews Publishers, 2005.

[14] "The European table of frequency allocations and applications in the frequency range 8.3 kHz to 3000 GHz (ECA table)," June 2016.

[15] S. W. Ellingson, *Radio Systems Engineering*. Cambridge, UK: Cambridge University Press, 2016.

[16] S. D. Robertson, "Targets for microwave radar navigation," *The Bell System Technical Journal*, vol. 26, pp. 852 – 869, October 1947.

[17] L. Lewin, "Reflections from flat sheet and angle reflectors," *Electrical Engineers - Part III: Radio and Communication Engineering, Journal of the Institution of*, vol. 95, pp. 485–488, November 1948.

[18] J. Stastny, S. Cheung, G. Wiafe, K. Agyekum, and H. Greidanus, "Application of radar corner reflectors for the detection of small vessels in synthetic aperture radar," *IEEE Journal of Selected Topics in Applied Earth Observations and Remote Sensing*, vol. 8, pp. 1099–1107, March 2015.

[19] J. D. Kraus, "The corner-reflector antenna," *Proceedings of the IRE*, vol. 28, pp. 513 – 519, November 1940.

[20] H. P. Neff and J. D. Tillman, "The design of the corner-reflector antenna," *Transactions of the American Institute of Electrical Engineers, Part I: Communication and Electronics*, vol. 78, pp. 293–296, July 1959.

[21] N. Inagaki, "Three-dimensional corner reflector antenna," *IEEE Transactions on Antennas and Propagation*, vol. 22, pp. 580 – 582, July 1974.

[22] M. T. Jusoh, O. Lafond, F. Colombel, and M. Himdi, "Performance and radiation patterns of a reconfigurable plasma corner-reflector antenna," *IEEE Antennas and Wireless Propagation Letters*, vol. 12, pp. 1137–1140, 2013.

[23] E. D. Sharp and M. Diab, "Van Atta reflector array," *IRE Transactions on Antennas and Propagation*, vol. 8, pp. 436 – 438, July 1960.

[24] D. Davies, "Some properties of van atta arrays and the use of 2-way amplification in the delay paths," *Proceedings of the Institution of Electrical Engineers*, vol. 110, pp. 507 – 512, March 1963.

[25] S. Andre and D. Leonard, "An active retrodirective array for satellite communications," *IEEE Transactions on Antennas and Propagation*, vol. 12, pp. 181 – 186, March 1964.

[26] S. L. Karode and V. F. Fusco, "Frequency offset retrodirective antenna array," *Electronics Letters*, vol. 33, pp. 1350 – 1351, July 1997.

[27] M. J. Withers, "An active Van Atta array," *Electrical Engineers, Proceedings of the Institution of*, vol. 111, pp. 982–984, May 1964.

[28] J. A. Vitaz, A. M. Buerkle, M. Sallin, and K. Sarabandi, "Enhanced detection of on-metal retro-reflective tags in cluttered environments using a polarimetric technique," *IEEE Transactions on Antennas and Propagation*, vol. 60, pp. 3727 – 3735, August 2012.

[29] A. A. M. Ali, H. B. E. Shaarawy, and H. Aubert, "Millimeter-wave substrate integrated waveguide passive van Atta reflector array," *IEEE Transactions on Antennas and Propagation*, vol. 61, pp. 1465 – 1470, March 2013.

[30] S.-N. Hsieh and T.-H. Chu, "Linear retro-directive antenna array using 90° hybrids," *IEEE Transactions on Antennas and Propagation*, vol. 56, pp. 1573 – 1580, June 2008.

[31] J.-W. Tsai, C.-H. Wu, and T.-G. Ma, "Novel dual-mode retrodirective array using synthesized microstrip lines," *IEEE Transactions on Microwave Theory and Techniques*, vol. 59, pp. 3375 – 3388, December 2011.

[32] J.-Y. Zou, C.-H. Wu, and T.-G. Ma, "Heterogeneous integrated beam-switching/retrodirective array using synthesized transmission lines," *IEEE Transactions on Microwave Theory and Techniques*, vol. 61, pp. 3128 – 3139, August 2013.

[33] S. Christie, R. Cahill, N. B. Buchanan, V. F. Fusco, N. Mitchell, Y. V. Munro, and G. Maxwell-Cox, "Rotman lens-based retrodirective array," *IEEE Transactions on Antennas and Propagation*, vol. 60, pp. 1343 – 1351, March 2012.

[34] D. M. Pozar, *Microwave engineering.* John Wiley & Sons, Inc., 4 ed., 2012.

[35] C. W. Pobanz and T. Itoh, "A conformal retrodirective array for radar applications using a heterodyne phased scattering element," in *Microwave Symposium Digest, 1995., IEEE MTT-S International*, vol. 2, (Orlando, FL, USA), pp. 905 – 908, May 1995.

[36] M. Skolnik and D. King, "Self-phasing array antennas," *Antennas and Propagation, IEEE Transactions on*, vol. 12, pp. 142 – 149, March 1964.

[37] B. Sichelstiel, W. Waters, and T. Wild, "Self-focusing array research model," *Antennas and Propagation, IEEE Transactions on*, vol. 12, pp. 150–154, Mar 1964.

[38] Y. Chang, H. R. Fetterman, I. L. Newberg, and S. K. Panaretos, "Microwave phase conjugation using antenna arrays," *IEEE Transactions on Microwave Theory and Techniques*, vol. 46, pp. 1910–1919, Nov 1998.

[39] R. Miyamoto, Y. Qian, and T. Itoh, "An active integrated retrodirective transponder for remote information retrieval-on-demand," *Microwave Theory and Techniques, IEEE Transactions on*, vol. 49, pp. 1658 – 1662, September 2001.

[40] G. S. Shiroma and W. A. Shiroma, "A 16-element two-dimensional active self-steering array using self-oscillating mixers," *IEEE Transactions on Microwave Theory and Techniques*, vol. 51, pp. 2476 – 2482, December 2003.

[41] K. M. K. H. Leong, Y. Wang, and T. Itoh, "A full duplex capable retrodirective array system for high-speed beam tracking and pointing applications," *IEEE Transactions on Microwave Theory and Techniques*, vol. 52, pp. 1479 – 1489, May 2004.

[42] D. S. Goshi, K. Leong, and T. Itoh, "A sparse retrodirective transponder array with a time shared phase-conjugator," *IEEE Transactions on Antennas and Propagation*, vol. 55, pp. 2367 – 2372, August 2007.

[43] T. Brabetz, V. F. Fusco, and S. Karode, "Balanced subharmonic mixers for retrodirective-array applications," *IEEE Transactions on Microwave Theory and Techniques*, vol. 49, pp. 465 – 469, March 2001.

[44] L. Chen, T.-L. Zhang, S.-F. Liu, and X.-W. Shi, "A bidirectional dual-frequency retrodirective array for full-duplex communication applications," *IEEE Antennas and Wireless Propagation Letters*, vol. 11, pp. 771 – 774, 2012.

[45] P. V. Brennan, "Investigation into the multipath performance of self-phased array," *IEE Proceedings H - Microwaves, Antennas and Propagation*, vol. 136, pp. 47–52, Feb 1989.

[46] V. Fusco, C. B. Soo, and N. Buchanan, "Analysis and characterization of PLL-based retrodirective array," *IEEE Transactions on Microwave Theory and Techniques*, vol. 53, pp. 730 – 738, February 2005.

[47] V. Fusco and N. B. Buchanan, "High-performance IQ modulator-based phase conjugator for modular retrodirective antenna array implementation," *IEEE Transactions on Microwave Theory and Techniques*, vol. 57, pp. 2301 – 2306, October 2009.

[48] V. F. Fusco and N. B. Buchanan, "Dual-mode retrodirective/phased array," *Electronics Letters*, vol. 45, pp. 139 – 141, January 2009.

[49] N. B. Buchanan, V. F. Fusco, and M. van der Vorst, "Satcom retrodirective array," *IEEE Transactions on Microwave Theory and Techniques*, vol. 64, pp. 1614 – 1621, May 2016.

[50] C. Tang and Q. Xue, "S-band full 360° high precision phase detector," in *2012 Asia Pacific Microwave Conference Proceedings*, pp. 97–99, Dec 2012.

[51] A. Hirai, K. Tsutsumi, Y. Takahashi, H. Nakamizo, K. Tajima, E. Taniguchi, M. Shimozawa, M. Hieda, and M. Nakayama, "Fast and highly accurate RF phase detector with analog integrator for APAA system," in *2013 Asia-Pacific Microwave Conference Proceedings (APMC)*, pp. 1–3, Nov 2013.

[52] G. S. Shiroma, R. Y. Miyamoto, and W. A. Shiroma, "A full-duplex dual-frequency self-steering array using phase detection and phase shifting," *IEEE Transactions on Microwave Theory and Techniques*, vol. 54, pp. 128 – 134, January 2006.

[53] N. Buchanan and V. Fusco, "Mirror image sawtooth phase conjugator circuit for retrodirective antenna applications," *IEEE Antennas and Wireless Propagation Letters*, vol. 6, pp. 503 – 505, 2007.

[54] R. Y. Miyamoto and T. Itoh, "Retrodirective arrays for wireless communications," *IEEE Microwave Magazine*, vol. 3, pp. 71 – 79, March 2002.

[55] L. D. DiDomenico and G. M. Rebeiz, "Digital communications using self-phased arrays," *IEEE Transactions on Microwave Theory and Techniques*, vol. 49, pp. 677 – 684, April 2001.

[56] D. S. Goshi, K. Leong, and T. Itoh, "A secure high-speed retrodirective communication link," *Microwave Theory and Techniques, IEEE Transactions on*, vol. 53, pp. 3548 – 3556, November 2005.

[57] V. F. Fusco, "Response of retrodirective array in the presence of multiple spatially separated sources," *IEEE Transactions on Antennas and Propagation*, vol. 54, pp. 1352 – 1354, April 2006.

[58] S. L. Karode and V. F. Fusco, "Use of an active retrodirective antenna array as a multipath sensor," *IEEE Microwave and Guided Wave Letters*, vol. 7, pp. 399 – 401, December 1997.

[59] R. C. Hansen, ed., *Microwave Scanning Antennas - Array Systems*, vol. 3 of *Microwave Scanning Antennas*. New York: Academic Press, 1966.

[60] V. Fusco and N. Buchanan, "Developments in retrodirective array technology," *Microwaves, Antennas & Propagation, IET*, vol. 7, pp. 131 – 140, January 2013.

[61] T. W. Nuteson, J. E. Stocker, J. S. Clark, D. S. Haque, and G. S. Mitchell, "Performance characterization of FPGA techniques for calibration and beamforming in smart antenna applications," *IEEE Transactions on Microwave Theory and Techniques*, vol. 50, pp. 3043–3051, Dec 2002.

[62] O. Castaneda, S. Jacobsson, G. Durisi, M. Coldrey, T. Goldstein, and C. Studer, "1-bit massive MU-MIMO precoding in VLSI," *IEEE Journal on Emerging and Selected Topics in Circuits and Systems*, vol. 7, pp. 508–522, Dec 2017.

[63] Y. Nakamura and T. Oshima, "A 1-gs/s 11.5-ENOB time-interleaved ADC with fully digital background calibration," in *2014 IEEE International Symposium on Circuits and Systems (ISCAS)*, pp. 1332–1335, June 2014.

[64] F. M. Gardner, *Phaselock Techniques*. Wiley, 3 ed., 2005.

[65] N. B. Buchanan and V. F. Fusco, "Triple mode PLL antenna array," in *Microwave Symposium Digest, 2004 IEEE MTT-S International*, vol. 3, pp. 1691 – 1694, June 2004. TH4C-4.

[66] N. Buchanan and V. Fusco, "Pilot tone reference-less phase conjugator for phase-modulated retrodirective antenna applications," *IEEE Antennas and Wireless Propagation Letters*, vol. 15, pp. 298–300, 2016.

[67] R. Best, *Theorie und Anwendungen des Phase-locked Loops*. Switzerland: AT Verlag, 2 ed., 1981.

[68] R. E. Best, *Phase-Locked Loops – Design, Simulation, and Applications*. New York: McGraw-Hill, 4 ed., 1999.

[69] R. E. Best, *Phase-Locked Loops*. New York: McGraw-Hill, 6 ed., 2007.

[70] I. N. Bronstein and K. A. Semendjajew, *Taschenbuch der Mathematik*. Thun: Verlag Harri Deutsch, 1989.

[71] A. Winterstein and J. A. Nossek, "Analytic signal model for flip-flop based phase-frequency detectors," *Electronics Letters*, vol. 54, pp. 200 – 202, February 2018.

[72] R. L. Miller, "Fractional-frequency generators utilizing regenerative modulation," *Proceedings of the IRE*, vol. 27, pp. 446–457, July 1939.

[73] S. L. Jang, S. J. Jian, and C. W. Hsue, "Wideband divide-by-4 injection-locked frequency divider using harmonic mixer," *IEEE Microwave and Wireless Components Letters*, vol. 27, pp. 924–926, Oct 2017.

[74] Z. Shu, K. L. Lee, and B. H. Leung, "A 2.4-GHz ring-oscillator-based CMOS frequency synthesizer with a fractional divider dual-PLL architecture," *IEEE Journal of Solid-State Circuits*, vol. 39, pp. 452–462, March 2004.

[75] Analog Devices, Norwood, MA, USA, *ADF4360-9 – Clock Generator PLL with Integrated VCO*, 2016. Rev. D.

[76] Analog Devices, Norwood, MA, USA, *ADF4355-3 – Microwave Wideband Synthesizer with Integrated VCO*, 2017. Rev. B.

[77] F. W. King, *Hilbert Transforms*, vol. 2 of *Encyclopedia of Mathematics and its Applications*. Cambridge University Press, 2009.

[78] T. F. Chun, M. K. Wannabe, A. Zamora, J. M. Akagi, and W. A. Shiroma, "Multiple interrogation of phase-conjugating arrays," in *Microwave Symposium Digest, 2009. MTT '09. IEEE MTT-S International*, (Boston, MA), pp. 1193 – 1196, June 2009.

[79] A. V. Oppenheim and R. W. Schafer, *Discrete-Time Signal Processing*. Upper Saddle River, NJ, USA: Pearson, 3 ed., 2010.

[80] A. Winterstein and A. Dreher, "Hardware-implemented adaptive calibration algorithms for antenna arrays," in *Phased Array Systems Technology, 2013 IEEE International Symposium on*, pp. 428–433, Oct 2013.

[81] A. Winterstein and L. A. Greda, "An adaptive calibration and beamforming technique for a GEO satellite data relay," *International Journal of Satellite Communications and Networking*, vol. 36, pp. 207 – 219, March/April 2018. sat.1213.

[82] C. E. Shannon, "Communication in the presence of noise," *Proceedings of the IRE*, vol. 37, pp. 10–21, Jan 1949.

[83] terasIC, Hsinchu City, Taiwan 300-70, *TR4 FPGA Development Kit – User Manual*, June 2015. V1.7.

[84] Altera, San Jose, CA 95134, *Stratix IV Device Handbook*, January 2016. SIV5V1-4.8.

[85] Altera, San Jose, CA 95134, *Data Conversion HSMC – Reference Manual*, March 2008. V1.0.0.

[86] "IEEE standard definitions of terms for antennas," April 2013.

[87] L. Chiu, Q. Xue, and C. H. Chan, "A 4-element balanced retrodirective array for direct conversion transmitter," *IEEE Transactions on Antennas and Propagation*, vol. 59, pp. 1185 – 1190, April 2011.

[88] J. P. Costas, "Synchronous communications," *Proceedings of the IRE*, vol. 44, pp. 1713 – 1718, December 1956.

[89] A. Winterstein, L. Greda, and A. Dreher, "A PLL-based retro-directive antenna system for communications with arbitrary frequency gaps," in *2015 9th European Conference on Antennas and Propagation (EuCAP)*, pp. 1–5, May 2015.

[90] A. Winterstein and A. Dreher, "Analysis of a PLL-based down converter and phase detection circuit for self-tracking arrays," in *Antennas and Propagation USNC/URSI National Radio Science Meeting, 2015 IEEE International Symposium on*, pp. 1546–1547, July 2015.

[91] L. A. Greda, A. Winterstein, and A. Dreher, "Retrodirektive Antennen für Anwendungen in der Satellitenkommunikation," in *4. nationale Konferenz Satellitenkommunikation in Deutschland*, (Bonn), DLR Raumfahrtmanagement, March 2015.

[92] L. S. Pereira and M. V. T. Heckler, "Dual-band dual-polarized microstrip antenna for Rx/Tx terminals for high altitude platforms," in *2015 9th European Conference on Antennas and Propagation (EuCAP)*, pp. 1–5, May 2015.

[93] A. Winterstein and A. Dreher, "A digital PLL based downmix and phase detection unit for retro-directive antenna systems," in *2016 IEEE International Symposium on Phased Array Systems and Technology (PAST)*, pp. 1–6, October 2016.

[94] M. P. Magalhaes, M. V. T. Heckler, A. Winterstein, and L. A. Greda, "A simulation technique for RF amplifier circuits using ANSYS electronics desktop," in *2016 IEEE International Symposium on Antennas and Propagation (APSURSI)*, pp. 739 – 740, June 2016.

[95] A. M. Engroff, L. A. Greda, M. P. Magalhaes, A. Winterstein, L. S. Pereira, A. G. Girardi, and M. V. T. Heckler, "Comparison of beamforming algorithms for retro-directive arrays with faulty elements," in *2016 10th European Conference on Antennas and Propagation (EuCAP)*, pp. 1–5, April 2016.

[96] A. Winterstein and A. Dreher, "Demonstration of a hybrid self-tracking receiver with DoA-estimation for retro-directive antenna systems," in *2017 IEEE MTT-S International Microwave Symposium (IMS)*, (Honolulu, HI, USA), pp. 590 – 593, June 2017.

[97] A. Winterstein and A. Dreher, "A hybrid self-tracking receiver implementation with direction-of-arrival estimation for retro-directive antenna systems," *IEEE Transactions on Microwave Theory and Techniques*, vol. 65, pp. 5422–5431, Dec 2017.

[98] D. L. Lemes, M. V. T. Heckler, and A. Winterstein, "A low-cost modular transmit front-end with analog beamforming capability," in *2017 SBMO/IEEE MTT-S International Microwave and Optoelectronics Conference (IMOC)*, pp. 1–5, Aug 2017.

[99] Analog Devices, Norwood, MA, USA, *ADF4356 – 6.8 GHz Wideband Synthesizer with Integrated VCO*, 2017. Rev. A.

[100] M. Frankiewicz, A. Golda, and A. Kos, "Design of CMOS analog and digital phase-locked loops based on resonant VCO," in *Mixed Design of Integrated Circuits and Systems (MIXDES), 2010 Proceedings of the 17th International Conference*, (Warsaw), pp. 247 – 250, June 2010.

[101] J. I. Brown, "A digital phase and frequency-sensitive detector," *Proceedings of the IEEE*, vol. 59, pp. 717–718, April 1971.

[102] O. H. Schmitt, "A thermionic trigger," *Journal of Scientific Instruments*, vol. 15, no. 1, p. 24, 1938.

[103] C. A. Balanis, *Antenna Theory – Analysis and Design.* The Harper & Row Series in Electrical Engineering, New York: Harper & Row, 1982.

[104] Texas Instruments, Dallas, Texas 75265, *DAC5672 – DUAL, 14-BIT 275 MSPS digital-to-analog converter*, Dec 2010. SLAS440C.

[105] Analog Devices Inc., One Technology Way, P.O. Box 9106, Norwood, MA 02062-9106, *HMC316MS8 / 316MS8E GaAs MMIC High IP3 Double-Balanced Mixer, 1.5–3.8 GHz.* v02.0505.

[106] Mini-Circuits, P.O. Box 350166, Brooklyn, NY 11235-0003, *BFCN-1945+ Data Sheet – LTCC Bandpass Filter.* Rev. D.

[107] MACOM Technology Solutions Inc., 100 Chelmsford Street, Lowell, MA 01851, *MAPS-010163 – Digital Phase Shifter 6-Bit, 1.4–2.4 GHz.* Rev. V5.

[108] Analog Devices Inc., One Technology Way, P.O. Box 9106, Norwood, MA 02062-9106, *ADL5240 Data Sheet – 100 MHz to 4000 MHz RF/IF Digitally Controlled VGA.* Rev. A.

[109] Hittite Microwave Corporation, 20 Alpha Road, Chelmsford, MA 01824, *HMC218AMS8E – GaAs MMIC SMT double-balanced mixer, 4.5–6 GHz*, v00.0411 ed. http://www.hittite.com/products/view.html/view/HMC218AMS8E.

[110] Mini-Circuits, P.O. Box 350166, Brooklyn, NY 11235-0003, *HFCN-6010+ Data Sheet – Ceramic High Pass Filter.* Rev. C.

[111] Mini-Circuits, P.O. Box 350166, Brooklyn, NY 11235-0003, *GALI 2+ Data Sheet – Surface Mount Monolithic Amplifier DC–8 GHz.* Rev. D.

[112] Analog Devices, *AD9254 – 14-Bit, 150 MSPS, 1.8 V Analog-to-Digital Converter*, 2006. Rev. 0.

[113] Hittite Microwave Corporation, 20 Alpha Road, Chelmsford, MA 01824, *HMC320MS8G / 320MS8GE – GaAs MMIC low noise amplifier, 5–6 GHz.* v03.0308.

[114] Hittite Microwave Corporation, 20 Alpha Road, Chelmsford, MA 01824, *HMC313 / 313E – GaAs InGaP HBT MMIC broadband amplifier gain block, DC–6 GHz.* v06.0109.

[115] Mini-Circuits, P.O. Box 350166, Brooklyn, New York 11235-0003, *RLP-137+ – Metal Shield Low Pass Filter DC to 137 MHz.* REV. A.

[116] Hittite Microwave Corporation, 20 Alpha Road, Chelmsford, MA 01824, *HMC681ALP5E – 0.5 dB LSB GaAs MMIC 6-bit digital variable gain amplifier w/ serial control, DC–1 GHz.* v00.0113.